

Analyses of field-aligned currents in Saturn's nightside magnetosphere

Thesis submitted for the degree of
Doctor of Philosophy
at the University of Leicester

by

Gregory James Hunt

Radio and Space Plasma Physics Group
Department of Physics and Astronomy
University of Leicester

October 2016

Analyses of field-aligned currents in Saturn's nightside magnetosphere

Gregory James Hunt

Abstract

This thesis is concerned with the study of magnetic field perturbations associated with large scale electrical current systems that flow along magnetic field lines. We will consider three such current systems within Saturn's magnetosphere. The first is associated with the subcorotation of plasma in Saturn's outer magnetosphere. The remaining two systems are directly associated with the northern and southern near-planetary period oscillations (PPOs) observed in Saturn's magnetic field, as well in other magnetospheric phenomena such as the Saturn kilometric radio emission and related auroral emissions.

Presented within this thesis are three detailed studies of the above current systems in Saturn's northern and southern nightside hemispheres during the 2008 interval of high-latitude orbits of the Cassini spacecraft. The first of these studies is a statistical analysis of the southern hemisphere field-aligned currents, which reveals for the first time their form, magnitude and position is modulated by the phase of the southern PPO system. By exploiting the symmetry properties for the two main field-aligned current systems, they are approximately separated. Due to the smoothing effects of the statistical study the second study focuses on the structure of the southern hemisphere field-aligned current sheets, in terms of their strength and position. The positional modulation is quantified, and the phasing indicates the origin of the southern PPO system is flows in the polar atmosphere. Finally, the third study concerns the northern hemisphere field-aligned current signatures, this reveals that these are modulated in form and magnitude by not only by the northern PPO system, but also the southern PPO system. This provides the first direct evidence of the proposed interhemispheric current flow. Together, these studies provide new insights into the behaviour of the field-aligned currents and can place constraints on the theoretical discussions of the origin and driving of the Saturn's aurora and periodicities.

Acknowledgements

Firstly, I would like to thank Stan for being a fantastic supervisor. His insight, knowledge and willingness to share these, have made working with him an excellent experience. I also thank Gabby for the office chats, I will miss these in the future! In addition, I thank Emma for being a great second supervisor. Also I thank my co-authors Igor, Elena, Vladimir, Michele, and Andrew for providing data central to this thesis.

I could not have asked for a better suited group to complete this thesis than RSPP. There are the perfect balances of work and play, tea and cake, pub and curry. So I thank everyone past and present during my time in the group for making it a truly enjoyable time over the last 3 years. It has been a privilege to be part of RSPP! Special thanks to the tea and milk bringers (Jasmine, Ben, Katie R, Sam), to the crossword printers (John, Roger), to the journal clubbers (John, Jasmine, James B, Maria) and to my office mates (Gabby, Katie R, Sam, Matt and Tim B) of F64A. Thanks for all the laughs, jokes, and Babs times!

I thank CrossCountry trains for providing a surprisingly reliable train service. I also now know it takes less time to complete a thesis than to complete the platforms at Birmingham New Street station!

I thank Mum, Dad, and Megan for their continued support, which has allowed me to be where I am now. Lastly, to Caitlin, without you there with encouragement, support, pointing out my achievements when I had doubts, and of course the odd cocktail or burger, I would not be here writing this.

Declaration

I, Gregory Hunt, declare that the work within this thesis is my own. The sources of the data present here are acknowledged, also I reference any material which is reproduced.

Sections of this thesis have been previously published in the following papers:

1. Hunt, G. J., S. W. H. Cowley, G. Provan, E. J. Bunce, I. I. Alexeev, E. S. Belenkaya, V. V. Kalegaev, M. K. Dougherty, and A. J. Coates (2014), Field-aligned currents in Saturn's southern nightside magnetosphere: Subcorotation and planetary period oscillation components, *J. Geophys. Res.*, 119, 9847-9899, doi:10.1002/2014JA020506.
2. Hunt, G. J., S. W. H. Cowley, G. Provan, E. J. Bunce, I. I. Alexeev, E. S. Belenkaya, V. V. Kalegaev, M. K. Dougherty, and A. J. Coates (2015), Field-aligned currents in Saturn's northern nightside magnetosphere: Evidence for interhemispheric current flow associated with planetary period oscillations, *J. Geophys. Res.*, 120, 7552-7584, doi:10.1002/2015JA021454.

Contents

1	Introduction	1
1.1	Overview	1
1.2	The physics of space plasmas	2
1.3	The heliosphere	9
1.4	Planetary plasma physics	11
2	The Saturnian system	21
2.1	Pre-Cassini observations	21
2.2	Overview of the Saturnian system	22
2.3	Saturn's magnetosphere	26
2.4	Periodic phenomena	42
2.5	Summary	55
3	Instrumentation and data methods	57
3.1	The Cassini-Huygens mission	57
3.2	Data analysis procedures	62
4	Southern hemisphere statistical analysis	70
4.1	Introduction	70
4.2	Data set	72
4.3	Survey of field-aligned current dependence on southern PPO phase	75
4.4	Statistical analysis	81
4.5	Discussion of statistical analysis results	93

4.6 Summary	99
5 Southern hemisphere four-sheet analysis	101
5.1 Four sheet analysis	101
5.2 Discussion of results	120
5.3 Summary	140
6 Interhemispheric current flow	143
6.1 Introduction	143
6.2 Overview of northern hemisphere data	144
6.3 Results	158
6.4 Summary and conclusions	188
7 Summary and conclusions	193
A Magnetospheric azimuthal fields	197
B Mapping azimuthal fields to the ionosphere	200
B.1 Subcorotation current system	200
B.2 PPO current system	202
B.3 Effect of the mapping	202
C Meridional current gradient limit	204
References	207

List of Figures

1.1	Sketch of a particles gyromotion along a magnetic field line	4
1.2	Heliospheric current sheet	10
1.3	Corotating interaction region	11
1.4	Magnetospheric configuration	12
1.5	Sketch of magnetic reconnection	14
1.6	Dungey cycle of Earth magnetosphere	15
1.7	Sketch of ionospheric Dungey cycle flow	18
1.8	Magnetosphere-ionosphere coupling currents	19
2.1	Pioneer 11, Voyager 1, and Voyager 2 flyby trajectories	22
2.2	Overview of atmospheric zonal winds	24
2.3	Enceladus' jets and plumes	25
2.4	Overview of Saturn's rings and inner moons	26
2.5	Empirical ion density models	30
2.6	Equatorial and ionospheric flows	33
2.7	Subcorotation field-aligned current system	35
2.8	Types of field-aligned current signatures from <i>Talboys et al.</i> [2011]	38
2.9	Field line distortion due to ring current	40
2.10	Voyager-1 and -2 SKR power spectra	43
2.11	Magnetic fields oscillations	44
2.12	<i>Andrews et al.</i> [2012] phases and periods	47
2.13	PPO fields and current systems	49
2.14	Southern hemisphere UV auroral PPO modulations	53

2.15 Plasma disk model <i>Gurnett et al.</i> [2007]	55
3.1 Cassini interplanetary trajectory	58
3.2 Schematic of the Cassini spacecraft	58
3.3 Principles of a fluxgate magnetometer	60
3.4 Photograph of the fluxgate magnetometer	61
3.5 Schematic of the Cassini Plasma Spectrometer	62
3.6 Southern PPO phase coordinate system	68
4.1 Southern hemisphere orbital plots	73
4.2 Southern hemisphere Rev data plots	76
4.3 Ionospheric azimuthal field $B_{\varphi i}$ vs southern PPO phase Ψ_S	82
4.4 Colatitudinal $B_{\varphi i}$ profiles divided into 8 non-overlapping 45° sectors of Ψ_S	85
4.5 Ionospheric horizontal meridional current I_m divided into 8 non-overlapping 45° sectors of Ψ_S	87
4.6 Separated southern hemisphere field-aligned currents depending on Ψ_S	90
4.7 Overview of southern hemisphere PPO-independent and PPO-related currents	95
5.1 Current sheet boundaries position and current as function of Ψ_S	103
5.2 Comparison of averaged I_m colatitudinal profile with four sheet profiles	105
5.3 Properties of the four current sheets as functions of Ψ_S	107
5.4 Boundary motion with Ψ_S	113
5.5 Shifted separated current colatitude profiles	115
5.6 Summary of overall southern hemisphere results	118
5.7 Estimate of the southern effective Pedersen conductivity	122
5.8 Radial mapping of field-aligned currents	129
5.9 Physical origin of boundary motion	133
5.10 Boundary oscillation phase delay	138
6.1 Northern hemisphere orbital plots	145

6.2	Comparison of northern and southern hemisphere $B_{\phi i}$ and I_m colatitudinal profiles	148
6.3	Individual northern hemisphere current colatitudinal profiles for different PPO phases	153
6.4	$B_{\phi i}$ vs $\Psi_{N,S}$ for different colatitude bands for both northern and southern hemispheres	160
6.5	I_m vs θ_{iN} divided into 16 sectors 90° of $\Psi_{N,S}$	165
6.6	Overview of the northern PPO-Independent current and both N and S PPO currents	169
6.7	Field-aligned currents when northern and southern PPO systems in phase or in antiphase	173
6.8	Northern and southern hemisphere I_m profiles	176
6.9	Data selection to investigate the variation of the oscillations' amplitudes along a flux tube	179
6.10	Latitude variation of the equatorial oscillations' amplitudes	181
6.11	Colatitude variation of polar oscillations' amplitudes	183
6.12	Northern ionospheric effective Pedersen conductivities	186
A.1	Comparison of magnetospheric models for different sub-solar magnetopause distance	198
B.1	Sketches of azimuthal field mapping	201
B.2	Effect of mapping the azimuthal field	203

List of Tables

2.1 Gauss coefficients for axisymmetric expansions for the internal magnetic field	27
5.1 Sinusoidal fits for the colatitude and the meridional current at current sheet boundaries in Figure 5.1	104
5.2 Sinusoidal fits for the current sheet parameters in Figure 5.3.	108

Chapter 1

Introduction

1.1 Overview

This thesis is concerned with the study of large-scale electrical current systems that flow along magnetic fields. These systems electrodynamically couple a planet's ionosphere and its magnetospheric environment through currents transverse to the magnetic field. We will consider three such current systems within Saturn's magnetosphere. The first is associated with the subcorotation of plasma in Saturn's outer magnetosphere. The remaining two systems are directly associated with the near-planetary period oscillations observed in Saturn's magnetic field, as well as with other magnetospheric phenomena such as the Saturn kilometric radio emission and related auroral emissions.

In this chapter, the fundamental physics which governs the behaviour of space plasmas will be reviewed, to provide the necessary framework to discuss the physics of Saturn's magnetosphere throughout this thesis. In Chapter 2 the Saturn system will be reviewed, with a particular focus on the magnetosphere and the ubiquitous planetary-period modulated phenomena. A brief discussion of the Cassini spacecraft, together with the data analysis procedures germane to this thesis, form Chapter 3. The work contained in Chapters 4 and 5 will focus on the field-aligned currents in the southern hemisphere, while Chapter 6 examines the northern hemisphere current signatures. Finally, an overview of the key results of the thesis is presented, together with possible

future directions of these studies, in Chapter 7.

1.2 The physics of space plasmas

A plasma is a gas where the atoms are dissociated into their positive and negative components, at least in part, such that on the whole the gas is electrically “quasi-neutral”. The distance over which charge separation can occur, the Debye length, λ_D , is given by

$$\lambda_D = \sqrt{\frac{\epsilon_0 k_B T_e}{n_e e^2}}, \quad (1.1)$$

where ϵ_0 is the permittivity of free space, k_B is Boltzmann’s constant, T_e the electron temperature, e the electron charge and n_e the number density of electrons. For the plasma to remain quasi-neutral the system size L must thus be large enough, such that $L \gg \lambda_D$ for collective shielding behaviour to happen. In addition there also needs to be enough electrons within the ‘Debye sphere’, given by

$$N_D = \frac{4\pi}{3} n_e \lambda_D^3, \quad (1.2)$$

for Debye shielding to be effective and the collective behaviour of the particles to be dominant, such that the plasma must therefore also satisfy $N_D \gg 1$.

A plasma does not need to be fully ionised, and can also contain a small fraction of neutrals. However, in an ideal plasma the occurrence of collisions between these and the charged components must be low enough that electromagnetic interactions still govern the behaviour of the gas. This can be examined by considering the electron plasma frequency given by

$$\omega_{pe} = \sqrt{\frac{n_e e^2}{m_e \epsilon_0}}. \quad (1.3)$$

This describes the oscillation frequency of electrons, of mass m_e about the ions in a quasi-neutral plasma. If neutrals are present, the average time between collisions between an electron and a neutral, τ_n , must be much greater than the period of the plasma oscillation, such that $\omega_{pe} \tau_n \gg 1$, for the gas to remain behaving as a plasma. As we see in section 1.4.2 collisions with neutrals can play an important role in deter-

mining the conductance of a plasma, and resulting currents.

Evidently the behaviours of electric and magnetic fields, \mathbf{E} and \mathbf{B} , are also fundamental to plasma physics, and are described by Maxwell's equations follows

$$\nabla \cdot \mathbf{E} = \frac{\rho_q}{\epsilon_0} \quad (1.4)$$

$$\nabla \cdot \mathbf{B} = 0 \quad (1.5)$$

$$\nabla \times \mathbf{E} = -\frac{\partial \mathbf{B}}{\partial t} \quad (1.6)$$

$$\nabla \times \mathbf{B} = \mu_0 \left(\mathbf{j} + \epsilon_0 \frac{\partial \mathbf{E}}{\partial t} \right), \quad (1.7)$$

where ρ_q is the charge density, \mathbf{j} is the current density, and μ_0 is the permeability of free space. Equations (1.4) and (1.5) are Gauss' laws of electric and magnetic fields, equation (1.6) is Faraday's law, and equation (1.7) is the Ampère-Maxwell law. Typically, in space plasmas the displacement current in equation (1.7) can be neglected for low frequency phenomena, so that equation (1.7) reduces to Ampère's law.

Firstly in this chapter we will consider the single particle motion picture, before introducing the fluid description, and then plasma environments important to the study of planetary magnetospheres.

1.2.1 Single particle motion

The simplest description of a plasma just considers the motions of the individual charged particles in the presence of electric and magnetic fields, with the collective behaviour of the charged particles not being dealt with.

Consider a particle with a mass m and charge q travelling through a magnetic field \mathbf{B} and electric field \mathbf{E} . This particle will experience a force \mathbf{F} given by

$$\mathbf{F} = q(\mathbf{E} + \mathbf{v} \times \mathbf{B}), \quad (1.8)$$

known as the Lorentz force. When $\mathbf{E} = \mathbf{0}$ and the magnetic field is uniform, it can be shown from equation (1.8) that the particle will gyrate around the magnetic field lines with an angular frequency

$$\omega_g = \frac{|q|B}{m}, \quad (1.9)$$

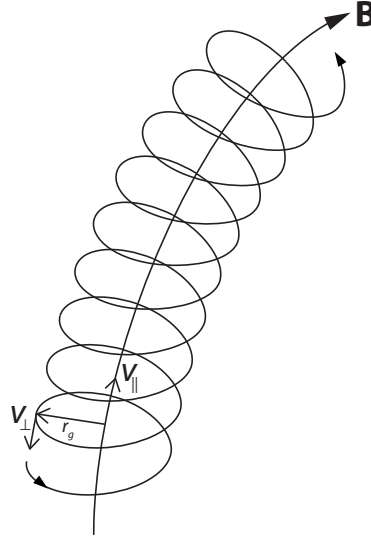


Figure 1.1: Sketch of a particle's gyromotion along a magnetic field line, \mathbf{B} . The parallel and perpendicular velocity component are labelled by v_{\parallel} and v_{\perp} , respectively.

where ω_g is called the gyrofrequency. The direction of the gyration is dependent on the particle's charge, such that if the magnetic field is out of the page a positive particle will move in a clockwise direction, while a negative particle will move in an anti-clockwise direction. The radius of a particle's circular orbit is found using the perpendicular velocity with respect to the magnetic field, as follows here

$$r_g = \frac{v_{\perp}}{\omega_g} = \frac{mv_{\perp}}{qB}. \quad (1.10)$$

This is called the gyroradius of the particle. The centre of the orbit is known as the guiding centre. The particle may also have a velocity component parallel to the magnetic field, v_{\parallel} , such that the gyrating particle will move along the field lines in a helical path, as show in Figure 1.1.

When considering both the v_{\perp} and v_{\parallel} components, their ratio defines the particle's 'pitch angle' α , shown by

$$\alpha = \tan^{-1} \left(\frac{v_{\perp}}{v_{\parallel}} \right). \quad (1.11)$$

This is the angle between the magnetic field and the particle's overall velocity vector \mathbf{v} . For $\alpha = 0^\circ$ the particle moves directly along \mathbf{B} , while for $\alpha = 90^\circ$ the orbit is circular.

In the presence of an electric field, \mathbf{E} , the particle's motion will be modified. Generally an electric field component parallel to the magnetic field in a space plasma is

cancelled out due to the mobility of electrons along a field line. However, in certain situations an E_{\parallel} component is required, such as in the auroral regions in the presence of strong currents where it is required to accelerate the electrons into the ionosphere [Knight, 1973]. In the presence of an electric field perpendicular to the magnetic field the particle guiding centre will drift in a direction perpendicular to both fields, given by

$$\mathbf{v}_E = \frac{\mathbf{E} \times \mathbf{B}}{B^2}. \quad (1.12)$$

We note that here the drift velocity \mathbf{v}_E is independent of the charge and mass of the particle, hence electrons and ions will drift in the same direction with the same velocity, known as the ‘ $\mathbf{E} \times \mathbf{B}$ drift’. It can be shown that this drift is equivalent to a frame transformation, such that in the frame of the moving particles the electric field is zero.

In general, the drift velocity, \mathbf{v}_D , due to any force, \mathbf{F} , acting upon a charged particle can be found from the expression

$$\mathbf{v}_D = \frac{\mathbf{F} \times \mathbf{B}}{qB^2}, \quad (1.13)$$

where \mathbf{E} in equation (1.12) is replaced by \mathbf{F}/q . Typical forces come from gradients and curvatures in the magnetic field, polarization, and gravitation. These forces are given by

$$\mathbf{F}_{\nabla} = -\mu \nabla B \quad (1.14)$$

$$\mathbf{F}_C = mv_{\parallel}^2 \frac{\mathbf{R}_C}{R_C^2} \quad (1.15)$$

$$\mathbf{F}_P = -m \frac{d\mathbf{E}}{dt} \quad (1.16)$$

$$\mathbf{F}_G = -m\mathbf{g}, \quad (1.17)$$

where \mathbf{R}_C is local radius of curvature of the magnetic field, \mathbf{g} the gravitational acceleration (typically in space plasmas this is negligible) and μ is the magnetic moment given by

$$\mu = \frac{mv_{\perp}^2}{2B} = \frac{W_{\perp}}{B}, \quad (1.18)$$

where W_{\perp} is the kinetic energy in the perpendicular gyration motion.

The magnetic moment of a particle is thus associated with its gyromotion, such that if the relative rate of change in the magnetic field is much less than the gyrofrequency, the magnetic moment is regarded as a characteristic constant. It is known as the first of three adiabatic invariants. Consider a particle moving from a region of low field strength to a high field strength region, for example in a converging magnetic field. As B increases, so does v_{\perp} to conserve μ . However, the particle's total energy ($W = W_{\parallel} + W_{\perp} = \frac{1}{2} m \mathbf{v}^2$) must remain constant too, assuming zero field-aligned electric field. As a result the particle's parallel energy, W_{\parallel} must decrease and hence its v_{\parallel} too. Consequently, when $\mathbf{v} = v_{\perp}$, such that $\alpha = 90^{\circ}$, the particle is reflected, or 'mirrored' back along the field. In the case of a planetary dipole field, there are two such mirror points at either end of a given flux tube, such that the particle bounces between the two mirror points and becomes trapped about the location of the field strength minimum.

The second invariant, J , also known as the longitudinal invariant, applies when a particle experiences changes in the field on a time scale that is long compared to that required for a particle to bounce between the mirror points, known as the bounce period. It is given by

$$J = m \oint v_{\parallel} ds, \quad (1.19)$$

taken around a bounce orbit. The third invariant, Φ , or drift invariant, is concerned with the conservation of magnetic flux enclosed by a particle's azimuthal drift orbit, and applies when the field is slowly varying relative to the period of the drift motion. As described above these invariants are constant so long as the spatial and temporal changes in the fields experienced by a particle are much slower than the oscillatory motion concerned. When a particle experiences field variations on a time scale shorter than a gyro/bounce/drift period then the corresponding invariant is no longer conserved.

1.2.2 Magnetohydrodynamics

The above description of single particle interactions with an electromagnetic field does not consider the collective behaviour of charged particles. To more fully describe this we can consider the particles as a charged (conducting) fluid using a theory known as ‘magnetohydrodynamics’ (MHD).

We can consider the motion of the plasma and field by combining equations (1.5)-(1.7), and a simplified Ohm’s law given by

$$\mathbf{j} = \sigma (\mathbf{E} + \mathbf{v} \times \mathbf{B}), \quad (1.20)$$

where the plasma conductivity, σ , is

$$\sigma = \frac{n_e e^2}{m_e \nu_c}, \quad (1.21)$$

where m_e is again the mass of an electron and ν_c is the collision frequency between ions and electrons, to show that temporal changes in the magnetic field are described by

$$\frac{\partial \mathbf{B}}{\partial t} = \nabla \times (\mathbf{v} \times \mathbf{B}) + \frac{1}{\mu_0 \sigma} \nabla^2 \mathbf{B}. \quad (1.22)$$

The two terms on the RHS are convective and diffusive, respectively. If the plasma is at rest then the first term vanishes leaving a diffusion equation. The diffusion is governed by the plasma conductivity as well as by the characteristic length, L , of field variations. Typically, in space plasmas these are very large, such that diffusion of the field is not significant. However, in regions where L or σ are small it does become more important, as we will see in later sections. For a highly conducting collisionless ($\nu_c \approx 0$) plasma, the convection term dominates the diffusion term, such that it can be shown that the field is tied to the motions of the plasma and vice versa. This phenomenon is known as the ‘frozen-in flux theorem’ or Alfvén’s theorem.

To better understand which of the two terms in equation (1.22) dominate, we introduce a dimensionless quantity known as the magnetic Reynolds number,

$$R_m = \frac{|\nabla \times (\mathbf{v} \times \mathbf{B})|}{|\nabla^2 \mathbf{B} / \mu_0 \sigma|} \approx \frac{VB/L}{B/\mu_0 \sigma L^2} = \mu_0 \sigma VL. \quad (1.23)$$

Here V is a typical perpendicular plasma velocity and L is the characteristic length over which \mathbf{B} varies. For collisionless space plasmas $\sigma \sim \infty$ and typically L is very large, such that $R_m \gg 1$, such that the diffusion term is neglected and the field is frozen into the flow. When $R_m \sim 1$, however, the diffusion term in equation (1.22) becomes important. This can occur when the collisional frequency becomes high, such as in an ionosphere, or L becomes small, as in the case of regions of the current sheets that separate regions of differing physical origin (see section 1.4.1). Under these conditions the field is no longer frozen to the plasma and will diffuse through it.

The macroscopic properties of a plasma are described in MHD by such parameters as the mass density, $\rho_m = nm$, the bulk velocity, \mathbf{V} , and the pressure, P . In this approach the electron and ion populations are combined, such that $n_e = n_i = n$, and quasi-neutrality holds. The mass continuity equation is given by

$$\frac{\partial \rho_m}{\partial t} + \nabla \cdot (\rho \mathbf{V}) = 0, \quad (1.24)$$

and the conservation of momentum equation by,

$$\rho_m \left(\frac{\partial \mathbf{V}}{\partial t} + (\mathbf{v} \cdot \nabla) \mathbf{v} \right) = -\nabla P + \mathbf{j} \times \mathbf{B} + \rho_m \mathbf{g}. \quad (1.25)$$

The terms on the RHS of equation (1.25) are the pressure gradient force, $-\nabla P$, the Lorentz force, $\mathbf{j} \times \mathbf{B}$, which can be derived by taking the cross product of Ampère's law (equation 1.7) with \mathbf{B} , resulting in

$$\mathbf{j} \times \mathbf{B} = \frac{1}{\mu_0} (\mathbf{B} \cdot \nabla) \mathbf{B} - \nabla \left(\frac{B^2}{2\mu_0} \right). \quad (1.26)$$

The first term on the RHS is the magnetic tension force due to a change in direction of the \mathbf{B} field, while the second term is the magnetic pressure force, which adds $B^2/2\mu_0$ to the overall pressure term. The final term in equation (1.25) is due to gravity and typically is neglected in space plasmas except for ionospheres. These equations, together with an equation of state, Maxwell's equations and Ohm's law, complete the system. It should be noted that this approach does not differentiate between species within the plasma, and as a result MHD is most applicable to systems that are slow changing and of large spatial scale. When frequencies approach the ion cyclotron frequency or length

scales are comparable to the ion gyroradius, MHD does not hold and a more complete theory, such as a multi-fluid MHD approach or consideration of the particle distribution functions is required. With the key concepts of space plasma thus discussed, we now apply these to the context of solar-planetary systems.

1.3 The heliosphere

The heliosphere is the region of space in which the Sun exerts its magnetic influence over the solar system, and ultimately also interstellar space. At its centre is the Sun, which is primarily comprised (by mass) of hydrogen ($\sim 73\%$), with the rest being helium ($\sim 25\%$) and heavier elements ($\sim 2\%$). Its total mass of $\sim 1.99 \times 10^{30}$ kg results in immense pressures in the core region, through quantum tunneling fusion of hydrogen to helium occurs, a process which heats the core to 15×10^6 K. The heat is transported outward over hundreds of thousands of km through radiation and convection processes to the visible surface, known as the photosphere, where the temperature is ~ 6000 K. The overlaying solar atmosphere, the solar corona, is substantially hotter at $\sim 1.5 - 2 \times 10^6$ K. Due to this high temperature and large pressure gradient between the solar corona and interstellar space, the pressure forces dominate over gravitational forces, leading to an outflow of plasma from the solar atmosphere, known as the ‘solar wind’ [Parker, 1958]. The solar wind starts as a sub-magnetosonic flow which then accelerates to super-magnetosonic velocity within a few solar radii. At larger distances the flow is of a near-constant velocity throughout the rest of the heliosphere. As the solar wind expands through the outer heliosphere, its density decreases as $n \propto 1/r^2$.

The large scale convective motion of plasma within the solar interior acts as a dynamo to generate, to first approximation, a dipolar field, which reverses polarity approximately every 11 years. Regions of intense field on the photosphere are known as sunspots due to their dark appearance compared to the disk of the Sun, indicating cooler regions, are associated with the origin of transient solar phenomena, such as solar flares and coronal mass ejections (CMEs). As a consequence of the ‘frozen-in’ field theorem (see section 1.2.2) the radial outward flow of the solar wind has the solar mag-



Figure 1.2: Artist's impression of the heliospheric current sheet. This illustrates the spiral form and reversal of polarity with respect to the planetary orbits, which are shown out to Jupiter. Image credit:GSFC/NASA

netic field embedded within it, known as the 'interplanetary magnetic field' (IMF). The Sun's rotation of ~ 27 days at the equator (longer at the poles) results in the field being pulled out into a spiral structure, which is known as the Parker Spiral [Parker, 1958]. At Saturn, the angle between the radial direction and a spiral arm is $\sim 87^\circ$, meaning the field is on average almost purely in the azimuthal direction [Jackman *et al.*, 2008]. This description is somewhat of a simplified picture, however, because due to the Sun's dipole being generally tilted relative to the spin axis, the IMF polarity will reverse twice per solar rotation. To separate these two senses a heliospheric current sheet is required, the form of which is shown near Solar minimum in Figure 1.2. This figure shows the three-dimensional, spiral, wave-like structure. At solar maximum the magnetic field structure is much more complex, due to the increased solar magnetic activity.

Observations of the solar wind have revealed there are two flow regimes, slow ($\sim 400 \text{ km s}^{-1}$) wind from the solar equatorial closed-field regions, and fast ($\sim 800 \text{ km s}^{-1}$) flows from 'coronal hole' open-field regions. When the fast solar wind interacts with the slow solar wind stable large scale structures form in the heliosphere, known as a corotating interaction region (CIR). Figure 1.3 shows the compression and rarefaction regions associated with a CIR. Ahead of the CIR a forward shock in the slow solar wind is formed, while behind there is a reverse shock. The regions of increased dynamic

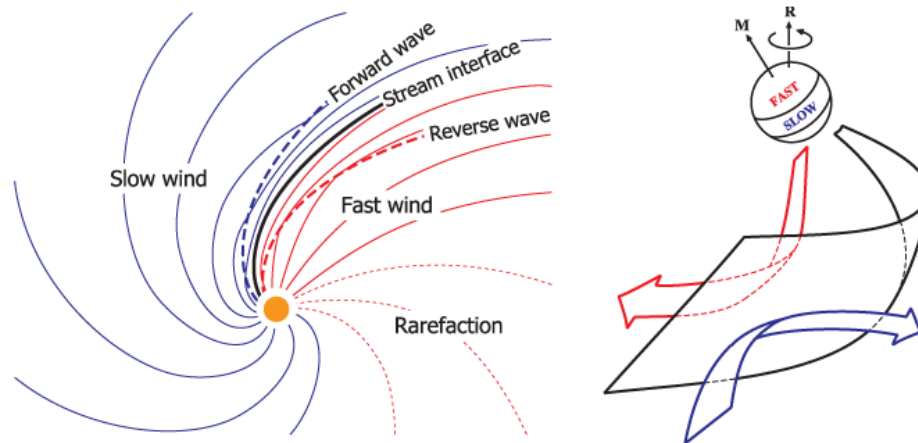


Figure 1.3: A sketch from *Owens and Forsyth* [2013] showing the interaction between different solar wind streams. On the left is the view in the ecliptic plane, fast wind is in red, while slow wind is in blue. On the right is a view from the Earth of the Sun with the offset of the magnetic axis, M , and rotational axis, R . The fast wind catches up the slow wind at the stream interface.

pressure associated with CIRs play a major role in driving the dynamics of Saturn's magnetosphere, as reviewed in the following chapter.

1.4 Planetary plasma physics

1.4.1 Planetary magnetospheres

A planetary magnetic field represents an obstacle in the supersonic outflow of the solar wind and embedded IMF. As a consequence of the frozen-in theorem discussed in section 1.2.2, the solar wind plasma and IMF, to a first approximation, cannot directly mix with the planetary field and plasma environment. Hence, a magnetic bubble is effectively formed around the planet, known as the 'magnetosphere'. A sketch of Earth's magnetosphere is shown in Figure 1.4. We focus on Earth as a 'standard model' of a magnetosphere before discussing Saturn's in Chapter 2. As discussed in section 1.3 the solar wind outflow is super-magnetosonic at the planets, such that the slowing of the flow to sub-sonic speeds results is achieved via the formation of a shock upstream of the planet. This is known as the 'bow shock' as shown by the dashed line in Figure 1.4. Beyond the bow shock is a region of shocked heated flow, subsonic at the

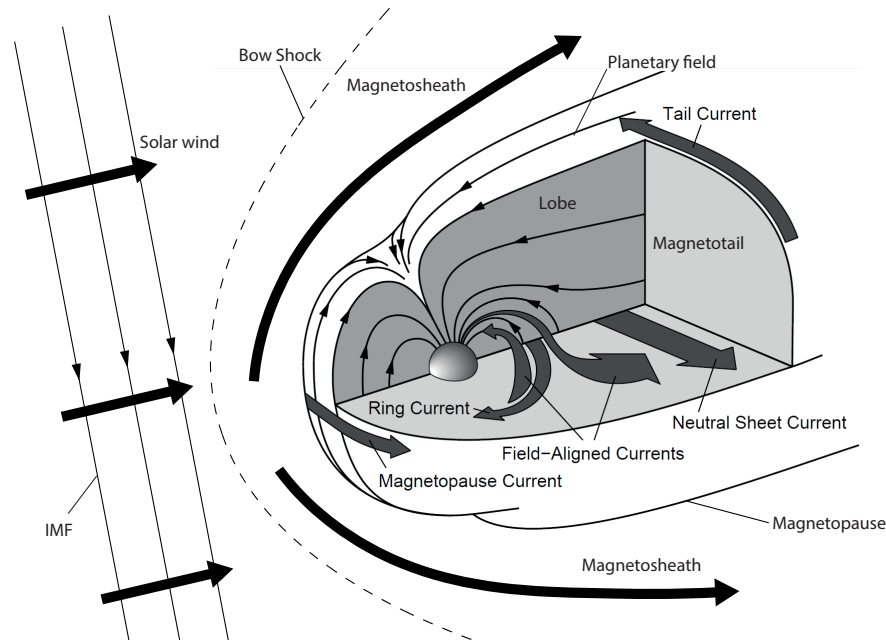


Figure 1.4: Sketch showing the magnetospheric configuration for Earth. The solar wind and IMF are to the left. The outer dashed line is the bow shock, followed by the magnetosheath and magnetopause. The magnetospheric currents are shown and directions indicated. In the case of Saturn these currents are oppositely directed due to the difference in magnetic field polarity. Adapted from *Baumjohann and Treumann [1997]*.

'nose' of the system, which is then deflected around the planetary field. This region is known as the magnetosheath. The magnetopause is then the boundary between solar wind-magnetosheath flow and the magnetospheric plasma environment. This scenario was first envisaged by *Chapman and Ferraro [1930]*, and results in the formation of a thin current sheet that effectively shields the solar wind flow from the planetary field, the associated currents being known as the Chapman-Ferraro currents. In Figure 1.4 these currents are shown to flow around the magnetopause boundary; they close on themselves and via the tail currents with a contribution to the cross tail neutral current sheet, which separates regions of oppositely directed field in the magnetotail, known as the lobes.

In addition to these large-scale current systems, the inner magnetosphere configuration is determined in part by the ring current. If we consider energetic particles trapped on magnetic field lines close to the planet, they will experience the magnetic gradient and curvature forces as described above by equations (1.13-1.15), and these forces will result in the particles drifting slowly around the planet in opposite direc-

tions. For the Earth's ring current the electrons drift eastward, while the ions move westward, this relative motion thus generating a westward current. In the case of Saturn's ring current it is comprised of currents due pressure gradient, pressure anisotropy and inertia of the rotating plasma [e.g., *Kellett et al.*, 2011]. The magnetic field generated by such a current acts to weaken the dipole field near the inner edge, while enhancing it in the vicinity of the outer edge. The behaviour distorts the field configuration outwards, leading to the formation of a 'magnetodisk' when the currents are strong, such as for Jupiter and Saturn. In the case of Saturn the planetary field has the opposite polarity to that of Earth and, consequently, the currents shown in Figure 1.4 that define Saturn's magnetosphere flow in the opposite directions.

Finally, currents can also flow along the magnetic field lines in order to couple the magnetosphere to the planet's polar ionosphere. These are known as field-aligned currents or Birkeland currents after the Norwegian physicist, Kristian Birkeland, who first proposed them. Typically, these are carried by the more mobile electrons, and will be discussed later in this chapter and in Chapter 2. These types of currents in Saturn's magnetosphere are the primary focus of this thesis.

The size of the magnetosphere is determined by the pressure balance between the dynamic ram pressure of the solar wind-magnetosheath flow and the magnetic pressure of the compressed planetary dipole field just inside the magnetosphere

$$\rho_{sw} V_{sw}^2 = \frac{B_{ms}^2}{2\mu_0}, \quad (1.27)$$

where ρ_{sw} and V_{sw} are the solar wind mass density and bulk velocity, respectively. The magnetic field just inside the magnetopause is given by B_{ms} , which is approximately twice the dipole field strength due to the thin current sheet that flows across the magnetopause. While this pressure balance is a good approximation for the Earth's magnetopause, at the gas giant planets the magnetospheric plasma pressure also acts to inflate the magnetosphere and extend the magnetopause subsolar stand-off distance.

The pressure balance and thin current sheet can both be described in terms of a single particle or fluid approach. Consider a non-magnetised flow of electrons and protons entering this boundary region, where they will experience a $\mathbf{v} \times \mathbf{B}$ Lorentz force,

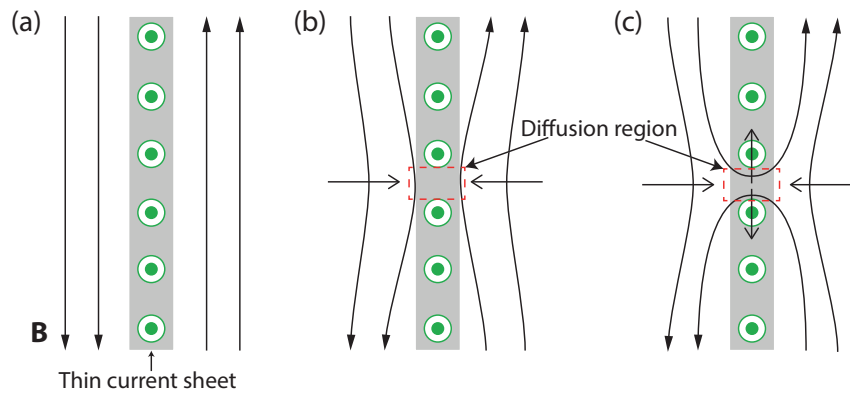


Figure 1.5: Sketches showing the process known as magnetic reconnection of oppositely directed fields. (a) shows the separation of these fields by a thin current sheet, which is out of the page. (b) and (c) show the diffusion of field lines through the current sheet resulting in a change of magnetic topology. The arrows indicate inflows and outflows, the red dashed box highlights the small diffusion region and reconnection site.

as shown by equation (1.8). Consequently, they will begin to gyrate; after half a gyration they will exit the magnetopause, effectively being reflected. The oppositely directed gyro-motion of ions and electrons corresponds to a current flow along the boundary that, in equilibrium, will support the switch in field across the boundary. Equivalently, in the fluid approach the rate of change of momentum associated with the reflection of particles at the boundary balances the magnetic pressure on the other side of the boundary.

In reality the solar wind flow is magnetised, which leads to a far more complex interaction between the solar wind and magnetosphere. In particular when magnetic fields are oppositely directed, a process known as magnetic reconnection can occur at the thin current sheet separating the different plasma and field regimes, such as at the magnetopause or in the magnetotail. This situation is sketched in Figure 1.5a. As a consequence of the small spatial scales involved, the frozen-in theorem can break down allowing the magnetic fields to diffuse through the current sheet, in a small region known as the diffusion region, as shown in Figure 1.5b,c. The magnetic field tends towards zero at the center of the current sheet, creating a null point and a 'X' like field geometry as also shown in Figure 1.5b. In three dimensions this point extends into and out of the page, and hence is known as a 'X line'. Within this region the IMF and plane-

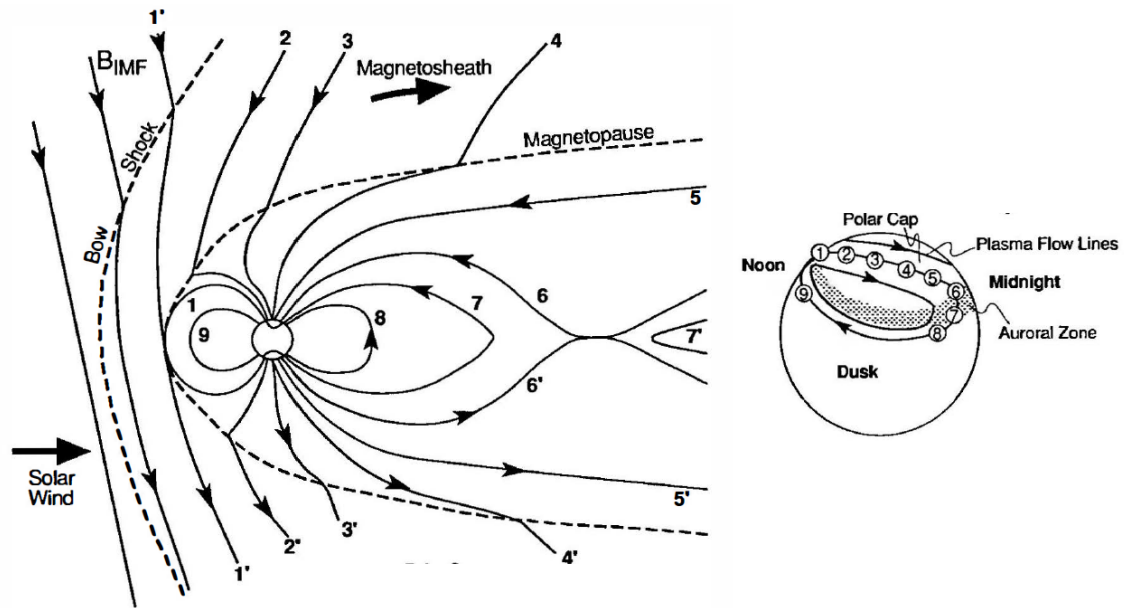


Figure 1.6: The Dungey cycle of the Earth's open magnetosphere. On the left is a magnetospheric view of a southward IMF field line reconnecting with the northward Earth field and then being transported by the solar wind into the magnetotail, where reconnection occurs sending the field line Earthward and back to the dayside via the flanks. Each stage of the cycle is numbered. On the right is the ionospheric projection of the cycle and resulting flows. From *Hughes* [1995].

tary field can become connected together, with the magnetic tension force of the newly connected field line causing it to contract away from the reconnection site along the current sheet, as shown in Figure 1.5c. If the field geometry is favourable for reconnection, the process can then continue. Therefore, magnetic reconnection is a means of changing the magnetic field topology, and by doing so also converts magnetic energy into particle heating and acceleration.

In the case of the Earth, reconnection between a closed northward planetary field and southward IMF can occur at the dayside magnetopause, as shown in Figure 1.6 by the field lines labelled 1 and 1'. This results in a newly opened field line with one footpoint in the ionosphere and the other connected to the solar wind; consequently, the flow of the solar wind transports this field line over the polar cap and into the tail region, as shown by field lines 2-5 in Figure 1.6.

Continuous southward IMF dayside reconnection and subsequent flux transport into the magnetotail causes a build-up of open flux in the tail. Magnetic reconnection then occurs in the cross tail current sheet, which closes the transported open field lines

6 and 6'. The newly closed field line is under tension due to the stretched configuration of the magnetotail, and as a result will relax into a dipolar-like field line, as shown by field lines 7 and 8. Finally, the closed flux will be transported back to the dayside via the dawn and dusk flanks, where if southward IMF is present the whole process can occur once more. This cyclic transport of magnetic flux within this 'open' magnetosphere is known as the Dungey cycle, after the original conception by *Dungey* [1961]. Magnetic reconnection between the solar wind and planetary fields allows the solar wind plasma populations to enter and mix with Earth's plasma populations at high latitudes and the driving of the magnetospheric system.

Figure 1.6 also includes an ionospheric projection of the motion of the footpoints of the labelled field lines, it shows one cell of the twin cell convection pattern that is imposed on the ionosphere. A full sketch of the Dungey cycle flows imposed on the ionosphere are shown by the black arrowed streamlines in Figure 1.7. These flows are directed antisunward over the pole from noon to midnight, and return as sunward flows in the dawn/dusk flanks. For the Earth, where in the northern hemisphere the \mathbf{B} field is directed into the planet and \mathbf{v} is antisunward this sets up a dawn-to-dusk electric field across the polar cap given by $-\mathbf{v} \times \mathbf{B}$ (see equation (1.12)), while the sunward return flows on the flanks result in an electric field directed poleward for the dusk section and equatorward for the dawn section. These are shown by the red arrows in Figure 1.7. Saturn's Dungey cycle flows will be discussed in Chapter 2, where Figure 2.6 illustrates, due to the rotational dominance of Saturn's magnetosphere, the Dungey return flow is 'resisted' to the dawn flank, such that it forms a single cell flow pattern.

1.4.2 Magnetosphere-ionosphere coupling

The upper atmosphere of a planet is partly ionized by solar UV, X-rays, and particle precipitation; therefore collisions can occur between the ions, electrons and neutrals as the flow from e.g. the Dungey cycle is imposed upon the ionosphere. These collisions will result in a velocity difference between the ions and electrons. Consequently, currents will flow, $\mathbf{j} = n_e e (\mathbf{v}_i - \mathbf{v}_e)$. We consider the equations of motion for both the

ions and electrons, which have the form

$$m \frac{d\mathbf{v}}{dt} = q(\mathbf{E} + \mathbf{v} \times \mathbf{B}) - m\nu_c(\mathbf{v} - \mathbf{u}), \quad (1.28)$$

where ν_c is the collision frequency, and \mathbf{u} is the velocity of the collisional particle. Using the neutral rest frame ($\mathbf{u} = \mathbf{0}$) and assuming steady-state conditions ($d\mathbf{v}/dt = 0$) this can be simplified to obtain expressions for \mathbf{v}_i and \mathbf{v}_e , from which the current density can be determined to be

$$\mathbf{j}_\perp = \sigma_P \mathbf{E}_\perp - \sigma_H \frac{\mathbf{E}_\perp \times \mathbf{B}}{B}, \quad (1.29)$$

where σ_P and σ_H are the Pedersen and Hall conductivities, respectively. These are given by

$$\sigma_P = n_e e^2 \left(\frac{1}{m_e} \frac{\nu_{en}}{\omega_e^2 + \nu_{en}^2} + \frac{1}{m_i} \frac{\nu_{in}}{\omega_i^2 + \nu_{in}^2} \right) \quad (\text{Pedersen}), \quad (1.30)$$

$$\sigma_H = n_e e^2 \left(\frac{1}{m_e} \frac{\omega_e}{\omega_e^2 + \nu_{en}^2} - \frac{1}{m_i} \frac{\omega_i}{\omega_i^2 + \nu_{in}^2} \right) \quad (\text{Hall}), \quad (1.31)$$

where $\nu_{in, en}$ are the frequencies of ion-neutral and electron-neutral collisions, and $\omega_{e, i}$ are the gyrofrequencies of the electrons and ions.

The current density described by equation (1.29) is comprised of two components. The first term describes the Pedersen current, which flows in the direction of \mathbf{E} , while the second term, the Hall current is in the direction $-\mathbf{E} \times \mathbf{B}$, opposite to the ionospheric flow pattern. Both are shown in Figure 1.7 by the solid and dashed green arrows, respectively. These currents in both cases are transverse to \mathbf{B} and therefore have associated $\mathbf{j} \times \mathbf{B}$ forces which act to balance the collisional drag forces. For the Pedersen current this is in the opposite direction to the $\mathbf{E} \times \mathbf{B}$ drift, while for the Hall current this is the opposite direction to \mathbf{E} . For a uniformly conducting ionosphere the Hall currents will fully close within the ionosphere effectively along the flow streamlines. These currents are also non-dissipative ($\mathbf{j} \cdot \mathbf{E} = 0$). On the other hand the Pedersen currents are dissipative and play a role in Joule heating due to the dissipation of electromagnetic energy into the ionosphere.

For a given plasma and field configuration, it can be seen from equations (1.30) and (1.31) that it is the relationship between the gyrofrequencies and the neutral collision

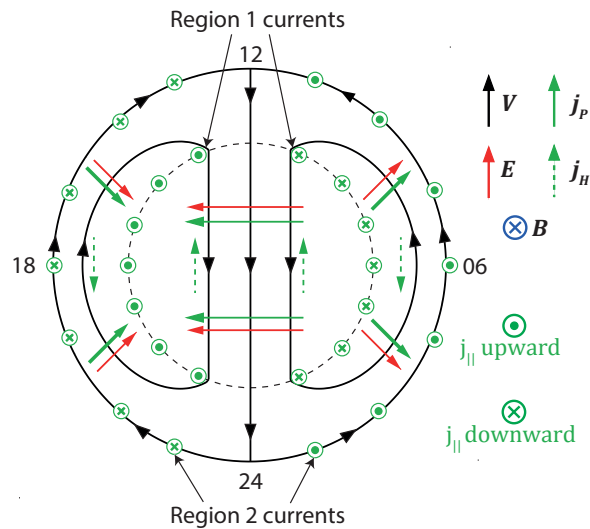


Figure 1.7: View of the Earth’s northern hemisphere ionospheric flows and regions of field-aligned currents associated with the Dungey cycle. Noon is at the top of the figure. The flows are shown by the black streamlines and electric field directions by the red arrows. The field-aligned currents are shown by the green circled dots and crosses, which indicate upward and downward currents. Ionospheric Hall currents, j_H , flow in the opposite direction to the plasma flows, while the Pedersen currents, j_P , flow in the direction of the \mathbf{E} field, as shown by the dashed and solid arrows, respectively. The background magnetic field here is into the page. The dashed circle is the boundary between open and closed field lines. Adapted from *Cowley* [2000].

frequencies that determines the resulting conductivity. Ultimately, these collisional frequencies depend directly on the number of neutrals within the ionosphere. While the Pedersen conductivity peaks near the point where the ion gyrofrequency and ion-neutral collision frequency are equal, the Hall conductivity peaks where the ions are collision-dominated, which occurs at a slightly lower altitude.

The flow imposed from the Dungey cycle over the polar cap pulls the magnetic field lines with it, while in the ionosphere due to the drag by ion-neutral collisions the field line footpoints lag behind the ‘pulling’ flow. The field and associated $\mathbf{j} \times \mathbf{B}$ forces extract energy from the magnetosheath flow. This flow shear transfers stress by the tilt of the field to the ionosphere as shown in Figure 1.8a, where the force applied balances the drag experienced by the ions. The direction of the energy transfer is given by the Poynting vector, \mathbf{N} , where $\mathbf{N} = (\mathbf{E} \times \mathbf{B})/\mu_0$, in this case as \mathbf{B} is downward and \mathbf{E} is out of the page, \mathbf{N} is downwards as shown by the red arrows in Figure 1.8a. In this view the ionosphere is the “load” ($\mathbf{j} \cdot \mathbf{E} > 0$) while the magnetosheath is the “generator” ($\mathbf{j} \cdot \mathbf{E} < 0$)

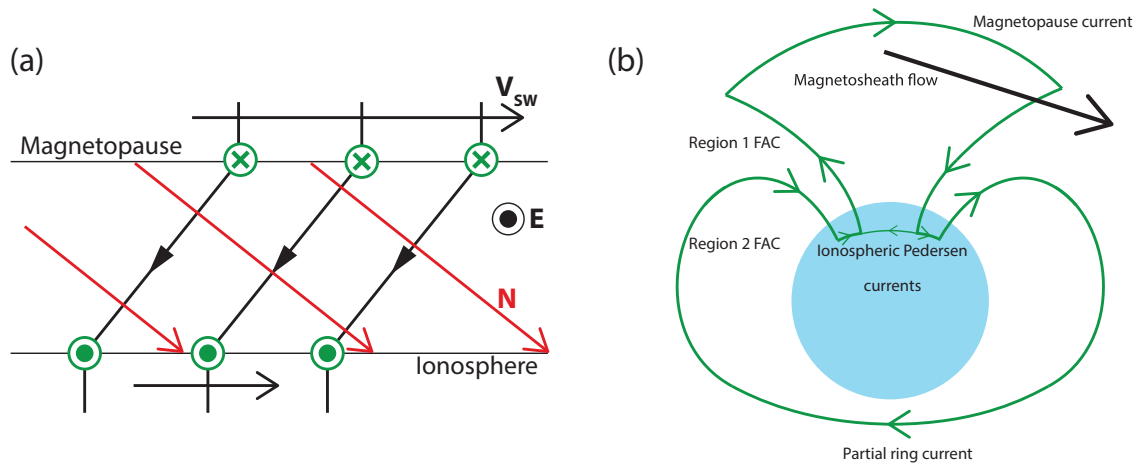


Figure 1.8: Sketches of the Magnetosphere-ionosphere coupling currents. (a) shows tilt of the magnetic field lines (black arrowed lines) due to the solar wind flow labelled V_{SW} . The transverse currents are shown by the green circled crosses (into page) and dots (out of page). The electric field is out of the page, such the Poynting vector is downward, N is downwards as shown by the red arrows. (b) shows the current circuit (green lines) which couples the magnetospheric and ionospheric currents.

in the planet rest frame. The tilt in the magnetic field implies through Ampere's law the presence of currents. The transverse currents in both regions are coupled by field-aligned currents to maintain quasi-neutrality and $\nabla \cdot \mathbf{j} = 0$, such that $j_{\parallel} = \nabla_{\perp} \cdot \mathbf{J}_{\perp}$, where \mathbf{J}_{\perp} is the ionospheric height-integrated horizontal current, which can be obtained from equation (1.29). Field-aligned currents, therefore, occur in regions with gradients in the Pedersen or Hall conductivities, as well as a diverging electric field.

The complete current circuit coupling the ionospheric Pedersen and the magnetopause currents is shown in Figure 1.8b. This figure illustrates coupling between the two plasma regimes and the ensuing transfer of stress. The current from the magnetopause flows into the ionosphere in the dawn sector at the boundary between open and closed field lines. Known as the Region 1 current, this is then closed by Pedersen currents to an equatorward set of oppositely directed field-aligned current known as Region 2 current, and partially across the polar cap. The current then flows through a partial ring current in the inner magnetosphere from dawn to dusk via midnight, back into the ionosphere as a Region 2 current at dusk and then out as a Region 1 current back to the magnetopause to complete the large scale system. These field-aligned current regions at Earth were first shown statistically by *Iijima and Potemra* [1976],

and now routinely seen in the Active Magnetosphere and Planetary Electrodynamics Response Experiment dataset [e.g., *Anderson et al.*, 2000].

In the case of Saturn, as will be discussed in the Chapter 2, the tilt in the field is typically in the opposite direction, such that the magnetic field in the magnetosphere lags its ionospheric footprint due to an internal plasma source within the magnetosphere. Consequently, momentum is transferred from the planet to the magnetospheric plasma, in the opposite direction as described here for the Earth. The Cassini spacecraft provided the first observations of auroral field-aligned currents at a planet other than Earth which showed this to be the likely case [e.g., *Bunce et al.*, 2008a; *Talboys et al.*, 2009a].

1.4.3 Summary

The description of magnetospheric dynamics and driving presented here has primarily focused on the Earth, where as we have seen the flow of energy and momentum is from the solar wind and ultimately ends in the ionosphere. For the gas giant planets the solar wind influence is decreased, in particular reconnection, such that the dynamics are much more controlled by the rapid rotation of the planet, with the transfer of momentum being from the planetary atmosphere to the magnetosphere. In addition, deep within Jupiter's and Saturn's magnetospheres there are volcanically active moons, which deposit large amounts of material into the magnetospheric environment. As this material becomes ionised and picked up by the magnetospheric flow it has a significant effect on the dynamics. A discussion of these effects for the case of Saturn follows in Chapter 2.

Chapter 2

The Saturnian system

2.1 Pre-Cassini observations

The Saturnian system has been studied from Earth for centuries with notable observers such as Galileo Galilei, Christiaan Huygens and Giovanni Cassini; together they identified the rings and larger moons. We had to wait until 1979 to have in situ measurements from the Pioneer 11 spacecraft. Following this fly-by there were another two spacecraft that visited Saturn in 1980 and 1981; these were the Voyager 1 and 2 missions, respectively. Equatorial trajectories of the three spacecraft are shown in Figure 2.1. The X axis points towards the Sun, while Y is towards dusk and Z completes the right handed set (Kronographic solar magnetic, KSM). Along the Voyager trajectories the day of year is marked together with bow shock (S) and magnetopause (M) crossings. From Figure 2.1 it can be seen that the three spacecraft entered Saturn's magnetosphere at approximately noon, passed closest to the planet at dusk and then Pioneer 11 and Voyager 2 exited at dawn, while Voyager 1 left in the morning sector some way down tail.

A key observation from the Voyager flybys was the modulation of the radio emission known as Saturn kilometric radiation (SKR). Due to SKR emission not being observable from Earth, the next opportunity to study the radio emission came from the Ulysses spacecraft. Its orbit took it out as far as Jupiter and highly inclined from the ecliptic plane, meaning it was able to detect the SKR emission remotely from Saturn. These measurements were obtained from the mid-90s until its mission end in 2009.

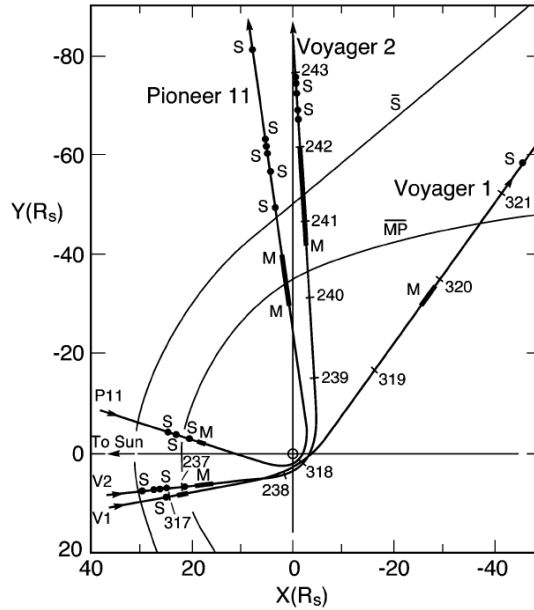


Figure 2.1: Plot showing the trajectories of the Pioneer 11, Voyager 1, and Voyager 2 flybys of Saturn in the X - Y plane, where X points towards the Sun and Y points toward Dusk. S and M mark the bowshock and magnetopause crossings, respectively. Taken from *Dougherty et al.* [2004].

Surprisingly, the SKR period that changed by $\sim 1\%$, implying the SKR period is not the planetary rotation period.

2.2 Overview of the Saturnian system

The body of Saturn is mainly composed of hydrogen ($\sim 96\%$) with helium being the next most abundant element ($\sim 3\%$), and the rest is methane ($\sim 0.4\%$) and other heavier elements [*Hubbard et al.*, 2009]. At the centre of Saturn is a rocky icy core of mass ~ 10 - $15 M_E$ (M_E Earth mass= 5.97×10^{24} kg) surrounded by an envelope of metallic hydrogen and helium, and it is this electrically conducting region that is thought to form the dynamo for Saturn's planetary magnetic field. Surrounding this region is an inhomogeneous mixed layer of hydrogen and helium and finally the outer molecular hydrogen and helium envelope. In total Saturn's mass is $\sim 95 M_E$. Saturn's rapid rotation results in its figure being an oblate spheroid, with a polar radius $R_P = 54364$ km and equatorial radius $R_E = 60268$ km; the latter radius is taken to define the "Saturn radius", R_S . The corresponding surface is defined as the 1 bar pressure level.

2.2.1 Atmosphere and ionosphere

Saturn's atmosphere is dominated by strong zonal (azimuthal) winds predominately in the eastward (E) direction, separated by much weaker westward (W) winds, leading to a highly variable atmosphere. It should be noted that in determining the azimuthal wind speed the planetary rotation was taken to be the System III (Voyager) rotation period as marked in Figure 2.2b. However, as mentioned in section 2.1, and discussed later in section 2.4, this value is not the internal planetary rotation rate, thus if a shorter period is used the westward (retrograde) flow speeds increase. Figure 2.2 from *Cowley and Provan* [2013] uses data from *García-Melendo et al.* [2011] to show these features in both the azimuthal velocity (panel a) and rotation period (panel b). The data shown here covers two altitude ranges $\sim 60 - 250$ mbar (green) and $\sim 350 - 700$ mbar (purple), where cover the tropopause and upper troposphere regions, respectively.

In panel b the zonal jet speeds are converted into rotation periods and compared with others as labelled in the figure, the blue and red bands show the period ranges of the northern and southern planetary period oscillations, respectively (see section 2.4 for more details). *Cowley and Provan* [2013] showed that there was no evidence of a physical link between the changes in magnetospheric and atmospheric periods, as proposed by *Fischer et al.* [2014], who associated the Great White Spot storm with such changes in SKR periods.

From the data provided by Cassini it has been shown that Saturn's upper atmosphere and ionosphere are highly variable in terms of species densities [*Nagy et al.*, 2009]. In addition, the thermospheric temperature of $\sim 300 - 500$ K is too high to be explained solely by the solar radiation input. *Cowley et al.* [2004b] argued that for the high latitude regions the additional energy input could be provided by Joule heating due to the closure of auroral currents. However, the redistribution of this heat globally is inhibited by rapid rotation [e.g., *Müller-Wodarg et al.*, 2006; *Smith et al.*, 2007].

Using radio occultations, ionospheric electron density profiles have been revealed over a wide latitudinal range. From these measurements it is then possible to infer ion densities through ionospheric models, which have shown that H^+ is the most domi-

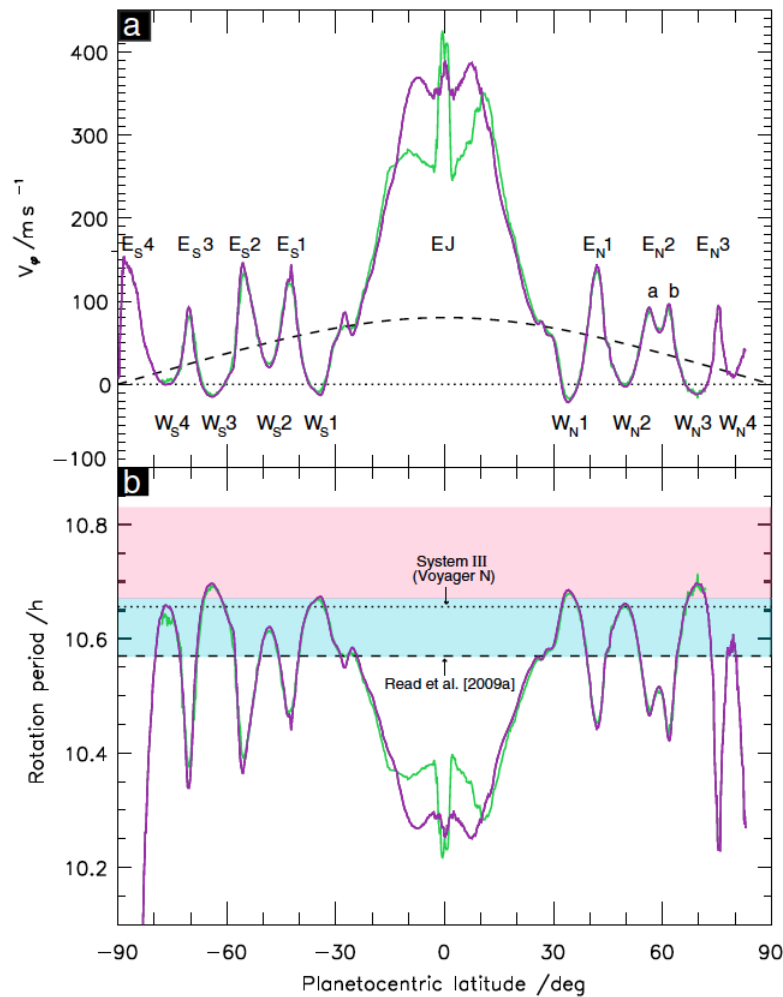


Figure 2.2: Overview of azimuthal (zonal) winds with respect to the System III Voyager rotation period (top panel), and in terms of rotation periods (bottom panel) vs latitude. E and W indicate the eastward (prograde) and westward (retrograde) directions. Taken from *Cowley and Provan [2013]*, data from *García-Melendo et al. [2011]*.

nant species at higher altitudes (>2000 km), while H_3^+ is more abundant at lower altitudes. The peaks in ion and electron densities are between 1000-3000 km, with the Pedersen layer at ~ 1000 km above the 1 bar pressure surface level, while the Hall layer is lower in altitude and broader [e.g., *Nagy et al., 2009; Galand et al., 2011*].

2.2.2 Moons and rings

There are more than 60 moons in orbit about Saturn, the majority of which are small, less than a few kilometres in size. One of the major results from the Cassini mission was the discovery that the small icy moon, Enceladus, located deep inside Saturn's magnetosphere at $\sim 4R_S$, is cryovolcanic. First evidence of this came from magnetometer

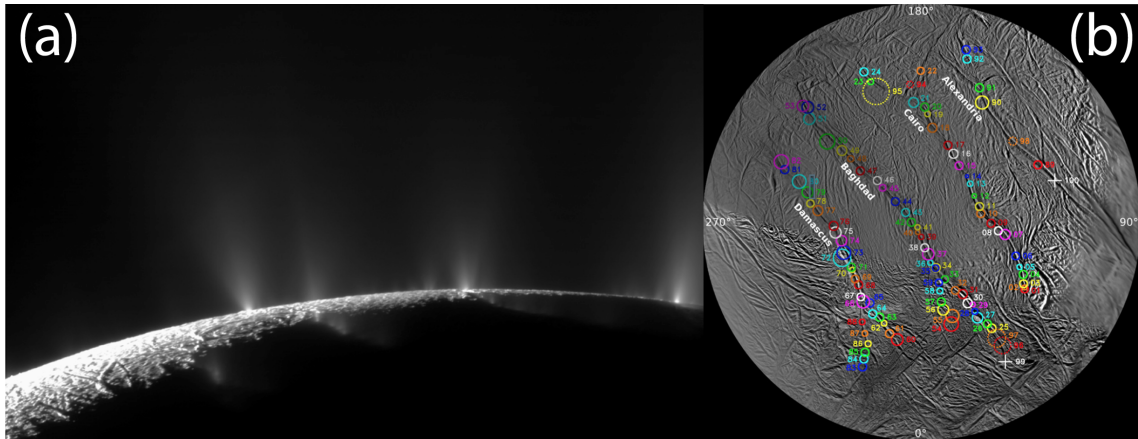


Figure 2.3: Images obtained by the ISS camera onboard Cassini, where (a) shows Enceladus’ jets along the cracks in the southern hemisphere, and (b) is a polar stereographic projection of the southern polar region with the locations of these jets marked. From *Porco et al.* [2014]

data, which indicated the presence of neutral outgassing from the southern polar region, due to the draping of the field around Enceladus [*Dougherty et al.*, 2006]. Additional observations from UV occultations of the plumes showed the presence of water vapour [*Hansen et al.*, 2006, 2008]. To date ~ 100 jets have been identified along the large cracks in the southern polar hemisphere known as the “tiger stripes”, as in Figure 2.3 [*Porco et al.*, 2006, 2014]. Ice particles in these jets have been shown to form structures in the E-ring [*Mitchell et al.*, 2015]. These jets and resulting plumes are, therefore, undoubtedly the major source of water group gas and plasma in Saturn’s magnetosphere. Estimates of the production rates are in the range $70\text{--}750\text{ kg s}^{-1}$ for neutrals, leading to $12\text{--}250\text{ kg s}^{-1}$ for plasma [*Bagenal and Delamere*, 2011]. The source of Enceladus’ cryovolcanism is thought to be due to a orbital resonance with Dione resulting in tidal motion and possible heating of the recently discovered subsurface ocean at the southern pole [*Spencer et al.*, 2009; *Iess et al.*, 2014].

Figure 2.4 depicts Saturn’s ring systems, which are defined as two types; dense rings (A,B and C) and tenuous rings (D,E and G), by their optical depth [*Colwell et al.*, 2009]. The dense rings span from $\sim 1.2\text{--}2.3R_S$. The E ring spans from the outer edge of the A ring to Titan ($\sim 20R_S$). They are comprised of ice grains ($\sim 99\%$), with the other 1% being made up of impurities like silicates and organics. The ring particles range in size from 1 cm to several metres, with 1-10 cm the most common [e.g., *Cuzzi et al.*, 2009].



Figure 2.4: Overview of Saturn's rings and inner moons Image Credit: <http://photojournal.jpl.nasa.gov/catalog/PIA03550>

2.3 Saturn's magnetosphere

2.3.1 Planetary magnetic field

The first measurements of Saturn's magnetic field were made during the Pioneer 11 flyby [Smith *et al.*, 1980], then again by both the Voyager spacecraft [Connerney *et al.*, 1982]. These early observations showed that Saturn's planetary magnetic field can be described by a magnetic dipole which is slightly displaced above the equator, and approximately aligned with the rotation axis, a unique property in the solar system. This description has been confirmed and expanded upon by the Cassini mission. Recent determinations of Saturn's internally-generated field have placed an upper limit on the dipole tilt of 0.1° [Burton *et al.*, 2010], while [Cao *et al.*, 2011] placed an upper limit of 0.06° on this tilt. By considering magnetic field measurements from Pioneer 11 through to Cassini, Cao *et al.* [2011] have also showed that there is no detectable secular variation.

In an approximately curl-free magnetic field, like that of the internal field, \mathbf{B} can be expressed as the gradient of a scalar potential, V , such that, $\mathbf{B} = -\nabla V$. Since $\nabla \cdot \mathbf{B} = 0$, V also satisfies $\nabla^2 V = 0$ and hence can be expressed in terms of spherical harmonics,

$$V = a \sum_{n=1}^{\infty} \left(\frac{a}{r}\right)^{n+1} \sum_{m=0}^n P_n^m(\cos\theta) [g_n^m \cos(m\varphi) + h_n^m \sin(m\varphi)]. \quad (2.1)$$

In the above expression a is the radius of the planet, r is the radial distance from the

Axisymmetric Models

Coefficients	<i>Connerney et al.</i> [1982]	<i>Davis and Smith</i> [1990]	<i>Dougherty et al.</i> [2005]	<i>Burton et al.</i> [2010]
	Z_3	<i>SPV</i>	<i>Cassini SOI</i>	
g_1^0 /nT	21535	21160	21084	21136
g_2^0 /nT	1642	1560	1544	1526
g_3^0 /nT	2743	2320	2150	2219

Table 2.1: Gauss coefficients for axisymmetric expansions for the internal magnetic field.

centre of the planet, θ is the colatitude, φ is the azimuth, P_n^m are Schmidt normalised Legendre functions of degree n and order m , g_n^m and h_n^m the Gauss coefficients for this spherical harmonic expansion of the field. These coefficients govern how strongly each harmonic determines the total field and are determined from data typically by a least-squares-fitting method. In reality spacecraft trajectories only give limited coverage in space for determining the Gauss coefficients, which can result in coupling and dependences between them. There have been various axisymmetric ($m = 0$) models fitted to magnetometer data from the Pioneer 11, Voyager 1 & 2, and Cassini spacecraft, the first three Gauss coefficients of which are shown in Table (2.1). It should be noted that the work presented later in this thesis employs the latest *Burton et al.* [2010] coefficients throughout.

The dipole tilt from the spin axis can be expressed as follows

$$\lambda_0 = \arccos \left(\frac{g_1^0}{\sqrt{(g_1^0)^2 + (g_1^1)^2 + (h_1^1)^2}} \right), \quad (2.2)$$

but for the models listed in Table (2.1) λ_0 is exactly zero due to the lack of current evidence for higher-order non-axial terms. Therefore, for the planetary field $B_\varphi \equiv 0$ [*Burton et al.*, 2010; *Cao et al.*, 2011]. The origin of Saturn’s apparently axisymmetric planetary field is still a major unanswered question, as currently this violates Cowling’s theory which states that it is impossible for a dynamo to support an axisymmetric field [*Cowling*, 1933]. Thus, the presence of an apparently axisymmetric field is troubling for dynamo theory. However, one leading explanation is the presence of a differential flow region above Saturn’s dynamo region which is effectively “axisymmetrizing” the measured field. This was developed by *Stevenson* [1980] and more recently shown

numerically by *Stanley* [2010].

Due to a relatively large quadrupole term g_2^0 the effective dipole is displaced from the equator toward the north along the spin axis by a distance given by

$$z_0 = a \left(\frac{g_2^0}{2g_1^0} \right). \quad (2.3)$$

Using the Gauss coefficients from the *Burton et al.* [2010] model given in Table 2.1 we find $z_0 = 0.036R_S$ or 2176 km, which results in the ionospheric magnetic field in the northern polar region being a factor of ~ 1.2 stronger than in the southern polar region.

2.3.2 Outer magnetospheric boundaries

As discussed in Chapter 1, a planetary magnetic field creates an obstacle in the solar wind flow leading to the formation of the bow shock and the magnetopause upstream of the planet. Saturn's outer boundaries had been modelled prior to Cassini, most notably by *Slavin et al.* [1985] who used the flybys shown in Figure 2.1 to fit the crossing data to a conical function to determine an empirical model, and who also showed that the sub-solar stand-off distances varied with the solar wind dynamic pressure in a power law relationship ($R_{BS,MP} \propto P_{sw}^{-a_2}$). Using Cassini data *Masters et al.* [2008] have shown that the bowshock is less flared compared to the *Slavin et al.* [1985] model and that $R_{BS} \propto P_{sw}^{-1/6}$. Typically the distance to Saturn's sub-solar bow shock is $\sim 25R_S$.

Saturn's magnetopause has been empirically modelled in a similar way, first by [*Slavin et al.*, 1985] and then by [*Arridge et al.*, 2006] who found typical values for $\alpha = 1/a_2 \sim 4.3$, with a typical distance to the sub-solar magnetopause of $\sim 22R_S$. Since these works several improvements have been made to the pressure balance equation. *Kanani et al.* [2010] included the internal warm and hot plasma pressures, while most recently *Pilkington et al.* [2014, 2015a,b] have included an internal suprathermal plasma pressure term, leading to revisions of $\alpha \sim 5.0-5.7$. *Achilleos et al.* [2008] showed that there was a bi-modal distribution of stand-off distances with peaks at $\sim 22R_S$ and $\sim 27R_S$ and suggested that this was in part due to internal processes, and not just solar wind variability. This was later investigated by *Pilkington et al.* [2015a], who showed

that for a constant solar wind dynamic pressure the magnetopause can move 10-15 R_S depending on the plasma properties close to the internal boundary. Again, a bimodal distribution was the most likely. A significant dawn-dusk asymmetry has been detected in the magnetopause; specifically, the magnetosphere on the dawn flank extends $\sim 7\%$ further out than the dusk flank [Pilkington *et al.*, 2015b].

At Saturn's magnetopause magnetic reconnection has been observed using in-situ measurements and auroral observations [e.g., McAndrews *et al.*, 2008; Jasinski *et al.*, 2016; Badman *et al.*, 2013; Meredith *et al.*, 2014a]. The role of magnetic reconnection in driving the outer magnetosphere has been debated. Early estimates of the reconnection voltage ranged from ~ 10 kV to ~ 200 kV [Jackman, 2004; Badman *et al.*, 2005], and more recently Masters [2015] derived similar values with the average being ~ 40 kV, which led the author to conclude that dayside reconnection is not typically a major driver. However, this figure does increase during solar wind compressions, and as Badman and Cowley [2007] suggested, the Dungey cycle can play a more important role during these times. In addition, Kelvin-Helmholtz instability has been observed on Saturn's magnetopause [e.g., Masters *et al.*, 2012]; these authors showed it is a common feature. However, there was a lack of dawn-dusk asymmetry in their position.

2.3.3 Plasma populations

There are many sources of plasma with the Saturnian system. The rings have an ionosphere consisting of mainly O^+ and O_2^+ ions produced by UV photosputtering and ionisation of the ring ice grains. Ionospheric outflow is a major source of plasma in Earth's magnetosphere. However, at Saturn there has been only one report of this by Felici *et al.* [2016], who propose ionospheric outflow could be a large source of plasma (H^+), especially during increased auroral activity. An unexpected result from the Cassini mission was that the moon Titan does not supply much plasma to the magnetosphere, inferred from the observed lack of N^+ , compared to Voyager measurements [Richardson and Sittler, 1990; Smith *et al.*, 2005].

Outside $\sim 3R_S$ the E ring, a large neutral torus of water and ice dominates Saturn's

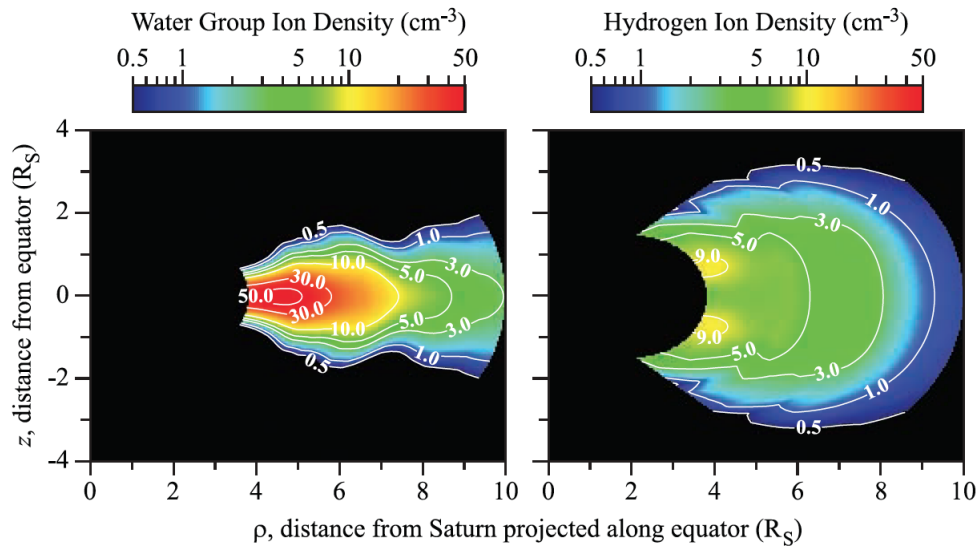


Figure 2.5: Contour plots from *Persoon et al.* [2009] showing modelled ion densities, with the water group and hydrogen ions separated.

magnetosphere. This ring has its origins in Encedulus' active jets, as discussed in section 2.2.2. Over time this neutral cloud is ionised through photoionisation and charge exchange to form a plasma of water group ions W^+ (O^+ , OH^+ , H_2O^+ , H_3O^+), in addition a H^+ ion plasma is formed. *Persoon et al.* [2009] determined (from Cassini Radio and Plasma Wave Science (RPWS) and Cassini Plasma Spectrometer (CAPS) measurements) models of these ion distributions. These are shown in Figure 2.5. It is clear that the heavier water group ions are more confined to the equatorial region due to centrifugal action compared to the lighter hydrogen ion plasma. This subcorotating magnetospheric plasma has a large influence on the structure of and dynamics of Saturn's magnetosphere.

Schippers et al. [2008] showed the inner magnetosphere is dominated by cold electrons, while in the outer magnetosphere only suprathermal electrons are observed. The cool dense plasma produced in the inner magnetosphere is transported radially outwards into the outer magnetosphere by the centrifugal interchange instability [e.g., *Mauk et al.*, 2009]. This instability leads to 'fingers' of the cool dense plasma extending outward into the hot lower density plasma; these flux tubes are replaced by ones containing the hot plasma which is then injected into the cool source region [e.g., *Burch et al.*, 2005; *Hill et al.*, 2005; *Dejong et al.*, 2010]. Recently *Thomsen et al.* [2016] showed

the penetration of suprathermal electrons into the inner magnetosphere supports the case for internal processes such as the interchange process in depositing hot electrons into the inner magnetosphere.

2.3.4 Dynamics and magnetosphere-ionosphere coupling

The dynamics of Saturn's magnetosphere have been determined from Voyager and Cassini spacecraft observations of significant subcorotating flows in the magnetosphere. Inside $\sim 3R_S$ plasma is corotating, and with increasing radial distance the angular velocities decrease, due to the conservation of angular momentum associated with outward radial transport. Typically, values are $\sim 80\%$ of rigid corotation between ~ 4 and $\sim 10R_S$, falling to $\sim 40 - 60\%$ out to $\sim 20R_S$, and to even smaller fractions on the nightside at larger distances [Richardson, 1986; Richardson and Sittler, 1990; Kane et al., 2008; Wilson et al., 2008, 2009; Müller et al., 2010; Thomsen et al., 2014]. Measurements of the ionospheric flows from infra-red observations of H_3^+ in the polar region shows flows are $\sim 30 - 50\%$ of rigid corotation [Stallard et al., 2004, 2007, 2008, 2012] in approximate agreement, while UV measurements show possible reconnection features near the auroral oval with values as low as $\sim 15\%$ [Radioti et al., 2013]. These observations provide evidence for substantial subcorotation in the polar cap region.

Figure 2.6a shows a conceptual sketch of the large-scale flows in Saturn's equatorial plane [Cowley et al., 2004a,b]. There are three flow regimes illustrated here. Firstly the innermost region is dominated by plasma production and subcorotation, in which the plasma is then transported radially outwards [Hill, 1979]. The inner dashed streamline marks the boundary at which plasma is lost downtail in the form of a plasmoid. As mass-loaded flux tubes rotate through the dusk sector into the nightside they are no longer confined by the magnetopause, and due to the large centrifugal forces the magnetic lines become stretched downtail until they reconnect, forming an 'X line' and releasing a plasmoid downtail and ultimately out of the magnetosphere. The emptied flux tubes then continue around to the dawn side within the outer dashed streamlines. This cycle is known as the Vasyliūnas cycle [Vasyliūnas, 1983]. Finally, the outermost

region is dominated by the solar wind interaction with the magnetosphere. In particular, reconnection at the dayside magnetopause with the IMF results in newly opened field lines being transported into the tail lobes over the poles, where reconnection in the tail occurs, closing the open flux tubes. As described in Chapter 2 section 1.4.1 this cycling of magnetic flux through a magnetosphere is known as the Dungey cycle. The Dungey return flow in the case of Saturn is then confined to the dawn side due to the Vasyliūnas cycle flows. *Badman and Cowley* [2007] suggested the Dungey cycle flows become significant in the outer magnetosphere during times when the magnetosphere is compressed, as the voltages associated with reconnection and the co-rotation of plasma then become comparable.

Evidence for both of these processes have been observed by the Cassini spacecraft, with plasmoids in the magnetotail being detected in magnetic field data [e.g., *Jackman et al.*, 2007, 2011, 2015; *Smith et al.*, 2016a]. These studies have shown the location of the X line to be highly variable. In addition plasmoids have been seen in plasma data [e.g., *Hill et al.*, 2008]. Recently, *Thomsen et al.* [2015] showed evidence of long-lasting Dungey-type reconnection in the magnetotail during a compression event as proposed by *Cowley et al.* [2005], where unbalanced reconnection during solar wind compressions leads to the tail collapse. Auroral and field-aligned current observations also support this process [*Nichols et al.*, 2014; *Meredith et al.*, 2014b; *Badman et al.*, 2016]. These observations support the view that Saturn's auroras are strongly influenced by solar wind conditions, as proposed by *Prangé et al.* [2004].

In Figure 2.6b these equatorial flows are mapped to the ionosphere, with the pattern of related field-aligned currents also being shown. These flows give rise to a four-sheet field-aligned current system, the structure moving from the pole is downward, upward, downward, and upward. The main upward current is associated with the auroral oval and is shown by the blue ring, positioned at the open-closed field line boundary.

Axisymmetry is an appropriate starting point for these discussions as it has been noted that the planetary spin and magnetic axes are closely aligned at Saturn to within

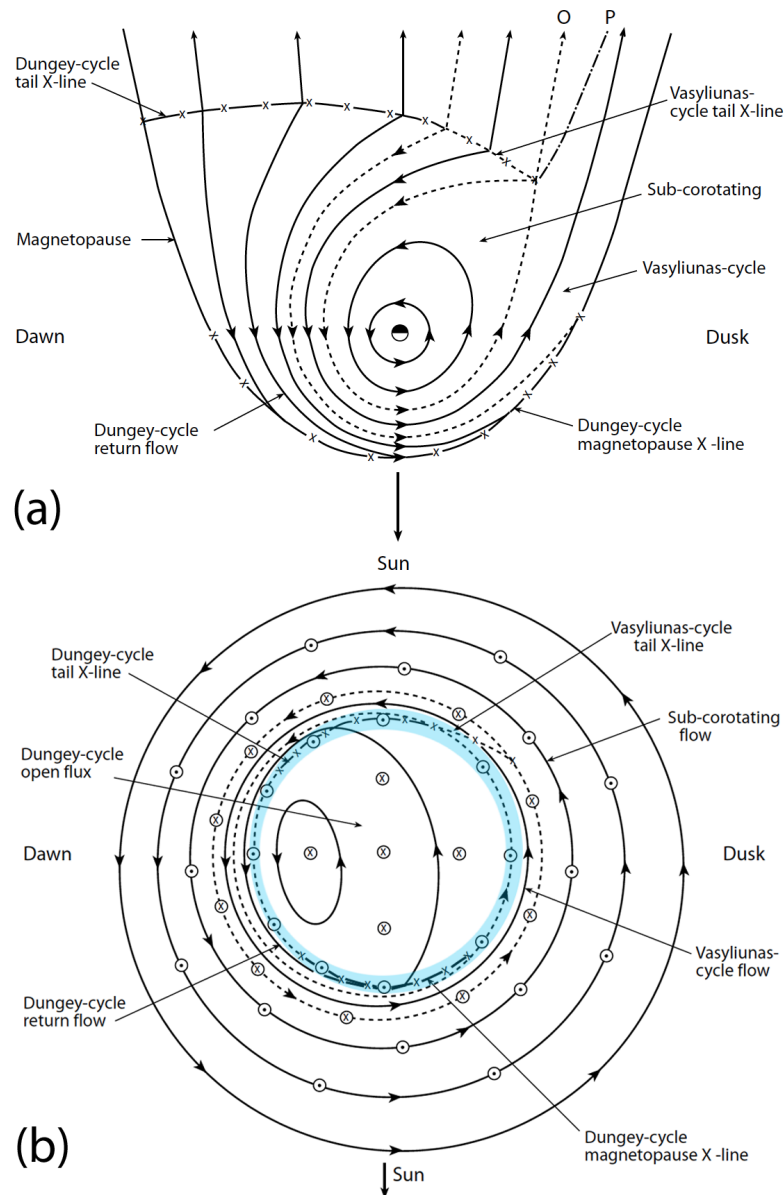


Figure 2.6: Sketches of the equatorial (a) and polar flows and field-aligned currents (b). The black arrowed lines are flow stream lines, the dashed lines are the boundaries between flow regimes. In (b) the blue circle highlights the position of the auroral oval, while the circled dots and crosses indicate the direction of the currents as upward and downward, respectively. In both sketches the Sun is to the bottom of the figure. Taken from *Cowley et al.* [2004a]

$\sim 0.1^\circ$ [Burton *et al.*, 2010], and that the principal processes are associated with sub-corotation of radially-transported plasma. Theoretical expectations based upon this and an earlier Jovian model [Cowley and Bunce, 2001] of these flows and field-aligned currents were first proposed for Saturn by Cowley and Bunce [2003]. Their model used an angular velocity profile for the magnetospheric plasma determined from the Voyager flybys and a constant 1 mho effective Pedersen conductivity. The field-aligned

current densities required to support the observed inner region of flows in Figure 2.6a were found to be insufficient to be the source of the the main auroral upward current, such that they concluded that the auroras were not associated with inner region corotation enforcement, as at Jupiter [e.g., *Hill, 1979*]. In the light of observations of polar ionospheric flow at $\sim 30\%$ corotation [*Stallard et al., 2004*], a modified angular velocity profile was used to include a velocity shear between the closed outer magnetosphere and the open polar region [*Cowley et al., 2004a,b*]. This shear gave a latitudinally narrow and intense upward field-aligned current capable of generating Saturn's main auroral oval, as highlighted in Figure 2.6b. Using data from the first high latitude passes of Cassini and concurrent HST UV auroral observations, this model could be modified once again. To achieve a better agreement between the modelled and observed values, the effective Pedersen conductivity was increased to 4 mho and the colatitudinal position was also modified [*Cowley et al., 2008; Bunce et al., 2008a; Bunce, 2012*]. These currents can also be affected by variations in the ionospheric Pedersen conductivity resulting from structured electron precipitation [*Galand et al., 2011*]. Such precipitation may be expected to be most intense at auroral latitudes, particularly in regions of upward field-aligned current, if the current densities are sufficient to require downward acceleration of magnetospheric electrons. Chapters 5 and 6 will investigate further the role at Saturn of the magnetospheric plasma angular velocity and the ionospheric Pedersen conductivity.

Physically, the subcorotation of magnetospheric plasma relative to the neutral atmosphere arises directly from pickup of the charged particles, together with the outward radial transport of this plasma and conservation of angular momentum (see Figure 2.7d) [e.g., *Hill, 1979; Pontius and Hill, 2009*]. This “mass loading” and radial transport results in the field lines being bent to later local times into a “lagging field” configuration (see Figure 2.7c), where on a given field line its equatorial part ‘lags’ behind its ionospheric footprint. The subcorotation of the plasma leads to an equatorward \mathbf{E} field in the neutral rest frame in the atmosphere and thus a horizontal equatorward Pedersen current flowing within the ionosphere. These transverse currents, must close

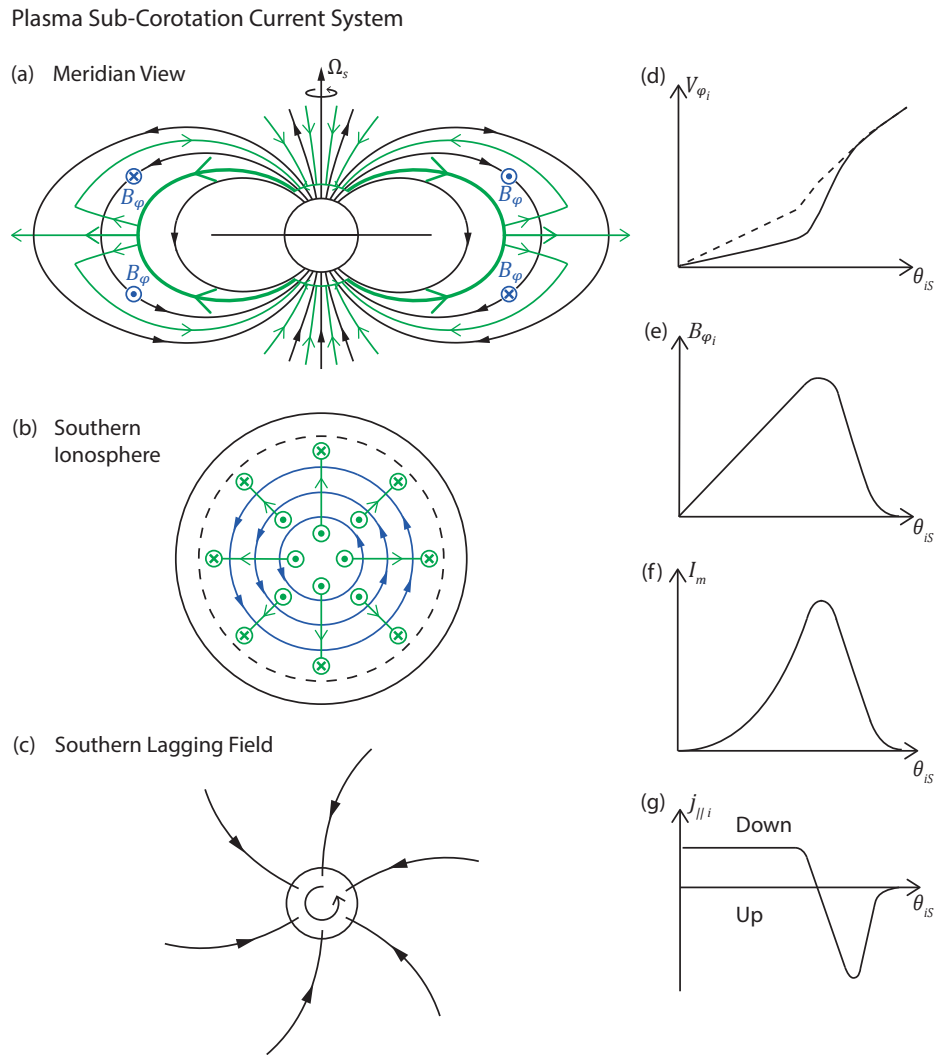


Figure 2.7: Sketches showing the field-aligned current system associated with subcorotation of plasma in Saturn’s magnetosphere. (a) is a meridian view, the black lines are the planetary field, green lines are the current system and the blue circled dots and crosses the B_ϕ . (b) shows in a similar format the southern ionosphere viewed from the north through the planet. Here the circled dots and crosses represent downward and upward currents, respectively. The dashed line is the equatorward limit of subcorotation. (c) depicts the lagging field configuration. On the right of the figure we show co-latitude profiles relative to the southern pole of key physical parameters, specifically (d) the plasma (solid line) and neutral atmosphere (dashed line) azimuthal velocities, (e) the azimuthal magnetic perturbation field just above the Pedersen layer of the southern ionosphere, (f) the associated meridional Pedersen current per radian of azimuth, and (g) the field-aligned current density, where, due to the downward direction of the southern background field (Figure 1a), positive values are downward and negative values upward.

along the field lines to ensure quasi-neutrality of the plasma ($\nabla \cdot \mathbf{j} = 0$).

The large scale current system (green lines) associated with magnetosphere ionosphere coupling that is fundamental in the transfer of angular momentum from the

planet's atmosphere to the magnetosphere is shown in Figure 2.7a. Due to the direction of Saturn's dipole magnetic field (black arrowed lines), the lagging configuration gives rise to negative and positive magnetic perturbations in the azimuthal direction, B_ϕ (blue), north and south of the equator, respectively. Through Ampère's law the associated current system consists of field-aligned currents directed downward over the polar region, followed a ring of upward (auroral) current at lower latitudes, which then close via Pedersen currents that flow equatorward in the ionosphere (Figure 2.7b, 2.7e, 2.7f, 2.7g), and then close in the equatorial plasma through a radially outward current (thus closing the circuit). A torque ($\mathbf{j} \times \mathbf{B}$) is applied to where these currents flow perpendicular to the magnetic field in the plasma. The torque applied in the ionosphere is balanced by the frictional torque from the collisions between ions and neutrals, this is transferred to the equatorial magnetospheric plasma through the bending back of the field lines, which acts to accelerate the magnetospheric plasma towards the angular velocity of the planet, Ω_S . There is a similar effect on the open field lines, where angular momentum is transferred to the magnetotail by a twisting of the tail lobe field lines [Isbell *et al.*, 1984].

Figures 2.7d-2.7g are sketches of expectations of key parameters based on the models of Cowley and Bunce [2003] and Cowley *et al.* [2004a,b], and the current system described above, plotted versus colatitude from the southern pole (θ_{iS}). Figure 2.7d shows the atmospheric (dashed line) and plasma (black line) azimuthal velocities ($V_{\phi i} \approx \rho \Omega_S$, where ρ perpendicular distance from magnetic/spin axis). In the polar region the plasma is subcorotating relative to this, before at lower latitude returning to corotation. Figure 2.7e shows the azimuthal field perturbation just above the ionosphere, $B_{\phi i}$, Figure 2.7f shows the meridional Pedersen current per radian of azimuth, I_m (ρ times the height-integrated current per meter of azimuth) where a positive gradient indicates upward field-aligned current while a negative gradient is indicative of a downward current, and Figure 2.7g shows the current density, $j_{\parallel i}$. The description here applies to the lagging configuration. If the plasma is supercorotating relative to the neutral atmosphere due to some dynamics, then the field configuration and per-

turbations are reversed, as is the direction of angular momentum transfer.

2.3.5 Previous field-aligned current observations

The first opportunity to study Saturn's field-aligned currents and make comparisons with the expectations discussed in section 2.3.4 came with the first set of highly inclined orbits of Cassini in late 2006 and early 2007. *Bunce et al.* [2008a] made a comparison between in-situ magnetic field and plasma measurements and concurrent HST observation of the southern summer UV auroral dayside oval. At the highest southern latitude a large positive B_ϕ indicating strongly subcorotating flows in the polar (open) region was observed, this then sharply decreased to small values which indicated near-rotation on closed field lines [*Bunce et al.*, 2008a; *Talboys et al.*, 2009a; *Southwood and Kivelson*, 2009], consistent with the model proposed by *Cowley et al.* [2004a,b]. The inferred net upward current per radian of azimuth was $\sim 5 \text{ MA rad}^{-1}$, with current densities in the range $\sim 280\text{-}320 \text{ nA m}^{-2}$. From these early observations it was clear that Saturn's main auroral oval is not due to corotation enforcement currents in the middle magnetosphere, like Jupiter. On these passes only weak azimuthal field perturbations were typically observed in the northern winter open polar region, while there was a stronger negative B_ϕ (lagging field) on outer closed lines, mostly likely due to enhanced ionospheric conductivity induced by particle precipitation. During this interval the latitude of the Sun in the south was $\sim 14^\circ$, such that the northern ionospheric open field region was in constant darkness, while the corresponding southern region was permanently sunlit. Overall, while generally these observations are in agreement with the modelling results of *Cowley and Bunce* [2003] and *Cowley et al.* [2004a,b, 2008], it is clear that it is necessary to include the effects of seasonal differences in ionospheric conductivity.

A second interval of high latitude passes occurred in 2008, providing ~ 40 similar orbits in the midnight sector for both the southern and northern hemispheres. This larger dataset provides detailed information on the typical signatures and also the variations. In terms of seasonal differences between the hemispheres, the latitude of the

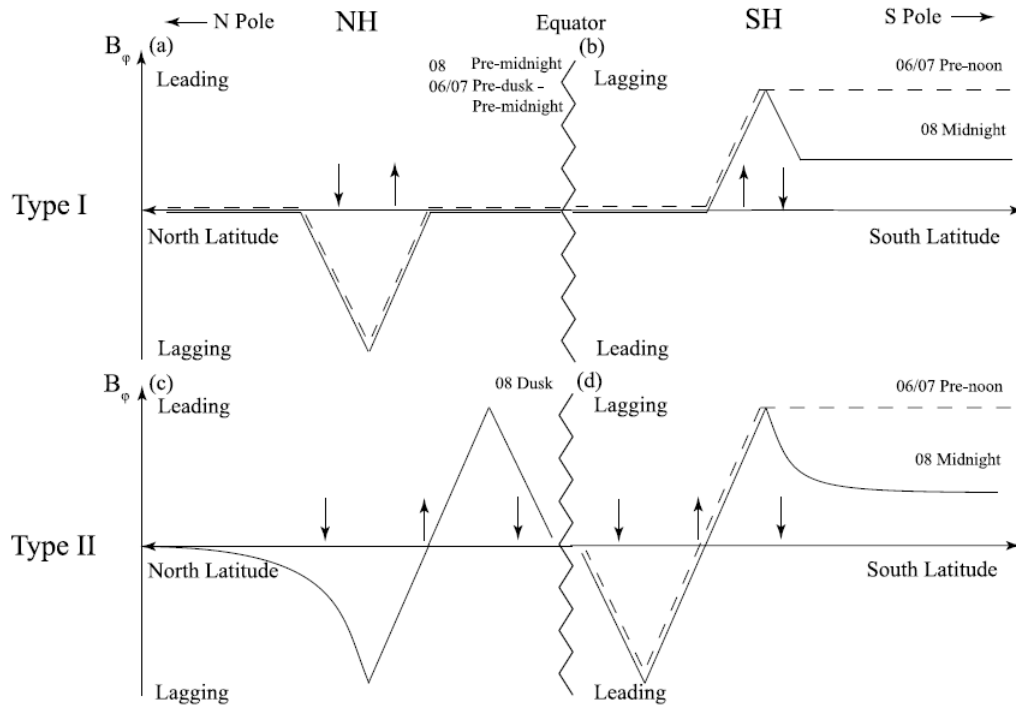


Figure 2.8: Sketch of the different observed B_ϕ structures during the pre-equinox intervals, plotted versus latitude and shown for both hemispheres. The arrows indicate the direction of the associated field-aligned current. From *Talboys et al.* [2011].

Sun at Saturn had decreased to $\sim 6^\circ$ in the south, meaning that much of the open ionospheric region in both hemispheres underwent day-night cycles. Figure 2.8 from *Talboys et al.* [2011] highlights the similarities and differences between the two intervals, as well as the two types of field-aligned current signatures observed [*Talboys et al.*, 2009b, 2011]. Type I is a purely lagging B_ϕ field perturbation, negative in the northern hemisphere and positive in the southern hemisphere. The structure of the B_ϕ in Figure 2.8a and b is indicative of downward and upward field-aligned current sheets carrying $\sim 1.4 \text{ MA rad}^{-1}$ and $\sim 2.2 \text{ MA rad}^{-1}$, respectively. The Type II signatures have a leading component, positive in the northern hemisphere and negative in the southern hemisphere, resulting in an increased upward current compared to Type I. Type II also has an additional downward current sheet equatorward of the upward current. Type II field-aligned currents are formed of poleward distributed downward current carrying $\sim 1.2 \text{ MA rad}^{-1}$, while the enhanced upward current carries $\sim 3.8 \text{ MA rad}^{-1}$, finally the equatorward downward current carries $\sim 1.8 \text{ MA rad}^{-1}$. In both types the poleward downward current is colocated with the boundary between open and closed

field lines, while the upward current maps to the outer closed magnetosphere and ring current. Revolution 89 displayed field-aligned currents that were unusually strong and were encountered at much higher latitudes than usual, in the presence of an unusual hot plasma population. *Bunce et al.* [2010] suggest this was the result of the closure of open flux in Saturn's magnetotail, likely to have been caused by a solar wind-induced compression of Saturn's magnetosphere [*Cowley et al.*, 2005]. *Jinks et al.* [2014] employed multiple datasets from these high latitude passes to show that the boundary between open and closed field lines (OCB) is $\sim 1.5^\circ - 1.8^\circ$ poleward of the poleward boundary of the auroral oval, thus placing the boundary in the south, on average, at 15.6° and in the at north 13.3° hemispheric colatitude.

More recently, 2013 saw a third set of high latitude passes. During April of that year there was an auroral observation campaign to coincide with these orbits. During the observations the magnetosphere underwent a solar wind compression as identified by an increase and extension to lower frequencies of the Saturn kilometric radiation [e.g., *Kurth et al.*, 2005, 2016]. The in-situ measurements and auroral observations showed a sequence of events, firstly the field-aligned currents intensified, next a localised region of bright aurora appeared at dawn, which was then followed by a contraction of the polar cap [*Badman et al.*, 2016]. These events were interpreted as evidence of the auroral response to tail reconnection following the compression [e.g., *Cowley et al.*, 2005; *Nichols et al.*, 2014]. Further work is required to fully assess how these passes differ from the earlier passes.

The above studies have all been based upon magnetic field measurements, from which the field-aligned currents were inferred. *Schippers et al.* [2012] claimed to identify field-aligned current systems using electron plasma spectrometer data close to the equatorial plane; however, the structure of these currents are not in agreement with those determined in the magnetic field studies. In addition, the current densities reported by *Schippers et al.* [2012] are several orders of magnitude too great compared with those deduced from previous magnetic field studies [e.g., *Bunce et al.*, 2008a; *Talboys et al.*, 2009a,b, 2011]. There is a further discussion of these results in Chapter 4

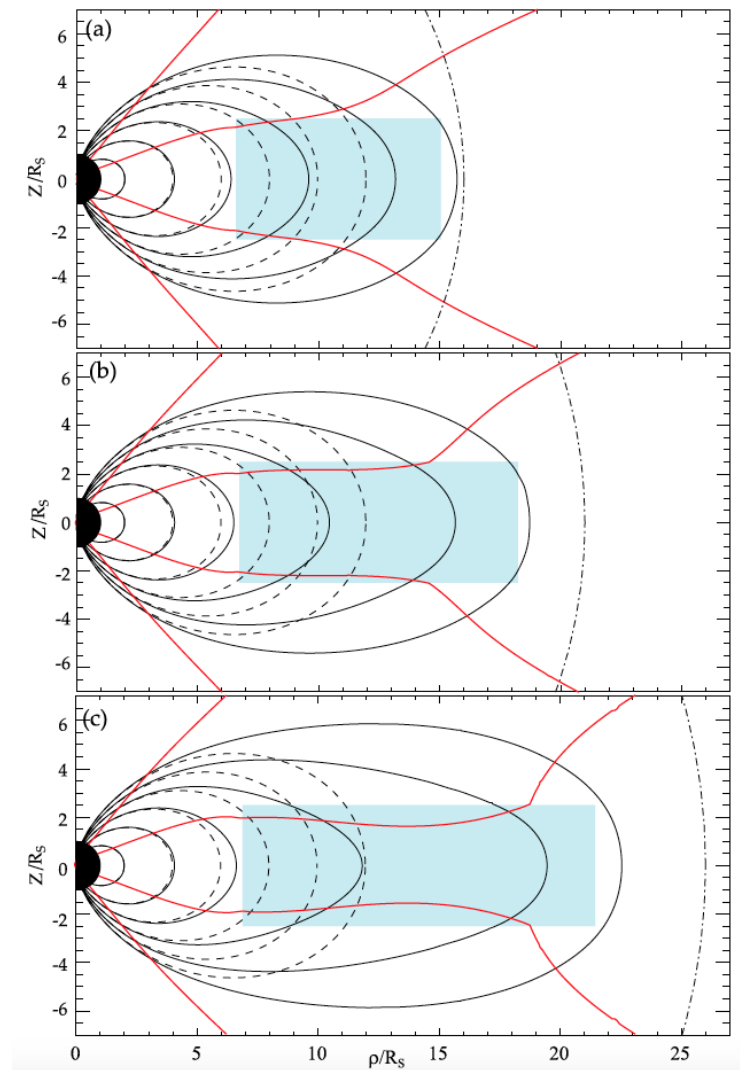


Figure 2.9: Plots of magnetic fields in a meridian plane showing the deformation due to the ring current. From top to bottom the magnetopause stand-off distance is 16, 21, and 26 R_S , as shown by the dot-dashed curve. The blue shaded area represents the modelled ring current as determined by *Bunce et al.* [2007]. The dashed lines are the internal field lines, while the black lines show the distended field. The red lines mark the region where the field line inclination is less than 30° from the equatorial plane. Taken from *Bunce et al.* [2008b].

section 4.5.

2.3.6 Magnetospheric currents

In addition to the B_ϕ perturbations due to field-aligned currents there are also azimuthal field contributions from the large-scale magnetospheric current systems, namely the magnetopause and tail currents. However, these are relatively small, larger-scale and curl-free within the magnetosphere. The effect of these large-scale currents is

to bend the field lines away from noon, thus on the dawn flank it is a lagging field, however, there is a leading configuration on the dusk flank [Bunce *et al.*, 2003]. The contribution of these current systems can be estimated using the paraboloid field model of Saturn's magnetosphere [Alexeev *et al.*, 2006; Belenkaya *et al.*, 2006, 2008]. First, the internal field is defined using the Gauss coefficients given in Table (2.1). This is then confined within a magnetopause which is assumed to be a paraboloid of revolution about the planet-Sun line. The calculated magnetopause current effectively shields the combined field from the dipole and a thin axisymmetric ring current from the IMF. The cross-tail current system then closes the system of magnetopause currents.

Saturn's ring current, to first approximation is axisymmetric, therefore, has no azimuthal magnetic field component [e.g., Kellett *et al.*, 2011]. However, its generated field acts to displace the planetary field lines away from planet. Saturn's ring current was first modelled by Connerney *et al.* [1983] using an axisymmetric disk of constant thickness, with the azimuthal current falling as $1/\rho$ from the dipole/spin axis. Using fits to Voyager data Connerney *et al.* [1983] determined the radial extent to be $8R_S \leq \rho \leq 15.5R_S$ with a thickness of $-3R_S \leq z \leq 3R_S$, also that the total azimuthal current flowing was ~ 10 MA. From Cassini measurements Bunce *et al.* [2007] showed that the total azimuthal current and outer radius were strongly correlated with the size of the magnetosphere, in particular the sub-solar magnetopause stand-off distance (R_{SSMP}). For a compressed magnetosphere ($R_{SSMP} \sim 16R_S$) the outer radius was found to be $\sim 15R_S$, whereas, for an expanded magnetosphere ($R_{SSMP} \sim 26R_S$) the ring current extends out to $\sim 21R_S$. This leads to a more developed 'magnetodisk' structure in the latter case than in the former case [Bunce *et al.*, 2008b; Arridge *et al.*, 2008a]. The distortion of modelled field lines is shown in Figure 2.9 [Bunce *et al.*, 2008b]. Bunce *et al.* [2007] concluded that the ring current is dominated by the inertial currents associated with the subcorotating Enceladus plasma, rather than hot plasma currents like at Earth. Kellett *et al.* [2011], however, showed that hot plasma (pressure) currents become important in the outer magnetosphere. They also showed that there is no significant evidence that the ring current parameters vary temporally or with local time. Due

to the seasonal variation of the solar wind on Saturn's magnetosphere, *Arridge et al.* [2008b], showed that further out in the magnetosphere the current sheet is warped into a bowl shape, with a 'hinging distance' of $\sim 29R_S$, such that in southern summer the current sheet is bent northwards.

2.4 Periodic phenomena

2.4.1 SKR observations and results

Gas giant planets have no visible surface features which can be used to determine the planetary rotation period, such that other means are required. In the case of Jupiter, modulated radio emissions were used to define its rotation rate [*Seidelmann and Divine*, 1977], also magnetic field oscillations inside the magnetosphere, due to the tilt of the rotating dipole. In the case of Saturn, a modulated radio emission known as Saturn kilometric radiation (SKR) was discovered by *Kaiser et al.* [1980]. Later *Desch and Kaiser* [1981] used Voyager radio time-series data to determine a period of modulation. The resulting high- and low-resolution power spectra are shown in Figure 2.10. In both panels there is a clear period at 10.6567h in the spectral power; this period was interpreted as the planetary rotation period and a slightly modified value of 10.65622 h was defined as Saturn's planetary rotation period by the IAU. The Voyager radio measurements showed that SKR emission is strongly circularly polarized, specifically that the SKR generated from the northern hemisphere is right handed while SKR generated from the southern hemisphere is left handed [*Warwick et al.*, 1981, 1982].

SKR emission is observed at frequencies ~ 20 -500 kHz and is characteristic of regions of upward current, generated by the cyclotron maser instability associated with downward-accelerated magnetospheric auroral electrons [*Lamy et al.*, 2010, 2011]. It was through observations of modulated SKR emissions that the first detection of distinct northern and southern periods in Cassini data was made [*Kurth et al.*, 2008; *Gurnett et al.*, 2009a]. The slow seasonal evolution of the periods was first observed in Ulysses observations remote from the planet [*Galopeau and Lecacheux*, 2000] which

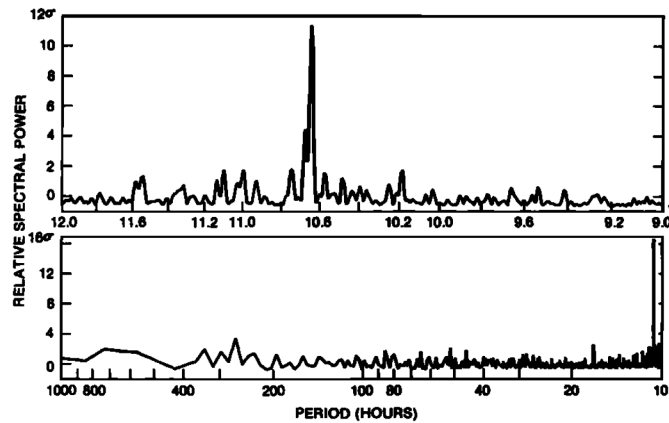


Figure 2.10: Power spectra of Voyager-1 and -2 SKR observations. The peak is at 10 h 39 min 24 sec (~ 10.66 h). From *Desch and Kaiser* [1981].

showed that the period changed by $\sim 1\%$ over a time scale of a few years, with subsequent variations in the Cassini-era [e.g., *Gurnett et al.*, 2011; *Lamy*, 2011]. Thus the initial interpretation of the radio period to be the internal rotation period was incorrect. The fundamentally rotational nature of these modulations was established for SKR by *Andrews et al.* [2011], *Lamy* [2011], and *Lamy et al.* [2013]. These studies showed that the strobe-like nature of SKR modulations initially deduced from Voyager observations results from the strong local time (LT) asymmetry in the power of the SKR sources. Like the UV auroras, the strongest of the hollow conically-beamed SKR emissions are those generated post-dawn at ~ 06 - 10 h LT [e.g., *Lamy et al.*, 2009]. These dominate the SKR emissions from post-midnight to noon via dawn, leading to strobe-like behaviour of the modulations in this wide sector, which encompassed both Voyager inbound and outbound fly-by trajectories. The existence of this LT asymmetry also indicates the possible presence of variations in the field-aligned current systems that are fixed in LT [*Southwood and Kivelson*, 2009].

2.4.2 PPO magnetic field perturbations and currents

Prior to the arrival of Cassini, the re-examination of the Pioneer and Voyager magnetometer data revealed a periodic signal in Saturn's magnetic field as shown in Figure 2.11, which was rather unexpected due to Saturn's near-axisymmetric planetary field (see section 2.3.1) [*Espinosa and Dougherty*, 2000]. Whilst this analysis did not reveal

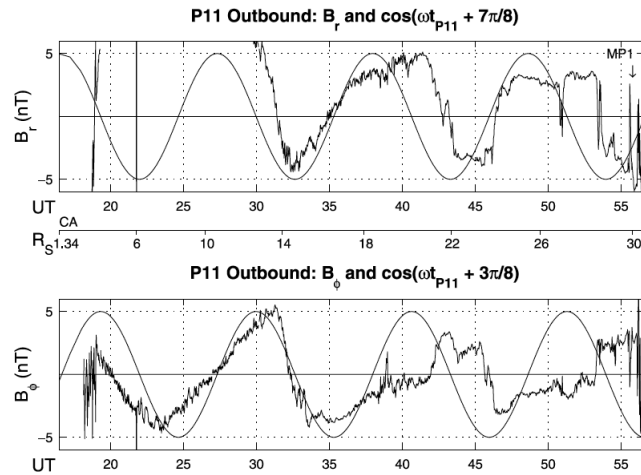


Figure 2.11: Magnetic field oscillations in the radial and azimuthal components from the Pioneer-11 fly-by shown as functions of time. Data shown are from CA to the magnetopause crossing. The overplotted sinusoidal function has the period shown in Figure 2.10, while in the bottom panel it is lagging by 90° ($\pi/2$ rads). From *Espinosa et al.* [2003a].

a precise period, the overplotted sinusoids at the 10h 39m 24s (10.6567 h) period from Voyager SKR measurements do show that the magnetic field oscillations are very similar in period. In addition, a key phase relation between the B_r and B_ϕ components was found, where B_ϕ is lagging B_r by 90° . Further analysis showed that the oscillations could not be the result of a tilted dipole due to the expected phase relation between B_r and B_ϕ being opposite to that observed [*Espinosa et al.*, 2003a]. Instead, an anomaly (potentially magnetic) was proposed to explain the observed periodicities by creating a longitudinal asymmetry, causing a compressional wave to spiral out through Saturn’s magnetosphere. This is analogous to a camshaft, and hence became known as the “camshaft” model [*Espinosa et al.*, 2003b].

The periods, phases and amplitudes of the magnetic field oscillations have been monitored throughout the Cassini mission and up to the time of writing. Following the “camshaft” model, *Cowley et al.* [2006] showed that the observed oscillation period due to the spiral wave would be Doppler shifted as a result of Cassini’s relative motion to the wave fronts and that this needs to be accounted for. By correcting for these shifts *Giampieri et al.* [2006] tracked a period of 10 h 47 min 6 s (10.79 h) over the first 14 orbits of Cassini and confirmed the azimuthal signal cannot be due to an internal non-axial magnetic field term. Following these came more in depth studies of the magnetic

field oscillations which estimated the form of the magnetic perturbation based upon the relative phases of the oscillation components with respect to a guide SKR phase [Kurth *et al.*, 2007, 2008]. In the equatorial core region (Dipole $L \leq 12R_S$), the r and θ components of the magnetic field were found to be in phase, while the φ component was lagging in quadrature (90°), the r and φ phase relation indicate a rotating quasi-uniform field at approximately the SKR period [Espinosa and Dougherty, 2000; Espinosa *et al.*, 2003a; Southwood and Kivelson, 2007; Andrews *et al.*, 2008, 2010a].

The first high-latitude orbits showed the oscillations also were present, if weaker, in the polar field regions [Provan *et al.*, 2009a]. However, it was evident that the phase relations had changed, the r and θ component were in phase with those components in the core region, while the polar φ components were in anti-phase with the core oscillation of the same component. These phase relations implied the form of the high latitude perturbation to be that of a rotating transverse dipole, although the phasing was not fully explained. The lack of phase order in the northern hemisphere was not clear until the discovery of two SKR periods [Gurnett *et al.*, 2009a]. Indeed, these data were re-examined by Andrews *et al.* [2010b], who showed the presence of two oscillation periods in the magnetic field data, one in the northern hemisphere and the other in the southern. These periods were shown to be within $\sim 0.01\%$ of the respective hemispheric SKR periods, ~ 10.6 h and ~ 10.8 h for the N and S hemispheres, respectively [Lamy, 2011]. It was also shown that at northern SKR maximum the quasi-uniform field pointed approximately toward the Sun, while at southern SKR maximum it pointed approximately downtail. These observations were interpreted as the result of two independent rotating field-aligned currents associated with each hemisphere, as opposed to the single interhemispheric field-aligned current system proposed by Southwood and Kivelson [2007]. To summarise, the polarizations of the field oscillation components are as follows,

- For southern core and polar oscillations, the r and θ components are in phase
- For northern core and polar oscillations, the r and θ components are in anti-phase

- For both N & S core oscillations, the φ components are in lagging quadrature with r
- For both N & S polar oscillations, the φ components are in leading quadrature with r

The two oscillations are superposed in the core region, such that they undergo constructive and destructive interference. The resulting combined oscillation is dependant upon the beat phase and the relative amplitudes of each oscillation. The phase ‘jitter’ noted by *Andrews et al.* [2008] was studied in more detail by *Provan et al.* [2011] in the light of the dual periods, and who showed that this is a consequence of the northern oscillations superposed on the southern oscillations in the equatorial region, with the deviations in phase occurring at the beat period. This provided further evidence that the field oscillations are the result of two rotating field-aligned current systems with differing periods.

Andrews et al. [2012] used the polarization of each system’s perturbations to directly determine both northern and southern phases, periods, and relative amplitudes. The oscillations can be expressed as sinusoidal functions such as

$$B_i(\varphi, t) = B_{0i} \cos(\Phi_g(t) - \varphi - \psi_i), \quad (2.4)$$

where i is the field component (r, θ, φ), Φ_g is a guide phase defined by a guide period τ_g close to the oscillation period, such that $\Phi_g(t) = 360t/\tau_g$, and φ is the azimuth as measured from noon increasing towards dusk. To determine the amplitude of each field component, B_{0i} , and the relative phase, ψ_i , equation (2.4) is fitted to magnetic field data with the internal field subtracted, which has also been filtered between 5 and 20h to isolate the PPO signals from signals which are much shorter in period and variations from large-scale currents which vary more slowly along Cassini’s orbit. The fit is done by a least squared method and on a pass-by-pass basis. The variation of ψ_i is controlled by the difference between the guide phase period and the field oscillation period, such that $\psi_i \approx \Phi_g(t) - \Phi_i(t)$ can be used to track the relative phase changes orbit by orbit.

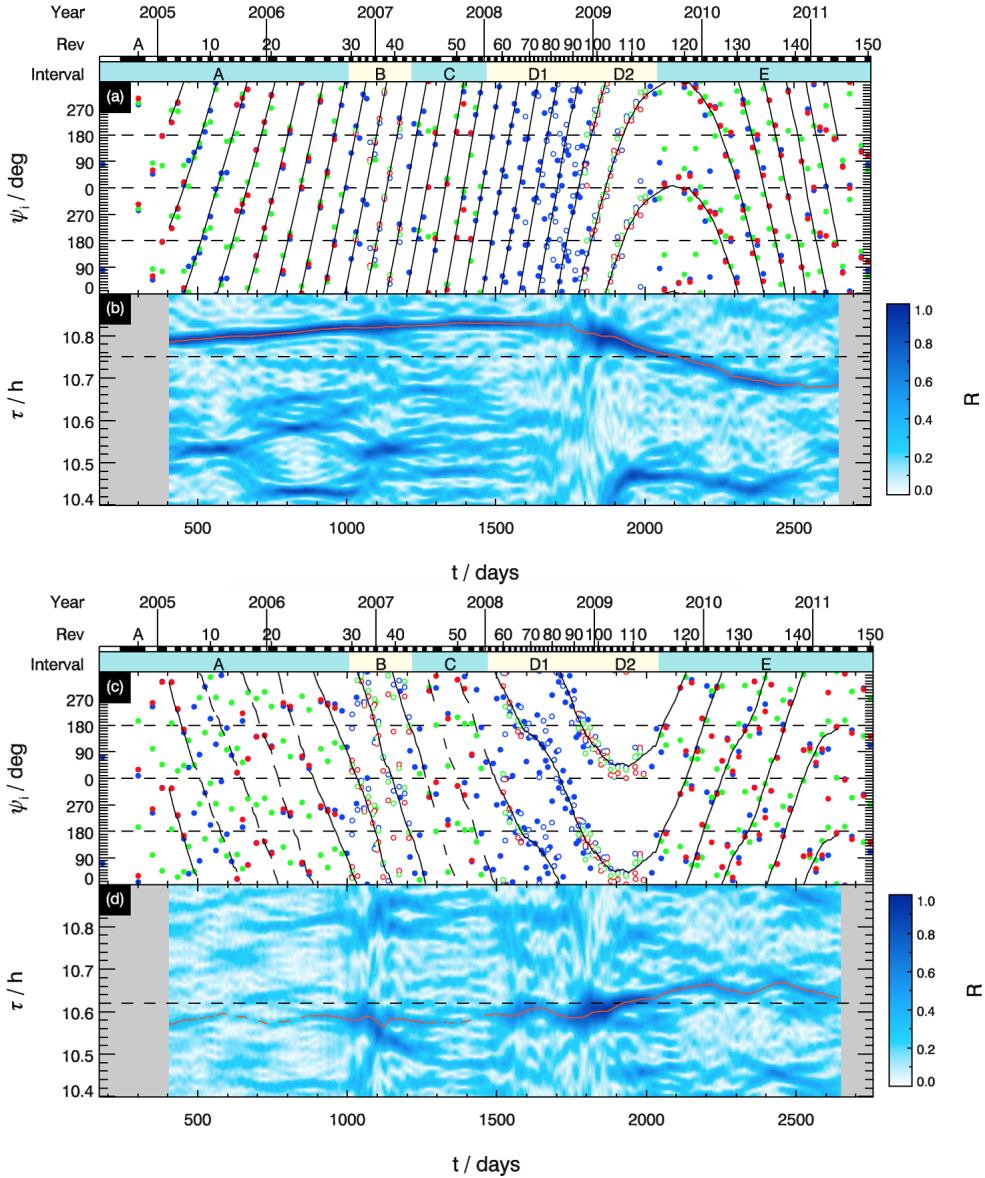


Figure 2.12: Magnetic field phase data and periodograms for both the southern (top) and northern (bottom) PPO systems from June 2004-July 2011. The phase data (panels a and c), ψ_i , for field components $i = (r, \theta, \varphi)$, are colour coded red, green, and blue, respectively. Filled circles indicate core data, while unfilled circles indicate polar data. The data shown here are in southern and northern format (see text for details). The black lines are determined from linear fits to 25 data points at a time. The periodograms (b and d) are formed from $\bar{R} = 1 - V$ where V is the variance of the linear fit. The period is determined from the continuous peak in \bar{R} , and is shown by the orange line. While this is complete for the southern period it is incomplete for the northern period (the dashed sections show this). The dashed black line shows the guide periods, τ_g used. From *Andrews et al.* [2012]

As discussed above, the observed oscillations in the core region are in fact a superposition of the northern and southern systems. The northern and southern phases $\Phi_N(t)$ and $\Phi_S(t)$ where $\Phi_{N,S} = \Phi_g(t) - \psi_{N,S}$ are determined by fitting equation (2.4) to

the measured magnetic field; from this ψ_i needs to be modified based upon the known polarization characteristics of the oscillations relative to the r component as indicated above. In Figure 2.12a and 2.12c the phase of the r component is plotted as observed, while the θ and φ components are adjusted according to their phase relations to r as discussed above. All components in Figure 2.12a would all line up if the oscillation was a pure southern oscillation, this being the southern (S) format. In Figure 2.12c they are adjusted such that they would all line up if the oscillation was a pure northern oscillation, this being the northern (N) format. It can be shown that in the presence of dual modulation, the phases in S format cluster about the southern phase ψ_{rS} , while the phases in N format cluster about the northern phase ψ_{rN} , so that both can be determined from a linear fit. For both the N and S format phase data such linear fits are applied to 25 data points, which spans ~ 200 days, then stepped along one data point at a time. From these fits the phases and periods for the northern and southern oscillations were determined. The periodograms based upon the variance, V , of these linear fits ($\bar{R} = 1 - V$) are shown in Figures 2.12b and 2.12d, with the periods $\tau_{N,S}$ shown by the orange lines, which trace the continuous peak in \bar{R} . Phases $\psi_{N,S}(t)$ are shown by the black lines in Figures 2.12a and 2.12c. The relative amplitudes of the oscillations revealed that during the interval from mid June 2004 to mid July 2011 as studied by *Andrews et al.* [2012] the northern oscillations' amplitude had increased by a factor of ~ 2 , while the southern oscillations' amplitude had decreased by ~ 0.75 , meaning they became nearly equal in the core region. In the polar regions, however, the oscillations were shown to be hemispherically pure to within $\sim 10\%$ by amplitude. This gives good evidence for a polar origin of these oscillations. The phases $\Phi_{N,S}(t)$ derived by *Andrews et al.* [2012] and shown in Figure 2.12 are central to the analyses in Chapters 4, 5, and 6.

The magnetic field perturbations discussed above can be explained by two rotating field-aligned current systems. Figure 2.13 depicts modified versions of these current systems proposed by *Southwood and Kivelson* [2007] and *Andrews et al.* [2010b] to include the discussions of interhemisphere and cross-field current closure by *Southwood*

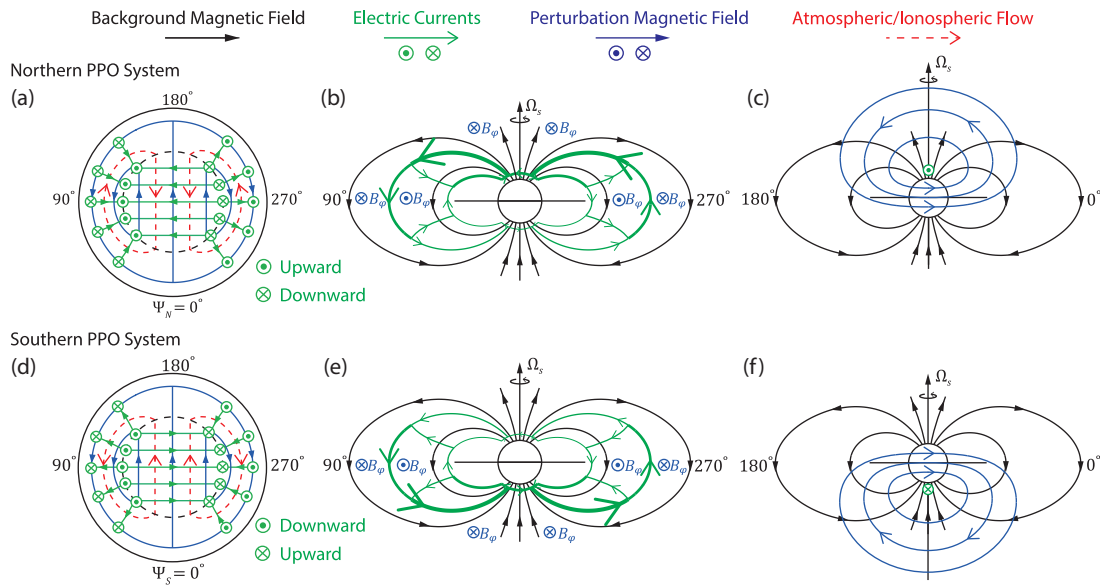


Figure 2.13: Sketches showing the northern (top row) and southern (bottom row) PPO current systems and field perturbations. Line format is give at the top of the figure. (a) and (d) show the northern and southern ionosphere, both viewed from the north, the currents, field perturbations and atmospheric flows to drive such a current system are shown. (b) and (e) show the current systems in the $\Psi_{N,S} = 90^\circ - 270^\circ$ meridian plane, together with the direction of the field perturbations. (c and f) illustrate in the $\Psi_{N,S} = 0^\circ - 180^\circ$ meridian plane the northern and southern perturbation fields associated with the current systems.

and Cowley [2014]. The top row shows the current system and field perturbation associated with the northern PPO system which rotates with the northern period, similarly the bottom row shows the southern PPO system that rotates with the southern period. The figures on the left show the current closure in the ionosphere for each respective hemisphere, as viewed from the north in both cases. The azimuthal coordinate used here is the phase function $\Psi_{N,S}$, which is 0° when the quasi-uniform field points radially outward, as shown in panels (c) and (f), and related to $\Phi_{N,S}$ by $\Psi_{N,S} = \Phi_{N,S} - \phi$. The angles $\Psi_{N,S}$ are employed throughout the work presented here and are discussed in more detail in Chapter 3 section 3.2.2. The centre figures in Figure 2.13 then show the principal currents of both systems, shown in the $\Psi_{N,S} = 90^\circ - 270^\circ$ meridian. The currents flow into the corresponding hemisphere’s auroral region on one side of the pole, across the polar cap as Pedersen currents, and out on the other side. The currents then close partly within the equatorial plasma, also partly as an interhemispheric field-aligned current system in the other hemisphere’s ionosphere, and finally partly

through weaker field-aligned currents at lower latitudes closer to the planet. *Andrews et al.* [2010a] showed using equatorial magnetic field data from 2004-2007 the presence of the rotating southern field-aligned current system carrying ~ 6 MA at $\sim 15R_S$; in addition there were weaker currents inside $\sim 5R_S$ carrying ~ 1 MA. It should be noted that field-aligned currents for both systems are oppositely directed with respect to the ionospheres. Hence, in the northern hemisphere the main (poleward) field-aligned current is out of the ionosphere at $\Psi_N = 90^\circ$ and into the ionosphere at $\Psi_N = 270^\circ$, while in the southern hemisphere the currents are out of ionosphere at $\Psi_S = 270^\circ$ and into the ionosphere at $\Psi_S = 90^\circ$.

By applying Ampère's law in the region between the inner and outer field-aligned currents we find a quasi-uniform field is produced out of the page in 2.13b and in 2.13e. The sketches on the right of Figure 2.13 show the field perturbations for each hemisphere's current system in the $\Psi_{N,S} = 180^\circ - 0^\circ/360^\circ$ meridian. The field perturbations show the quasi-uniform field in the equatorial region, pointing radially outward at $\Psi_{N,S} = 0^\circ$ and radially inward at $\Psi_{N,S} = 180^\circ$, while there is a quasi-dipolar field outside the outer field-aligned currents and over the poles, as shown by the reversal of the B_ϕ field across the field-aligned current. These systems then rotate with the respective magnetic oscillation period causing the observed behaviour of the magnetic perturbations. The symmetry of this ' $m = 1$ ' field and current system should be noted, varying near-sinusoidally with azimuth as $e^{jm\phi}$ to a first approximation, compared with the near-axisymmetric $m = 0$ current system associated with subcorotation in Figure 2.7. This difference will be exploited in the analysis in subsequent chapters.

As discussed in section 2.4.1 the SKR emission is generated in regions of upward field-aligned current and is rotational in nature; thus it is expected to have a common source to the magnetic oscillations [*Southwood and Kivelson, 2009*]. The periods and phases derived by *Andrews et al.* [2012] were compared to those derived from the SKR emission by *Lamy* [2011] and *Gurnett et al.* [2011], and were found to agree to within a few tens of seconds the southern hemisphere periods. Observed drifts in phase were similar to those reported by *Andrews et al.* [2008, 2010b] and *Provan et al.* [2009a],

which has been shown by *Andrews et al.* [2011] to be due to the rotational nature of the SKR sources thus challenging the previous assumption that the SKR emissions were strobe-like. The northern periods were also found to be in good agreement. However, there were intervals in which the period and phase could be not reliably determined, as defined by $\bar{R} \leq 0.3$ as shown by dashed lines in Figure 2.12c and 2.12d. As the Saturnian year approached equinox in mid-2009 the northern and southern periods started to converge, in the case of the SKR periods they were reported to have crossed [*Gurnett et al.*, 2010], however, *Andrews et al.* [2012] found no evidence of this in the periods derived from the magnetic oscillations.

2.4.3 PPOs post equinox

Post-equinox, the periods of both SKR and magnetic oscillations converged to a similar period of ~ 10.68 h in mid-2010, and then diverged again to values where the northern period was still shorter compared with the southern period (10.64 h and 10.69 h) respectively [*Andrews et al.*, 2012; *Provan et al.*, 2013]. While these periods remained fairly stable around these values until mid-2013, large and sudden changes in the relative amplitudes of the northern and southern oscillations were observed [*Provan et al.*, 2013, 2014]. *Provan et al.* [2015] showed that these could be due to large solar wind compressions of Saturn's magnetosphere. A good agreement between the SKR and magnetic periods has been shown [*Provan et al.*, 2014; *Fischer et al.*, 2014; *Cowley and Provan*, 2015], although this has been contested by *Fischer et al.* [2015] who stated that the SKR periods had crossed after equinox. In response to this *Cowley and Provan* [2016] showed that this difference was likely due to misidentification of the periods as a result of dual modulation in the polarization-separated SKR data, like that seen previously by *Lamy et al.* [2011]. However, the cause of this dual modulation is currently unknown. Most recently, from mid-2013 to mid 2014 the periods converged again and the oscillations were locked in antiphase, before crossing with the northern period becoming longer at ~ 10.78 h while the southern remained at ~ 10.70 h, and with the northern oscillation becoming dominant in the core region [*G. Provan and S. W. H.*

Cowley, private communication, 2016]. The behaviours of both the SKR and magnetic oscillations as observed by Cassini show that there is strong evidence for long-term seasonal dependence of the PPOs.

2.4.4 Plasma and auroral emission effects associated with PPOs

The PPO perturbation systems also result in significant modulations in the magnetospheric plasma properties and energetic particle fluxes as they sweep azimuthally near the planetary rotation period through the subcorotating plasma [e.g., *Carbary and Krimigis, 1982; Carbary et al., 2007, 2008*]. In the inner region ($<5R_S$) of the plasma disc *Gurnett et al. [2007]* showed that an asymmetry in the electron density rotates in phase with the B_ϕ perturbation field at the *Kurth et al. [2007]* SKR period. In addition, during the same southern summer interval as investigated by *Andrews et al. [2010a]*, the equatorial plasma was found to move radially outward and inward at the period of the stronger southern system [*Burch et al., 2009*]. The outward bulge occurs in the PPO system sector in which the azimuthal component of the equatorial quasi-uniform field is positive, i.e., on the right side in Figures 2.13d and 2.13e, $\Psi_S = 270^\circ$. Associated phenomena include periodic oscillations of the position of the magnetopause and bow shock on the dayside [*Clarke et al., 2006, 2010a,b*], and north-south modulations of the plasma sheet on the nightside [*Arridge et al., 2011; Provan et al., 2012*]. The periodic thinning and outward motion of the plasma sheet has also recently been linked to plasmoid release [*Jackman et al., 2016*].

Given the expected connection between electron precipitation and field-aligned currents noted above, the rotating system of PPO currents may also be expected to lead to rotational modulations of the auroras and related auroral radio emissions, in addition to SKR. Corresponding modulations of the UV aurora were found initially in Voyager data by *Sandel and Broadfoot [1981]* and *Sandel and Shemansky [1982]*, and more recently by *Nichols et al. [2010a, 2016]* and *Carbary [2013]* using Hubble Space Telescope (HST) and Cassini UVIS images, respectively. Figure 2.14 from *Nichols et al. [2016]* shows HST observations of Saturn's southern UV auroras plotting with PPO $\Psi_{N,S}$

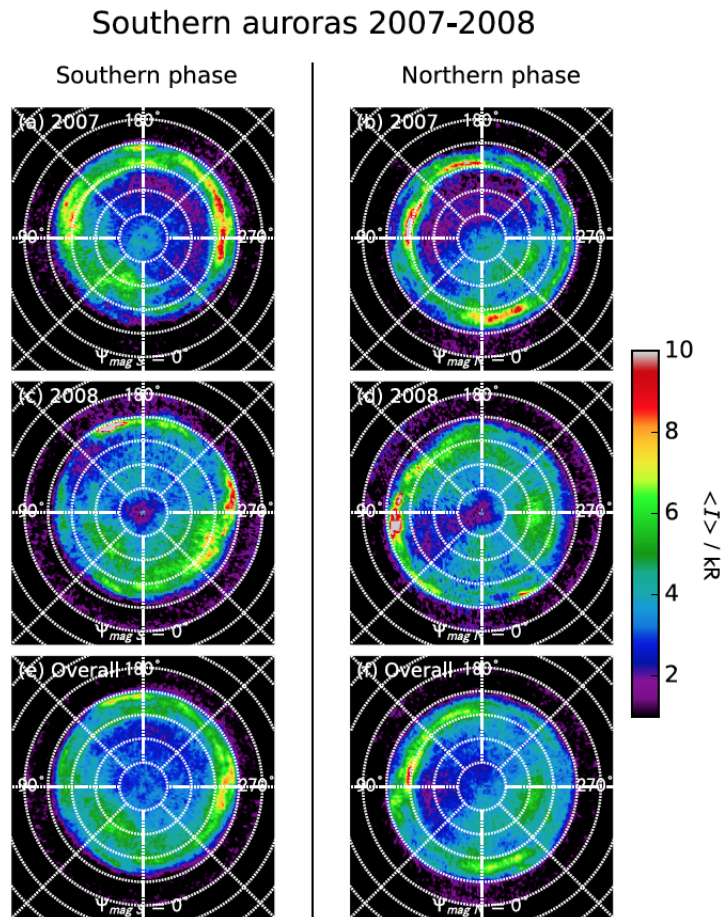


Figure 2.14: Plots showing co-added HST images of the southern auroras from 2007 to 2008. The right column is organised by Ψ_S , while the left column is by Ψ_N , with $\Psi_{N,S} = 0$ at the bottom of the plots. The rows are for 2007, 2008, and overall. The latitudes are plotted every 5° . Taken from *Nichols et al.* [2016].

phase. These observations show increased UV auroral emission in the sector of southern PPO phase associated with upward current i.e. $\Psi_S = 270^\circ$. *Badman et al.* [2012] have also shown the presence of rotating modulations of H_3^+ IR emission in Cassini VIMS data. The northern and southern auroral ovals have also been observed to oscillate in latitude with amplitude $\sim 1^\circ$ - 2° at the corresponding PPO periods [*Nichols et al.*, 2008, 2010b; *Bunce et al.*, 2014; *Badman et al.*, 2016], and in relation to the equatorial oscillations [*Provan et al.*, 2009b]. Regions of downward field-aligned current are associated with distinctive wave emissions at frequencies typically below ~ 100 Hz known as auroral hiss, this emission has been shown to be modulated at the PPO periods [*Gurnett et al.*, 2009b; *Kopf et al.*, 2010].

2.4.5 Proposed models for the PPOs

There have been many published models to explain Saturn's planetary period oscillations. One that is central to the work of this thesis is the rotating field-aligned current systems proposed by *Southwood and Kivelson [2007]*, *Southwood and Kivelson [2009]*, *Andrews et al. [2010b]*, and *Southwood and Cowley [2014]*. The driving source of these currents is still debated. However, one leading explanation is the upper atmosphere/ionosphere in the two polar regions. Indeed, *Jia and Kivelson [2012]* and *Jia et al. [2012]* imposed twin vortex convection cells in each hemisphere's ionosphere, each vortex rotating at close to the 2005-2006 periods, within a MHD simulation. These vortices then drove field-aligned current systems in the magnetosphere similar to those proposed above. The results showed that this scenario can produce the observed periodicities in a wide range of properties, including the magnetic field, plasma, neutrals and radio emissions. Using similar simulations *Kivelson and Jia [2014]* also showed that the rotating current systems drive compressional waves through Saturn's magnetosphere, giving rise to the flapping of the plasma sheet and the motion of the magnetopause boundary. The driver of flows in the ionosphere remained unspecified, however, it could be related to asymmetric auroral heating in the thermosphere [*Smith, 2006, 2011; Smith and Achilleos, 2012*] or to upward-propagating Rossby waves from lower altitudes [*Smith et al., 2016b*]. However, currently there have been no observations to support the required flows in the ionosphere, and those imposed by *Jia and Kivelson [2012]*; *Jia et al. [2012]* maybe energetically unrealistic [*Smith, 2014*]. In addition it has been proposed that the flows could be imposed lower in the atmosphere ~ 750 km above the 1 bar pressure level [*Smith, 2014*]. Again, as of yet, no observations of these required atmospheric flows have been made.

Other models to explain the PPOs have focused on the equatorial magnetospheric plasma and assume a longitudinal asymmetry that rotates at the period of the PPOs [e.g., *Gurnett et al., 2007; Goldreich and Farmer, 2007; Burch et al., 2008*]. The *Gurnett et al. [2007]* model is shown by the illustrations in Figure 2.15, the basis of which is a twin-cell convection pattern driven by a centrifugal imbalance, resulting in the

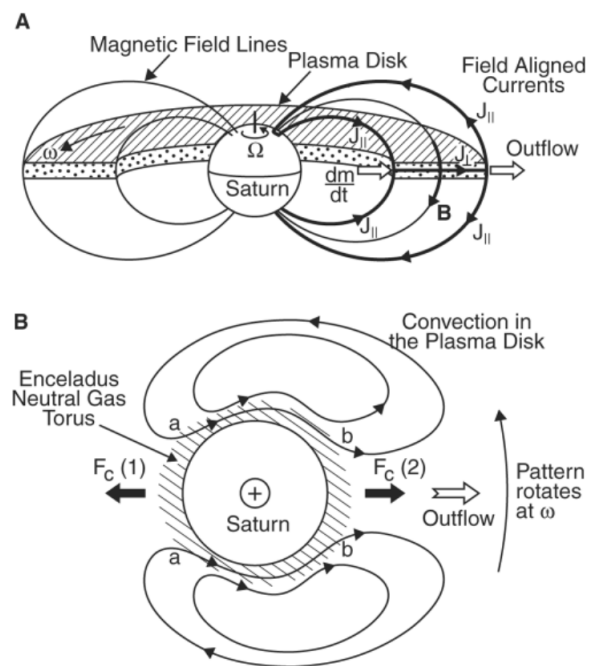


Figure 2.15: Sketches showing the field-aligned current system that couples the ionosphere to the plasma disk, together with the equatorial plasma flows through the neutral torus. Taken from *Gurnett et al.* [2007].

preferential outflow of plasma in one longitudinal sector. This picture thus provides explanation for giving the electron density enhancement and B_ϕ modulation in the inner magnetosphere, which correspond to the ‘cam’ like oscillations further out. The plasma disk is coupled to the planet via field-aligned currents. However, it is not clear how such models explain the dual periods observed, nor the long term stable $m = 1$ asymmetry also required. In addition, a rotating partial ring current has been proposed as a source of the signals; however again, this cannot explain the dual hemispheric period observed and pure polar signals [e.g., *Provan et al.*, 2009a; *Brandt et al.*, 2010]. In the outer magnetosphere, the periodicities have been explained by magnetodisk models [e.g., *Khurana et al.*, 2009; *Arridge et al.*, 2011], but as discussed above these can also be interpreted as a rotating current systems.

2.5 Summary

In this chapter it has been shown that Saturn’s magnetosphere is a highly variable environment, which is influenced by internal and external processes. Field-aligned cur-

rents play a critical role in angular momentum transfer from the planet to the magnetosphere, the generation of the auroral and radio emissions, and are also thought to be vital in mediating the PPO phenomenon throughout Saturn's magnetosphere. Chapters 4, 5, and 6 of this thesis contain detailed studies of the field-aligned current signatures previously studied by *Talboys et al.* [2009b, 2011], specifically in relation to the PPO phases as derived by *Andrews et al.* [2012]. In Chapter 4 the southern hemisphere signatures are shown to be modulated by the southern PPO phase, and the subcorotation current system (section 2.3.4) is separated from the southern PPO field-aligned current (section 2.4.2). In Chapter 5 the individual southern current sheets' strength and position are shown also to be modulated by the southern PPO system. Finally, in Chapter 6 the first direct evidence of interhemispheric current in the northern hemisphere is presented. Before these studies, the following chapter introduces the Cassini-Huygens mission, instruments, data analysis procedures and PPO phases systems relevant to this thesis.

Chapter 3

Instrumentation and data methods

3.1 The Cassini-Huygens mission

The Cassini spacecraft was launched on the 15th October 1997 from Cape Canaveral, USA. After its launch Cassini headed into the inner solar system to perform two flybys of Venus, before starting its voyage to Saturn with a flyby of the Earth on the 18th August 1999. These were done to pick up speed to send it out to Saturn. During the Earth flyby the 11 metre magnetometer boom was deployed. As shown in Figure 3.1, Cassini then travelled past Jupiter before orbit insertion at Saturn on the 1st July 2004. Cassini thus became the fourth spacecraft to reach Saturn, and become the first to enter orbit. Currently Cassini has completed over ~230 orbits, covering a wide regions of Saturn's magnetosphere, both in latitude and LT, together with the upstream solar wind and magnetosheath.

The NASA Cassini spacecraft with the ESA Huygens lander attached is shown in Figure 3.2 most of the key features, science packages and instruments are labelled. The Cassini orbiter is a three-axis stabilized robotic spacecraft powered by three radioisotope thermoelectric generators (RTGs). The ~1 hour light travel time between Earth and Saturn means direct control of the spacecraft is not possible, such that Cassini acts on a pre-planned routine of procedures. There are 12 science instruments on board, which can be grouped into three main types: optical remote sensing, microwave remote sensing and magnetic field, particles and waves. This thesis relies on data from

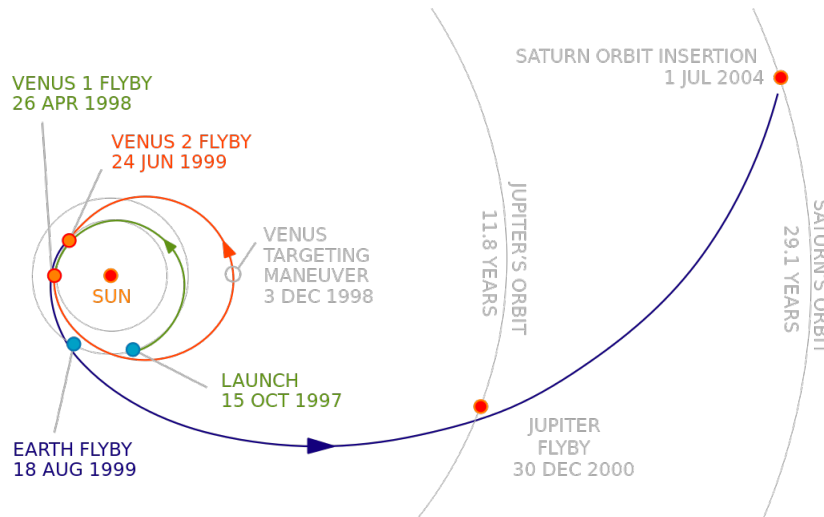


Figure 3.1: Sketch showing the interplanetary trajectory of the Cassini-Huygens mission from launch to orbit insertion. The key fly-bys are as indicated in the figure. Image credit: NASA/JPL.

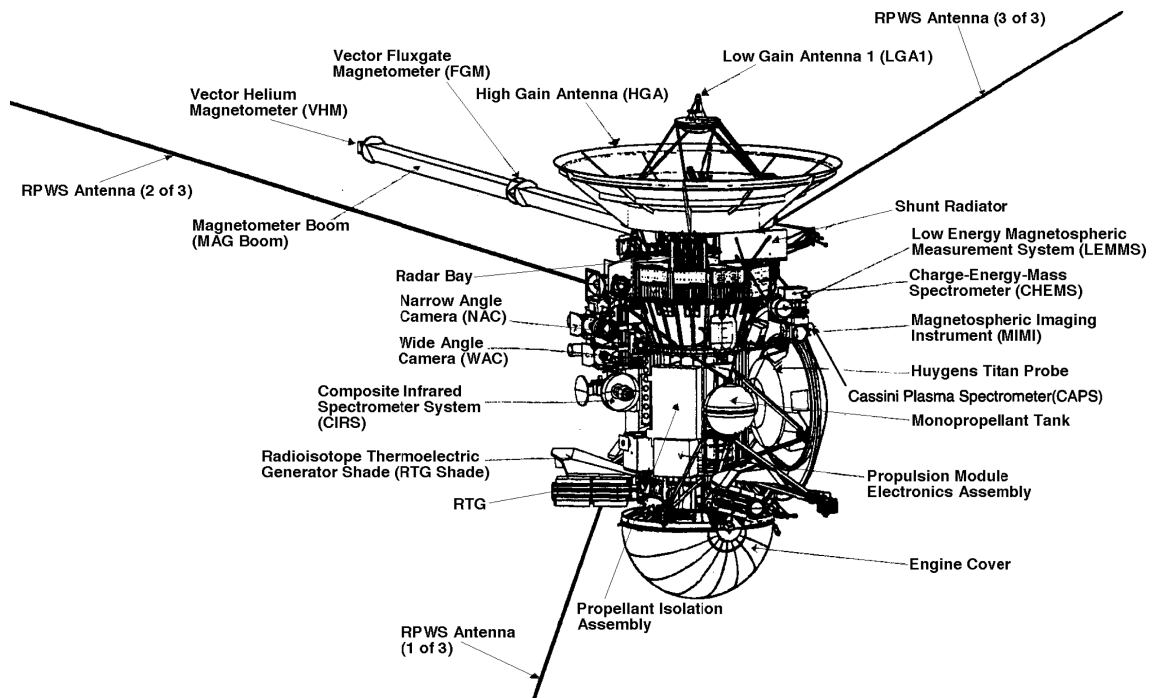


Figure 3.2: Schematic of the Cassini-Huygens mission, with most of the key instruments labelled. In this figure the spacecraft roll axis (z) is directed vertically upward. Image credit NASA/JPL.

the magnetic field investigation, specifically we employ data obtained from the fluxgate magnetometer. In addition data from the Cassini Plasma Spectrometer investigation is also presented. Both of these investigations will be described below. The optical remote sensing instruments also complement the study of field-aligned current through auroral observations, specifically observations in the far ultraviolet channel

by the Ultraviolet Imaging Spectrograph (UVIS) [Esposito *et al.*, 2004]. These have been used by Carbery [2012] to derive auroral boundaries in both hemispheres, thus giving us an approximate location of the upward currents at ionospheric heights.

3.1.1 The Cassini magnetic field investigation

The magnetic field investigation on board Cassini is comprised of two magnetometers, a fluxgate magnetometer (FGM) and a vector helium magnetometer (VHM). Their positions along the 11m magnetometer boom are shown in Figure 3.2, with the FGM located approximately halfway along, and the VHM at the end of the boom. Unfortunately, the VHM ceased operation late 2005, therefore no data from this magnetometer is used in this thesis. We thus restrict the discussion below to the FGM. The full details of this investigation are given by Dougherty *et al.* [2004], such that only the relevant physical and operational details are given here.

The science objectives of this investigation cover a wide range of topics from defining the internal planetary field, to understanding magnetospheric dynamics and moon-magnetosphere interactions. These objectives place operational and design requirements on the instrument, such that in regions of high background field strength at closest approach (~ 10000 nT) the magnetometer needs to be sensitive enough to measure the weak higher order terms of the internal field which are of the order to tens of nT, while in the outer magnetosphere magnetic field changes of ~ 0.1 nT in a weak background field (~ 10 nT) need to be measured. To achieve these aims a large dynamic range is needed. In addition, to ensure these capabilities, the spacecraft itself underwent a strict program of magnetic cleanliness to reduce the spacecraft field to ~ 1 nT at the FGM and ~ 0.1 nT at the VHM [Narvaez, 2004]. The calibration of the FGM is achieved by rolling the spacecraft about its Z axis as defined in Figure 3.2.

The FGM is comprised of three perpendicularly positioned ring cores of highly permeable material, each of which has a drive winding, that is fully enclosed in the sense winding. This is shown by the sketches in Figure 3.3. A square wave current is driven through the drive coil at a frequency of 15.625 kHz resulting in the generation of a field

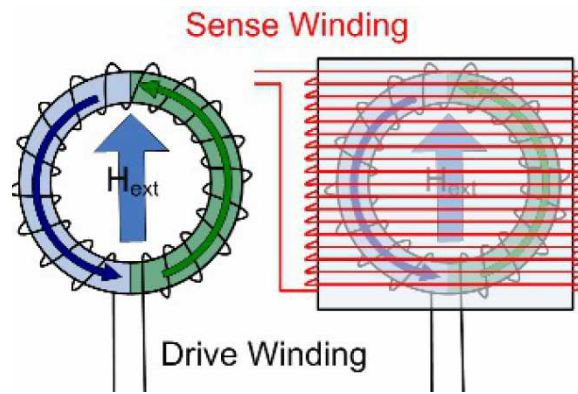


Figure 3.3: Sketches of a single axis fluxgate magnetometer. In the left sketch the blue and green arrows shown the fields in the core induced by the drive winding. H_{ext} is an external magnetic field. On the right the red coil shows the sense winding encasing the core and drive winding. Image credit: Imperial College London.

in each half of the coils, as shown by the blue and green arrows in Figure 3.3. The material in each half of the core is forced through its hysteresis loop. If no external field ($H_{ext} \equiv 0$) is present, each half of the core will go in and out of saturation symmetrically, such that there is no net change of flux, and so no voltage is induced in the sense winding. However, in the presence of an external field ($H_{ext} \neq 0$) aligned parallel to the axis of the coil, the half of the core generating a field in the opposite direction to the external field will come out of saturation before the other half, therefore the saturation is asymmetric. The resulting net flux change will induce a voltage at twice the drive frequency in the sense winding. The strength and phase of the induced voltage indicates the magnitude and direction of the external field. The signal is then amplified, and then sent back to the sense winding to cancel out the external field. By varying this feedback current the FGM can be operated in four automatically selected ranges, varying from ± 40 nT with a resolution of 4.9 pT, up to the maximum range of ± 44000 nT at a resolution of 5.4 nT. In terms of time resolution, the FGM can capture 32 vectors per second. To ensure the mutually perpendicular alignment of the three cores, they are mounted on a ceramic block, and retained in a temperature range -30° to $+50^\circ\text{C}$ by a 1 W heater. Figure 3.4 is a photograph of the Cassini FGM with the cover removed, together with the magnetometer electronics board.

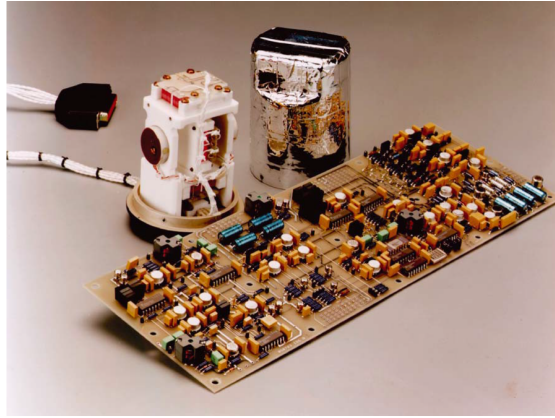


Figure 3.4: Photograph of the Cassini fluxgate magnetometer with the cover removed and the electronics board that is housed on-board Cassini. Taken from *Dougherty et al.* [2004].

3.1.2 The Cassini plasma spectrometer

The Cassini Plasma Spectrometer (CAPS) investigation focuses on the lower energy plasma populations with the aim to have coverage from ~ 1 eV to ~ 50 keV. CAPS consists of three instruments. The operation of CAPS is based on the motions of charged particles in electrostatic fields in order to separate the particles by their energy to charge ratio before being measured by micro-channel plate (MCP) detectors [Young *et al.*, 2004]. The configuration of the instruments is shown in Figure 3.5 with example particle trajectories shown by the dot-dashed lines and fields of view as the grey wedges. Since Cassini is not a spinning spacecraft, to ensure the best possible coverage CAPS is mounted on a rotating platform, which can rotate through $\sim 180^\circ$. This capability allows approximately 2π sr of the sky to be viewed every 3 min.

The Electron Spectrometer (ELS) instrument is designed to sample the electron populations in the energy range of 0.6 to 28750 eV over 64 logarithmically-spaced energy values every 2s. The instantaneous field-of-view is 5.2° in azimuth and 160° in elevation, which, over the eight MCP anodes that constitute the detector results, in an angular resolution in elevation of 20° . The energy range of ELS allows for a wide spectrum of the electrons to be sampled, from the cool inner magnetosphere to the hot outer magnetospheric populations. The resulting spectrograms will be used in this thesis to readily distinguish between the principal plasma regions.

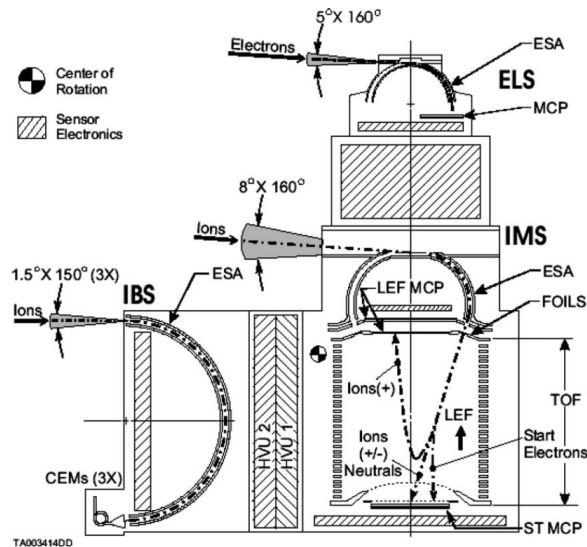


Figure 3.5: Schematic of the Cassini Plasma Spectrometer onboard Cassini, where the vertical axis is the spacecraft Z axis. Fields-of-view are shown by the grey wedges, together with particle trajectories shown by the dot-dash lines. Taken from *Young et al.* [2004].

The other two instruments that form CAPS examine the ion populations; these are the Ion Beam Spectrometer (IBS) and the Ion Mass Spectrometer (IMS). They both have similar energy ranges from 1 eV to ~ 50 keV. IBS has a high energy and angular resolution in order to study ion beam structures. IMS has the primary focus of surveying the ion atomic and molecular species through a time-of-flight method. This allows the detection of ions with mass to charge ratios between 1 – ~ 400 amu/q. Unfortunately, due to an electrical short CAPS was switched off indefinitely in mid-2012.

3.2 Data analysis procedures

3.2.1 Estimating the ionospheric horizontal meridional current

The primary indicator of field-aligned coupling currents is the presence of structured magnetic perturbations in the azimuthal (φ) field component referenced to the planet's spin/magnetic axis in spherical polar coordinates. Processing of the observed B_φ field values, based in this thesis on 1-min field averages, consists of two main steps. We first estimate and subtract from the data the large-scale magnetospheric azimuthal magnetic fields that are not associated with magnetosphere-ionosphere cou-

pling, using a magnetic field model. As discussed in section 2.3.1 of Chapter 2, the planetary field itself is very closely axisymmetric using the best determination to date [Burton *et al.*, 2010], and thus makes no contribution, and neither, to a first approximation, does the inner ring current, which is similarly closely axisymmetric [e.g., Kellett *et al.*, 2011]. The principal magnetospheric contributions to B_ϕ thus come from the magnetopause-tail current system, which have been estimated using the Saturn paraboloid field model whose parameters have been selected using data from both the Pioneer 11 flyby and Cassini [e.g., Alexeev *et al.*, 2006; Belenkaya *et al.*, 2006, 2008]. These currents and their effects on the magnetic field were discussed in section 2.3.6 of Chapter 2. The sense of B_ϕ produced by these currents reverses across both the noon-midnight meridian plane and near the equator, and takes positive values in the principal quadrants of both the inbound and outbound segments of the Cassini orbits employed here (i.e., Y and Z both positive inbound, and both negative outbound, see Figure 4.1c), with small values near periapsis when the spacecraft lies close to both the equator and to the midnight meridian. Further detail is provided in Appendix A, where it is shown that these fields vary slowly on the Cassini trajectory and take typical peak values of ~ 1 nT or less. They are therefore well distinguished from the sharply varying azimuthal fields associated with the magnetosphere-ionosphere coupling currents, which peak at order of magnitude larger values on the passes examined here. While we have thus taken account of these magnetospheric fields in this study, specifically using the “intermediate” model of Belenkaya *et al.* [2008] for a subsolar magnetopause radius of $22 R_S$, they are found in the present case to produce only a marginal effect on the results.

The second step is to map the modified B_ϕ field along magnetic field lines to the planet’s ionosphere. The method of field line tracing used is the same as that outlined by Cowley and Bunce [2003]. This procedure is intended to “correct” the data for variations in the radial distance at which the spacecraft crosses the field-aligned current sheets within the overall data set, typically between ~ 3 and $\sim 5 R_S$ (see Figure 4.1), thus allowing direct pass-to-pass comparison, as well as providing a direct basis

for discussion of ionospheric currents. The mapping employs a magnetic model consisting of the internal planetary field of *Burton et al.* [2010], combined with a typical empirical ring current model derived by *Bunce et al.* [2007]. The ring current models are parametrized in terms of the subsolar radius of the magnetopause, which has been taken here to have a fixed intermediate value of $22 R_S$, corresponding to a solar wind dynamic pressure of ~ 0.02 nPa according to the model of *Kanani et al.* [2010]. However, for the near-planetary passes considered here, the mapping results are not sensitively dependent on this choice. The “ionosphere” is taken to correspond to the surface 1000 km above the IAU 1 bar reference spheroid [*Galand et al.*, 2011], we use equatorial and polar ionospheric radii of 61,268 and 55,364 km, respectively. Cassini’s ionospheric footpoint is found by equating the magnetospheric and ionospheric flux functions as given by *Cowley and Bunce* [2003]. We further assume that ρB_ϕ is approximately constant on a field line between the point of observation and the top of the ionospheric Pedersen layer, where ρ is the perpendicular distance to the magnetic axis. This relation applies specifically to the region of field-aligned currents flowing between the field-transverse “closure” currents in the ionosphere, and those in the equatorial magnetosphere and, possibly, the conjugate ionosphere. As shown in Appendix B, the constancy of this quantity along field lines is exact in the case of axisymmetry, such as the ideal $m = 0$ system associated with plasma subcorotation discussed in Chapter 2 (Appendix B.1), and is also approximately satisfied for the current system associated with the $m = 1$ PPO current system also discussed in Chapter 2 (Appendices B.2 and B.3). In this case the azimuthal field just above the ionosphere, B_ϕ , is given in terms of the observed (modestly modified) value B_ϕ by

$$B_{\phi i} = B_\phi \left(\frac{\rho}{\rho_i} \right), \quad (3.1)$$

where ρ_i is the perpendicular distance of the field line foot in the ionosphere. It is shown in Appendix B that this procedure does act to somewhat enhance the pass-by-pass commonality of the azimuthal field data.

The value of the azimuthal field just above the ionosphere so obtained then allows the associated height-integrated current intensity flowing horizontally in the iono-

sphere in the meridional direction, i_m , to be determined. From Ampère's law we have directly $i_m = \mp B_{\phi i} / \mu_0$ (in Ampères per meter of azimuth), where μ_0 is the permeability of the vacuum and here the upper sign corresponds to the northern hemisphere and the lower to the southern. As indicated by this formula, this current is taken to be positive when directed from the pole to the equator in both hemispheres. As indicated in Chapter 2 section 2.3.4, the parameter more generally employed in this study is the horizontal meridional current per radian of azimuth, I_m , given by

$$I_m = \rho_i i_m = \mp \frac{\rho_i B_{\phi i}}{\mu_0}, \quad (3.2)$$

again positive in the equatorward direction as in Figure 2.7 in Chapter 2. From equation (3.1) this ionospheric current flowing at the feet of the field lines is given directly in terms of local magnetospheric quantities by

$$I_m = \mp \frac{\rho_i B_{\phi i}}{\mu_0} = \mp \frac{\rho B_{\phi}}{\mu_0}. \quad (3.3)$$

This is the quantity appearing directly in the divergence of the horizontal ionospheric current, and hence in the expression for the field-aligned current density just above the ionospheric current layer, given by current continuity as

$$j_{\parallel i} = \mp \frac{1}{\rho_i \cos \alpha_i} \left[\frac{\partial I_m}{\partial s_m} + \frac{\partial i_{\phi}}{\partial \varphi} \right]. \quad (3.4)$$

In this expression, s_m is path length in the ionosphere in the meridional direction from the corresponding pole towards the equator ($ds_m \approx R_{pi} d\theta_{iN,S}$ near the southern pole, where R_{pi} is the polar radius of the ionosphere and $\theta_{iN,S}$ is the colatitude angle measured from the corresponding pole), i_{ϕ} is the azimuthal component of the height-integrated ionospheric current intensity, and α_i is the angle of the background field to the local vertical in the ionosphere. The upper and lower signs again refer to the northern and southern hemispheres and the sign of the field-aligned current is with respect to the direction of the background field, such that, for example, positive $j_{\parallel i}$ implies an upward current with respect to the ionosphere in the northern hemisphere but a downward current in the southern hemisphere. We further note that in the limit that the second term on the right side of equation (3.4) can be neglected, the meridional gradi-

ent of I_m given in terms of the observed B_ϕ profiles through equations (3.1) and (3.2), then yields the meridional profile of the field-aligned current density. In Appendix C we derive an empirical limit on the meridional gradient of I_m above which we can be confident that the azimuthal gradient of the azimuthal current can be neglected, such that the meridional gradient of the current is associated with field-aligned current flow. When this condition is satisfied (corresponding to meridional current gradients above ~ 0.3 MA per radian of azimuth per degree of colatitude), the total field-aligned current per radian of azimuth flowing into the ionosphere between two meridional positions s_{m1} and s_{m2} (and taking $s_{m2} > s_{m1}$) is simply given from current continuity by

$$I_{\parallel} \approx \mp (I_m(s_{m2}) - I_m(s_{m1})), \quad (3.5)$$

a quantity that is then fixed on the background field lines concerned between the ionosphere and the region of field-transverse closure current in the magnetosphere. Here again the upper and lower signs are appropriate to the northern and southern hemispheres, and the sign of the current is with respect to the direction of the background field.

It should be noted that due to single spacecraft measurements, we are unable to ascertain whether a current sheet is spatical fixed or rapidly moving with respect to the planet. This could lead to effectively ‘passing’ through the same current sheet twice on a given orbit. However, we can expect that these effects will be reduced by the multi-orbit statistical nature of the studies presented here, and given short crossing time of ~ 3 hours.

3.2.2 PPO phase systems

Following the discussion of the PPO systems in section 2.4.2 of Chapter 2, here further details of the phase angles $\Psi_{N,S}$ are given, which are crucial in determining the field-aligned current dependence on the PPO systems. These phase functions depend both on time and on azimuthal position (i.e., on LT). The function of time involved, $\Phi_{N,S}(t)$, defines the azimuthal angle measured from noon at time t at which the northern and

southern PPO-related equatorial quasi-uniform fields point directly radially outward from the planet. This is illustrated in Figure 3.6 for the southern PPO system in a view looking down on the equatorial plane from the north, with the sunward direction (X) at the top of the plot and dusk (Y) to the left. The outer black dot-dashed line represents the magnetopause, typically located at radial distances $\sim 20\text{-}24 R_S$ at noon depending mainly on the solar wind dynamic pressure [Arridge *et al.*, 2006; Kanani *et al.*, 2010]. Following the results of Andrews *et al.* [2010a], the black dashed circle shows the location at $\sim 15 R_S$ where the main PPO-related field-aligned currents flow through the equatorial plane as indicated in Figure 2.13 in Chapter 2. The instantaneous currents are indicated by the green symbols, circled dots showing current flow out of the equatorial plane from the southern ionosphere and circled crosses current flow into the equatorial plane to the southern ionosphere. The blue lines show the associated perturbation field lines projected on the equatorial plane, quasi-uniform inside the main current ring, and quasi-dipolar outside. Secondary currents of opposite polarity flow inside $\sim 5 R_S$ shielding the quasi-uniform field from the innermost region, as in Figure 2.13 in Chapter 2. With regard to the apparent divergence of the perturbation field, we note that a co-latitudinal field component is also present, for the southern system it is directed into the plane of the diagram in the 180° southern PPO phase sector centered on $\Psi_S = 0^\circ$, and out of the plane of the diagram in the 180° phase sector centered on $\Psi_S = 180^\circ$, such that the central perturbation field lines curve around and close over the southern polar region. At the instant shown, the quasi-uniform field points radially outward at 15 h LT in the post-noon sector, such that $\Phi_S(t) = 45^\circ$ as indicated in the figure. We then define the southern PPO phase Ψ_S as

$$\Psi_S(\varphi, t) = \Phi_S(t) - \varphi, \quad (3.6)$$

where φ is the azimuthal angle at any spatial point again measured from noon. Meridians of principal values of Ψ_S are shown by the dashed straight lines in Figure 3.6, increasing clockwise around the planet, where we note that the main field-aligned current flows down into the southern ionosphere around $\Psi_S \approx 90^\circ$, and upward from the southern ionosphere around $\Psi_S \approx 270^\circ$. Similar considerations apply to the northern

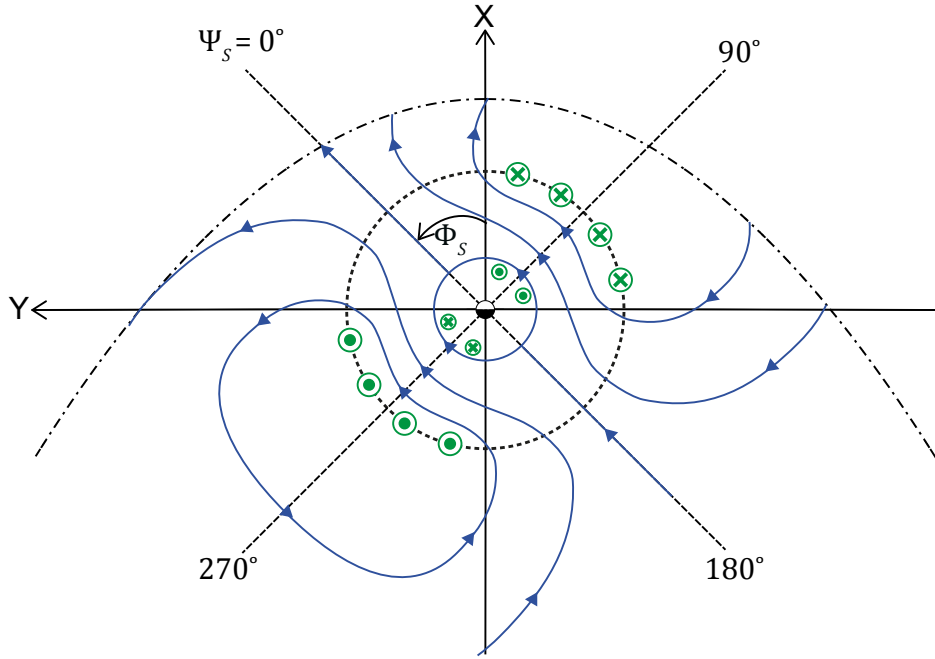


Figure 3.6: Sketch showing the form of the perturbation magnetic field lines of the southern PPO system (blue lines) in Saturn's equatorial region, in relation to the PPO phase functions employed, following *Andrews et al.* [2010a]. The view is from the north, with the KGS X and Y axes pointing sunward and to dusk, respectively. The outer black dot-dashed line represents the magnetopause, while the inner black dashed circle indicates the approximate location of the main PPO-related field aligned currents as they pass through the equatorial plane at $\sim 15 R_S$. The perturbation field is illustrated so that the phase angle $\Phi_S(t) = 45^\circ$ at this instant. The principal meridians of the PPO phase function at this instant are given by equation 3.6 and shown by the dashed straight lines, marked by the value of $\Psi_{N,S}$ in degrees, increasing clockwise around the figure. The sense of the field-aligned currents implied by the perturbation field are shown by the green symbols, circled crosses for current flow into the plane of the figure, and circled dots for current flow out of the plane of the figure. Secondary currents of opposite polarity inside $\sim 5 R_S$ are shown.

PPO system, except with the opposite sense of B_θ such that field lines close over the northern pole. Thus similarly

$$\Psi_N(\varphi, t) = \Phi_N(t) - \varphi. \quad (3.7)$$

While the northern perturbation is similar to Figure 3.6, the direction of the field-aligned current is opposite with respect to the northern ionosphere, such that the main field-aligned currents flow down into the northern ionosphere around $\Psi_N \approx 270^\circ$ and upward from the northern ionosphere around $\Psi_N \approx 90^\circ$.

Equivalent plots showing $\Psi_{N,S}$ meridians relative to the northern and southern ionospheric current system and polar perturbation fields are shown in Figure 2.13c

and 2.13f. The quasi-uniform perturbation fields interior to the primary PPO-related field-aligned currents (thick green lines shown in Figures 2.13b and 2.13e) can then be expressed as

$$B_r(\varphi, t) = B_{r0} \cos \Psi_{N,S}, \quad (3.8a)$$

$$B_\theta(\varphi, t) = \pm B_{\theta0} \cos \Psi_{N,S}, \quad (3.8b)$$

$$B_\varphi(\varphi, t) = B_{\varphi0} \sin \Psi_{N,S}, \quad (3.8c)$$

such that at a fixed point in space the field components oscillate with the same period, with the azimuthal component oscillating in lagging quadrature with the radial. The colatitudinal component oscillates in phase with the radial component in the southern hemisphere (upper sign in equation (3.8b)), and in anti-phase in the northern hemisphere (lower sign in equation (3.8b)). The overall quasi-uniform perturbation field formed by these components then rotates in the sense of planetary rotation with a slowly-varying rotation period given by

$$\tau_{N,S}(t) = \frac{360}{\left(\frac{d\Phi_{N,S}}{dt}\right)}, \quad (3.9)$$

where $\Phi_{N,S}(t)$ is expressed in degrees. Outside of the primary PPO-related field-aligned currents, however, the radial and colatitudinal components remain as in equations (3.8a) and (3.8b) (neglecting for simplicity radial propagation effects at modest distances [e.g., *Clarke et al.*, 2010a]), while the sense of the azimuthal field reverses to vary as $-\sin \Psi_{N,S}$, as illustrated in Figure 2.13b and 2.13e. The phase relations between the three field components are listed in Chapter 2 section 2.4.2.

The specific phase functions $\Phi_{N,S}(t)$ employed here are derived from linear fits to ~ 200 days of Cassini magnetic field data by *Andrews et al.* [2012], see section 2.4.2 in Chapter 2 for a detailed discussion of the determination of these phase functions. The field data examined within this thesis span ~ 290 days from mid-February to early December 2008, such that the phase functions employed also use data from adjacent intervals of equatorial orbits during the initial and final segments.

Chapter 4

Statistical analysis of the southern hemisphere subcorotation and planetary period oscillation current components

4.1 Introduction

In this chapter, the field-aligned current signatures observed in the southern hemisphere will be studied. As discussed in Chapter 2, observations indicate two principal current systems are present. The first is associated with subcorotation of the magnetospheric plasma relative to the neutral upper atmospheric flow, which causes field lines to bend out of magnetic meridian planes into “lagging” field configuration. The associated torques are such that angular momentum is transferred from the planetary atmosphere to the magnetospheric plasma. The basic form of the magnetosphere-ionosphere coupling current system and field perturbations theoretically expected are as shown in Chapter 2 (Figure 2.7). Given the sense of the planetary dipole field at Saturn, the lagging configuration is associated with positive and negative azimuthal magnetic field, B_ϕ , south and north of the equator, respectively. From Ampère’s law, the

associated current system then consists of field-aligned current directed downwards at high latitude, in both hemispheres, and upward, at lower latitudes, closing in Pedersen currents that flow equatorward in the ionosphere at one end, and magnetospheric currents that flow radially outward in the equatorial plasma at the other.

The existence of the second system has been revealed by the observation of magnetic oscillations near the planetary rotation period that are ubiquitous throughout Saturn's magnetosphere. These "planetary period oscillations" (PPOs) in the field appear to be due to two large-scale current systems flowing between the ionosphere and magnetosphere, one associated with the northern hemisphere and the other with the southern as illustrated in Figure 2.13, which rotate with slightly differing periods [Southwood and Kivelson, 2007; Andrews *et al.*, 2010b; Provan *et al.*, 2011]. The primary currents of the southern PPO system have the form of field-aligned currents that flow into the southern ionosphere on one side, across the polar ionosphere as Pedersen currents, and out along field lines on the other side. They close partially through the equatorial magnetospheric plasma transverse to the background field, and partially through the ionosphere in the opposite hemisphere, also involving a weaker pair of inner field-aligned currents of opposite polarity. The field perturbations, form of the field-aligned current and possible physical origins are discussed in greater detail in Chapter 2 section 2.4.2 and Chapter 3 section 3.2.2.

Due to the near-axisymmetry of both the planetary field [Burton *et al.*, 2010] and the inner ring current field produced by the equatorial plasma primarily of Enceladus origin [Kellett *et al.*, 2011], the effects of field-aligned currents are most readily detected in the azimuthal field perturbations observed on spacecraft passes over the polar regions of the planet. Previous studies of the B_ϕ perturbations associated with field-aligned currents were discussed in Chapter 2 section 2.3.5. Southwood and Kivelson [2009] and Talboys *et al.* [2009a] have provided initial evidence that variations in the field signatures are related to the PPOs for the late 2006 and early 2007 sequence of ~ 8 Cassini orbits. A second sequence of high-latitude Cassini orbits took place during 2008 was investigated by Talboys *et al.* [2009b, 2011]. Who showed that the azimuthal

field data have similar but variable forms as discussed in Chapter 2 and shown in Figure 2.8 compared to the 2006-2007 pre-noon and dusk data.

The relationship of these variable current signatures to the PPO phenomenon was not examined in these studies. However, initial examination here has shown that the current signatures in the southern hemisphere are indeed modulated by the stronger southern PPO system present during this pre-equinox interval, while those in the northern hemisphere are modulated by both northern and southern PPO systems. In this chapter we therefore limit attention to the more straightforward case of the southern hemisphere field-aligned current data, where we provide an overall statistical analysis, while the PPO-dependence of the structured auroral zone current layers is treated in more detail in a Chapter 5. The related northern data are thus left to Chapter 6. We begin in the next section by examining the nature of the data set, determined principally by the spacecraft orbit, before proceeding to present the results of an overall statistical analysis in following sections.

4.2 Data set

As indicated in section 4.1 and Chapter 3, the magnetic data employed in this study were obtained on a sequence of similar Cassini orbits that were sufficiently highly tilted out of Saturn's equatorial plane that the spacecraft crossed auroral field lines at radial distances $\sim 3-5 R_S$ both north and south during periapsis passes in the midnight sector. The passes concerned correspond to Cassini Revs 59-95 that occurred pre-equinox between February and December 2008. Of these 37 Revs, two were excluded due to the occurrence of substantial data gaps (Revs 70 and 71), while following an initial survey of the data, a further four were excluded as showing large and unusual signatures that did not follow the general trends (Revs 66, 77, 89, and 94). One of these, Rev 89, has previously been the subject of detailed individual study as an example showing the effects of an open flux closure event in Saturn's tail, possibly associated with a solar wind compression of the magnetosphere [Bunce *et al.*, 2010]. The data from the remaining 31 Revs examined here are thus taken to be representative of typical conditions in the

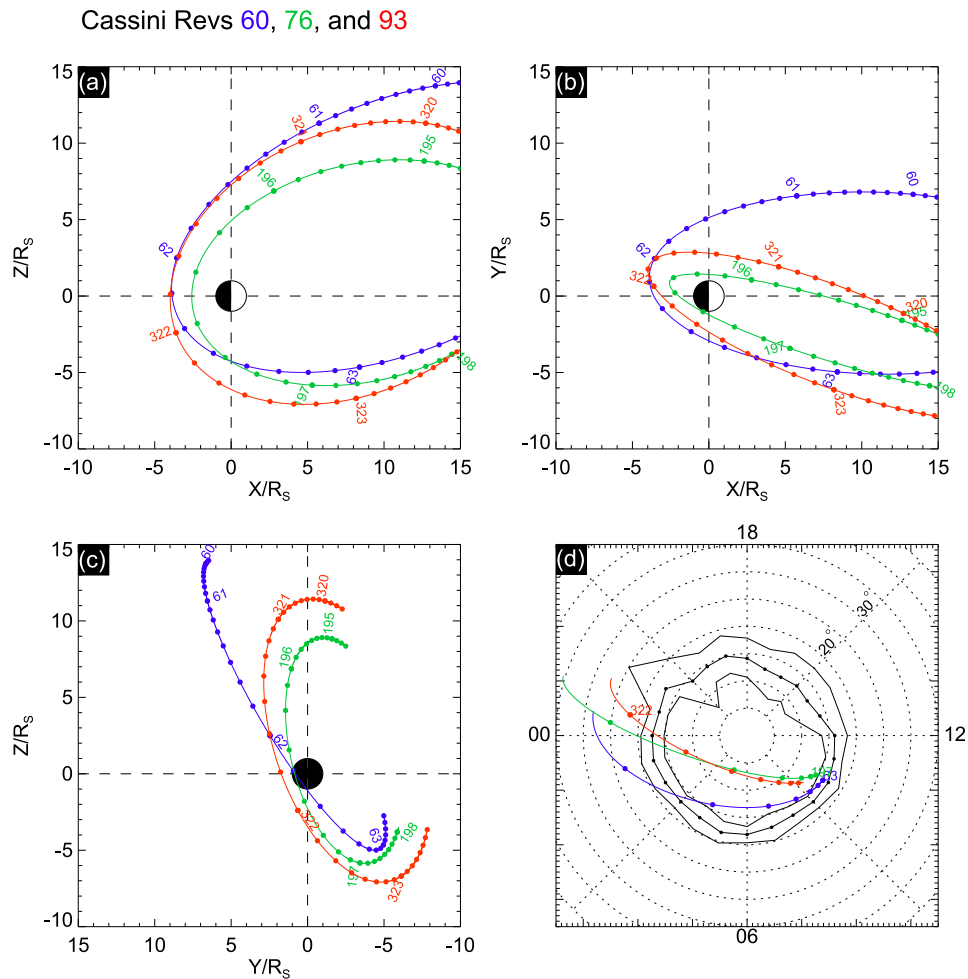


Figure 4.1: Plots showing properties of the Cassini orbits employed in this paper. Periapsis segments of three Cassini orbits from near the beginning (Rev 60, blue), middle (Rev 76, green), and end (Rev 93, red) of the interval are shown projected into (a) the X-Z, (b) the X-Y, and (c) the Y-Z planes in KGS coordinates (Z points along Saturn's spin/magnetic axis, the X-Z plane contains the Sun, and Y completes the right-hand triad pointing to dusk). Panel (c) shows the same trajectory segments as (a) and (b). Solid circles are plotted at 3 h intervals, labelled with the day of year number (2008) at the start of each day. In panel (d) the southern segments of these trajectories are projected along model magnetic field lines into the southern ionosphere, starting at the point on the left of the plot where the trajectories achieve their largest colatitude with respect to the northern and southern poles. The view is through the planet from the north with noon at the right and dusk at the top, with a dotted 5° grid in colatitude and 3 h in LT being shown. The black lines in this plot show the statistical location of the southern UV auroral oval derived by *Carbary* [2012] from Cassini UVIS data. The dotted centre line shows the position of peak intensity, while the outer and inner lines show the half power points.

midnight sector, which allow the variations in the field-aligned current signatures with the southern PPO phase to be investigated.

In Figure 4.1 the periapsis segments of three representative spacecraft orbits are

shown in Kronographic (KGS) coordinates, in which the Z axis is the planet's spin and magnetic axis, the X - Z plane contains the Sun, and the Y axis completes the right-hand triad pointing towards dusk. The trajectories shown are taken from near the beginning (Rev 60, blue), middle (Rev 76, green), and end (Rev 93, red) of the above set, and are shown projected into the X - Z , X - Y , and Y - Z planes in Figures 4.1a to 4.1c, respectively. Solid circles are shown at 3 h intervals along each trajectory, labeled with the day of year number at the start of each day. It can be seen that the spacecraft passed inbound towards periapsis on the dusk side of the northern polar region, crossed the equator prior to periapsis in the southern hemisphere in the pre-midnight sector (~ 23 h local time (LT)), and then passed outbound on the dawn side of the southern polar region. The radial distances of periapsis for these orbits are 3.7, 2.7, and 4.3 R_S for Revs 60, 76, and 93, respectively.

In Figure 4.1d we show southern segments of these trajectories projected along model magnetic field lines into the southern ionosphere, starting from the near-periapsis point on the trajectory with the largest mapped colatitude with respect to the southern (and northern) pole. The view is again through the planet from the north, with noon on the right and dusk at the top, with dotted colatitude circles being shown at 5° intervals. The magnetic mapping of Cassini's footprint is discussed in Chapter 3.

For reference purposes in Figure 4.1d we also show the averaged location of the southern UV auroras obtained from Cassini Ultraviolet Imaging Spectrograph (UVIS) data over essentially the same interval as that examined here [Carbary, 2012]. The centre line marked by black solid circles shows the position of maximum UV intensity, while the lines on either side show the half-intensity points. It can be seen that the spacecraft trajectory rapidly (~ 1 hour) traversed the mean auroral oval from north to south on each of the trajectories shown, crossing in the midnight to post-midnight sector. We note for future reference that the maximum auroral intensity in this sector (00-03 h LT) occurs consistently at $\sim 17.5^\circ$ colatitude with respect to the southern pole, with poleward and equatorward half intensity points at $\sim 15.5^\circ$ and $\sim 19.5^\circ$, respectively, as seen in Figure 4.1d. While the 2008 data set does not, therefore, provide

significant coverage of southern field-aligned current properties with LT, it does provide a suitable basis to examine variations with PPO phase within an essentially fixed, post-midnight, LT sector.

4.3 Survey of field-aligned current dependence on southern PPO phase

4.3.1 Initial survey of field-aligned current signatures

The auroral zone passes during the first interval of high-latitude Cassini orbits in 2006-07, studied by *Bunce et al.* [2008b] *Talboys et al.* [2009a], and *Southwood and Kivelson* [2009] as discussed in section 4.1 and Chapter 2, took place at radial distances $\sim 5-12 R_S$, such that the field-aligned current signatures were crossed over intervals of $\sim 2-6$ h, thus generally involving a significant change in PPO phase. The southern high-latitude passes in 2008 examined here, however, took place at smaller distances $\sim 3-5 R_S$, with the current layers being crossed in $\sim 1-2$ h [*Talboys et al.*, 2009b, 2011], thus having more the character of snapshots at a given PPO phase.

Figures 4.2a-4.2d show data from four such passes that exemplify conditions for southern phases $\Psi_S \sim 90^\circ$ (Rev 92), $\sim 180^\circ$ (Rev 61), $\sim 270^\circ$ (Rev 78), and $\sim 0^\circ/360^\circ$ (Rev 72), respectively. The actual phases are given together with the Rev number at the top of each data plot, specifically the phase where the spacecraft maps in the ionosphere to a southern colatitude $\theta_{iS} = 19^\circ$, chosen to correspond to a point that generally lies centrally within the main region of auroral zone field-aligned currents. The panels in each figure show, from top to bottom, (i) an electron count rate spectrogram covering the energy range ~ 0.6 eV to 28 keV (colour-coded as shown at upper right) obtained by the Cassini plasma spectrometer/electron spectrometer (CAPS/ELS) instrument, used here to aid region identification, (ii) the ionospheric azimuthal magnetic field $B_{\phi i}$ produced by field-aligned currents, derived from observed B_ϕ values (with the small magnetospheric contribution removed) using equation (3.1), and (iii) the southern PPO

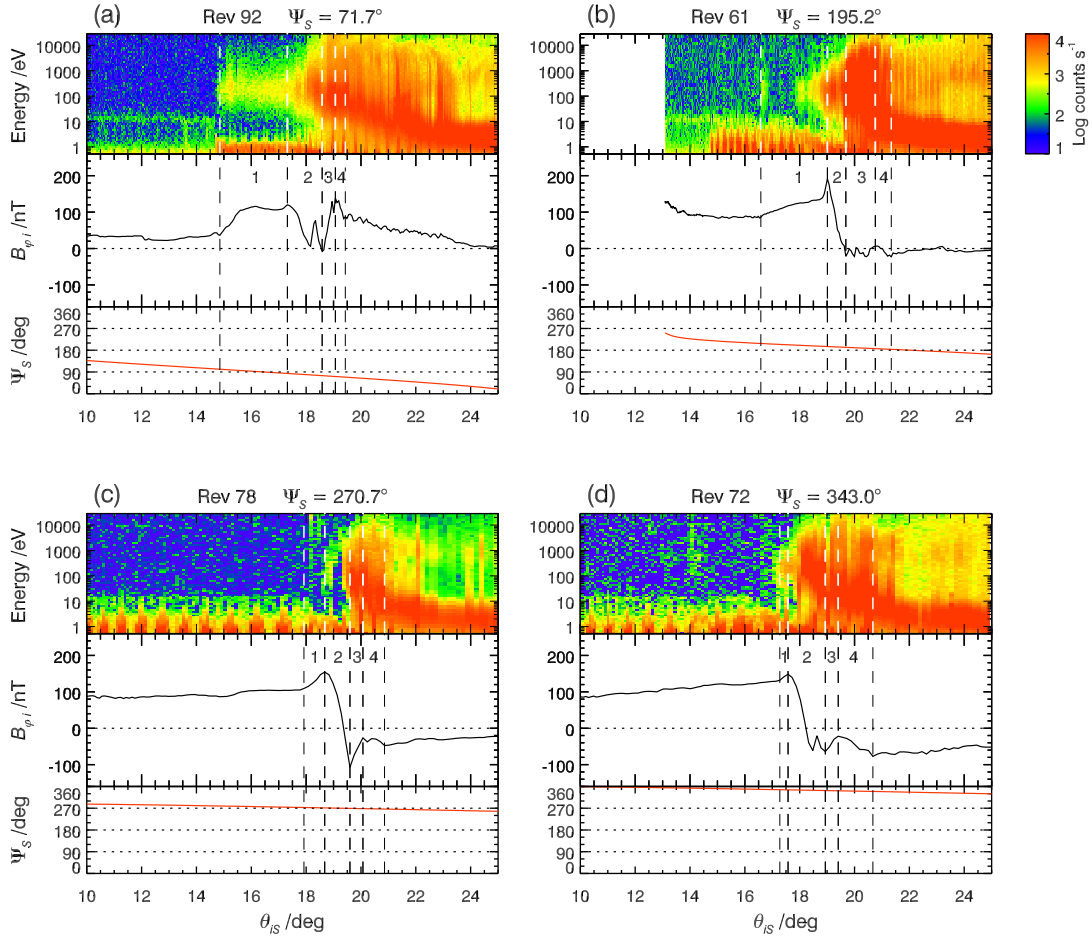


Figure 4.2: Four data plots exemplifying the dependence of the southern auroral field-aligned currents on the southern PPO phase Ψ_S , specifically for (a) Rev 92 for $\Psi_S \sim 90^\circ$, (b) Rev 61 for $\Psi_S \sim 180^\circ$, (c) Rev 78 for $\Psi_S \sim 270^\circ$, and (d) Rev 72 for $\Psi_S \sim 360^\circ$. The panels in each plot show from top to bottom (i) a CAPS/ELS electron count rate spectrogram covering the energy range ~ 0.6 eV–28 keV colour-coded as shown at upper right, (ii) the ionospheric azimuthal magnetic field $B_{\phi i}$ (nT) derived using equation (3.1) from the observed B_ϕ values (with small magnetospheric contribution removed as in Appendix A), and (iii) the southern PPO phase Ψ_S (deg), all plotted versus mapped southern ionospheric colatitude θ_{iS} (deg) over the range 10° – 25° . The magnetic mapping uses the same magnetic model employed in Figure 4.1d. The Ψ_S value at the point where $\theta_{iS} = 19^\circ$ is given at the top of each plot, together with the Cassini Rev number. Vertical dashed lines indicate four main field-aligned current sheets in each plot drawn between extrema in the field values, numbered from pole to equator, and directed down, up, down, and up with respect to the southern ionosphere.

phase Ψ_S from equation (3.6). These are plotted versus ionospheric colatitude with respect to the southern pole, θ_{iS} , mapped along field lines from the observation point using the same internal field plus ring current magnetic model used in Figure 4.1d (see section 4.2). We show the θ_{iS} range between 10° and 25° in each case, spanning the main current sheets lying centrally within each plot, noting that for Rev 61 in Figure

4.2b the mapped orbit did not reach to the smaller of these values. The right hand edge of each plot at $\theta_{iS} = 25^\circ$ maps along the model field to an equatorial radial distance of $\sim 5 R_S$, while (as we will see) the left hand edge at $\theta_{iS} = 10^\circ$ maps effectively to infinity, corresponding to open field lines in the tail lobes. These plots thus span essentially the whole of the nightside plasma regimes in the post-midnight sector as seen at radial distances $\sim 3-5 R_S$, from the inner magnetosphere to the tail lobe. We also note that increasing time runs from right to left in these plots as the spacecraft moves outbound from periapsis (see Figure 4.1), so that Ψ_S increases with decreasing θ_{iS} (the effect of the LT variation on the trajectory generally being small). As indicated above, the change in PPO phase during the current sheet crossings is seen usually to be modest, though somewhat dependent on the radius and hence speed of the traversal.

Examination of the magnetic data in Figure 4.2 shows that the effect of field-aligned currents can be seen in the sharp changes in azimuthal field in the central region of each plot, marked by the vertical dashed lines as discussed below. If we begin by examining the data equatorward of the current sheets (larger θ_{iS}), however, we see that the values are small but positive in Figure 4.2a, near-zero in Figure 4.2b, and negative in Figures 4.2c and 4.2d. This is the signature of the quasi-uniform perturbation field interior to the primary PPO field-aligned current sheets varying as $\sim \sin \Psi_S$ (equation (3.8c)), as may be seen by comparing with the concurrent phase values plotted at the bottom of each figure. Similarly, if we examine the data poleward of the current sheets (smaller θ_{iS}), it can be seen that the values are positive throughout, but smaller in Figure 4.2a than in the other examples. This is the signature of the reversed azimuthal fields of the quasi-dipolar perturbations outside (poleward) of the primary PPO field-aligned currents varying as $\sim -\sin \Psi_S$, but now superposed on an additional positive (i.e., lagging) azimuthal field that indicates plasma subcorotation throughout the high-latitude region. This effect is similar to that reported by *Bunce et al.* [2008b] and *Talboys et al.* [2009a] in the pre-noon southern summer hemisphere during the 2006-2007 season of inclined Cassini orbits, as discussed in Chapter 2. We note that no such overall lagging configuration is evident in the equatorward region, however.

Comparing the azimuthal fields on either side of the current layers in each plot, it can be seen that a large decrease in $B_{\phi i}$ occurs across the current region in Figures 4.2b-4.2d, indicative of a net upward current across the layer, while only small changes occur across the layer in Figure 4.2a. This indicates that the PPO and subcorotation currents combine to produce a large upward current across the central layer for PPO phases around $\sim 270^\circ$, while tending to cancel to produce little net field-aligned current for PPO phases around $\sim 90^\circ$. Nevertheless, well-defined upward and downward current sheets clearly persist within the central region in the latter case (Figure 4.2a).

Turning now to the field-aligned current region itself, examination of the full ensemble of 31 southern passes studied here shows that the main field variations on each pass can usually be described in terms of four current sheets, such as those bounded by the five vertical dashed lines in each plot in Figure 4.2, drawn at the extrema of the field variations (with no gaps). These sheets are numbered from 1 to 4 from pole to equator as shown, where we note that intervals in which the azimuthal field increases or decreases with θ_{iS} are indicative of downward or upward currents, respectively. In all cases, the overall field gradients are such that we can be confident that field-aligned currents are involved according to the criterion derived in Appendix C. These boundaries are employed in Chapter 5 to better characterise the individual current sheets.

As noted previously by *Talboys et al.* [2009b, 2011], the most poleward current layer (sheet 1) is always directed downwards into the ionosphere associated with increasing positive (i.e., lagging) $B_{\phi i}$, though it is of variable width. The same behaviour was found by *Talboys et al.* [2009a] in the pre-dusk northern winter data in 2006-07, as noted in section Chapter 2. The field then decreases in a region of upward current in each case (sheet 2), the decrease eventually leading to a reversal in sign of $B_{\phi i}$ from positive to negative (i.e., from lagging to leading fields) for PPO phases around $\sim 270^\circ$ as seen in Figure 4.2c. In these cases, the azimuthal field then returns to smaller values via a second sharp region of downward current (sheet 3 in Figures 4.2c and 4.2d), while overshooting somewhat, and returning to the negative values of the quasi-uniform PPO field at larger colatitudes via a secondary region of upward current (sheet 4 in

these figures). For PPO phases around $\sim 90^\circ$, however, as in Figure 4.2a, the decrease in $B_{\phi i}$ in the main upward current layer (sheet 2) is generally smaller. The upward current layer in these cases is then followed by a downward current of comparable magnitude (sheet 3), in which $B_{\phi i}$ increases back towards similar positive values as before, leading to a characteristic “V-shaped” notch in the azimuthal field profile. In some cases, though not in Figure 4.2a, a brief interval of negative (i.e., leading) field values occur at the bottom of the “V”. The positive value of the field at the peak of this current sheet again generally over-shoots that of the positive quasi-uniform PPO field at larger co-latitudes, to which it then returns via a secondary region of upward current (sheet 4). This presentation, together with examination of the data on other Revs not shown here, thus demonstrates definitively that the southern post-midnight current signatures observed in the 2008 data are strongly ordered by the southern PPO phase, following the related discussion of the smaller earlier pre-noon and pre-dusk data sets by *Southwood and Kivelson [2009]* and *Talboys et al. [2009a]*. The PPO-related behaviour just described also clearly forms the basis of the current signature “types” discussed previously by *Talboys et al. [2009b, 2011]*. A major goal of the following sections will be to untangle the clearly superposed effects in the overall currents that are due to plasma subcorotation and to the PPO current system.

4.3.2 Physical regimes of the field-aligned currents

The electron data in Figure 4.2, together with the other passes surveyed, allow us to briefly address the issue of the physical regimes corresponding to the current layers, following the earlier discussion by *Talboys et al. [2009b, 2011]*. It can first be seen that the increased lagging fields associated with the poleward downward current is often associated with the sudden appearance of weak fluxes of warm and hot electrons (~ 100 eV to few keV) in the electron spectrogram, indicative of trapped plasma on outer plasma sheet closed field lines (e.g., Figures 4.2a, 4.2c, and 4.2d). The poleward region is generally devoid of such particles (mottled blue-green regions of the spectrogram), and is thus taken to map to open field lines in the tail lobes (the intense electron fluxes

below ~ 10 eV energy in these regions are spacecraft photoelectrons). Current sheets 2-4 then generally span the region of intense keV electron fluxes mapping to the middle magnetosphere, with the main upward current region (sheet 2) spanning the outer region, and the subsidiary downward and upward currents (sheets 3 and 4) the inner region. The equatorward boundary of the overall current layer is generally associated with the transition between the region containing intense fluxes of hot keV electrons and the inner region dominated by cool few eV electrons, though the higher-energy electron fluxes at larger colatitudes beyond the current region seem to be enhanced at PPO phases $\sim 90^\circ$ (Figure 4.2a) compared with those at $\sim 270^\circ$ (Figure 4.2c), possibly in association with hot plasma injection events, clearly seen in the data in Figure 4.2a.

This description of the main plasma electron populations parallels that given previously by *Schippers et al.* [2008] from an examination of near-equatorial ELS data. The main hot (\sim keV) electron population (their “region 2”) was observed to be confined between equatorial radial distances of ~ 8 and $\sim 15 R_S$, with the inner region (their “region 1”) being dominated by dense cold plasma (~ 1 eV), and the outer region (their “region 3”) by weaker fluxes of cooler (few 100 eV) electrons. According to our simple planetary plus ring current magnetic field model described in section 4.2, $\sim 8 R_S$ in the equatorial plane maps to $\sim 20.5^\circ$ colatitude in the southern ionosphere, in general agreement with the colatitude of the equatorward boundary of the keV electrons and the overall current layer in Figure 4.2, while $\sim 15 R_S$ maps to $\sim 17.5^\circ$ colatitude, in general agreement with the colatitude of the poleward boundary of the main keV electron population and the main upward current region (sheet 2). Of course, the mapping of the spacecraft location along field lines to the equatorial plane (as opposed to the ionosphere) becomes increasingly uncertain with increasing radial distance.

Beyond the steady picture presented by *Schippers et al.* [2008], however, it is also evident from Figure 4.2, and from the other passes examined, that the plasma electron population is also strongly modulated by the PPO phase. Specifically, the main hot electron population is strongly confined in latitude for PPO phases around $\sim 270^\circ$ as in Figure 4.2c, but expands significantly poleward at phases around $\sim 90^\circ$ as in Figure

4.2a, as well as being enhanced somewhat in the equatorward region as noted above. The difference in the mapped latitude profiles of the plasma electrons between these PPO phase sectors is very marked. The poleward expansion occurs in the same southern PPO phase sector, $\sim 90^\circ$, as the clearly related effect observed in equatorial plasma ions by *Burch et al.* [2009] (see also *Clarke et al.* [2010a]). *Dejong et al.* [2010] have also previously noted the presence of enhanced fluxes of large pitch angle ~ 10 -100 eV electrons at similar oscillation phases at inner radial distances ~ 6 -9 R_S . It is also apparent from Figure 4.2 (and other examples) that the field-aligned current layers generally lie further poleward at PPO phases around $\sim 90^\circ$ than at $\sim 270^\circ$. Detailed quantification of these PPO-related modulations in the strength and position of the current layers will be undertaken in Chapter 5.

4.4 Statistical analysis

4.4.1 Comparison of large and small colatitude data with the PPO phase model

We now examine the PPO dependency of the currents through statistical analysis of the $B_{\phi i}$ values obtained on all 31 spacecraft passes employed in the study. We begin, however, by examining the data at large and small colatitudes θ_{iS} with respect to the southern pole, in order to compare with the southern PPO phase model $\Psi_S(\varphi, t)$ obtained from the *Andrews et al.* [2012] analysis. We recall from equation (3.8c) that $B_{\phi i}$ should vary as $\sin \Psi_S$ in the region equatorward of the field-aligned current layers, and as $-\sin \Psi_S = \sin(\Psi_S - 180^\circ)$ in the region poleward of the current layers.

Noting that the main current layers in Figure 4.2 are typically located in the southern colatitude range $\sim 15^\circ$ - 22° , in Figure 4.3a we show all the $B_{\phi i}$ data obtained in the range 24° - 27° equatorward of the current sheets plotted versus Ψ_S , the data being colour-coded by spacecraft Rev according to the scheme at the top of the figure. In order to account for the differing density of data points versus Ψ_S from Rev to Rev depending on the speed of the spacecraft traversal through the colatitude regime in

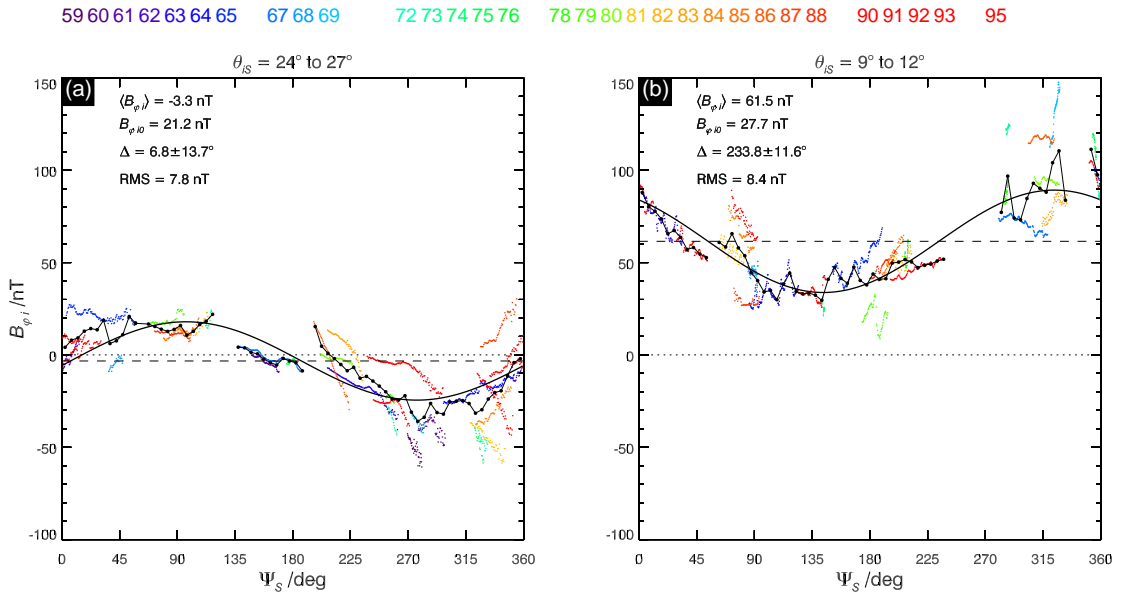


Figure 4.3: Plots showing the variation of the ionospheric azimuthal field $B_{\phi i}$ (nT) with the southern PPO phase Ψ_S (deg), for comparison with the *Andrews et al.* [2012] model. Two bands of southern ionospheric colatitude θ_{iS} (deg) are employed, (a) 24° - 27° equatorward of the current sheets, and (b) 9° - 12° poleward of the current sheets. The data from each Rev are colour-coded as shown at the top of the plot, while the black dots joined by black lines show weighted means in 5° bins of PPO phase determined as described in section 4.4.1. The thick black lines show the sinusoidal function $B_{\phi i}(\Psi_S) = \langle B_{\phi i} \rangle + B_{\phi i0} \sin(\Psi_S - \Delta)$ fitted to the weighted means, with the fit parameters given in each panel together with the RMS deviation of the mean data from the fitted line.

question (see, e.g., Figures 4.1 and 4.2), we have first averaged the data from each Rev in 5° bins of phase, and have then combined these Rev averages into an overall average in each bin using a weighted mean of all the contributing Revs. A logarithmic weight was employed, $W = \log_{10}(N)$, where N is the number of data points contributed to a bin by a given Rev, such that an “average” obtained from one data point is discounted, while that derived from ten points has a weight of one, and that from a hundred points a weight of two. This procedure results in the data from each Rev being treated on a more equal basis, such that the averages are not simply dominated by contributing Revs with the highest density of data points. The weighted averages are shown in the figure by the black circles joined by thin black lines.

The thick black line in Figure 4.3a shows a sinusoidal fit to these averages of the form $B_{\phi i}(\Psi_S) = \langle B_{\phi i} \rangle + B_{\phi i0} \sin(\Psi_S - \Delta)$, obtained using a Levenberg-Marquardt least squares minimization algorithm [Markwardt, 2009]. The parameters of the fit are

shown within the figure panel, specifically an amplitude $B_{\phi i0}$ of ~ 21 nT, a near-zero mean $\langle B_{\phi i} \rangle$ of ~ -3 nT, and a RMS deviation between the mean data and the fitted line of ~ 8 nT. The near-zero mean firstly confirms the lack of a significant steady subcorotation field in this inner region, mapping to ~ 4.3 - $5.5 R_S$ in the equatorial plane. Indeed, the negative mean value could be taken to imply a weakly leading background field in this region, a physically unlikely circumstance given the modest plasma subcorotation observed in this region (see section 2.3.4 in Chapter 2), as will be discussed further in section 4.5. Most importantly, however, the phase deviation $\Delta = 6.8^\circ \pm 13.7^\circ$ deg is zero within error, such that the best-fit line is very close to the expected $\sin \Psi_S$ dependency. (The uncertainty in Δ has been estimated by determining the parameter range that gives a significant 10% increase in the RMS deviation.) If we allow the RMS increase to be 100%, we find the uncertainty in Δ to $\pm 52.7^\circ$ and $\pm 45.7^\circ$ in Figures 4.3a and b, respectively. In addition from the chi-squared values the fits are shown to be significant. We thus conclude that the *Andrews et al.* [2012] phase model employed here provides an accurate overall representation of the orientation of the quasi-uniform equatorial perturbation field over the interval examined here, typically to within $\sim 10^\circ$.

In Figure 4.3b we show a similar analysis of the $B_{\phi i}$ data obtained in the colatitude range 9° - 12° , poleward of the current sheets. As anticipated, this shows an approximately opposite sinusoidal behaviour of amplitude ~ 28 nT, now about a significant non-zero mean of ~ 62 nT, due to evident steady plasma subcorotation in the open field region. However, the phase deviation $\Delta = 233.8^\circ \pm 11.6^\circ$ is rather larger than the $\sim 180^\circ$ expected, indicating that the orientation of the polar perturbation field lags in phase by $\sim 50^\circ$ compared with that expected on the basis of the simple picture outlined in section 2.4.2 Chapter 2. We note this finding for future reference below, though no systematic deviations of this nature have previously been deduced from related studies [e.g., *Andrews et al.*, 2010b, 2012].

4.4.2 PPO Phase Dependence of Field and Current Colatitude

Profiles

In Figure 4.4 we show southern colatitude profiles of the $B_{\phi i}$ data for all 31 Revs, again colour-coded according to the scheme shown at the top of the figure, now divided into eight non-overlapping 45° southern PPO phase sectors centred on 0° in Figure 4.4a, 45° in Figure 4.4b, and so-on. The panels are arranged in two rows such that “opposite” PPO phases, separated by 180° , are shown one above the other. Figures 4.4a and 4.4e centred on 0° and 180° in the first column on the left should therefore represent conditions with small expected PPO-related currents (see Figure 2.13 in Chapter 2), thus mainly exhibiting effects of plasma subcorotation, while Figures 4.4c and 4.4g centred on 90° and 270° should represent conditions of near-maximum superposed downward and upward directed PPO current, respectively. The black circles joined by black lines show values averaged in overlapping 1° colatitude bins, evaluated every 0.5° . The averaging technique employed is similar to that in Figure 4.3, such that the data from each Rev in each bin were first separately averaged, weighted according to the logarithm of the number of number of data points employed, and then further averaged over all contributing Revs.

Although it can be seen that there is considerable Rev-to-Rev scatter in the $B_{\phi i}$ data at a detailed level, the overall behaviour leads to mean profiles that follow the discussion of Figure 4.2 in section 4.3. At both PPO phases $\Psi_S \sim 0^\circ$ and $\sim 180^\circ$ (Figures 4.4a and 4.4e), $B_{\phi i}$ is consistently positive, i.e., lagging, at the smallest ionospheric colatitudes observed $\sim 5^\circ$ - 10° , indicative of plasma subcorotation on polar field lines, increases as the auroral region is approached at $\sim 15^\circ$, indicative of downward current, and then falls sharply across $\sim 17.5^\circ$ - 20° to small averaged values at larger colatitudes, indicative of a major layer of upward current. Our field model maps the location of this upward-directed current sheet to ~ 10 - $15 R_S$ in the equatorial plane, outside of which the perturbation fields are consistently strongly lagging to polar latitudes, and inside of which the mean perturbation fields are near zero. For phases $\Psi_S \sim 270^\circ$ (Figure

59 60 61 62 63 64 65 67 68 69 72 73 74 75 76 78 79 80 81 82 83 84 85 86 87 88 90 91 92 93 95

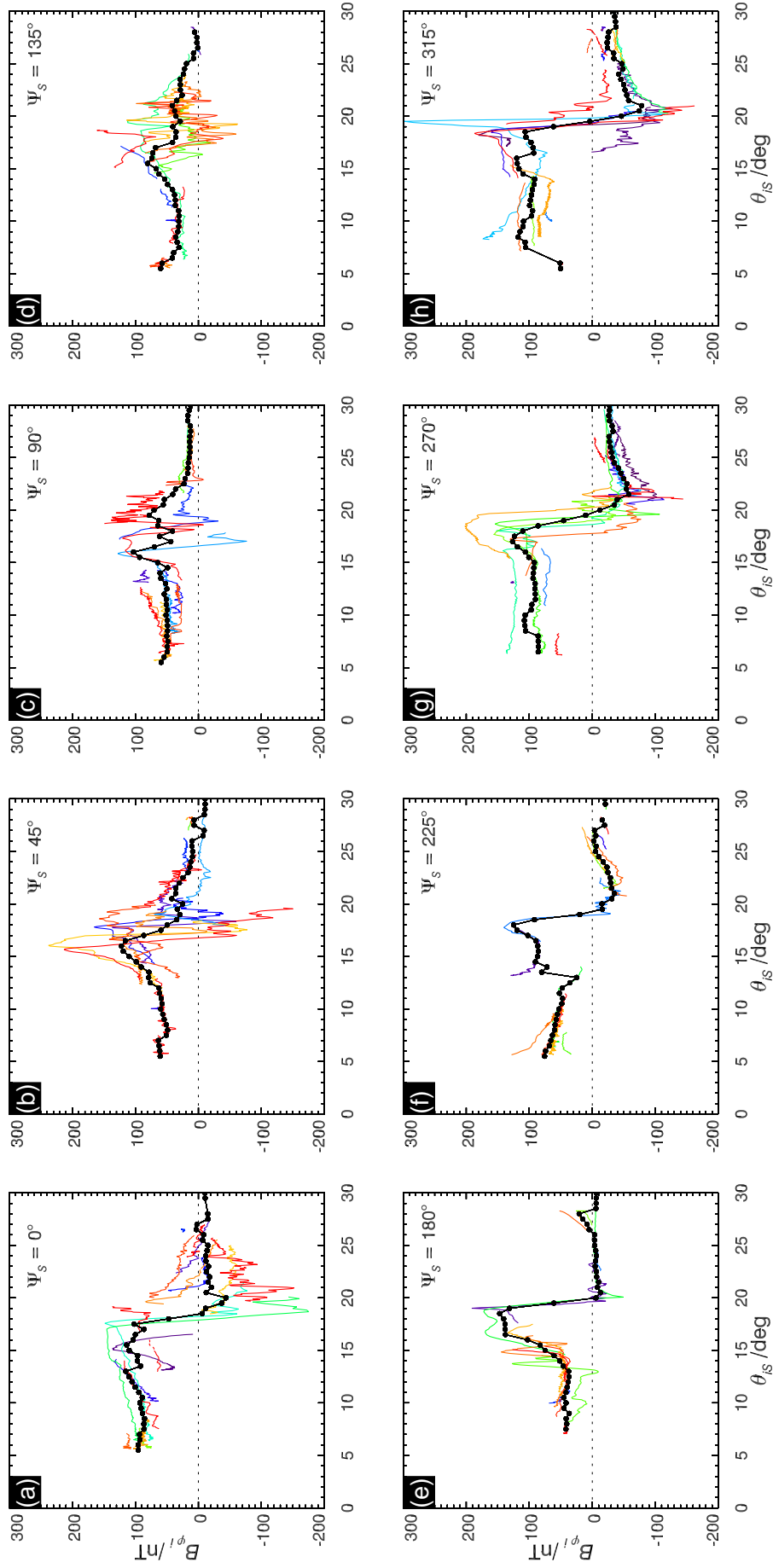
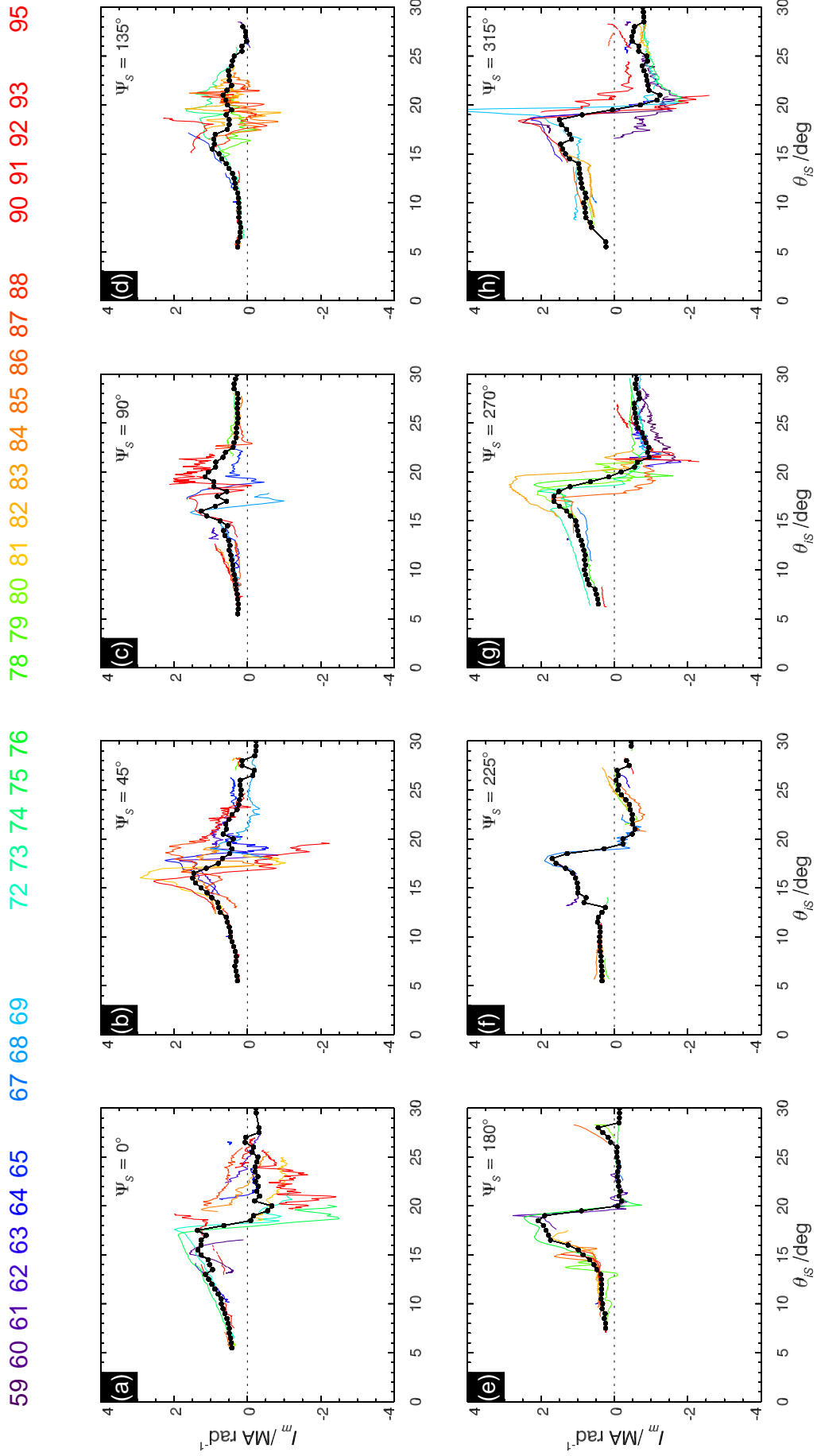


Figure 4.4: Plots showing southern colatitude profiles of B_{ϕ_i} data (nT) divided into eight non-overlapping 45° sectors of PPO phase Ψ_S , the centre values of which are indicated in the top right corner of each plot. The data for each Rev are colour-coded according to the scheme shown at the top of the figure, with the black circles joined by black lines showing weighted averages in overlapping 1° bins of colatitude every 0.5° , determined as described in section 4.4.2. Profiles for “opposite” values of PPO phase, differing by 180° , are shown one above the other.

4.4g), however, the perturbation fields consistently extend to negative leading values at large colatitudes, indicative of additional superposed upward currents near $\sim 19^\circ$, while for phases $\Psi_S \sim 90^\circ$ (Figure 4.4c) a smaller upward current at $\sim 17^\circ$ reverses to a further downward current at $\sim 19^\circ$ and then upward current again at $\sim 21^\circ$, leading to a “V-shaped” notch in the overall positive (i.e. lagging) field perturbations at that phase. The general four current sheet structure noted in section 4.3 thus remains evident in the averaged profiles for $\Psi_S \sim 90^\circ$, while for $\Psi_S \sim 270^\circ$ the smaller subsidiary currents at larger colatitudes are suppressed by the averaging procedure. In the following chapter we provide an analysis specifically focusing on the current sheets that avoids this effect. Figure 4.4 shows, however, that there is a clear relationship between the $B_{\phi i}$ field profiles and the southern PPO phase over the full 31 Rev data set examined here, which is in good accord with the individual cases discussed in section 4.3.1 and shown in Figure 4.2. We also note the significant Rev-to-Rev variability present, superposed on the main PPO-dependent variations. For example, the main upward current sheet at $\Psi_S \sim 270^\circ$ is clearly seen to be variably located between $\sim 17.5^\circ$ and $\sim 20^\circ$ colatitude, again leading to a broadening of this feature in the averaged values.

In order to discuss the currents more clearly, we now transform the ionospheric $B_{\phi i}$ field data into horizontal meridional ionospheric current per radian of azimuth, I_m , using equation (3.2), and in Figure 4.5 show colatitude profiles of this current in the same format as Figure 4.4. We recall that positive and negative values indicate equatorward and poleward-directed currents, respectively, relating to lagging and leading fields. We also recall from section 3.2 that in the limit that the azimuthal gradient of the azimuthal current can be neglected in considerations of current continuity, the field-aligned current is directly related to the meridional gradient of this quantity (equation (3.4)), with the total field-aligned current per radian of azimuth entering or leaving the ionosphere between two colatitudes being given by the difference in their respective I_m values (equation (3.5)). As mentioned in section 3.2, and in Appendix C we show that a suitable limiting magnitude of the meridional current gradient above which we can be confident that this approximation is well satisfied is ~ 0.3 MA per rad^{-1} per degree



59 60 61 62 63 64 65 67 68 69 72 73 74 75 76 78 79 80 81 82 83 84 85 86 87 88 90 91 92 93 95

Figure 4.5: Southern colatitude profiles of the horizontal meridional current per radian of azimuth, I_m (MA rad^{-1}), derived using equation (3.2), divided into eight non-overlapping 45° sectors of PPO phase Ψ_S , shown in the same format as Figure 4.4.

of colatitude, a gradient that is generally well exceeded by the individual current layers in the main current region as indicated above, but not by the more gradually-varying currents at both smaller and larger colatitudes. Concentrating on the main current layers, therefore, it can be seen that the main upward current layer, where I_m falls sharply with increasing colatitude, is strongly modulated by the PPO phase, carrying a total upward current of $\sim 1.5 \text{ MA rad}^{-1}$ for phases $\Psi_S \sim 0^\circ$ and $\sim 180^\circ$, increasing to $\sim 2.5 \text{ MA rad}^{-1}$ for $\Psi_S \sim 270^\circ$, and reducing to $\sim 0.5 \text{ MA rad}^{-1}$ for phases $\Psi_S \sim 90^\circ$. These upward currents are then flanked on the poleward side by a downward current of typically $\sim 0.5 \text{ MA rad}^{-1}$, not obviously modulated by PPO phase, and on the equatorward side by a further downward and upward currents of $\sim 0.5 \text{ MA rad}^{-1}$ for phases $\Psi_S \sim 90^\circ$. As previously mentioned in section 4.3.1, the effect is that the overall current layer, typically located between $\sim 15^\circ$ and $\sim 20^\circ$ southern colatitude, carries a net upward current of $\sim 2 \text{ MA rad}^{-1}$ for $\Psi_S \sim 270^\circ$, but reduces to near zero for $\Psi_S \sim 90^\circ$.

4.4.3 Sum and difference colatitude profiles

Using these results, we can now exploit the expected “ $m = 1$ ” symmetry of the PPO currents with respect to PPO phase to approximately separate the currents that are associated with the PPO oscillations from those that are not, the latter being taken to be associated with overall subcorotation of the plasma. To do this we simply add or subtract the averaged I_m current profiles for “opposite” phases of the PPO oscillations separated by 180° , and divide the sum or difference by two. Summing these profiles should approximately remove the anti-symmetric PPO currents to yield the subcorotation current profile independent of PPO phase, while differencing the profiles should approximately remove the PPO phase-independent subcorotation currents to yield the PPO current profile as a function of PPO phase. The results are shown in Figure 4.6, where the top row (Figures 4.6a-4.6d) shows half the sum of the top (Figures 4.5a-4.5d) and the bottom (Figures 4.5e-4.5h) rows of Figure 4.5, while the bottom row (Figures 4.6e-4.6h) shows half the differences, as indicated at the top of each panel. Thus, for example, Figure 4.6a shows the half sum of the profiles in Figures 4.5a and 4.5e, while

Figure 4.6e shows half the difference. Specifically, the blue profiles in the bottom row of Figure 4.6 show the bottom row in Figure 4.5 subtracted from those in the top row, and vice-versa for the red profiles. Therefore, adding the blue difference profile to the summed profile above it in Figure 4.6 retrieves the profiles in the top row of Figure 4.5, while adding the red differenced profile to the summed profile above it in Figure 4.6 retrieves the profiles in the bottom row of Figure 4.5. Thus, for example, the blue profile in Figure 4.6e added to the profile in Figure 4.6a retrieves Figure 4.5a, while the red profile in Figure 4.6e added to the profile in Figure 4.6a retrieves Figure 4.5e. The blue profiles thus represent the PPO-related currents associated with the PPO phases in the top row of Figure 4.5, as marked in Figure 4.6, while the red profiles represent the oppositely-signed PPO-related currents associated with the PPO phases in the lower row of Figure 4.5, as also marked in Figure 4.6.

Examining the four summed profiles in Figures 4.6a-4.6d, it can first be seen that they are all quite similar to each other as expected, approximately independent of PPO phase, though formed from entirely independent sets of field data. Moving from the pole towards larger colatitudes, we first see a near-linear increase in positive (i.e., lagging field) I_m values over the colatitude range from 7.5° to $\sim 15^\circ$, thus implying sub-corotating plasma in the polar region with a continuous downward current, as depicted in Figure 2.7 (section 2.3.4 Chapter 2) and in the theoretical models of *Cowley et al.* [2004b, 2008]. Beyond this a stronger downward current then flows for $\sim 1^\circ$ - 2° until the equatorward meridional current peaks at $\sim 1.3 \text{ MA rad}^{-1}$ near $\sim 16^\circ$, with the current then falling rapidly to near-zero values at $\sim 20^\circ$ colatitude indicative of a major layer of upward field-aligned current, beyond which the values then remain small to the largest colatitudes reached of $\sim 28^\circ$. In three of the four panels (Figures 4.6a, 4.6c, and 4.6d) it can be seen that I_m preferentially takes small negative (i.e., leading field) values in the large colatitude regime, a result that links to the small negative average value of the azimuthal field in this region found in Figure 4.3a, noted in section 4.4.1. As will be discussed in section 4.5, however, rather than indicating plasma supercorotation in this region, a more likely explanation is in terms of departures of the PPO

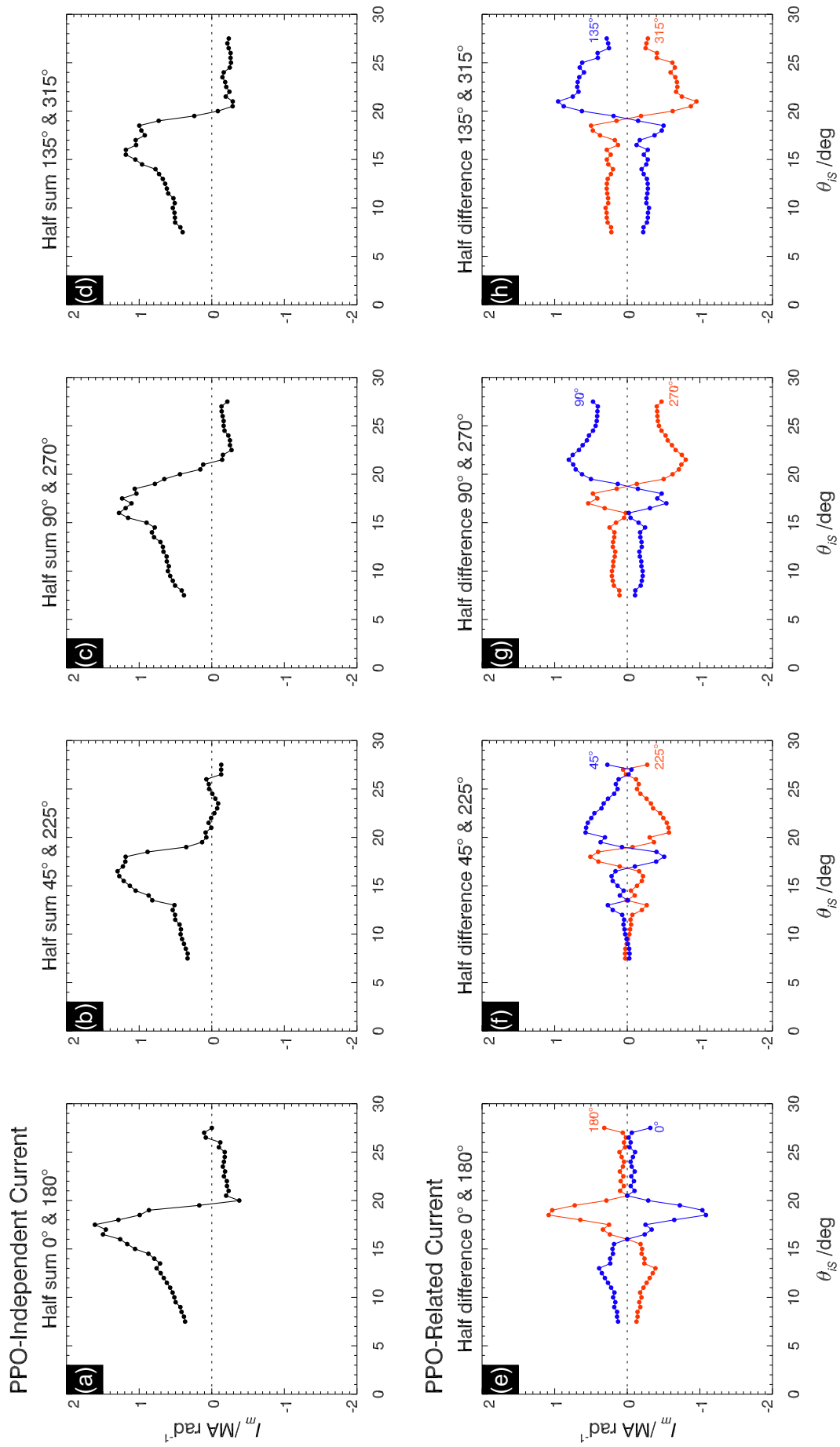


Figure 4.6: See overleaf.

currents from strict $m = 1$ symmetry, as will be discussed in section 4.5. Apart from this, however, the results in Figures 4.6a-4.6d are consistent with a PPO-independent current system associated with subcorotation of the plasma as sketched in Figure 2.7 (Chapter 2), thus likely with approximate $m = 0$ axisymmetry, in which distributed downward currents flow over the whole polar region, terminated by a layer of upward current at $\sim 17^\circ$ - 20° colatitude. The latter location is then entirely compatible with that of the main UV auroral oval in the post-midnight hours, shown by the results of *Carbary* [2012] reproduced in Figure 4.1d.

We now turn to the differenced profiles shown in Figures 4.6e-4.6h. Based on the simple picture discussed in Chapter 2 section 2.4.2, Chapter 3 section 3.2.2 and illustrated in Figure 2.13 (also Figure 3.6 in Chapter 3), we would expect I_m values poleward of the PPO-related field-aligned current layer to slowly increase in magnitude with colatitude, positive (i.e., equatorward current) for phases around $\sim 270^\circ$ and negative (i.e., poleward current) for $\sim 90^\circ$, followed by a switch in sign across the main PPO current sheet to larger magnitudes that slowly decline in value with increasing colatitude. The largest such currents should occur at phases near $90^\circ/270^\circ$, declining at both $45^\circ/225^\circ$ and $135^\circ/315^\circ$, and reducing to near-zero at $0^\circ/180^\circ$. The results in Figures 4.6e-4.6h show some evident similarities with these expectations, but also some differences. If we consider the profiles for $90^\circ/270^\circ$ in Figure 4.6g, for example, we observe near-constant values $\sim \pm 0.2 \text{ MA rad}^{-1}$ at the smallest colatitudes observed, fluctuating to reach largest values of the same sign $\sim \pm 0.5 \text{ MA rad}^{-1}$ near $\sim 17.5^\circ$, then reversing to

Figure 4.6: Southern colatitude profiles of the PPO-independent horizontal meridional current per radian of azimuth (top row Figure 4.6a-4.6d), likely associated with plasma subcorotation, and of the PPO-related current (bottom row Figures 4.6e-4.6h), obtained assuming $m = 1$ symmetry of the PPO currents. The top row of panels were obtained by summing the I_m profiles in each column of Figure 4.5 and dividing by two, as indicated at the top of each panel, while the bottom row of profiles were similarly obtained by differencing these profiles and dividing by two, as also indicated. The blue profiles in Figures 4.6e-4.6h correspond to the PPO-related currents associated with the PPO phases in Figures 4.5a-4.5d, as indicated by the PPO phases marked in the panels, while the oppositely-signed red profiles similarly correspond to the PPO phases in Figures 4.5e-4.5h, as also marked.

reach peak values of the opposite sign $\sim \pm 0.8 \text{ MA rad}^{-1}$ near $\sim 21^\circ$, before slowly falling to half these values with increasing colatitude. No sharp reduction to small values is observed at the largest colatitudes covered, however, indicating that the expected inner current layer was not clearly crossed at the largest colatitudes covered by these data (mapping to $\sim 4.1 R_S$ in the equatorial plane). However, the falling values with increasing colatitude could indicate the presence of a more distributed PPO-related current in this region. The sign reversal around $\sim 19^\circ$ is associated with a downward current of $\sim 1.3 \text{ MA rad}^{-1}$ for $\Psi_S = 90^\circ$ and an upward current of the same strength for $\Psi_S = 270^\circ$. Similar effects are also seen for phases $135^\circ/270^\circ$ in Figure 4.6h, and to a smaller extent for $45^\circ/225^\circ$ in Figure 4.6f, where the currents are $\sim 1.4 \text{ MA rad}^{-1}$ and $\sim 1.1 \text{ MA rad}^{-1}$, respectively. The PPO-related currents thus have comparable strength to those of the subcorotation system in the upper panels of Figure 4.6, thus strongly modulating the latter as indicated in section 4.4.2, being generally centred close to but slightly equatorward of the upward current region of the subcorotation system.

The results in Figures 4.6e-4.6h also show a number of departures from the simple paradigm illustrated in Chapters 2 and 3 (sections 2.4.2 and section 3.2.2). First, a sharp prominent peak centred near $\sim 18.5^\circ$ colatitude occurs in the profiles in Figure 4.6e for $0^\circ/180^\circ$, which is associated with little net change in I_m value. This effect results from the fact that the main averaged upward current layer in Figure 4.5a for $\Psi_S = 0^\circ$ is centred at a slightly smaller colatitude than that in Figure 4.5e for $\Psi_S = 180^\circ$, $\sim 18^\circ$ in the former case compared with $\sim 19.5^\circ$ in the latter. Differencing these profiles then gives rise to a spike in the differenced current profile suggesting closely-spaced near-equal upward and downward field-aligned current sheets. Given the considerable Rev-to-Rev variability in the location of this boundary evident in Figure 4.5, as mentioned in section 4.4.2, this result seems likely to be accidental. However, smaller similar features with the same sense can be seen in all of the panels in Figures 4.6e-4.6h, indicating that the main upward current layer in Figures 4.5e-4.5h is generally located slightly equatorward of that in Figures 4.5a-4.5d. A related effect was already noted in the discussion of individual examples in section 4.3.2. These shifts in colat-

itude will be further discussed, quantified, and taken into account in the analysis in Chapter 5.

Second, the derived PPO-related currents clearly do not quite behave in the expected simple symmetrical way about peak values for $\Psi_S \sim 90^\circ/270^\circ$. This is related to the phase asymmetry effect noted in the discussion of Figure 4.3, in which the equatorial oscillations in Ψ_S at large colatitudes (and the consequent meridional currents) vary closely as $\sin \Psi_S$, as expected, while the polar oscillations at small colatitudes lag by $\sim 50^\circ$ of phase from the anticipated anti-phase behaviour. Thus while the deduced PPO-related currents in the large colatitude regime are indeed larger positive and negative around $90^\circ/270^\circ$ (Figure 4.6g) and fall to near-zero values for $0^\circ/180^\circ$ (Figure 4.6e), those in the small colatitude regime are largest in magnitude around $135^\circ/315^\circ$ (Figure 4.6h), i.e., in the phase sector lagging by 45° from $90^\circ/270^\circ$, and fall to near zero at $45^\circ/225^\circ$ (Figure 4.6f), i.e., in the phase sector lagging by 45° from $0^\circ/180^\circ$.

4.5 Discussion of statistical analysis results

We now further discuss the results in Figure 4.6, starting with the PPO-independent current profiles in Figures 4.6a-4.6d. In Figure 4.7a we show the average of these four independently-obtained meridional current profiles, while in Figure 4.7b we show a corresponding profile of the field-aligned current density just above the ionosphere. Due to the expected approximate axisymmetry of this specific current system, we note that the second term in equation (3.4) for the ionospheric field-aligned current density should be negligible compared with the first independent of the magnitude of the meridional current gradient. Thus $j_{\parallel i}$ can be deduced from the meridional current profile over its full colatitude range. The profile in Figure 4.7b has then been obtained by applying equation (3.4), with second term neglected, to centred 1° steps in colatitude evaluated every 0.5° .

Figure 4.7a shows that the PPO-independent meridional current grows from ~ 0.37 MA rad^{-1} , equatorward-directed, at the poleward limit of our observations at $\sim 7.5^\circ$ southern colatitude, to a broad peak of ~ 1.25 MA rad^{-1} between $\sim 16^\circ$ and $\sim 17.5^\circ$, thus

implying a consistent downward current flowing throughout the observed poleward region totaling $\sim 0.9 \text{ MA rad}^{-1}$. The associated field-aligned current density in Figure 4.7b initially reduces from $\sim 10 \text{ nA m}^{-2}$ in the poleward-most region observed, to $\sim 5 \text{ nA m}^{-2}$ at $\sim 9^\circ - 12^\circ$, before rising to a peak of $\sim 20 \text{ nA m}^{-2}$ at $\sim 15^\circ$. The overall mean value associated with the increase in I_m between $\sim 7.5^\circ$ and $\sim 16^\circ$ is $\sim 10 \text{ nA m}^{-2}$. These results also imply that a net current of $\sim 0.37 \text{ MA rad}^{-1}$ flows downward into the ionosphere in the region poleward of our observations, between the pole where the axisymmetric equatorward current must go to zero, and the $\sim 7.5^\circ$ limit of observations. The associated mean field-aligned current density in the unobserved poleward region is then $\sim 14 \text{ nA m}^{-2}$, shown by the horizontal dashed line on the left of Figure 4.7b. We note that a distributed field-aligned current over the whole polar region associated with subcorotation of high-latitude field lines, directed downward for the planetary field polarity at Saturn, is likely a common feature of rotation-dominated systems, as in the theoretical models proposed by Cowley *et al.* [2004b, 2008]. Assuming axisymmetry, the total downward current flowing in Saturn's southern ionosphere during this interval is $\sim 8 \text{ MA}$, very comparable with the 5-10 MA deduced in these theoretical studies, noted in Chapter 2.

Beyond the polar region of consistent downward current and the broad peak of the averaged profile, the meridional current in Figure 4.7a then falls monotonically to near zero over $\sim 2.5^\circ$ colatitude between $\sim 17.5^\circ$ and $\sim 20^\circ$, associated with a narrow layer of upward-directed current. Theoretically, this may be due to a sudden increase in the plasma angular velocity with colatitude towards rigid corotation and/or a sudden decrease in ionospheric Pedersen conductivity, as will be further investigated in section 6.1. The mean current density in the upward current layer implied by the change in meridional current is $\sim 30 \text{ nA m}^{-2}$, compared with peak values $\sim 40 \text{ nA m}^{-2}$ in the profile in Figure 4.7b. It should be borne in mind, however, that the averaging procedure employed to produce Figure 4.7a will tend to lower peak meridional current values somewhat and spread the current in colatitude, due both to the natural variation in current layer locations noted in section 4.4.2 and the latitudinal variations with the

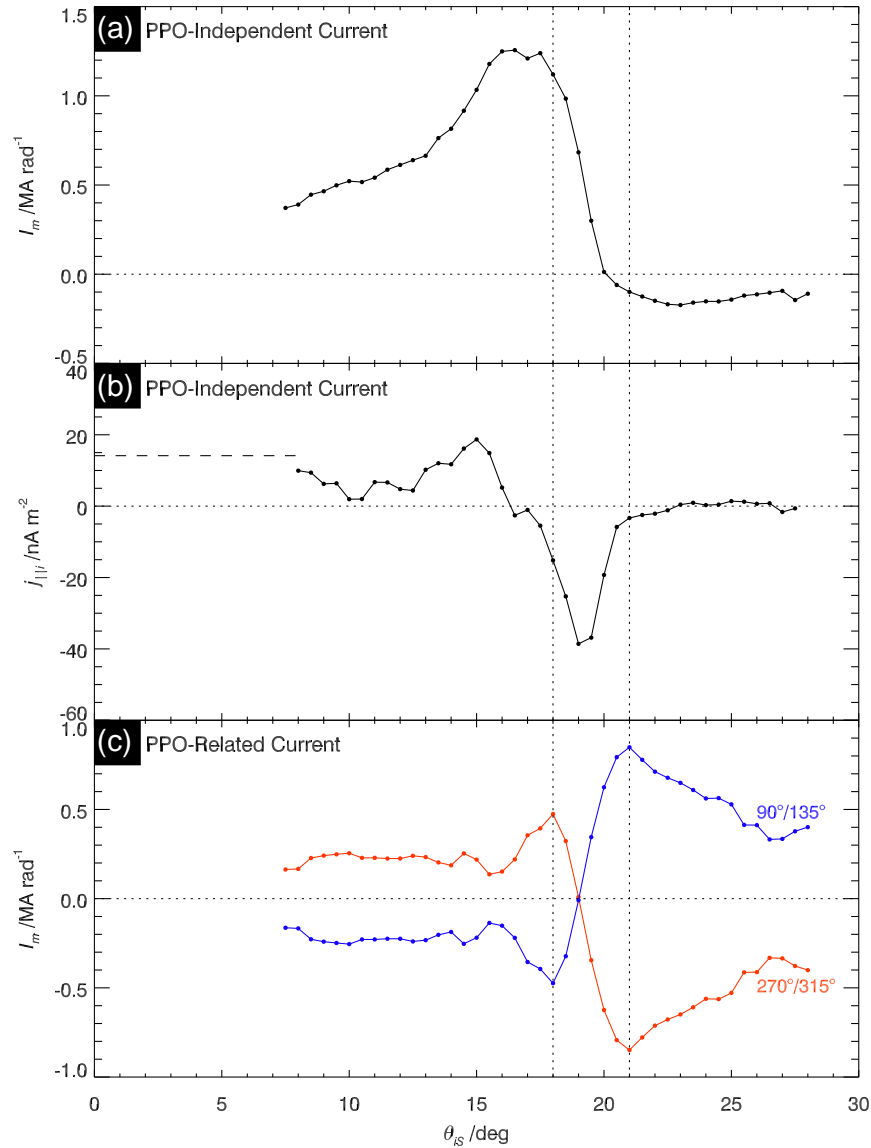


Figure 4.7: See overleaf.

PPO phase noted in section 4.3.2, both effects lowering the current density from actual peak values. In particular, we note that the smaller structured current layers observed at larger colatitudes, demonstrated in Figure 4.2, have been averaged away by these procedures. In the following chapter we further analyze these current sheets using a procedure that better preserves the integrity of their structure.

The equatorward edge of the main upward current region in Figure 4.7a at $\sim 20^\circ$ southern colatitude maps in the equatorial plane to $\sim 9 R_S$ according to our simple field model, though this value may be a little close-in if the sheet is spread in colatitude as indicated above. Equatorward of this colatitude, however, thus mapping inside $\sim 9 R_S$

in the equatorial magnetosphere, the derived meridional current values in Figure 4.7a are small, near-constant, and negative. Formally, negative values imply a poleward current and a leading field structure, but, as indicated in section 4.4.3, this seems physically at odds with the consistent observation of mildly subcorotational plasma flow in this region by $\sim 10\text{-}20\%$ [e.g., *Wilson et al.*, 2008, 2009; *Müller et al.*, 2010; *Thomsen et al.*, 2010, 2014; *Carbary and Mitchell*, 2014], as noted in section 4.1. It therefore seems more likely that these negative values arise from a lack of perfect anti-symmetry in the PPO currents assumed in their derivation. We noted already in section 4.3.2 that the downward PPO current layer for $\sim 90^\circ$ typically flows at a smaller colatitude than does the upward PPO current for $\sim 270^\circ$, an effect related to the *Burch et al.* [2009] “plasma cam” asymmetry in the equatorial magnetosphere. Such a difference indeed implies a small departure from anti-symmetry, which may result in slightly weaker perturbation fields occurring during the positive part of the B_ϕ cycle for $\Psi_S \sim 90^\circ$ than during the negative for $\Psi_S \sim 270^\circ$ (see Figure 2.13 in Chapter 2), if the downward currents flow at somewhat larger distance than the upward. In Figure 4.3a we already found such a difference, associated with a small negative mean B_ϕ in the large colatitude regime equatorward of the current sheets. Irrespective of the origin of this effect, however, the results in Figures 4.7a and 4.7b are in any case sufficient to show the lack of major currents within the inner region at a level of $\sim 0.1\text{-}0.2 \text{ MA rad}^{-1}$, extending inward from ~ 9

Figure 4.7: Overview of PPO-independent and PPO-related currents derived in Figure 4.6. Panel (a) shows the southern colatitude profile of the PPO-independent meridional currents I_m (MA rad^{-1}) averaged over the four independent determinations shown in Figures 4.6a-4.6d. Panel (b) shows the corresponding profile of the ionospheric current density given by equation (3.4) with the second term on the right side neglected, obtained by differencing the I_m values in panel (a) in 1° centred colatitude intervals evaluated every 0.5° . Positive values indicate downward current in the southern hemisphere and negative values upward current. The dashed horizontal line indicates the averaged current density that must flow in the unobserved polar region inside $\sim 7.5^\circ$ colatitude such that I_m reaches the observed value $\sim 0.37 \text{ MA rad}^{-1}$ at the poleward limit of observations. Panel (c) shows the averaged PPO-related current profiles for PPO phases centred at 90° and 135° (blue data), and 270° and 315° in Figures 4.6g and 4.6h (red data), representing the peak of the downward and upward PPO currents, respectively. Vertical dotted lines indicate the colatitude extent of the PPO-related field-aligned current region between 18° and 21° southern colatitude.

R_S to an equatorward observational limit of $\sim 28^\circ$ colatitude in the ionosphere, mapping to $\sim 4 R_S$ in the equatorial plane. The limiting ionospheric field-aligned current density in this region is a few nA m^{-2} , as indicated in Figure 4.7b.

We note that these latter results are significantly at variance with the field-aligned “electron currents” deduced by *Schippers et al.* [2012] from net plasma electron fluxes obtained from statistical analysis of near-equatorial electron data. The form of the southern nightside currents derived in this study bears little resemblance to those found here, with significant upward currents being deduced carried by cold electrons between ~ 4 and $\sim 8 R_S$, the region found here to be devoid of major currents. In addition, the current densities deduced are around two orders of magnitude larger than those expected on the basis of our results, and those of previous authors [e.g., *Bunce et al.*, 2008a; *Talboys et al.*, 2009a,b, 2011]. By order of magnitude, our results indicate current densities $\sim 10\text{-}100 \text{ nA m}^{-2}$ at ionospheric heights, translating typically to the order of $\sim 0.01\text{-}0.1 \text{ nA m}^{-2}$ in the equatorial region. Here we have used $j_{\parallel}/B = \text{const}$ along field lines in the region between the field-perpendicular closure currents flowing in the ionosphere and in the equatorial plasma, expressing continuity of the field-aligned current flowing between these regions. By comparison, the equatorial field-aligned electron currents deduced by *Schippers et al.* [2012] are of typical magnitude $\sim 1\text{-}10 \text{ nA m}^{-2}$, two to three orders larger than expected, which would translate to $\sim 1\text{-}10 \mu\text{A m}^{-2}$ at ionospheric heights, way beyond realistic values. While the origin of the net electron fluxes deduced by these authors remains unclear, they clearly do not correspond to the magnetosphere-ionosphere coupling currents deduced from magnetic field data in the present study.

In Figure 4.7c we compare the PPO-related meridional current profiles with the PPO-independent profile shown in Figure 4.7a. Specifically we show an average of the profiles in Figures 4.6g and 4.6h, where the blue data thus correspond to PPO phases centred at 90° and 135° and the red data to phases centred at 270° and 315° , representing the peak of the PPO currents as outlined in section 4.4.3. Due to the overall nature of the current system in this case, we cannot necessarily interpret the whole

meridional current profile in terms of field-aligned currents due to the presence of the unknown and now generally non-negligible second term in equation (3.4). We thus restrict attention only to those current gradients that exceed the limit of 0.3 MA rad^{-1} per degree of colatitude. The only gradient in Figure 4.7c that meets this criterion is the main variation between $\sim 18^\circ$ and $\sim 21^\circ$ colatitude marked by the vertical dotted lines in the figure. The slower fall to lesser magnitudes in the large colatitude regime does not meet this criterion, though it remains possible that part of this variation could be associated with field-aligned currents of the opposite sign to those of the main sheet.

Concentrating, then, on the central PPO-related current layer, for which the associated field-aligned currents are directed downward for phases $90^\circ/135^\circ$ and upward for phases $270^\circ/315^\circ$, we first note that these currents are approximately co-located with the main upward current sheet of the PPO-independent system in Figure 4.7a, though centred slightly to the equatorward side of the latter, and overlapping with the equatorward region of near-zero currents in the averaged PPO-independent profile. The colatitude range of the PPO current, between $\sim 18^\circ$ and $\sim 21^\circ$, maps to the equatorial plane between ~ 8 and $\sim 13 R_S$ according to our field model, somewhat closer than the $\sim 15 R_S$ radial distance indicated by the analysis of equatorial data by *Andrews et al.* [2010a]. The total current flowing in the layer is $\sim 1.3 \text{ MA rad}^{-1}$, thus comparable with that in the main upward current layer of the PPO-independent system. The mean current density determined from equation (3.4), then neglecting the second term on the right hand side, is $\sim 25 \text{ nA m}^{-2}$, though again this value is likely systematically reduced from true peak values by the averaging procedure. Significant rotating modulations of auroral and radio emission from this region is thus readily understood on this basis, as reported by numerous authors [e.g., *Sandel and Broadfoot*, 1981; *Nichols et al.*, 2008, 2010a,b; *Andrews et al.*, 2011; *Lamy et al.*, 2011; *Badman et al.*, 2012; *Carbary*, 2013; *Lamy et al.*, 2013].

4.6 Summary

Following the initial discussions by *Southwood and Kivelson* [2009] and *Talboys et al.* [2009a], in this chapter we have made a first systematic investigation of the dependence of the magnetosphere-ionosphere coupling currents in the Saturn system on PPO phase. Using a series of Cassini periapsis passes during 2008 over the post-midnight sector auroral zones at $\sim 3\text{-}5 R_S$ radial distance, and concentrating in the first instance on the southern hemisphere, our principal results are as follows.

1. Field-aligned currents are strongly modulated in form and magnitude by the PPO phase, giving rise to the differing ‘types’ of colatitude current profiles noted previously by *Talboys et al.* [2009b, 2011] and as discussed in Chapter 2 and section 4.1.
2. By exploiting the symmetries involved, the currents can be approximately separated into components that do and do not depend on the PPO phase, the latter taken generally to correspond to the effects of magnetospheric plasma subcorotation (to be discussed in more detail in Chapter 5).
3. The PPO-independent current system comprises of (i) a distributed downward current $\sim 5\text{-}15 \text{ nA m}^{-2}$ that likely flows over the whole polar region of open field lines, (ii) a layer of enhanced downward current on closed field lines mapping to the outer magnetosphere, and (iii) an adjacent layer of upward current, $\sim 1.3 \text{ MA rad}^{-1}$ in averaged current profiles, that closes these downward currents. The upward current flows at $\sim 17^\circ\text{-}20^\circ$ southern colatitude, co-located with the UV auroral zone. Weaker secondary layers of downward and upward current also flow adjacent to the equatorward boundary of the main upward current region whose elucidation requires a more refined analysis than the overall statistical study undertaken here. No significant regions of steady field-aligned current are found to flow in the inner magnetosphere at southern colatitudes greater than $\sim 21^\circ$, mapping to $\sim 8 R_S$ in the equatorial plane, within an observational colatitude limit of

$\sim 28^\circ$. The radial mapping of the field-aligned current will be discussed in Chapter 5 section 5.2.2.

4. The PPO-related currents are approximately co-located with the main upward current of the PPO-independent system, though centred slightly equatorward, mapping to the inner part of the main hot magnetospheric plasma regime. The rotating upward and downward PPO currents in this region are comparable in magnitude to the main upward current of the PPO-independent system, such that when the PPO current is also directed upward, for PPO phases $\Psi_S \sim 270^\circ$, the total current is approximately doubled, and when it points downward, for PPO phases $\Psi_S \sim 90^\circ$, the two currents approximately cancel, though significant near-equal and opposite upward and downward current sheets remain present in such cases.
5. The colatitude of the auroral region current layers is modulated by PPO phase, with maximum colatitudes at phases $\Psi_S \sim 270^\circ$ and minimum colatitudes at phases $\Psi_S \sim 90^\circ$. A related variation is observed in the colatitude extent of hot magnetospheric electrons, mirroring the “plasma cam” effect previously observed in the equatorial radial distribution of plasma ions [Burch *et al.*, 2009]. Further analysis is required to more precisely quantify this effect.
6. A phase difference of $\sim 50^\circ$ has been found between the expected phases of the PPO field oscillations on either side of the main current sheet layer, in the equatorial region on one side and in the polar region on the other. Such a shift has not previously been noted, and requires further study with other high-latitude data sets.

A number of the above issues will be addressed with greater precision in Chapter 5, which employs the same data set to focus on the structure and PPO-related modulation of the general four-current sheet structure observed in Saturn’s southern post-midnight auroral region, as exemplified in Figure 4.2.

Chapter 5

Four-sheet analysis of the southern hemisphere subcorotation and planetary period oscillation current components

5.1 Four sheet analysis

5.1.1 Current sheet boundary colatitudes and meridional currents

In this chapter an analysis that focuses directly on the current sheets for each Rev within the present data set is performed. We can determine the southern ionospheric colatitude θ_{iS} and horizontal meridional current I_m at each of five contiguous current sheet boundaries, defined specifically by extrema in the meridional current values with no gaps between, and note the concurrent value of the southern PPO phase at each boundary (see Figure 4.2). From these we can subsequently determine (in section 5.1.3) the colatitudinal width of each current sheet, the field-aligned current per radian of azimuth flowing in the sheet from equation (3.5), and the ionospheric field-aligned current density from equation (3.4). Initial results are shown in Figure 5.1, where the upper and lower rows show the southern colatitude θ_{iS} (Figures 5.1a-5.1e) and the

meridional Pedersen current I_m (Figures 5.1f-5.1j) at each boundary, respectively, plotted versus Ψ_S . The boundaries are numbered from poleward to equatorward, such that boundary 1 corresponds to the poleward boundary of downward current sheet 1, boundary 2 to the equatorward boundary of sheet 1 and the poleward boundary of the main upward current sheet 2, and so on. Any PPO-related modulations must obviously be periodic in Ψ_S , and thus expressible as a corresponding Fourier series. Due to the evident scatter in the data, here we determine only the lowest order variations, given by the mean value and a sinusoid in Ψ_S of the form

$$X = \langle X \rangle + X_0 \cos(\Psi_S - \Delta) \quad (5.1)$$

where we note that phase angle Δ gives the PPO phase Ψ_S at which the parameter concerned, X , has its maximum value, with a corresponding minimum at $\Delta \pm 180^\circ$. The fit parameters are obtained by a Levenberg-Marquardt least squares minimization algorithm [Markwardt, 2009], with results being shown by the red lines in Figure 5.1, where the dashed red lines show the mean values $\langle X \rangle$. The mean values $\langle X \rangle$, amplitudes X_0 , and phase angles Δ for each fit are recorded in Table 5.1, together with the RMS deviation of the data about the fitted lines. As a simple measure, it seems reasonable to suppose that the sinusoidal variations deduced are “significant” provided that the peak-to-peak amplitude of the oscillations are greater than the RMS deviations, a limit that is well satisfied by all of the fits shown in Figure 5.1 (see Table 5.1).

The red dashed lines in the upper row of Figure 5.1 show the equatorward progression of the mean positions of the current sheet boundaries, from $\sim 15.7^\circ$ for boundary 1 to $\sim 20.5^\circ$ for boundary 5, thus spanning $\sim 5^\circ$ of colatitude. The solid red lines show that, despite the scatter in the data, modulation in the position of each boundary with southern PPO phase is clearly present with amplitude $\sim 1^\circ$ (Table 5.1). Minimum colatitudes consistently occur near $\Psi_S \sim 90^\circ$ and maximum colatitudes near $\sim 270^\circ$, as previously noted in section 4.3.2 with regard to Figure 4.2. Closer inspection reveals, however, that with the exception of boundary 5, a consistent progression of the minima and maxima to larger phases with decreasing colatitude is also present (see phase angle Δ values in Table 5.1). Thus for boundaries 4 and 5 the peak colatitude occurs

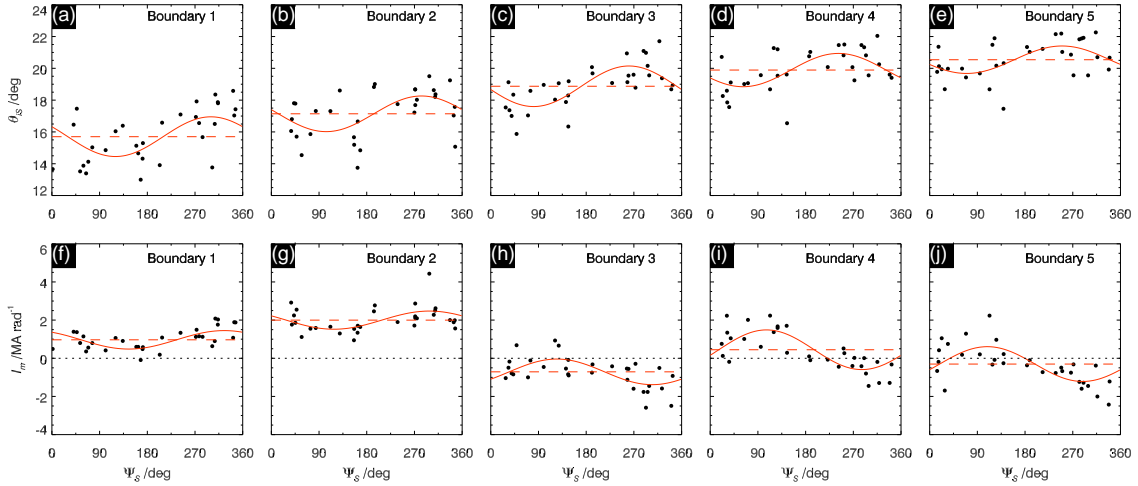


Figure 5.1: Plots showing the position and meridional current at the five current sheet boundaries for each of the 31 Revs employed in the study. Upper panels (a-e) show the southern ionospheric colatitude θ_{iS} (deg) of the current sheet boundaries plotted versus southern PPO phase Ψ_S , while lower panels (f-j) similarly show the meridional current per radian of azimuth I_m (MA rad^{-1}) at each boundary. Boundary numbers, indicated in each panel, increase from smaller to larger southern colatitudes. Red solid lines show sinusoidal fits of the form of equation (5.1) to each set of data, with fit parameters being recorded in Table 5.1. The dashed horizontal lines show the mean values.

near $\Psi_S = 245^\circ$, progressively increasing to $\Psi_S = 300^\circ$ for boundary 1. This $\sim 55^\circ$ phase shift appears to mirror the $\sim 50^\circ$ shift in phase of the polar field oscillations relative to the equatorial oscillations found in Figure 4.3b in section 4.4.1.

The red dashed lines in the lower row of Figure 5.1 similarly show the variation of the mean Pedersen current from boundary 1 to boundary 5, increasing with colatitude across layers associated with downward current, i.e., between boundaries 1 and 2 (Figures 5.1f and 5.1g), and 3 and 4 (Figures 5.1h and 5.1i), and decreasing across layers with upward current, i.e., between boundaries 2 and 3 (Figures 5.1g and 5.1h), and 4 and 5 (Figures 5.1i and 5.1j). The values are also positive for boundaries 1, 2, and 4, strongly so for boundaries 1 and 2, thus associated with an equatorward meridional current and a lagging field configuration, but are weakly negative for boundaries 3 and 5, associated with a poleward current and a leading field configuration. The I_m values at boundaries 1 and 2 are also seen to be modulated with amplitude $\sim 0.5 \text{ MA rad}^{-1}$ in PPO phase with phase angles $\Delta \sim 300^\circ - 325^\circ$, similar to that of the poleward $B_{\phi i}$ field oscillations in Figure 4.3b of Chapter 4, as expected. Those at boundaries 3-5 are sim-

<i>Colatitude of Boundary</i>				
Boundary	Mean ^a $\langle\theta_{IS}\rangle$ (deg)	Amplitude ^a (deg)	Phase Angle ^a (deg)	RMS Deviation (deg)
1	15.7	1.25	300.0	1.38
2	17.1	1.12	282.3	1.24
3	18.9	1.28	260.8	0.97
4	19.9	1.05	241.9	1.06
5	20.5	0.86	249.7	0.97
<i>Meridional Current per Radian of Azimuth at Boundary</i>				
Boundary	Mean ^a $\langle I_m \rangle$ (MA rad ⁻¹)	Amplitude ^a (MA rad ⁻¹)	Phase Angle ^a (deg)	RMS Deviation (MA rad ⁻¹)
1	0.97	0.48	325.1	0.41
2	2.00	0.48	298.1	0.56
3	-0.71	0.67	124.7	0.62
4	0.45	1.04	106.2	0.64
5	-0.30	0.91	108.8	0.73

^a Mean value $\langle X \rangle$, amplitude X_0 , and phase angle Δ are defined by equation (5.1)

Table 5.1: Sinusoidal fits for the colatitude and the meridional current at current sheet boundaries in Figure 5.1

ilarly modulated with amplitude ~ 0.9 MA rad⁻¹ at phase angles $\Delta \sim 105^\circ - 125^\circ$, nearer the phase of the equatorward $B_{\phi i}$ field oscillations in Figure 4.3a (Table 5.1). The jump in phase between boundaries 2 and 3 shows that the principal (though not the exclusive) field-aligned current to be modulated by the PPO is that flowing between boundaries 2 and 3, i.e. the main upward current sheet, consistent with the findings in section 4.4.3, as will be examined in more detail in section 5.1.2.

The fitted sinusoids in Figure 5.1 constitute a four-sheet model of the structure of the sharp southern nightside current layers at Saturn and their dependence on southern PPO phase, which is interesting to compare with the averaged profiles derived in section 4.4.2. In Figure 5.2 the black circles and lines show the meridional current profiles from Figure 4.5 averaged over non-overlapping 45° sectors of PPO phase, while the red stars joined by straight lines show the fitted boundary currents and positions from Figure 5.1 corresponding to the centre PPO phase in each panel. While a good correspondence is seen overall, the comparison makes clear the degree to which the averaging in section 4.4 attenuates the typical peaks and troughs of the current sheets, completely removing the effects of the subsidiary sheets at larger colatitudes around $\Psi_S \sim 270^\circ$, as noted in section 4.4.2. The only significant discrepancy occurs

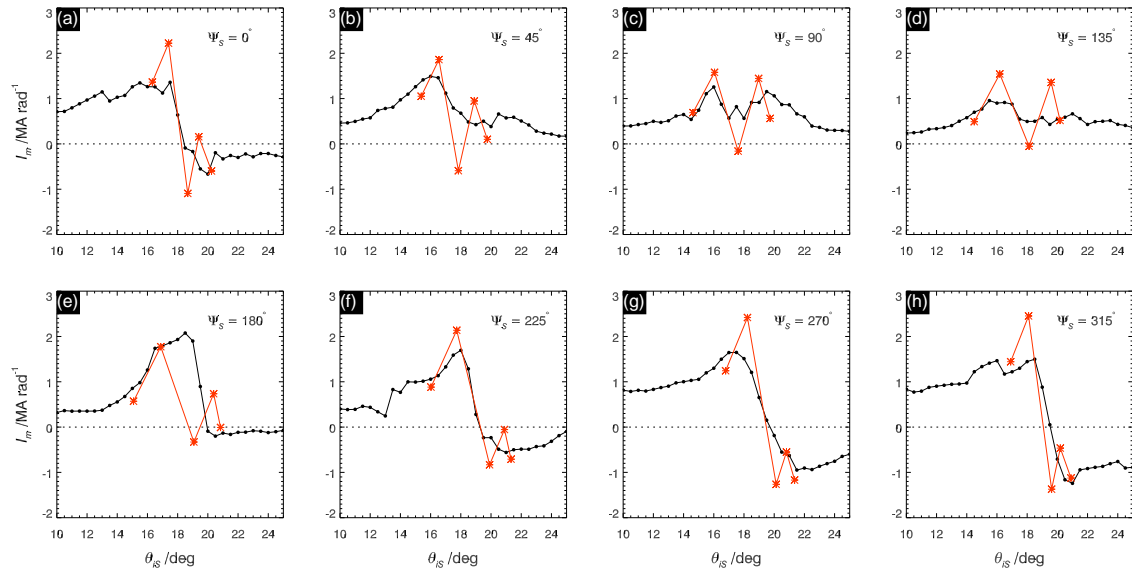


Figure 5.2: Comparison of averaged meridional current colatitude profiles from Figure 4.5 of Chapter 4 (black circles and lines) with the four-sheet values corresponding to the fitted sinusoids in Figure 5.1 (red stars joined by straight lines). The data from Figure 4.5 were averaged over non-overlapping 45° Ψ_S phase sectors centred at the values shown in each panel, while the red stars show the boundary values from Figure 5.1 corresponding to the specific phases indicated.

for $\Psi_S \sim 180^\circ$ in Figure 5.2e, where the main upward current in the averaged profile occurs at significantly larger colatitude than for the four-sheet model. It can be seen in Figure 4.5, however, that only two Revs contributed data in this region, both with main upward current sheets at larger colatitudes than those of “surrounding” data.

5.1.2 Current sheet positions, widths, and field-aligned currents

As indicated above, we can also use the boundary data in Figure 5.1 to derive values for the mean position of the field-aligned current sheets, their width, the associated field-aligned current flowing in the sheet, and the overall field-aligned current density. For these parameters, the associated Ψ_S values are taken to be those at the centre of the layer on each Rev, noting from Figure 4.2 that the change in PPO phase during each sheet crossing, or indeed over the $\sim 5^\circ$ width of the whole layer, is generally small. Results are shown in Figure 5.3, where the rows corresponds to one of the four parameters noted above, while the columns correspond to the current sheets marked at the top of the figure, again numbered from pole to equator (as in Figure 4.2) shown from

left to right, with the fifth column representing the whole four-current sheet layer. We note the different plot scales for the latter in the second and third rows. The red solid lines in each panel again show sinusoidal fits in the form of equation (5.1), with the red dashed line showing the mean value, with all the fit parameters being given in Table 5.2, together with the RMS deviations. The blue lines are alternative sinusoidal representations shown for comparison, as mentioned below.

The top row of Figure 5.3 shows the centre southern colatitude of each sheet, the red dashed lines showing consistent equatorward progression of the mean values from 16.4° for sheet 1 to 20.2° for sheet 4. In particular, the main layer of upward current, sheet 2, is centred at 18.0° (Figure 5.3b), in excellent agreement with the peak in auroral UV emission in the post-midnight sector at $\sim 17.5^\circ$ found by *Carbary* [2012] (see Figure 4.1d in Chapter 4). The average centre position of the whole four-sheet layer is $\sim 18.1^\circ$ (Figure 5.3e), i.e., centred in the main upward current layer. In addition, the red solid lines fitted to these data show that the position of each sheet oscillates with southern PPO phase about these mean positions with amplitude $\sim 1^\circ$ (Table 5.2), with largest equatorward displacements near $\sim 270^\circ$. We again note, however, that these phases increase systematically by $\sim 50^\circ$ from sheet 4 to sheet 1, being close to 270° for sheet 2 (Table 5.2). All these oscillations are regarded as significant, with peak-to-peak amplitudes exceeding the RMS deviations (Table 5.2). The blue lines show the centre positions deduced from the boundary fits in the upper row of Figure 5.1, obtained by averaging the fitted values for adjacent boundaries at fixed PPO phase. This procedure is seen to produce closely similar results.

The colatitudinal width of each current sheet is shown in the second row of Figure 5.3. These data show considerable scatter, but indicate that the main upward current, sheet 2, is typically the widest at $\sim 1.7^\circ$, while the secondary upward current, sheet 4, is the narrowest at $\sim 0.7^\circ$ (Table 5.2). The width of the whole layer is on average $\sim 4.8^\circ$. We thus note that the width of the individual sheets is comparable to their $\sim 1^\circ$ amplitude of oscillation in the PPO cycle as seen in the upper row of Figure 5.3, such that, as discussed in section 5.1.3 below, the latter oscillation should be taken into account

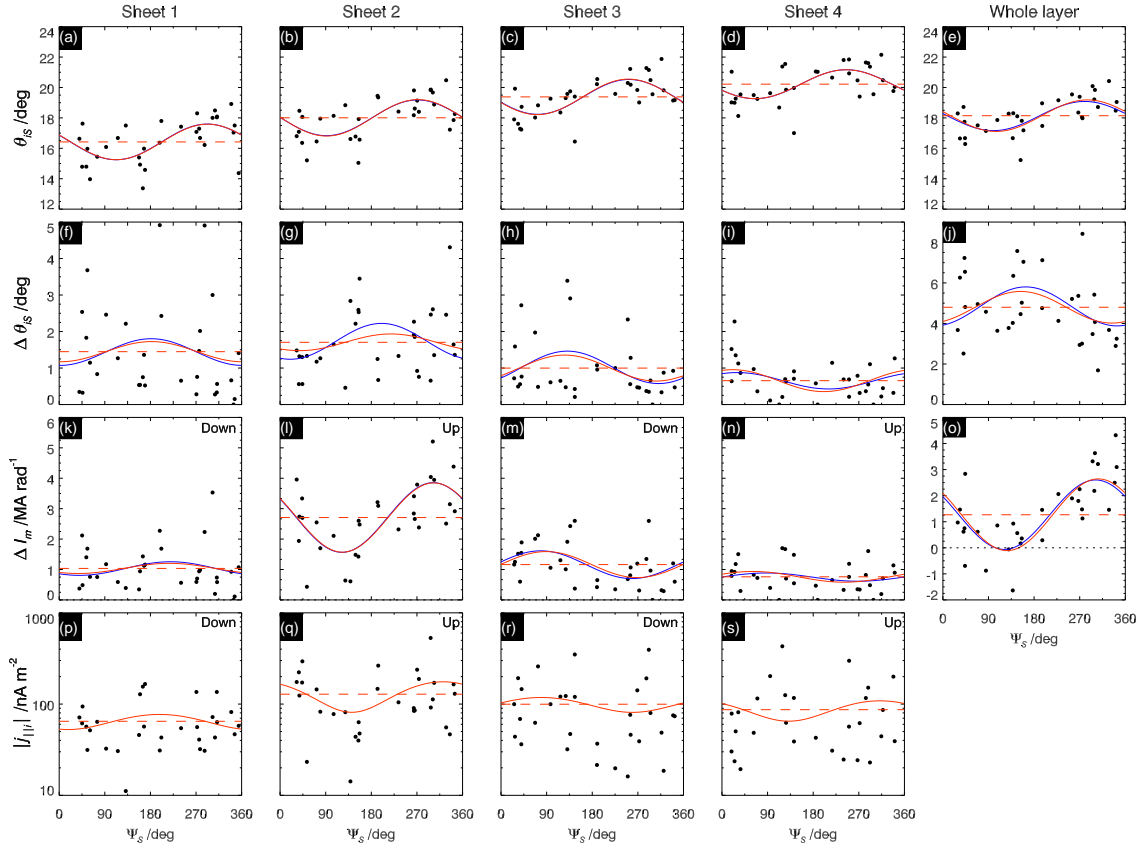


Figure 5.3: Plots showing properties of individual current sheets observed on each Rev, and of the overall four-sheet layer, as marked at the top of the figure, plotted versus southern PPO phase Ψ_S . Sheets are numbered from poleward to equatorward as in Figure 4.2. The top row (panels (a-e)) shows the centre southern colatitude of each sheet, the second row (panels (f-j)) the colatitudinal width, the third row (panels (k-o)) the magnitude of the change in Pedersen current per radian of azimuth across the sheet, and the fourth row (panels (p-s)) the magnitude of the field-aligned current density flowing in each sheet in log plot format. In the second and third rows we note the different vertical axis scales in the “whole layer” plots in the fifth column. In the third and fourth rows we indicate whether the current is directed “up” or “down” with respect to the planet for each individual current sheet. The red solid lines in all panels show sinusoidal fits to the data of the form given by equation (5.1), fitted to the unlogged current density data in the fourth row, with the fit parameters being recorded in Table 5.2. The red dashed lines show the mean values. The blue curves in the first to third rows show alternative sinusoidal representations derived from differencing the boundary fit parameters in Figure 5.1.

when attempting to separate the PPO-related and non-PPO-related currents in these sheets in a manner similar to that undertaken in section 4.4.3. The sheet widths themselves show only weak modulations with PPO phase of amplitude $\sim 0.3^\circ$ (solid red lines in Figures 5.3f to 5.3i), with peak values around $\sim 180^\circ$, except for sheet 4 which has a small minimum near this phase. These variations combine to produce an oscilla-

<i>Centre Colatitude of Current Sheet</i>				
Sheet (Figure)	Mean ^a $\langle\theta_{IS}\rangle$ (deg)	Amplitude ^a (deg)	Phase Angle ^a (deg)	RMS Deviation (deg)
1	16.4	1.17	293.1	1.61
2	18.0	1.20	271.8	1.66
3	19.4	1.17	251.3	1.65
4	20.2	0.95	245.1	0.99
Total	18.1	1.04	285.0	0.86
<i>Colatitude Width of Current Sheet</i>				
Sheet (Figure)	Mean ^a $\langle\Delta\theta_{IS}\rangle$ (deg)	Amplitude ^a (deg)	Phase Angle ^a (deg)	RMS Deviation (deg)
1	1.45	0.28	182.1	1.28
2	1.71	0.23	218.5	0.88
3	1.00	0.36	125.7	0.79
4	0.65	0.30	381.0	0.46
Total	4.80	0.78	153.6	1.52
<i>Magnitude of Change in Meridional Current Across Sheet</i>				
Sheet (Figure)	Mean ^a $\langle \Delta I_m \rangle$ (MA rad ⁻¹)	Amplitude ^a (MA rad ⁻¹)	Phase Angle ^a (deg)	RMS Deviation (MA rad ⁻¹)
1	1.04	0.17	217.5	0.76
2	2.71	1.14	303.1	1.41
3	1.16	0.43	89.0	0.78
4	0.76	0.18	60.9	0.47
Total	1.27	1.38	306.7	0.88
<i>Magnitude of Ionospheric Field-Aligned Current Density in Sheet</i>				
Sheet (Figure)	Mean ^a $\langle \Delta j_{\parallel} \rangle$ (nA m ⁻²)	Amplitude ^a (nA m ⁻²)	Phase Angle ^a (deg)	RMS Deviation (nA m ⁻²)
1	64.8	12.2	197.9	39.4
2	128.3	47.0	321.5	94.9
3	99.6	18.4	79.3	91.4
4	86.8	21.8	311.8	89.6

^a Mean value $\langle X \rangle$, amplitude X_0 , and phase angle Δ are as defined by equation (5.1)

Table 5.2: Sinusoidal fits for the current sheet parameters in Figure 5.3.

tion in the width of the whole layer of amplitude $\sim 0.8^\circ$, with peak values at PPO phase $\Psi_S \sim 150^\circ$ (Figure 5.3j). Judging from the scatter in the data and the RMS deviations in Table 5.2, however, these modulations may be regarded as being at best of marginal significance, though the averaged values are still meaningful. We recall that the data in Figures 5.3f to 5.3j represent the sheet widths observed on individual Revs ordered by the PPO phase at their colatitude centre point. An alternative estimate may be obtained from the fits to the individual boundary positions shown in the upper row of Figure 5.1, by subtracting boundary colatitudes at a given PPO phase. These values are shown by the blue lines in Figures 5.3f to 5.3j, and despite the scatter in the data, are

found to be in good agreement with the red line fits.

The third row of Figure 5.3 shows the difference in the meridional currents per radian of azimuth between the two boundaries of each sheet (moduli values are given in these cases), and across the whole layer. Since the current gradients for these sheets exceed the limit derived in Appendix C, these differences give the net currents per radian of azimuth flowing into or out of the ionosphere within each sheet (equation (3.5)). By their definition, the field-aligned currents are directed downward for sheets 1 and 3, and upward for sheets 2 and 4, as indicated in each panel. The fits to these data (solid red lines) indicate averaged values (dashed red lines) of ~ 1.0 and ~ 1.2 MA rad^{-1} for downward sheets 1 and 3, and ~ 2.7 and ~ 0.8 MA rad^{-1} for upward sheets 2 and 4 (Table 5.2). Overall, therefore, there is an average net upward current out of the whole layer of ~ 1.3 MA rad^{-1} (Figure 5.3o), that must be balanced by a distributed downward current of the same magnitude over the wider polar region not included in this current sheet analysis (see section 5.2.1 below). With regard to modulation by the PPO phase, it can be seen that poleward sheet 1 and equatorward sheet 4, downward and upward respectively, are only modestly (and insignificantly) modulated about their means with amplitudes ~ 0.2 MA rad^{-1} . As indicated above, however, upward sheet 2 is very strongly modulated with an amplitude of ~ 1.1 MA rad^{-1} , while sheet 3 is also significantly modulated (within the above limit) with an amplitude ~ 0.4 MA rad^{-1} (Table 5.2), as may already be anticipated from consideration of Figures 4a and 4c. The upward current in sheet 2 peaks at ~ 3.9 MA rad^{-1} near $\Psi_S \sim 300^\circ$ with minimum values of ~ 1.6 MA rad^{-1} at $\Psi_S \sim 120^\circ$, while the adjacent downward current in sheet 3 peaks at ~ 1.6 MA rad^{-1} at $\Psi_S \sim 90^\circ$ and has a minimum value ~ 0.7 MA rad^{-1} at $\Psi_S \sim 270^\circ$. The consequence of these variations is that the net current across the layer shown in Figure 5.3o reduces to near zero for phases near $\Psi_S \sim 90^\circ$, while increasing to ~ 3 MA rad^{-1} near $\Psi_S \sim 270^\circ$. The upward current in the layer due to the subcorotation system is thus largely cancelled by the PPO current when it is directed downward, and doubled when it is directed upward, in agreement with the results in Chapter 4. Again, an alternative estimate of the net currents may be obtained from the fits to the I_m values

at each boundary shown in the lower row of Figure 5.1, by subtracting fitted boundary values at a given PPO phase. These are shown by the blue lines in the third row, and are again found to be in good agreement with the red line fits to the data from individual Revs as shown.

The bottom row of Figure 5.3 shows the magnitude of the overall current density in each current layer, displayed in a log plot due to the large range in the individual values, with the directions of the current again being marked as “down” or “up” within each panel. These have been calculated using the net current flowing in each layer on each Rev, shown in the third row of Figure 5.3, and the colatitude position and width of the layer as shown in the first and second rows. No plot is included in column 5 since no meaning is attached to the current density for the whole multi-sheet layer. The calculation employed uses equation (3.4), neglecting the term involving the azimuthal gradient of the azimuthal current as indicated above, and assuming the ionospheric current layer is an oblate spheroid located 1000 km above the 1 bar surface [e.g., *Cowley and Bunce* [2003]; *Bunce et al.* [2008a]]. Closely similar results are obtained, however, using a spherical surface at the polar ionospheric radius. The red lines show sinusoidal fits to the unlogged data of the form given by equation (5.1). The averaged current densities are seen typically to be $\sim 100 \text{ nA m}^{-2}$, well above the approximate limiting value of $\sim 20 \text{ nA m}^{-2}$ associated with the limiting meridional current gradient, though the current densities are somewhat smaller for sheet 1 with an averaged value of $\sim 65 \text{ nA m}^{-2}$ (Table 5.2). The largest value is for main upward current sheet 2, with an averaged current density of $\sim 130 \text{ nA m}^{-2}$. This current sheet also displays the largest modulation with PPO phase, of amplitude $\sim 50 \text{ nA m}^{-2}$, at the marginal level of significance according to the above limit (RMS deviation $\sim 100 \text{ nA m}^{-2}$), with a phase that approximately follows the phase of the current itself, peaking at $\Psi_S \sim 300^\circ$, compared with $\sim 300^\circ$ for the total current in the sheet. The modulation amplitudes $\sim 10\text{-}20 \text{ nA m}^{-2}$ for the other three current sheets are not regarded as significant.

With regard to Saturn’s auroras, we note that upward-directed current densities of order $\sim 100 \text{ nA m}^{-2}$, and above, are expected to be associated with downward accelera-

tion of magnetospheric electrons by field-aligned voltages, with resulting bright auroral emissions [Bunce *et al.* [2008a]; Cowley *et al.* [2008]]. We should recognise, however, that the current densities reported here represent mean values that assume the total field-aligned current flowing in the sheet is uniformly distributed across the width. Examination of individual cases (e.g., Figure 4.2) shows, however, that this is not always the case, such that within the sheets we identify regions with stronger and weaker field-aligned current density, as indicated by the gradient of the meridional current, such that the actual emissions may often be narrower and brighter than those indicated by the widths and intensities of the currents given here. Nevertheless, on the basis of our results we would expect the main upward current layer, sheet 2, to be associated with the main UV oval emissions, and that a secondary, narrower dimmer emission associated with sheet 4 should generally be present $\sim 2^\circ$ equatorward of it. Although the structure of nightside emissions has yet to be the subject of large-scale study at this level of detail, examples of such multiple nightside arcs are known in the literature [Melin *et al.* [2011]; Bunce *et al.* [2014]]. With regard to modulation by the PPO oscillation, we note that the total current and the current density in upward current sheet 2 are modulated by a factor of more than ~ 2 over the PPO cycle. This should lead to strong variations in the emission intensity in proportion to the square of the current density, due to the precipitating energy flux of accelerated electrons being proportional to the square of the current density [e.g., Bunce *et al.*, 2008a], while the related modulations in sheet 4 are significantly smaller. With regard to downward current regions and possible modulated auroral hiss [Gurnett *et al.* [2009b]; Kopf *et al.* [2010]], we note that the largest and most modulated current is that in sheet 3, whose total current varies by a factor of more than ~ 2 over the PPO cycle, in approximate anti-phase with the modulation of the upward current in sheet 2.

5.1.3 Sum and difference current sheet profiles

We now attempt to separate the currents in the overall four-current layer that are dependent on the PPO phase from those that are not using the “half sum and difference”

approach previously employed on the mean current profiles in 4.4.3. In order to do this, however, account must be taken of the oscillatory motion of the overall layer, whose $\sim 1^\circ$ amplitude is comparable with the thicknesses of the current sheets themselves, as noted above.

An alternative view of the latitudinal motion of the current sheets in the post-midnight sector is shown in Figure 5.4a, where the fitted boundary positions in the upper row in Figure 5.1 are shown versus Ψ_S in polar rather than linear format. The dotted grid thus shows southern colatitude circles at 5° intervals, with “longitude” lines of southern PPO phase increasing clockwise around the plot, effectively in a view looking down from the north (see Figure 2.13d). The numbered blue and red bands show the layers of downward and upward current, respectively, with boundaries given by the sinusoidal fits in the upper row of Figure 5.1. The black dots and crosses on the left of the plot show the positions of minimum southern colatitude of the boundaries and centres of the current sheets, respectively, while those on the right show corresponding positions of maximum southern colatitude, displaced by 180° in phase. These show a consistent progression to later phases with decreasing colatitude by $\sim 55^\circ$, indicative of poleward phase propagation, noted previously in section 5.1.1 with regard to the current sheet boundaries, and in section 5.1.2 with regard to the current sheet centres. This behaviour is investigated further in section 5.2.4. Overall, however, the results show a poleward displacement of the overall layers centred near $\Psi_S \sim 90^\circ$, and an equatorward displacement near $\Psi_S \sim 270^\circ$.

In Figure 5.4b we show the colatitudinal displacement $\delta\theta_{iS}$ of each observed current sheet boundary from its overall mean position shown by the dashed lines in the upper row of Figure 5.1, plotted versus Ψ_S , where the data for each boundary are colour-coded as shown in the figure. A general sinusoidal fit to all of these data of the form given by equation (5.1) is found to yield a mean value close to zero, as expected, and a phase close to $\sim 270^\circ$. For simplicity we have therefore fitted a sinusoid to these data with exactly zero mean and a phase of 270° , as shown by the black solid line, yielding an amplitude of 1.04° with an RMS deviation of 1.17° . The uncertainty in the

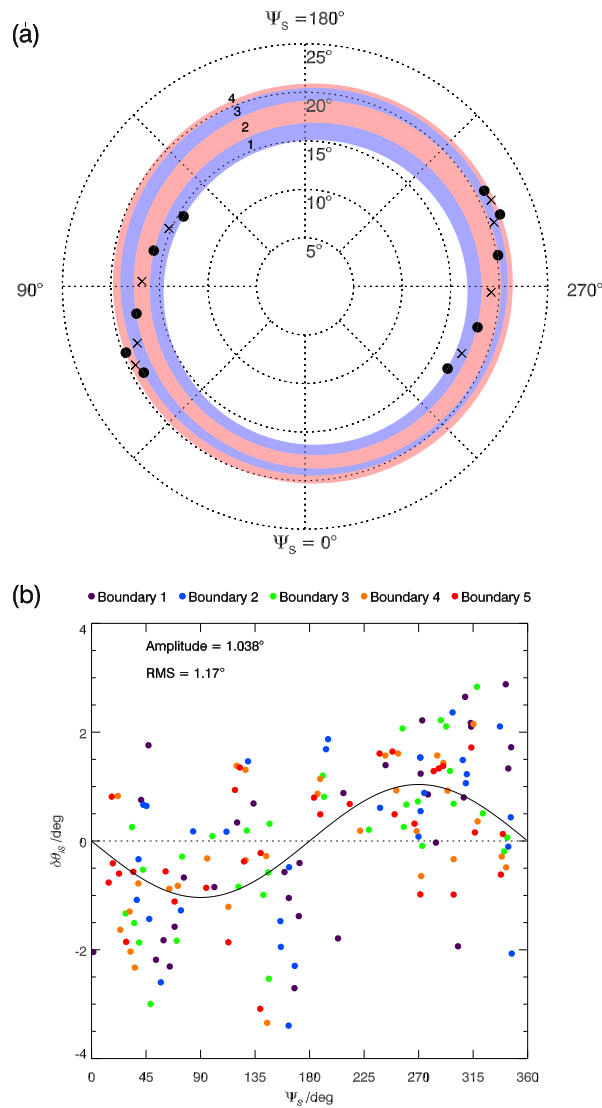


Figure 5.4: See Overleaf.

amplitude has been estimated from the formal uncertainty in the slope of a linear fit to these data plotted versus $\sin \Psi_s$, this yielding a modest uncertainty of $\sim \pm 0.13$ deg. The Pearson correlation coefficient for this linear fit is -0.55, which given the sample size of 155 this correlation is within the 0.95 and 0.99 confidence intervals. In order to compare current layer structures with varying southern PPO phases we thus use this model to “shift” the location of the layers to their overall mean positions at $\Psi_s = 0^\circ / 180^\circ$.

Results are shown in Figure 5.5, where the upper row shows the “shifted” profiles for “opposite” southern PPO phases, 0° and 180° in Figure 5.5a, 45° and 225° in Figure 5.5b, and so on. As indicated in the figure, the blue and red symbols and lines refer to the smaller and larger of these pairs of values, respectively. The stars and solid lines

show results for the four-sheet analysis developed in this section, while the circles and dashed lines show results for the averaged current profile analysis in Chapter 4 and section 4.4, to which the same “shift” procedure has been applied for comparison purposes. Specifically, we have shifted the colatitude of all of the boundary data in the upper row of Figure 5.1 and all of the I_m data shown in Figure 4.5 according to their Ψ_S values using the fit in Figure 5.4b, and have then re-calculated the analyses that follow as described in section 5.1.1 for the four-sheet analysis, and in sections 4.4.2 and 4.4.3 of Chapter 4 for the mean profile analysis. Only a restricted colatitude range 14° to 22° is shown in the figure, encompassing the main current sheets, in order to give a close-up view of the current layers. It can be seen that the procedure does result in closely over-lapping current regions for “opposite” pairs of PPO phase values, as designed.

The second and third rows of Figure 5.5 show the “half sum and difference” profiles derived from these data, similar to Figure 4.6 in section 4.4 of Chapter 4, where the “four-sheet” values shown by the stars and solid lines are simply obtained by combination of the piecewise linear profiles in the upper row of Figure 5.5, over the colatitude ranges where both exist. The “half sum” profiles in the second row are seen to be essentially independent of PPO phase, as expected. Each shows the presence of a poleward downward current of ~ 0.5 MA rad^{-1} flowing in a strongly lagging field region

Figure 5.4: Plots exhibiting the colatitudinal motions of the four field-aligned current layers with PPO phase. Panel (a) shows a phase dial plot of current sheet boundary colatitude versus southern PPO phase, effectively looking down onto the southern ionosphere through the planet from the north (see Figure 2.13d). Dotted circles represent southern colatitude at 5° intervals, while dotted straight lines indicate PPO phase Ψ_S increasing clockwise around the diagram. The numbered blue and red bands represent regions of downward and upward field-aligned current, respectively, with boundaries given by the sinusoidal fits shown by the solid red lines in the upper row of Figure 5.1 (Table 5.1). The black dots and crosses on the left of the plot show points of minimum southern colatitude for the current sheet boundaries and centres, respectively, while those on the right show the corresponding points of maximum colatitude, displaced in phase by 180° . Panel (b) shows observed current sheet boundary displacements $\delta\theta_{iS}$ (deg) from overall mean values for each boundary (red dashed lines in Figure 5.1) plotted versus Ψ_S , data for each boundary being colour-coded as indicated in the figure. The solid black line shows a fit to these data assumed for simplicity to be of the form $\delta\theta = -A \sin \Psi_S$.

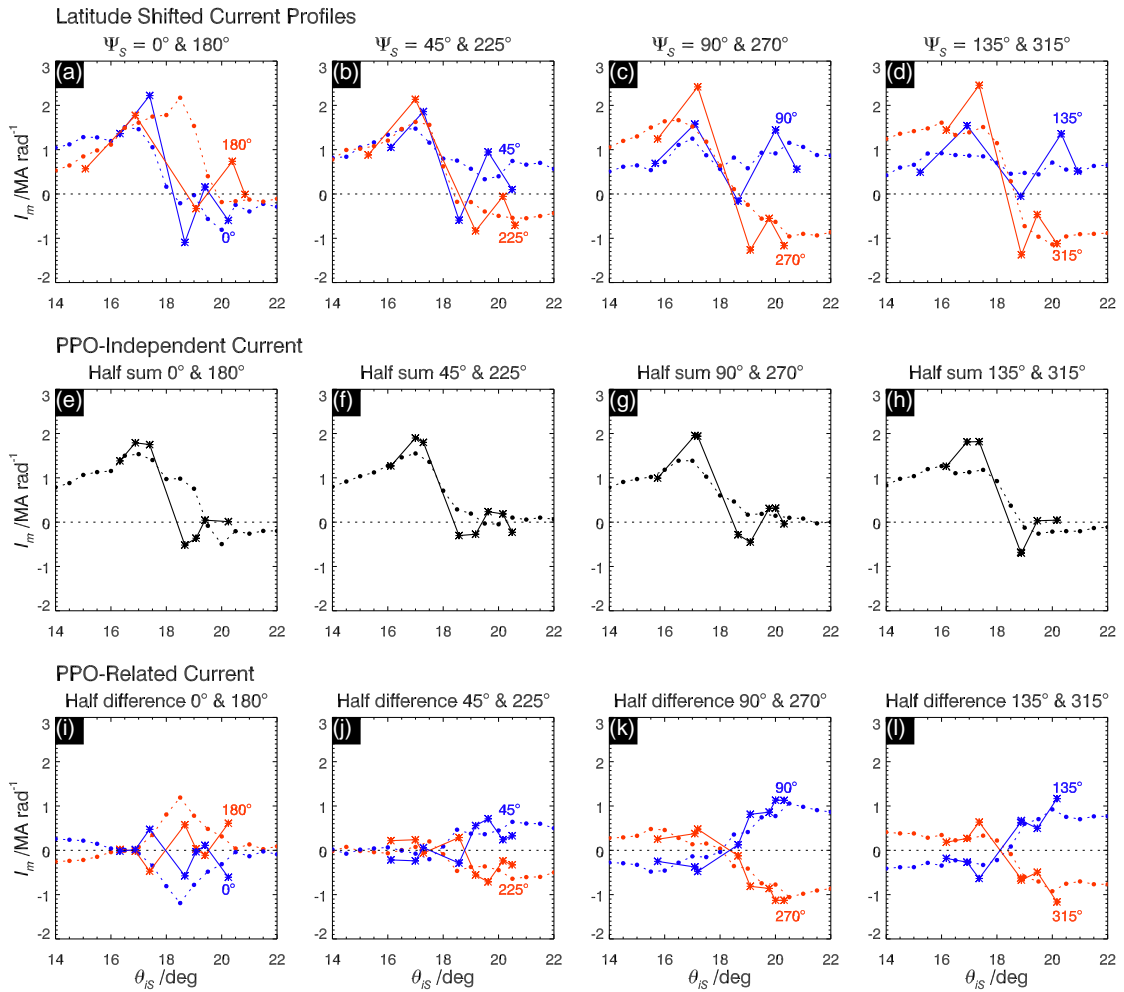


Figure 5.5: Southern colatitude profiles of the horizontal meridional current per radian of azimuth I_m (MA rad^{-1}) showing results related to Figure 4.6 but using data shifted in colatitude according to the results in Figure 5.4b. The top row (panels (a-d)) shows the shifted current profiles for pairs of opposite values of the southern PPO phase, blue data for the smaller of the two values in each panel, and red for the larger (by 180° in each case), where the stars and solid lines correspond to the four-current sheet analysis, and the solid circles and dashed lines to the similarly-shifted mean current profiles. The middle row (panels (e-h)) shows half the sum of these pairs of profiles, representing the PPO-independent currents, for the similarly coded four-sheet analysis and mean current profiles. The bottom row (panels (i-l)) shows half the differences, such that adding the blue profile to the corresponding profile in the middle row yields the blue profile in the upper row, while adding the equal but opposite red profile to the middle profile yields the red profile in the upper row.

between $\sim 16^\circ$ and 17° colatitude, a main upward current of $\sim 2.5 \text{ MA rad}^{-1}$ flowing between $\sim 17^\circ$ and $\sim 19^\circ$ associated with a transition from a strongly lagging field on its poleward side to a weakly leading field on its equatorward side, a second downward current of $\sim 0.5 \text{ MA rad}^{-1}$ flowing between $\sim 19^\circ$ and $\sim 20^\circ$ associated with a return to either an almost unperturbed or weakly lagging field, and finally in two cases where

the data extend sufficiently, indication of a secondary upward current at $\sim 20^\circ - 20.5^\circ$ of $\sim 0.5 \text{ MA rad}^{-1}$. The “shifted” mean profiles shown by circles with dashed lines in these panels exhibit overall comparable features, but where the current extrema, gradients, and details at larger colatitudes are significantly attenuated by the averaging procedure, as anticipated in section 4.4 of Chapter 4. With regard to the colatitude ranges indicated above, we note that the layers are actually displaced $\sim 1^\circ$ equatorward of those quoted for $\Psi_S \sim 270^\circ$, and $\sim 1^\circ$ poleward for $\Psi_S \sim 90^\circ$, in accordance with Figure 5.4b.

The “half difference” profiles are shown in the third row of Figure 5.5 in a similar format to the upper row of the figure (see also the lower row of Figure 4.6). Thus the blue profile added to the “half sum” profile above it yields the blue profile in the upper row of the figure, while the equal but opposite red profile added to the same “half sum” profile yields the red profile in the upper row. The mean profile results (circles with dashed lines) for $\Psi_S = 0^\circ / 180^\circ$ in Figure 5.5i are similar to those in Figure 4.6e and for related reasons, though only scattered values, are somewhat less in peak magnitude than in Figure 4.6e, obtained from the four-sheet data. The other three panels, however, show the clear presence of downward (blue data) and upward (red data) current layers that generally span the colatitude range of both main upward current sheet 2 in the second panel and adjacent downward current sheet 3, between $\sim 17.5^\circ$ and $\sim 20^\circ$ (shifted by -1° for $\Psi_S \sim 90^\circ$ and by $+1^\circ$ for $\Psi_S \sim 270^\circ$). The currents carried are $\sim 1 \text{ MA rad}^{-1}$ for $\Psi_S = 45^\circ / 225^\circ$, increasing to $\sim 1.6\text{-}1.8 \text{ MA rad}^{-1}$ for both $\Psi_S = 90^\circ / 270^\circ$ and $\Psi_S = 135^\circ / 315^\circ$. The corresponding peak current densities are $\sim 40 \text{ nA m}^{-2}$. As in the corresponding discussion of Figure 4.6, we note that at large colatitudes, greater than $\sim 20^\circ$, the largest difference between the red and blue curves occurs at phases 90° and 270° , and the smallest at 0° and 180° , as expected, while at small colatitudes, less than $\sim 16^\circ$, the largest difference occurs at phases 135° and 315° , and the smallest at 45° and 225° . This effect is directly related to the $\sim 50^\circ$ phase lag of the polar PPO oscillations compared with expectations based on the equatorial oscillations found in Figure 4.3 in section 4.4.1 of Chapter 4.

5.1.4 Discussion of four current sheet analysis results

In Figure 5.6 we provide an overview of the principal results of this section, which will be compared with the related overview of the statistical analysis results of section 4.4, shown in Figure 4.7 from Chapter 4. Figure 5.6a shows averaged colatitude profiles of the PPO-independent meridional current determined from the “half sum” profiles in Figures 5.5e to 5.5h, in which the overall PPO-dependent oscillation of the current layer has been taken into account. The profiles shown correspond to $\Psi_S \approx 0^\circ/180^\circ$, and are shifted by $\sim 1^\circ$ poleward for $\Psi_S \approx 90^\circ$ and by $\sim 1^\circ$ equatorward for 270° , as shown in Figure 5.4. The solid line shows the average of the four independent profiles derived from the four current sheet analysis, where the vertical black dotted lines mark the mean positions of the current sheet boundaries from Table 5.1, in close agreement with the boundaries and extrema of this profile, as expected. The circles joined by dashed lines then show the average of the “half sum” mean current profiles in Figure 5.5e-5.5h. Comparison with the related averaged mean profile shown in Figure 4.7a, in which the PPO-related motion of the current layer was not taken into account but simply averaged over, shows that these are very similar, but that the mean profile in Figure 5.6a peaks at slightly higher values than the latter at the boundary of sheets 1 and 2. Comparison with the results of the four-sheet analysis, however, illustrates how the overall mean profile analysis attenuates peak currents and smooths gradients in the auroral region, hence reducing deduced current densities, as well as completely removing the non-monotonic behaviour associated with current sheets 3 and 4 at larger colatitudes.

The mean current profile does, however, provide information on the more distributed PPO-independent currents flowing outside the auroral region on either side. It can be seen that distributed downward currents flow throughout the ionosphere on the poleward side, as discussed in section 4.4 of Chapter 4, producing an increasing equatorward meridional (Pedersen) current that reaches $\sim 1 \text{ MA rad}^{-1}$ at the poleward boundary of current sheet 1. No such currents are detected in the equatorward region. However, as in section 4.5 of Chapter 4, we regard the small near-constant negative I_m values deduced in this region as more likely due to a lack of exact anti-symmetry of the

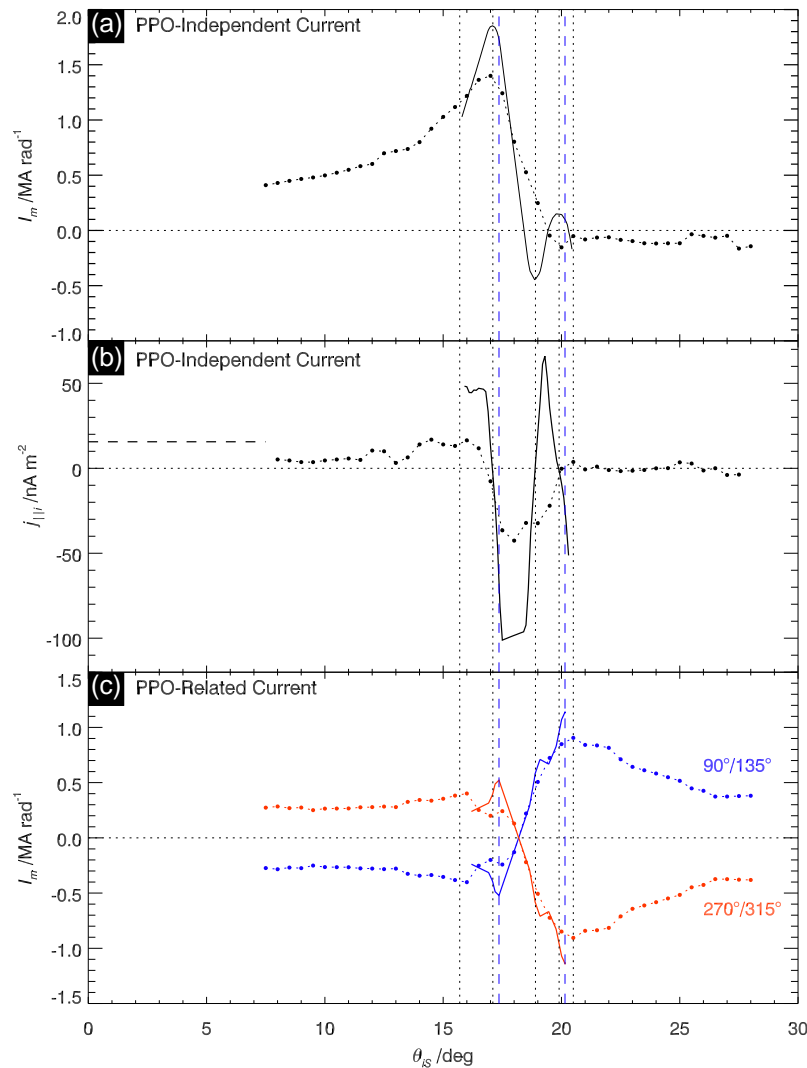


Figure 5.6: See Overleaf.

PPO-related currents assumed in the analysis, rather than being indicative of a leading field configuration in a region where the magnetospheric plasma is consistently observed to modestly sub-corotate (see section 5.2.1 below). Nevertheless, these results indicate that the ionospheric current values are small in this region, of order $\sim 0.1 \text{ MA rad}^{-1}$, or less.

Figure 5.6b then shows profiles in corresponding formats of the field-aligned current density just above the ionosphere, derived from equation (3.4) with the neglect of the second term on the right independent of the current gradient, assuming a quasi-axisymmetric PPO-independent current system. The results derived from the four current sheet analysis (solid line), obtained by differencing the corresponding meridional current curve in Figure 5.6a across centred 0.2° intervals of southern colatitude every

0.1° , show peak downward current densities in sheets 1 and 3 of ~ 50 and $\sim 60 \text{ nA m}^{-2}$, respectively, comparable with but a little less than the overall mean values in these current sheets in Table 5.2, while peak upward current densities in sheets 2 and 4 are similarly ~ 100 and $\sim 50 \text{ nA m}^{-2}$, respectively. These compare with downward currents in sheet 1 of $\sim 15 \text{ nA m}^{-2}$ derived from the “shifted” mean current profile (circles and dashed lines), obtained by differencing the current values across centred 1° intervals every 0.5° , together with an upward current peaking at $\sim 40 \text{ nA m}^{-2}$ that is spread across the regions occupied by sheets 2 and 3, similar to the results in Figure 4.7b. This profile also shows, however, that distributed downward currents $\sim 5\text{-}15 \text{ nA m}^{-2}$ flow over the whole poleward region observed to $\sim 7.5^\circ$ colatitude, a factor of $\sim 5\text{-}10$ less than that flowing in sheet 1. The finite equatorward meridional current $\sim 0.4 \text{ MA rad}^{-1}$ flowing at the poleward limit of observations also implies a mean downward current of density $\sim 15 \text{ nA m}^{-2}$ flowing over the area between the pole and that limit, shown by the horizontal dashed line in Figure 5.6b. By comparison, field-aligned currents are small throughout the equatorward region with colatitudes greater than $\sim 21^\circ$ (mapping to the equatorial plane inside $\sim 8 R_S$), with values of a few nA m^{-2} , or less.

Figure 5.6: Summary plot showing an overview of the results obtained from the “half sum and difference” analysis in Figure 5.5 which takes account of the $\sim \pm 1^\circ$ latitudinal motion of the current layer in the PPO cycle, shown here for $\Psi_S \approx 0^\circ/180^\circ$ when the shift is zero. Panel (a) shows profiles of the PPO-independent meridional ionospheric current obtained by averaging the four “half sum” profiles in Figure 5.5e to 5.5h. The solid lines correspond to the four current sheet analysis, and the circles and dashed lines to the mean current profiles, shown in similar formats in Figure 5.5. Vertical dotted lines show the boundaries of the individual current sheets corresponding to the mean positions in Table 5.1. Panel (b) shows field-aligned current density profiles in a corresponding format, determined from equation (3.4) with neglect of the second term on the right side. The horizontal dashed line on the left shows the averaged current density that must flow between the pole and the poleward limit of observations to achieve the value $I_m = 0.41 \text{ MA rad}^{-1}$ at that boundary. Panel (c) shows the PPO-related currents near their peak values, obtained by averaging the two “half difference” profiles shown in Figures 5.5k and 5.5l. The blue data correspond to PPO phases $90^\circ/135^\circ$ and the red to $270^\circ/315^\circ$ as marked. Results from the four-sheet analysis are shown by solid lines, while those from the mean profile analysis are shown by circles and dashed lines. The main PPO-related field-aligned current sheet lies at “shifted” colatitudes between $\pm 17.5^\circ$ and 20° , marked by the vertical blue dashed lines.

Figure 5.6c then shows the PPO-related current profiles near their peak southern phase, specifically the mean of the two “half difference” profiles in Figures 5.5k and 5.5l, the blue data corresponding to PPO phases $90^\circ/135^\circ$, and the red to $270^\circ/315^\circ$, as indicated in the figure. The solid lines again show the mean of the two profiles derived from the four current sheet analysis, while the circles joined by dashed lines show the corresponding results derived from the colatitude-“shifted” versions of the mean current profiles. These profiles correspond to the peak PPO-related currents flowing in this region, and demonstrate that the magnitude of the current is $\sim 1.7 \text{ MA rad}^{-1}$, flowing in a $\sim 2.5^\circ$ colatitude region, $\sim 17.5^\circ - 20^\circ$, that overlaps principally with current sheets 2 and 3 in Figure 5.6a, as marked by the blue vertical dashed lines. The corresponding mean current density is $\sim 35 \text{ nA m}^{-2}$. We note again, however, that while Figure 5.6c correctly shows the location of these PPO-related currents relative to the “shifted” PPO-independent currents in Figure 5.6a, in reality both are shifted $\sim 1^\circ$ colatitude poleward for $\Psi_S \sim 90^\circ$ blue curves in Figure 5.6c), and both $\sim 1^\circ$ equatorward for $\Psi_S \sim 270^\circ$ (red curves in Figure 5.6c).

5.2 Discussion of results

5.2.1 PPO-independent current system and plasma subcorotation

In this section we now discuss some physical implications of the results obtained in this chapter. We begin with the PPO-independent current system summarised in Figures 5.6a and 5.6b, and consider its relation to magnetospheric plasma subcorotation, as over-viewed initially in Chapter 2. Specifically we compare the PPO-independent ionospheric current profile with plasma flow observations, and consider what inferences may be drawn.

The physics of the plasma subcorotation current system requires that the meridional ionospheric current is a Pedersen current, which, assuming approximate axisymmetry, is given (per radian of azimuth) by (see *Cowley et al.* [2008] and references

therein)

$$I_m = \frac{\Sigma_P^* \rho_i^2 B_i \Omega_S}{\cos \alpha_i} \left(1 - \frac{\omega}{\Omega_S} \right). \quad (5.2)$$

Here Ω_S is the angular velocity of the planet, ω the angular velocity of the plasma (constant along a field line in the axisymmetric approximation), B_i the ionospheric field strength, α_i the angle of the ionospheric field to the local vertical, ρ_i is the perpendicular distance of the field line foot in the ionosphere, and Σ_P^* the effective height-integrated ionospheric Pedersen conductivity, possibly reduced from the true value Σ_P by the excitation of azimuthal neutral winds resulting from the drag due to ion-neutral collisions. These conductivities are related by

$$\Sigma_P^* = (1 - k) \Sigma_P, \quad (5.3)$$

where

$$k = \left(\frac{1 - (\Omega_S^*/\Omega_S)}{1 - (\omega/\Omega_S)} \right), \quad (5.4)$$

and Ω_S^* is the angular velocity of the neutral atmosphere in the Pedersen layer. Thus k has a minimum value of zero when the neutral atmosphere rigidly corotates, $\Omega_S^* = \Omega_S$, such that the effective Pedersen conductivity is then the true value, and a maximum value of unity when the neutral atmosphere rotates with the plasma, $\Omega_S^* = \omega$, when the effective Pedersen conductivity is zero (no electric field in the neutral atmosphere frame). Modeling work suggests that the appropriate value for Saturn is $k \approx 0.5$, midway between these limits [Galand *et al.*, 2011]. The factor in equation (5.2) associated with the departure of the field from the local vertical assumes the presence of a small field-aligned current local to the ionosphere such that the total current, the true Pedersen current transverse to the field plus the small field-aligned current, flows horizontally in the ionosphere as required. The quantity I_m used throughout this study corresponds specifically to this horizontal meridional ionospheric current, slightly larger than the true meridional Pedersen current flowing perpendicular to the tilted magnetic field lines.

In Figure 5.7a we reproduce the colatitudinal I_m profiles of the PPO-independent

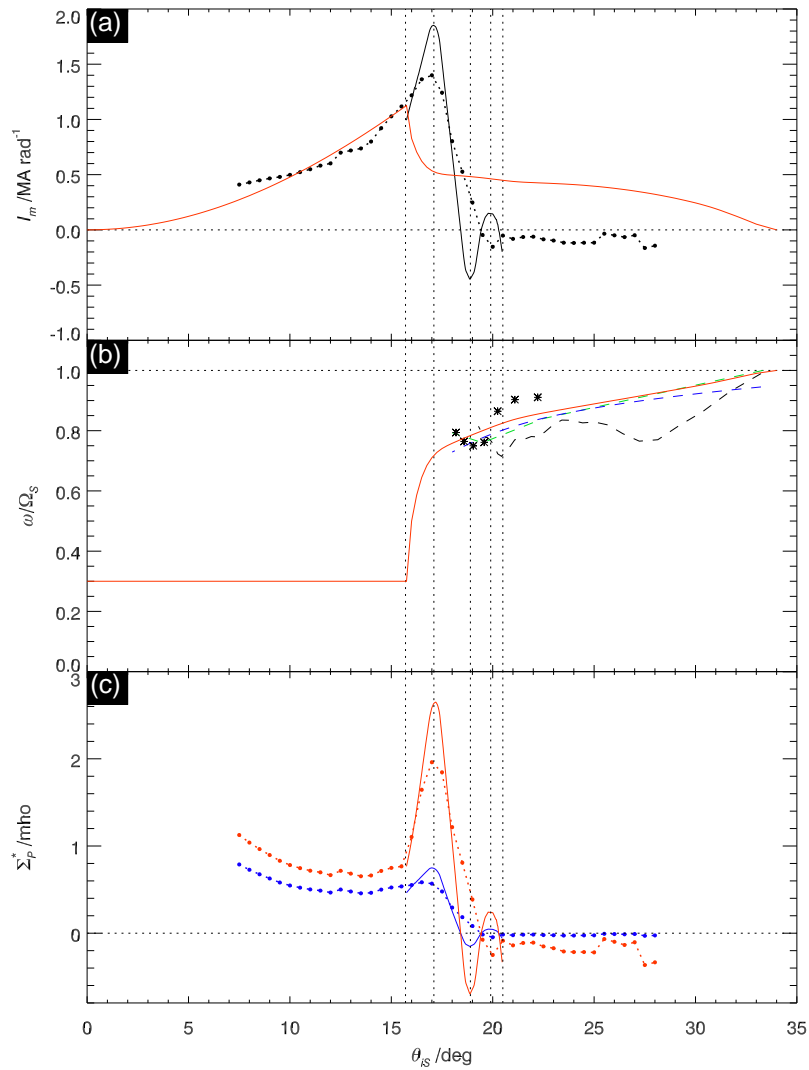


Figure 5.7: See Overleaf.

current shown in Figure 5.6a, determined from averaging the four independent “half sum” profiles in Figures 5.5e to 5.5h. The vertical dotted lines again mark the mean positions of the current sheet boundaries given in Table 5.1. Figure 5.7b then shows various empirical estimates of the plasma angular velocity normalised to the planetary angular velocity, (ω/Ω_S) , together with a suggested overall empirical model (red solid line) that will be used for purposes of discussion. The horizontal dotted line at unity indicates rigid corotation of the plasma, where for definiteness we have taken Saturn’s rotation period to be the IAU System III value of 10.65622 h, based on, but slightly modified from, the equinoctial northern Voyager SKR PPO period of *Desch and Kaiser* [1981]. The empirical angular velocity profile has been constructed as follows.

First, plasma azimuthal velocities in the inner part of the equatorial magnetosphere

determined using a variety of techniques have been converted to angular velocity and mapped along field lines into the ionosphere using the internal plus ring current model employed throughout this study. This direct mapping has been limited to equatorial radial distances inside $\sim 13 R_S$, corresponding to southern ionospheric colatitudes greater than 18° , where the field line mapping is likely to be reasonably accurate (the outer edge of the model ring current where the model becomes clearly unrealistic is at $\sim 19 R_S$). Specifically, the data shown are from (a) fits to ion velocity distribution functions by *Wilson et al.* [2009] shown by the black dashed line (3 to $10 R_S$), (b) piecewise averages of nightside ion velocity moments determined by *Thomsen et al.* [2014] shown by black stars (~ 6 to $\sim 40 R_S$), (c) analysis of energetic ion and electron dispersion signatures following plasma injection events by *Müller et al.* [2010] shown by the green dashed line (3 to $13 R_S$), and (d) analysis of rotating plasma ‘blobs’ observed in energetic neutral atom images by *Carbary and Mitchell* [2014] shown by the blue dashed line (~ 5 to $\sim 20 R_S$). Despite some deviations, these data consistently indicate a growing departure from rigid corotation with the planet with increasing equatorial radial distance, from near-rigid corotation at $\sim 3 R_S$, mapping to the southern ionosphere at

Figure 5.7: Comparison of ionospheric meridional current and plasma angular velocity profiles plotted versus southern colatitude over the range 0° - 35° . In panel (a) the black solid lines and circles joined by dashed lines show averaged colatitude profiles of the horizontal ionospheric current per radian of azimuth, I_m (MA rad $^{-1}$), derived from the four-current sheet analysis and mean profiles, respectively, as shown in Figure 5.6a. Vertical dotted lines show the mean boundaries of current sheets 1 to 4 from Table 5.1. The red solid line shows the profile obtained from equation (5.2) using the empirical plasma angular velocity profile in panel (b) assuming a fixed effective ionospheric Pedersen conductivity of 0.75 mho. Panel (b) shows the plasma angular velocity normalised to the planetary angular velocity, (ω/Ω_S) , where for definiteness Ω_S is taken to be the IAU System III value. The data shown equatorward of $\sim 18^\circ$ represent equatorially measured values mapped along model field lines into the southern ionosphere. The black, green, and blue dashed lines are from *Wilson et al.* [2009], *Müller et al.* [2010], and *Carbary and Mitchell* [2014], respectively, while the black stars are derived from the data presented by *Thomsen et al.* [2014]. The red line shows our overall model based on these and other data as discussed in section 5.2.1. The red lines in panel (c) show profiles of the effective ionospheric Pedersen conductivity (mho) derived from equation (5.5) using the corresponding black current profiles in panel (a) and the empirical angular velocity model in panel (b). The blue lines show minimum effective conductivity profiles derived similarly by putting $(\omega/\Omega_S) \approx 0$ in equation (5.5).

$\sim 33^\circ$ colatitude, to $\sim 75\%$ of rigid corotation at $\sim 13 R_S$, mapping to $\sim 18^\circ$ colatitude. The red line then shows our empirical model intended to exemplify the behaviour in this regime, mapping to the equatorward part of main upward current sheet 2, secondary current sheets 3 and 4, and the region equatorward thereof, as can be seen in Figure 5.7a.

Second, beyond these distances, poleward of $\sim 18^\circ$ colatitude in the southern ionosphere, the results of *Thomsen et al.* [2014] show that the plasma azimuthal velocity in the nightside magnetosphere continues to fall approximately monotonically with equatorial radial distance, reaching $\sim 50\%$ of rigid corotation at $\sim 20\text{-}25 R_S$, and $\sim 30\%$ of rigid corotation at $\sim 40\text{-}50 R_S$ in the more distant plasma sheet. Although we do not know the detailed field-line mapping from these larger radial distances on the nightside, we do know that they must lie between the $\sim 18^\circ$ limit discussed above, and the boundary between open and closed field lines that we can place typically at $\sim 15.7^\circ$ southern colatitude, corresponding to the averaged poleward edge of current sheet 1 (Table 5.1), as discussed in Chapter 2. We note that this identification is in close agreement with the recent results of *Jinks et al.* [2014], who used a multi-instrument study to determine an averaged location of the polar cap boundary in the southern ionosphere at 15.6° colatitude. The overall empirical model shown by the red line in Figure 5.7b is thus taken to decline monotonically from $\sim 75\%$ of rigid corotation at $\sim 18^\circ$ to 30% of rigid corotation at 15.7° , thus producing a relatively sharp angular velocity gradient in the ionosphere due to the field mapping, though none is present in the magnetosphere.

Third, at smaller colatitudes on open field lines we have little detailed knowledge of plasma flows, so as a minimum assumption we have simply taken continued angular velocities of 30% of rigid corotation (horizontal red line) over the whole polar region, similar to the theoretical model, e.g., of *Cowley et al.* [2004b]. We already noted above, of course, the consistent ‘lagging’ fields (positive equatorward I_m) observed over the whole southern polar region, indicative of significant plasma subcorotation.

Using this empirical angular velocity model, we can first derive from equation (5.2)

the meridional current profile that would be produced assuming a constant value of the effective Pedersen conductivity Σ_p^* . This is shown by the red line in Figure 5.7a, where we have used the value $\Sigma_p^* = 0.75$ mho, such that the Pedersen current is in approximate accord with the observed values in the polar region. This conductivity is of the same order but somewhat higher than those expected on the basis of the modeling results of *Galand et al.* [2011], who found solar-produced values of the true Pedersen conductivity at high latitudes for equinoctial conditions and no precipitation of ~ 0.7 mho at noon and ~ 0.2 mho near midnight. We note that the planetocentric latitude of the Sun at Saturn varied between $\sim 8^\circ$ and $\sim 4^\circ$ during the pre-equinox interval of Cassini orbits employed here, such that the ionosphere concerned in Figure 5.7 did indeed undergo near-equinoctial day-night cycles of solar illumination. It can be seen in Figure 5.7a that while the Pedersen current profile so derived is comparable, by design, to the observed polar values, it falls significantly short of the peak observed current values near $\sim 17^\circ$ colatitude, indicative of significantly enhanced effective conductivities in this region, while being considerably in excess of the small (negative) values observed beyond $\sim 20^\circ$, indicative of significantly reduced effective conductivities at larger colatitudes mapping to the inner magnetosphere.

To examine this further, we can invert equation (5.2) to derive the effective Pedersen conductivity profile from the observed current profiles and the empirical angular velocity profile

$$\Sigma_p^* = \frac{\cos \alpha_i I_m}{\rho_i^2 B_i \Omega_S \left(1 - \frac{\omega}{\Omega_S}\right)}. \quad (5.5)$$

Results are shown in Figure 5.7c by the red profiles with a line format corresponding to Figure 5.7a. The related blue profiles show minimum effective conductivity values obtained by putting $(\omega/\Omega_S) = 0$ in equation (5.5) (assuming steady angular velocities do not take negative values). The conductivities obtained from equation (5.5) are then successively larger for angular velocities successively closer to rigid corotation. It can first be seen that the conductivity profile in the polar region derived assuming a fixed value of the angular velocity declines slowly with increasing colatitude, from ~ 1.2 mho

at $\sim 7^\circ$ to ~ 0.7 mho at $\sim 14^\circ$ assuming $(\omega/\Omega_S) = 0.3$, or from ~ 0.8 to ~ 0.5 mho between these colatitudes assuming $(\omega/\Omega_S) = 0$. The conductivity must thus lie in the relatively tight band between these profiles if the plasma angular velocity lies between these limits within this region. The conductivity could be essentially constant at ~ 0.7 mho if the plasma angular velocity decreased from $\sim 30\%$ of rigid corotation at the larger of the above colatitudes towards zero at the smaller. For higher assumed values of the polar plasma angular velocity nearer to rigid corotation, the conductivities would then be higher, possibly unlikely given the results of *Galand et al.* [2011].

On moving in Figure 5.7c to outer closed field lines near $\sim 16^\circ$ colatitude the effective conductivity then strongly increases (red lines), reaching a peak of ~ 2.5 mho near $\sim 17^\circ$, such that the increasing Pedersen current with colatitude related to the downward current in sheet 1 is produced by a strong increase in the ionospheric conductivity, despite a significant increase in the plasma angular velocity towards rigid corotation across this region that works in the opposite direction. The strong decrease in Pedersen current related to main upward current sheet 2 is then likely associated with further modest increase in the plasma angular velocity towards rigid corotation (as in our empirical model), but more so to a strong decrease across the region in effective ionospheric Pedersen conductivity, that must be associated with the pattern of precipitation across these current regions. According to the results of *Galand et al.* [2011], the peak effective Pedersen conductivity of ~ 2.5 mho, indicative of a true conductivity of ~ 5 mho if $k \approx 0.5$ in equation (5.3), requires a peak precipitating electron energy flux of ~ 0.2 mW m $^{-1}$ if consisting of ~ 10 keV auroral electrons, sufficient in this case to produce a weak UV aurora of ~ 2 kR.

At larger colatitudes there are no known systematic variations in the plasma angular velocity data that might account for the field variations in current sheets 3 and 4 in Figure 5.7a, and, evidently, the negative conductivity values obtained from the negative (poleward) currents derived in regions of observed plasma subcorotation are not physically meaningful. Nevertheless, it seems reasonable to infer that the Pedersen current values beyond $\sim 20^\circ$ colatitude are likely less than ~ 0.1 MA rad $^{-1}$ (see Figure

5.7a), which with the observed values of plasma subcorotation implies effective Pedersen conductivities of ~ 0.1 mho or less. The inference is that, somewhat contrary to expectation, the larger colatitude ionosphere equatorward of the auroral current regions is significantly less effectively conducting than the polar ionosphere poleward of the current regions. This could mean that the polar region is rendered more conducting by precipitation of some sort, noting the polar IR auroral emissions that are sometimes evident [e.g., *Stallard et al.* [2008]], despite the fact that it is a region of distributed if relatively weak downward field-aligned currents as noted above. Alternatively, the distinction might lie in the dynamics of the neutral atmospheric gas, if for reasons unknown the neutral upper atmosphere in the sub-auroral region is much more responsive to the plasma flow than it is at polar latitudes, i.e., if the k value in equations (5.3) and (5.4) is smaller in the polar region than in the equatorial.

We now briefly discuss these findings in relation to the previous theoretical results of *Cowley et al.* [2004b, 2008], who presented models of Saturn's magnetosphere-ionosphere coupling current system based on empirically-motivated profiles of the plasma angular velocity together with fixed values of the effective ionospheric Pedersen conductivity. We firstly note that the empirically-determined plasma angular velocity colatitude profile discussed here (Figure 5.7b), based on Cassini rather than Voyager data as for the initial models, nevertheless has the same essential feature, namely a sharp increase in the angular velocity toward rigid corotation immediately equatorward of the open-closed field boundary. Assuming a fixed value of the effective ionospheric Pedersen conductivity then yields a Pedersen current profile of the form shown by the red line in Figure 5.7a, where we note that the profile in the figure assumes a value of 0.75 mho as indicated above, compared with the value of 1 mho taken by *Cowley et al.* [2004b]. The field-aligned currents implied by the gradients of this meridional current profile then consist of a distributed downward current over the polar open field line region integrating to ~ 1 MA rad^{-1} at the open-closed boundary, followed by a layer of strong upward current $\sim 1^\circ$ wide carrying ~ 0.5 MA rad^{-1} flowing just equatorward of the boundary, giving way to a region of weak distributed upward

current at larger colatitudes. Minor details aside, this behaviour is essentially that predicted by the theoretical models. The results in Figure 5.7, however, show that despite the increase in angular velocity downward currents continue to flow equatorward of the open-closed boundary enhanced from polar values due to a significant increase in the effective Pedersen conductivity on the closed field side of the boundary, then giving way to a layer of upward current $\sim 1.5^\circ$ colatitude inside the boundary in association with a significant decrease in the conductivity to low values at larger colatitudes. It is thus evident that latitudinal variations in the effective Pedersen conductivity of the ionosphere are at least as important in determining the structure of the field-aligned current system as the variations in the plasma angular velocity.

5.2.2 Radial mapping of field-aligned current layers

A possible reason for the lack of significant subcorotation perturbation fields at larger colatitudes (compare the red and black curves in Figure 5.7a) is that the spacecraft, at near-periapsis radial distances $\sim 3-5 R_S$, may already have entered the near-equatorial region where these currents close in the magnetospheric plasma, thus reducing the perturbation field. In this section we thus examine the Cassini trajectory in relation to the spatial structure of the observed current regions and the equatorial plasma distribution, and show that this is unlikely to be the case.

This is illustrated in Figure 5.8, where the numbered red and blue bands show the extensions of the main upward and downward field-aligned current layers, respectively, along field lines between the southern ionosphere and the planetary equator in a meridian plane. Here we have employed the same simple field model as described in Chapter 4 sections 4.2 and 3.2, whose limitations in this context are discussed briefly below. The pale blue region at smallest southern colatitudes represents the distributed downward polar currents associated with the subcorotation current system. Specifically, we show the mapping of the mean current sheet boundary positions shown by the red dashed lines in the upper row of Figure 5.1. Superposed on these current bands we show model magnetic field lines (arrowed black lines), drawn at 5° intervals from 0°

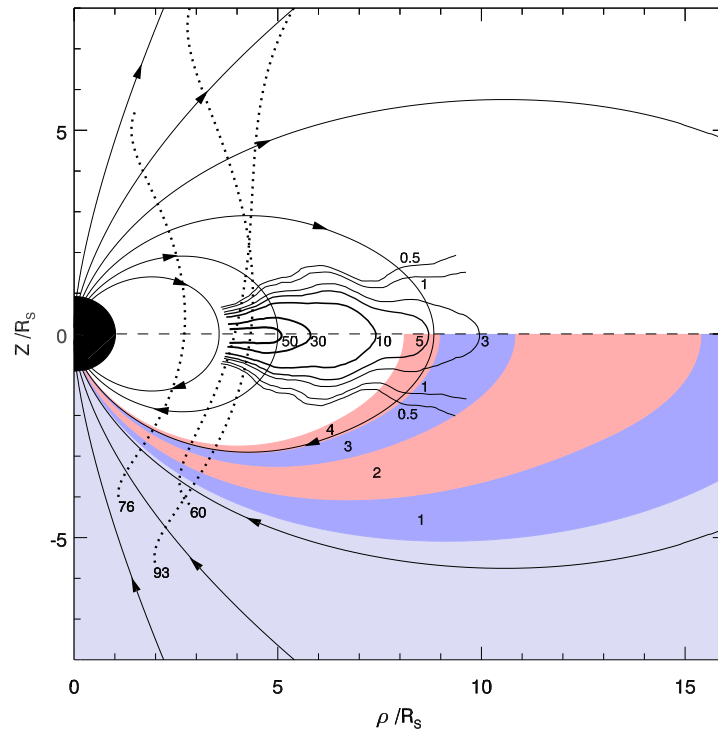


Figure 5.8: Plot in a magnetic meridian plane using cylindrical (ρ , z) co-ordinates showing the magnetic mapping of the four main southern current sheets between the southern ionosphere and the equatorial plane, shown by the numbered red and blue bands for upward- and downward-directed currents, respectively. The pale blue region at smallest southern colatitudes represents the distributed polar region of downward currents. The superposed arrowed solid black lines show model field lines starting at 5° intervals of southern colatitude between 0° and 30° , while the solid black lines near the equatorial plane show empirical model contours of water-group ion density derived by *Persoon et al.* [2009], labelled in ions cm^{-3} . The dotted black lines show the periapsis passes of three contributing Cassini Revs in cylindrical coordinates passing from north to south across these structures, specifically for Revs 60, 76, and 93, as in Figure 4.1 in Chapter 4. These are plotted between their points of highest northern and highest southern mapped ionospheric colatitudes.

to 30° in the southern ionosphere, together with contours of the empirical cool water-group ion density model derived from Cassini data between ~ 4 and $\sim 10 R_S$ by *Persoon et al.* [2009], the primary component of the inner magnetospheric plasma. The contours are labelled with number density of water ions cm^{-3} . Outside of the region occupied by this cool ion distribution, the main hot plasma population exists on field lines extending between ~ 8 and $\sim 15 R_S$ in the equatorial plane [*Schippers et al.* [2008]; *Kellett et al.* [2011]], with the outer plasma sheet and tail lobes beyond. Typical Cassini periapsis pass trajectories in cylindrical coordinates are shown by the black dotted lines, illustrating the motion of the spacecraft through these structures. Specifically we show

the trajectories for Revs 60, 76, and 93, as in Figure 4.1 in Chapter 4, plotted between the points of minimum northern and southern mapped ionospheric colatitudes.

As noted above, in generating Figure 5.8 we have employed the simple internal field plus ring current model described in Chapter 3 section 3.2 which has been used to map the observed fields into the southern ionosphere. Since the model ring current terminates at a cylindrical radial distance of $\sim 19 R_S$, the mapping becomes obviously inappropriate at comparable distances and beyond, since the tail current, into which the ring current merges on the nightside, is not included. Figure 5.8 is thus terminated at a cylindrical radial distance of $16 R_S$, where we recognise that the model may not fully represent the distension of the nightside field lines away from the planet in the outer part of the region shown.

With this caveat in mind, we note that, from the inside out, upward current sheet 4 maps from 8.2 to $9.0 R_S$ in the equatorial plane, downward sheet 3 from 9.0 to $10.8 R_S$, main upward current sheet 2 from 10.8 to $15.6 R_S$, and downward sheet 1 outward from $15.6 R_S$ to near the boundary of open field lines well beyond the region of validity of the model. We thus quantitatively confirm the conclusions of the discussion in section 4.3.2 of the individual examples in Figure 4.2 that current sheets 2-4 map to the main hot plasma region in Saturn's magnetosphere, spanning equatorial distances between ~ 8 and $\sim 15 R_S$, or maybe somewhat beyond on the nightside. If main upward current sheet 2 then corresponds to the UV auroral oval, as discussed in section 5.25.1.2, the implication is that the nightside UV oval similarly maps to this hot plasma region, thus mirroring the related results of *Belenkaya et al.* [2014] who mapped dawn arc emissions observed by the HST along model field lines principally into the ring current region. Sheet 1 then maps to the cooler less dense outer magnetospheric plasma, corresponding to the tail plasma sheet beyond $\sim 15 R_S$ on the nightside, and the distributed downward current region to open field lines. In terms of the two main components of the current, dependent and independent of the PPO phase, we note that the current layer locations indicated in Figure 5.8 are entirely representative of those associated with the PPO-independent currents shown in Figures 5.5 and 5.6a. The PPO-

dependent currents mapping between $\sim 17.5^\circ$ and $\sim 20^\circ$ in the southern ionosphere (Figure 5.6c) then modulate the current in the region between ~ 9 and $\sim 14 R_S$ in the equatorial plane (or maybe a little beyond), overlapping with the inner part of sheet 2 and sheet 3. We note, however, that the study of the PPO-related equatorial magnetic perturbations by *Andrews et al.* [2010a] centres the main PPO-related currents at $\sim 15 R_S$ on the nightside as noted in Chapter 2 section 2.4.2, potentially indicating the extent to which the model employed underestimates the degree of outer field line extension into the tail on the nightside.

We can be clear, however, that in the inner region no major currents are observed mapping to the equatorial region inside $\sim 8 R_S$, at least to an inner observational limit of $\sim 4 R_S$ (corresponding to a southern colatitude of $\sim 28^\circ$). This is the region dominated by cool equatorially confined water-ion plasma of Enceladus origin whose density contours are shown in Figure 5.8. Although cool plasma of this nature is indeed generally observed inside the location of current sheet 4, as can be seen in the examples in Figure 4.2, Figure 5.8 shows that a significant gap is always present along the spacecraft trajectories between the inner edge of current sheet 4 and the main cool plasma layer in the equatorial region where subcorotation currents would be expected mainly to close. The magnetic effects of significant additional currents would then clearly have been detected on these inner field lines if any had been present. While we might certainly expect that coupling currents and associated lagging fields must exist in this region, associated with pick-up and transport of Enceladus plasma, they are clearly not of sufficient magnitude to figure in the present study.

5.2.3 Physical implication of the boundary oscillation phase

A significant result of the above analysis is the finding that the overall current sheet layer oscillates in colatitude with an amplitude $\sim 1^\circ$, with largest colatitudes being reached near a southern PPO phase of $\sim 270^\circ$ where the upward PPO current maximises, and smallest colatitudes at $\sim 90^\circ$ where the downward PPO current maximises (Figures 5.1, 5.3, and 5.4 and Tables 5.1 and 5.2). A related effect was noted in section

4.3.2 in regard to the hot electron fluxes in Figure 4.2 which also extend to smallest colatitudes for PPO phases $\sim 90^\circ$, an effect taken to correspond to results previously reported in plasma ion data by *Burch et al.* [2009], in which equatorial ion fluxes are found to extend to largest radial distances, mapping to smallest ionospheric colatitudes, near a southern PPO phase of $\sim 90^\circ$ (see Figure 12 of *Clarke et al.* [2010a]). Previous results on UV auroral oscillations, however, suggest displacements to maximum southern colatitudes near southern PPO phases $\sim 180^\circ$ and correspondingly to minimum colatitudes near $\sim 0^\circ$ [*Nichols et al.*, 2008, 2010b], in approximate quadrature with those found here, suggesting the need for further comparative study. Here we briefly consider the physical origin of the oscillation of the overall current layer, while in section 5.2.4 we examine the phase delay with decreasing colatitude which has also been found.

The boundary motions must involve oscillatory flow of the field and plasma directed poleward and equatorward, corresponding to radially outward and inward flow in the equatorial magnetosphere, that is superposed on the overall azimuthal subcorotation flow. We thus consider the plasma flow associated with the PPO current system shown in schematic form in Figure 2.13, the sense of which depends on the nature of the currents, and whether the flows are driven from the magnetosphere or from the atmosphere. Here we assume that the relevant currents are primarily Pedersen currents as for the subcorotation current system, and in Figures 5.9a and 5.9b illustrate the case where the flow is driven from the magnetosphere, where Figure 5.9a is a view of the southern ionosphere “through” the planet from the north, while Figure 5.9b shows a cross-section through the polar ionosphere in a view of Figure 5.9a from the right. In the latter diagram, the background field lines are directed from the magnetosphere (“M”), through the ionosphere (“I”), and into the atmosphere (“A”), as appropriate to Saturn’s southern polar region. In Figure 5.9a the black vortices represent the perturbation magnetic field lines and the green symbols the related current system, shown schematically as involving a downward current into the ionosphere on the left (circled dots) and an upward current out of the ionosphere on the right (circled

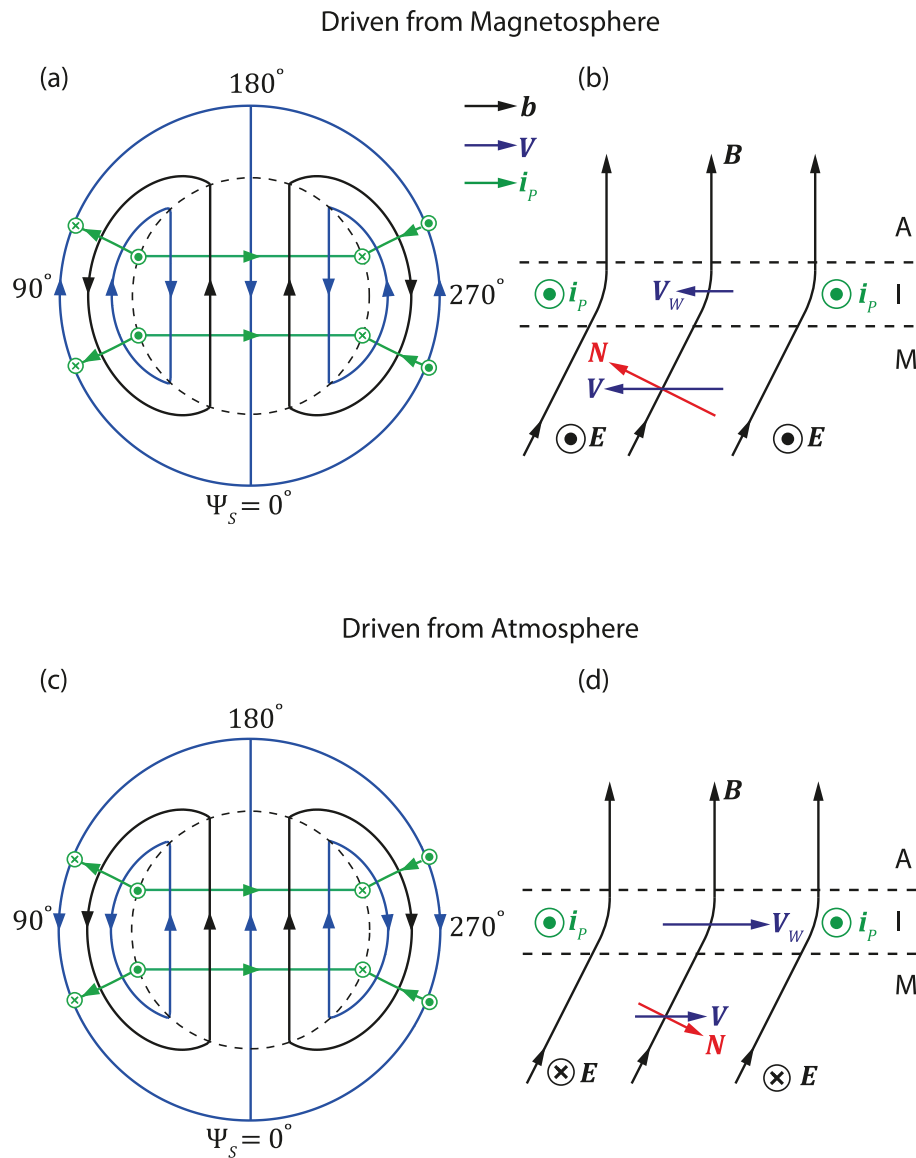


Figure 5.9: See Overleaf.

crosses), joined by an ionospheric Pedersen current directed from left to right (see Figure 2.13 for a fuller representation). The related southern PPO phase is shown around the perimeter of the diagram. If this system is driven from the magnetosphere, the related plasma flow in Figure 5.9b is directed to the left as shown, opposite to the field perturbations, the field tilt being related to the drag on the feet of the field lines due to ion-neutral collisions within the ionosphere. The related plasma flows are thus shown by the oppositely-directed blue vortices in Figure 5.9a. We note that the electric field in the frame of the diagram associated with the plasma flow, $\mathbf{E} = -\mathbf{V} \times \mathbf{B}$, is directed out of the plane of Figure 5.9b parallel to the height-integrated ionospheric Pedersen current

\mathbf{i}_P . The latter current is given in turn by $\mathbf{i}_P = \Sigma_P \mathbf{E}' = -\Sigma_P (\mathbf{V} - \mathbf{V}_W) \times \mathbf{B}$, where Σ_P is the height-integrated ionospheric Pedersen conductivity, \mathbf{E}' the electric field in the frame of the neutral atmosphere in the Pedersen layer, and \mathbf{V}_W a neutral atmospheric wind, parallel to but smaller than the plasma velocity, that may be driven by the frictional force due to ion-neutral collisions. The energy per area of ionosphere transferred from the electromagnetic field to the gas, $\mathbf{i}_P \cdot \mathbf{E}$, is then positive, fed by a downward component of the magnetospheric Poynting vector $\mathbf{N} = \mathbf{E} \times \mathbf{B} / \mu_0$, as shown in Figure 5.9b.

The case in which the same current system is driven from the atmosphere is similarly illustrated in Figures 5.9c and 5.9d. In this case in Figure 5.9d we have an atmospheric wind \mathbf{V}_W directed to the right in the Pedersen layer as shown, which drives a smaller plasma flow to the right in the ionosphere and magnetosphere due to ion-neutral collisions, such that the flow now has the same direction as the perturbation field as shown in Figure 5.9c. In this case the electric field associated with the flow points into the plane of Figure 5.9d as shown, such that $\mathbf{i}_P \cdot \mathbf{E}$ is negative (though $\mathbf{i}_P \cdot \mathbf{E}'$ is still positive), with a component of the Poynting vector being directed upward from

Figure 5.9: Sketches showing the electrodynamics of the southern polar ionosphere in the cases where the PPO current system is driven from the magnetosphere (panels (a) and (b)), or from the atmosphere (panels (c) and (d)). Sketches (a) and (c) show views of the southern ionosphere viewed from the north “through” the planet (as in Figure 2.13c and B2a), in which blue solid lines show the plasma flow \mathbf{V} , black solid lines the perturbation field \mathbf{b} , and green lines the ionospheric Pedersen current \mathbf{i}_P . The green circled symbols indicate field-aligned currents, circled dots into the ionosphere (directed out of the plane of the diagram), and circled crosses out of the ionosphere (into the plane of the diagram). Panels (a) and (c) differ only by the direction of the plasma (and neutral atmosphere) flow relative to the field perturbations and currents. Southern PPO phase, defined relative to the magnetic perturbations, is shown around the perimeter of the figures. Panels (b) and (d) show cross-sections through the polar ionospheric region (viewed from the right of panels (a) and (b)), where the background field \mathbf{B} points towards the planet from the magnetosphere (“M”), through the ionosphere (“I”), and into the neutral atmosphere (“A”), i.e., out of the plane of the diagrams in panels (a) and (c), corresponding to Saturn’s southern hemisphere. Blue vectors show the plasma (\mathbf{V}) and atmospheric (\mathbf{V}_W) velocities, green circled dots the ionospheric Pedersen current \mathbf{i}_P pointing out of the plane of both diagrams, black circled dots and crosses the electric field $\mathbf{E} = -\mathbf{V} \times \mathbf{B}$ associated with the plasma flow pointed out of (panel (b)) or into (panel (d)) the plane of the diagrams, and the red vectors the Poynting flux of electromagnetic energy \mathbf{N} .

the ionosphere to the magnetosphere.

Figures 5.9a and 5.9c show the systems at some instant of time, following which the pattern of perturbation field and flow rotate anti-clockwise relative to the sub-corotating plasma. We then consider the frame of the sub-corotating plasma and the effect of the superposed flow perturbations as the above patterns rotate anti-clockwise around. In Figure 5.9a the plasma moves equatorward during the half cycle centred on $\Psi_S = 0^\circ$ and poleward during the half-cycle centred on 180° , and vice versa in Figure 5.9c. As the pattern rotates anticlockwise a given fluid element in Figure 5.9a must thus achieve its maximum displacement from the southern pole at $\Psi_S = 90^\circ$ and its minimum at $\Psi_S = 270^\circ$, and vice versa in Figure 5.9c. Our results, e.g. in Figure 5.4, show that it is the latter condition that prevails, thus showing that the PPO current system, like the subcorotation current system, is driven outwards from the neutral atmosphere rather than inwards from the magnetosphere, as illustrated in Figures 5.9c and 5.9d. This result is in overall agreement with the modeling assumptions of *Jia and Kivelson [2012]* and *Jia et al. [2012]*, and with the sense of the atmospheric and plasma flows already illustrated in Figure 2.13d, as discussed in section 2.4.2 of Chapter 2. While the PPO phenomenon could thus be the magnetospheric manifestation of a flow driven directly by a purely atmospheric phenomenon, we note that other possibilities exist in which the causative atmospheric flow is driven externally, e.g., by self-sustained asymmetric heating of the upper atmosphere [*Smith, 2011; Smith and Achilleos, 2012*]. We further note that the physical picture suggested here, in which a rotating pattern of twin-cell flow is imposed from the atmosphere on the coupled ionosphere-magnetosphere system, leading in particular to the “plasma cam” effects noted above, rotating ‘wave-like’ through the equatorial plasma, differs fundamentally from the plasma interchange picture recently discussed by *Goldstein et al. [2014]*, in which the plasma perturbations are instead inescapably fixed in the convecting sub-corotating plasma. The interchange paradigm does not fit the PPO-related facts.

With regard to the magnitude of the PPO-related flows relative to the subcorotation flows, we note that in the physical picture discussed here, illustrated in Figure

5.9c, the atmospheric PPO-related flow enhances the anti-clockwise planetary atmospheric flow poleward of the main field-aligned current ring for Ψ_S near $\sim 270^\circ$, and equatorward of the current ring near $\sim 90^\circ$, thus promoting lagging azimuthal fields in these sectors, as seen in Figure 4.4. Similarly, the PPO-related atmospheric flow reduces the planetary atmospheric flow poleward of the current ring for Ψ_S near $\sim 90^\circ$, and equatorward of the current ring near $\sim 270^\circ$, thus reducing the lagging field signature in the former case, and actually reversing it to a leading field signature in the latter, as also seen in Figure 4.4. The latter condition then implies that the plasma azimuthal flow actually exceeds the reduced atmospheric azimuthal flow. The implication of the reversal in sense of the perturbation fields from lagging to leading depends in detail on how much the plasma flow responds to the periodic driving of the PPO-related atmospheric flow relative to the steady driving of the subcorotation flow, but overall it requires that the PPO-related azimuthal atmospheric flows near $\sim 90^\circ/270^\circ$ equatorward of the current ring are comparable to or in excess of the corotation-related atmospheric flows. Allowing for some lag caused by drag due to ion-neutral collisions, the corotation-related atmospheric flows near $\sim 20^\circ$ colatitude, say, are $\sim 2.5 \text{ km s}^{-1}$, thus implying PPO-related atmospheric flows of comparable order.

The PPO-related plasma flows in the system can be estimated from the colatitudinal motion of the current layers observed in the PPO cycle, assuming that these move essentially with the PPO-related flow. A colatitudinal oscillation of amplitude $\sim 1^\circ$ (i.e., $\sim 1000 \text{ km}$), as found in section 5.1, over an interval comparable to (or a little longer than) the PPO period implies a velocity amplitude of $\sim 0.1 \text{ km s}^{-1}$. The plasma flow across the region poleward of the current ring in Figure 5.9c is then of similar order. Given a southern polar magnetic field strength of $\sim 60,000 \text{ nT}$, such a flow over the region poleward of $\sim 19^\circ$ colatitude implies a voltage associated with the twin-vortex system of $\sim 250 \text{ kV}$. Given a return flow at lower latitudes concentrated over a region $\sim 5^\circ$ wide, say, on either side, the implied plasma flow speeds in this region will be $\sim 0.5 \text{ km s}^{-1}$, i.e., some fraction of the PPO-related atmospheric flow inferred above, compatible with effective super-corotation flow for Ψ_S near $\sim 270^\circ$. Specifically, in this region

where rigid corotation flows are $\sim 3 \text{ km s}^{-1}$ we might envisage a sub-corotating atmospheric flow of $\sim 2.5 \text{ km s}^{-1}$ modulated by an atmospheric PPO-related oscillation of amplitude, say, $\sim 1.25 \text{ km s}^{-1}$, compared with a plasma sub-corotating flow of $\sim 2 \text{ km s}^{-1}$ modulated by a plasma PPO-related oscillation of $\sim 0.5 \text{ km s}^{-1}$, thus giving rise to plasma speeds $\sim 1.5 \text{ km s}^{-1}$ greater than atmospheric speeds $\sim 1.25 \text{ km s}^{-1}$, and hence leading fields, where both flows reach minimum values around $\Psi_S \sim 270^\circ$. Such conditions are more difficult to achieve in the more strongly sub-corotating plasma flows poleward of the PPO field-aligned currents (see section 5.2.1).

5.2.4 Inferred colatitude and radial phase propagation of the PPO perturbations

Although the overall layer of field-aligned currents is found to oscillate in colatitude with $\sim 1^\circ$ amplitude during the PPO cycle as discussed in section 5.1.3, it has also been found that these motions lag increasingly in phase with decreasing colatitude across the layer, suggesting poleward propagation of the disturbance pattern (Figure 5.4a and Tables 5.1 and 5.2). This is shown explicitly in Figure 5.10a where we plot the oscillation phase Δ (see equation (5.1)) versus southern colatitude θ_{iS} for both the current sheet boundaries and centres (numbered circles and crosses, respectively, as in Figure 5.4a). The phase angles are those in the fourth columns of Tables 5.1 and 5.2, respectively, while the colatitudes correspond to the mean southern colatitudes shown in the second column of these tables. The phase dependence is seen to be approximately linear, with slope $g = d\Delta/d\theta_{iS} \approx -13$ degrees of phase per deg of colatitude shown by the black line, least-squares fitted using the values from the poleward boundary of sheet 1 (circle 1) to the centre of sheet 3 (cross 3). This corresponds to a total phase lag of $\sim 60^\circ$ across $\sim 4.5^\circ$ of colatitude. The corresponding poleward phase speed is given by

$$V_\theta (\text{km s}^{-1}) = \frac{360L(\text{km})}{|g|\tau_S(\text{sec})}, \quad (5.6)$$

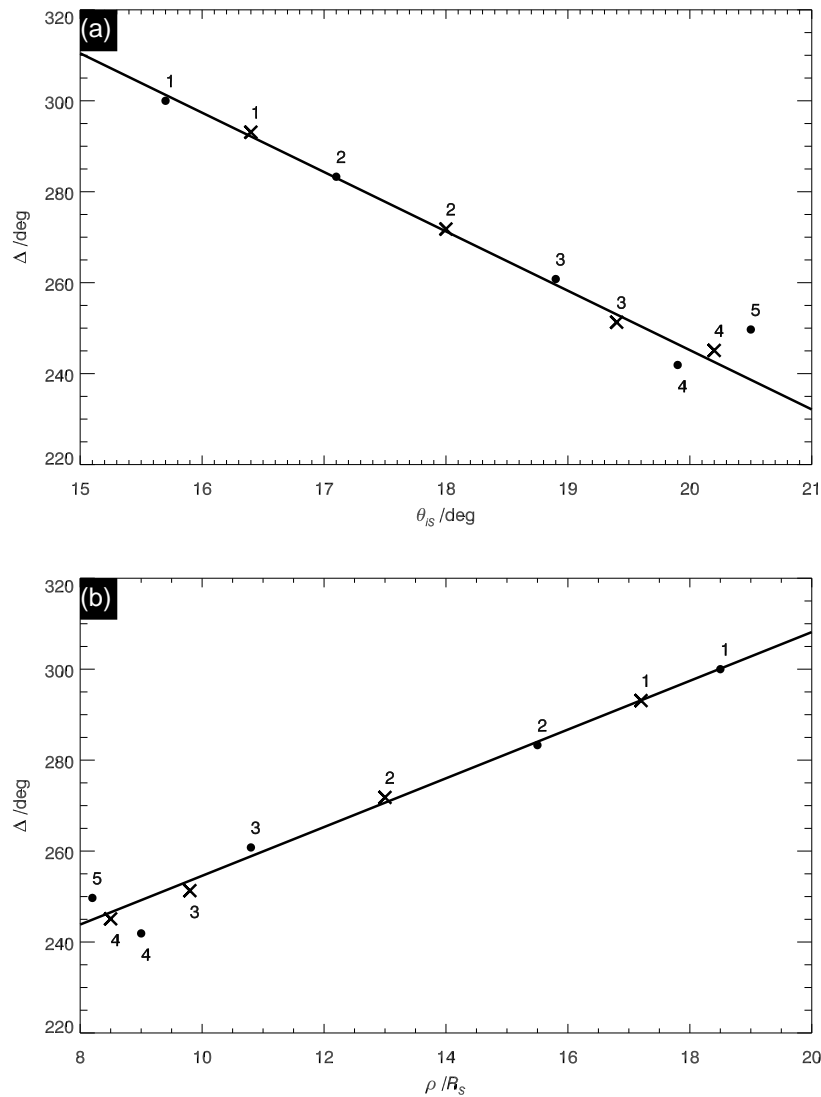


Figure 5.10: See Overleaf.

where, as above, gradient g is in degrees of phase per deg of colatitude, L is the distance in the polar ionosphere corresponding to 1° of colatitude in the relevant colatitude region (~ 970 km), and τ_S is the southern oscillation period ~ 10.82 h during the interval. Using the above gradient we find a poleward phase speed of ~ 700 m s $^{-1}$ in the polar ionosphere.

Given the magnetospheric mapping of the field lines discussed in section 5.2.2, it seems reasonable to suppose that this gradient mirrors a related phase gradient with increasing radial distance in the nightside magnetosphere, such as has been investigated previously by *Arridge et al.* [2011] and *Provan et al.* [2012]. In Figure 5.10b we show the oscillation phases plotted versus the mapped equatorial radial distances cor-

responding to the mean southern colatitudes employed in Figure 5.10a. A closely linear dependence is again found over the radial range $\sim 9-19 R_S$ with slope $g = d\Delta/d\rho = 5.36 \text{ deg } R_S^{-1}$ shown by the black line, least-squares fitted to the same data points as in Figure 5.10a. Values previously inferred by *Arridge et al.* [2011] over the radial range $\sim 15-40 R_S$ lie in the range $2.1-6.7 \text{ deg } R_S^{-1}$, with a mean of $\sim 3.7 \text{ deg } R_S^{-1}$, while *Provan et al.* [2012] found a value over the range $\sim 10-50 R_S$ of $\sim 2.5 \text{ deg } R_S^{-1}$. The value found here is thus comparable with, but on the high side of the range of values found in these previous studies, but would be reduced, of course, if the field lines actually mapped to somewhat larger radial distances as discussed in section 5.2.2. The radial phase speed implied by the radial phase gradient is

$$V_\rho (\text{km s}^{-1}) = \frac{360 R_S (\text{km})}{g (\text{deg}) R_S^{-1} \tau_S (\text{sec})}, \quad (5.7)$$

such that with the above value of g from Figure 5.10b we find a radial phase speed of $\sim 104 \text{ km s}^{-1}$, which is correspondingly on the slow side of the range $84-270 \text{ km s}^{-1}$ found by *Arridge et al.* [2011], with an average of 170 km s^{-1} , and similarly to the value $\sim 210 \text{ km s}^{-1}$ found by *Provan et al.* [2012] in the relevant radial range. Again, if the field lines actually mapped to larger distances than modeled here, the gradient would be reduced and the phase speed enhanced.

Figure 5.10: Plots showing the boundary oscillation phase delay with decreasing colatitude in the southern ionosphere. Panel (a) shows the phase angle Δ (deg) (see equation (5.1)) of current sheet boundary (circles) and centre (crosses) colatitude oscillations plotted versus the mean southern colatitude of those boundaries and sheet centres. The current sheet boundary phases are given in the fourth column of the upper part of Table 5.1, with the mean colatitude of the boundary being given in the second column. The current sheet centre phases are similarly given in the fourth column of the upper part of Table 5.2, with the mean colatitude of the sheet being given in the second column. The numbers shown correspond to the boundary (circles) and sheet centre (crosses) numbers indicated in Tables 5.1 and 5.2. The black line shows a least-squares fit to the data from the poleward boundary of sheet 1 (circle marked “1”) to the centre of sheet 3 (cross marked “3”), with a phase gradient of $13^\circ (\text{colatitude deg})^{-1}$. In panel (b) these phase data are shown versus equatorial radial distance when the mean colatitudes are mapped along field lines to the equatorial plane (as in Figure 5.8). The black line shows a least-squares fit to these data (using the equivalent points as in panel (a)) with a gradient of $5.36^\circ R_S^{-1}$.

5.3 Summary

In this chapter we have expanded upon an investigation of the PPO-dependence of southern hemisphere post-midnight field-aligned current signatures in Chapter 4 by providing an analysis of the auroral region current sheets that better describes the positions, widths, and currents flowing in these structures than does the overall statistical analysis in Chapter 4. We again separate the currents into components that do and do not depend on the PPO phase by using the symmetries involved, where the PPO-independent currents are taken primarily to relate to plasma subcorotation in the magnetosphere. Our results are as follows.

1. The PPO-independent system comprises the following currents, where the southern colatitude positions refer specifically to PPO phases $\Psi_S \sim 0^\circ/180^\circ$ (see item (5) below)
 - (a) a distributed downward current over the whole polar region that reaches a peak meridional Pedersen current of $\sim 1.1 \text{ MA rad}^{-1}$ at the boundary of the polar region at $\sim 15.5^\circ$, with an implied mean downward field-aligned current density of $\sim 10 \text{ nA m}^{-2}$, in agreement with the results of Chapter 4
 - (b) an enhanced downward current of $\sim 50 \text{ nA m}^{-2}$ in a layer $\sim 1.5^\circ$ wide at $\sim 15.5^\circ - 17^\circ$ colatitude (sheet 1) carrying $\sim 0.8 \text{ MA rad}^{-1}$, which further increases the equatorward Pedersen current to peak values of $\sim 1.9 \text{ MA rad}^{-1}$
 - (c) an upward current sheet of $\sim 100 \text{ nA m}^{-2}$ in a layer $\sim 2^\circ$ wide at $\sim 17^\circ - 19^\circ$ (sheet 2) carrying $\sim 2.3 \text{ MA rad}^{-1}$, across which the Pedersen current changes sign to small poleward-directed values $\sim 0.4 \text{ MA rad}^{-1}$
 - (d) two subsidiary downward then upward current sheets of $\sim 50 \text{ nA m}^{-2}$, with $\sim 1.5^\circ$ combined width lying between $\sim 19^\circ$ and $\sim 20.5^\circ$ (sheets 3 and 4) of smaller $\sim 0.5 \text{ MA rad}^{-1}$ magnitude, that result in the meridional Pedersen current oscillating about zero.

Not including the distributed polar currents, the main four-sheet auroral

region current layer is $\sim 5^\circ$ wide centred at $\sim 18^\circ$ southern colatitude and carries a net upward current of $\sim 1.2 \text{ MA rad}^{-1}$.

2. Plasma data combined with field line mapping indicates that the distributed downward polar currents map to open field lines, enhanced downward current sheet 1 to outer closed lines, main upward current sheet 2 to the outer part of the main hot magnetospheric plasma regime $\sim 11\text{-}16R_S$ in the equatorial plane (or maybe a little beyond), and sheets 3 and 4 to the inner part of the hot plasma regime $\sim 8\text{-}11 R_S$. No currents of comparable magnitude are detected inside this region, dominated by cool equatorial plasma of Enceladus origin, to an observational inner equatorial limit of $\sim 4 R_S$ ($\sim 28^\circ$ southern colatitude).
3. Comparison with observed and estimated plasma angular velocities indicates effective height-integrated ionospheric Pedersen conductivities of at least $\sim 0.5\text{-}0.8$ mho over the polar region, increasing to ~ 2 mho on closed field lines mapping to the outer regions of hot magnetospheric plasma (sheets 1 and 2), and dropping to ~ 0.1 mho or less in the interior region dominated by cool Enceladus plasma, equatorward of the auroral current region. The outer downward current sheet (sheet 1) results from the increase of conductivity with colatitude, from open to closed field lines, despite the expected increase in plasma angular velocity towards rigid corotation within the sheet, while the principal sheet of upward current (sheet 2) relates to a significant decrease in conductivity with increasing colatitude, no doubt involving feedback effects associated with auroral precipitation from the outer hot plasma region of Saturn's magnetosphere. Overall, it is evident that latitudinal variations in the effective Pedersen conductivity of the ionosphere are at least as important as variations in the plasma angular velocity in determining the large-scale structure of the field-aligned current system. There is no indication, e.g., in published plasma angular velocity profiles, of the physical origin of current sheets 3 and 4.
4. The PPO-related currents are co-located with the main part of upward current

sheet 2 and with downward current sheet 3 at $\sim 17.5^\circ$ - 20° southern colatitude, thus mapping into the main hot plasma regime at equatorial radial distances ~ 9 - $14 R_S$ (or maybe somewhat beyond). The upward and downward currents flowing in this layer peak at $\sim 1.7 \text{ MA rad}^{-1}$, corresponding to a current density of $\sim 35 \text{ nA m}^{-2}$, while summing over azimuth, the total upward and downward currents flowing are $\sim 3.5 \text{ MA}$. These currents thus approximately double the net upward current flowing in the overall auroral current sheet layer when directed upwards, while reducing it to small values when directed downward.

5. The overall auroral current layer is modulated in southern colatitude during the PPO cycle with amplitude $\sim 1^\circ$. Maximum colatitudes occur at PPO phases $\Psi_S \approx 270^\circ$ near where the upward PPO-related current maximises, with minimum colatitudes at PPO phases $\Psi_S \approx 90^\circ$ near where the downward PPO-related current maximises, mirroring the “plasma cam” effect observed in equatorial plasma ion distributions [Burch *et al.*, 2009]. Consideration of the related plasma and atmospheric flows shows that the PPOs are driven from the atmosphere outwards, rather than directly from the magnetosphere inwards.
6. The boundary oscillations also show a phase drift across the current sheet layer of $\sim 13^\circ$ per degree of colatitude, indicative of poleward propagation, that may be associated with the $\sim 50^\circ$ phase shift found between the equatorial and polar magnetic oscillations in Chapter 4. In the equatorial plane, this dependency maps to a radial phase gradient of $\sim 5^\circ$ per Saturn radius, corresponding to a phase speed of $\sim 100 \text{ km s}^{-1}$. The phase gradient is on the high side of previous related direct determinations using nightside equatorial data [Arridge *et al.*, 2011; Provan *et al.*, 2012], possibly reflecting an insufficient stretching away from the planet of the model field lines in the nightside magnetosphere.

In the following chapter we investigate the northern auroral zone passes on the same Cassini Revs as examined here.

Chapter 6

Evidence for interhemispheric current flow associated with the planetary period oscillations in the northern hemisphere

6.1 Introduction

In this chapter we focus on the northern hemisphere auroral region passes, as well as examining the behaviour of the planetary period oscillations in the equatorial and polar regions. As previously discussed in section 4.1 (Chapter 4) following initial examination of these data, it was apparent that the northern field-aligned current signatures observed within the B_ϕ component of the magnetic field were modulated by the northern PPO system, however, it was evident that these signatures were also in part modulated by the southern PPO system. Therefore, to fully investigate this the methods presented in Chapter 4 will be suitably modified to include both the northern and southern PPO phase systems, which were described in Chapters 2 and 3, and given by equations (3.7) and (3.6), respectively.

The magnetic perturbations associated with field-aligned currents in the nightside

southern hemisphere on a sequence of near-polar Cassini orbits in 2008 were investigated in Chapter 4 and 5. It was found that the form of the currents was well-organised by the southern PPO phase, and that these PPO-related variations give rise to the differing current morphologies noted previously by *Talboys et al.* [2009b, 2011]. No obvious evidence was found for a strong influence at the northern period, the hypothesised interhemispheric currents shown in Figures 2.13b and 2.13e. It was also found that the rotating PPO field-aligned currents were essentially co-located with the main upward current region of the PPO-independent subcorotation system (see Figure 2.7a for current digram), and of approximately equal strength. Thus when the PPO-related currents were also directed upwards the net current within the auroral current layer was approximately doubled, while when it was directed downwards the net current was reduced to near zero, though individual layers of upward and downward current remained present. In this chapter we examine the northern hemisphere data in these terms, and show that both northern and southern period currents were present in this case, thus providing the first direct evidence for the PPO-related inter-hemispheric currents hypothesised by *Southwood and Kivelson* [2007]. We also further re-examine the southern data for evidence of northern period currents, and show that weaker effects are indeed present.

6.2 Overview of northern hemisphere data

6.2.1 Northern hemisphere data set

The data set and analysis procedures employed in this paper have been fully described and justified in Chapters 3 and 4 sections and 3.2 and 4.2, such that only a brief outline of the main features will be provided here. The data originate from the same high latitude passes of the Cassini spacecraft as employed in Chapters 4 and 5. The orbits concerned are Revs 59-95, inclusive, occurring between February and December 2008. Of the 37 northern inbound passes examined here, one (Rev 71) is missing due to an extended data gap, while two others (Revs 84 and 89) have been excluded from the

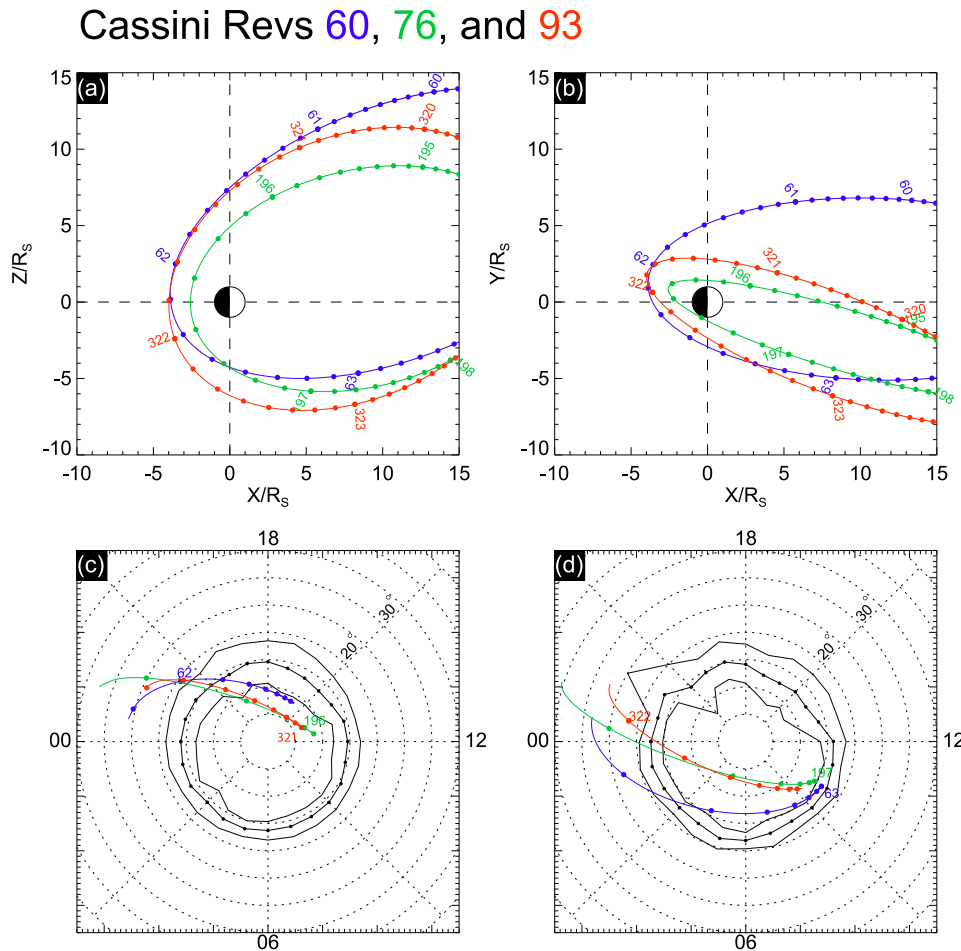


Figure 6.1: Periapsis segments of three Cassini Revs from near the beginning (Rev 60, blue), middle (Rev 76, green), and end (Rev 93, red) of the interval studied in this paper, shown projected into (a) the X-Z, and (b) the X-Y planes in KGS coordinates (Z points along Saturn’s spin/magnetic axis, the X-Z plane contains the Sun, and Y completes the right-hand triad pointing to dusk). Solid circles are plotted at 3 h intervals, labeled with the day of year number (2008) at the start of each day. In panels (c) and (d) the northern inbound and southern outbound segments of these trajectories are projected along model magnetic field lines into the northern and southern ionospheres, respectively. The format of this is the same as figure 4.1 in Chapter 4.

study as showing unusually large signatures that do not follow the general trends. One of the latter, Rev 89, has previously been the subject of special examination as a case likely associated with a major compression of the magnetosphere by the solar wind [Bunce *et al.*, 2010]. In this study we also further examine and compare these data with the southern outbound passes studied in Chapters 4 and 5, two of which (Revs 70 and 71) are missing due to data gaps, while four (Revs 66, 77, 89, and 94) were similarly excluded as showing atypical signatures. Here we thus employ the data from 34 northern and 31 southern passes over Saturn’s nightside auroral regions.

The periapsis segments of three representative Revs are shown in Figure 6.1 in KGS coordinates, where the Z axis is Saturn's spin/magnetic axis, the X - Z plane contains the Sun, and Y completes the right-handed triad pointing towards dusk. The Revs shown are 60, 76, and 93 spanning the interval of the study, shown by the blue, green, and red lines, respectively. Figures 6.1a and 6.1b show the trajectories projected onto the X - Z (noon-midnight) and X - Y (equatorial) planes, respectively, where solid circles are plotted every 3 h along the trajectories, labelled with the "day of year" number at the start of each day. The near-polar nature of these orbits is evident, with periapsis just south of the equator in the pre-midnight sector, such that the inbound northern polar passes in the pre-midnight sector occur at slightly larger radii than the southern outbound polar passes in the midnight and post-midnight sector.

In Figures 6.1c and 6.1d we show the northern and southern segments of these trajectories mapped along model field lines into the northern and southern ionospheres, respectively, starting from the near-periapsis point where the mapped northern and southern colatitudes are simultaneously the largest with respect to the corresponding poles. The view is from the north in both cases, thus "through" the planet in Figure 6.1d, with dusk at the top and noon to the right. Dotted latitude circles and longitude lines are shown at intervals of 5° and 3 h LT, respectively. The magnetic field mapping employed here is that described in section 3.2 and used in Chapters 4 and 5. We also show in these figures the mean northern and southern auroral "ovals" obtained from Cassini UVIS data by *Carbary* [2012]. The centre line with black circles indicates the location of maximum mean auroral emission, while the lines on either side show the half-intensity points. It can be seen that the inbound passes crossed through the northern mean auroral region in the post-dusk to pre-midnight sector, where the oval is centred at $\sim 15^\circ$ colatitude, while the outbound passes similarly crossed the auroral region in the southern midnight to post-midnight sector, where the oval is centred at $\sim 17.5^\circ$ colatitude. The difference in colatitude is principally a result of the north-south asymmetry in the planetary magnetic field associated with the axial quadrupole field [*Burton et al.*, 2010], which results in northern field lines mapping closer to the pole by

a degree or two compared with their southern counterparts.

The data analysis procedures employed here are those detailed in Chapter 3 section 3.2 such that they will not be repeated here. The equations stated in Chapter 3 refer to both the northern hemisphere and southern hemisphere, thus in this chapter the upper sign (–ve) versions of equations (3.2), (3.3), and (3.4) apply.

6.2.2 Initial overview and PPO-independent perturbations

In this section we overview the northern hemisphere data, and begin with Figure 6.2 by showing overall colatitude profiles combining and averaging all the mapped data from the Revs included as indicated in section 6.2.1. We also show for comparison corresponding plots of the southern data, not shown in this form in Chapters 4 or 5. Figures 6.2a and 6.2b thus show the northern $B_{\phi i}$ profiles obtained from the modified data using equation (3.1), and the corresponding I_m profiles obtained from equation (3.3), respectively, both plotted versus colatitude from the northern pole. Figures 6.2c and 6.2d show the corresponding southern $B_{\phi i}$ and I_m profiles, both plotted versus colatitude from the southern pole. The averaged position of the OCB in each hemisphere determined by *Jinks et al.* [2014] is indicated for future reference by the vertical dashed lines, located at 13.3° in the north and 15.6° in the south. (The vertical dotted lines in Figures 6.2c and 6.2d also indicate the polar and equatorial regions whose field data are employed in the analyses in sections 6.3.1 and 6.3.4). The data from each Rev are colour-coded according to the scheme at the top of the figure, while the black solid circles joined by straight lines show values averaged in overlapping 1° colatitude bins evaluated every 0.5° . We note that the density of data values per degree varies significantly from pass to pass due to the varying radial distance and hence speed of the spacecraft. In order to avoid the averages being overly dominated by contributing Revs with the highest density of data points, we first average all the data from a given Rev contributing to a colatitude bin, and then derive a weighted average over all the contributing Revs as shown. The chosen weights are logarithmic, $W = \log_{10} N$, where N is the number of data points contributed to a bin from a given Rev, such that the

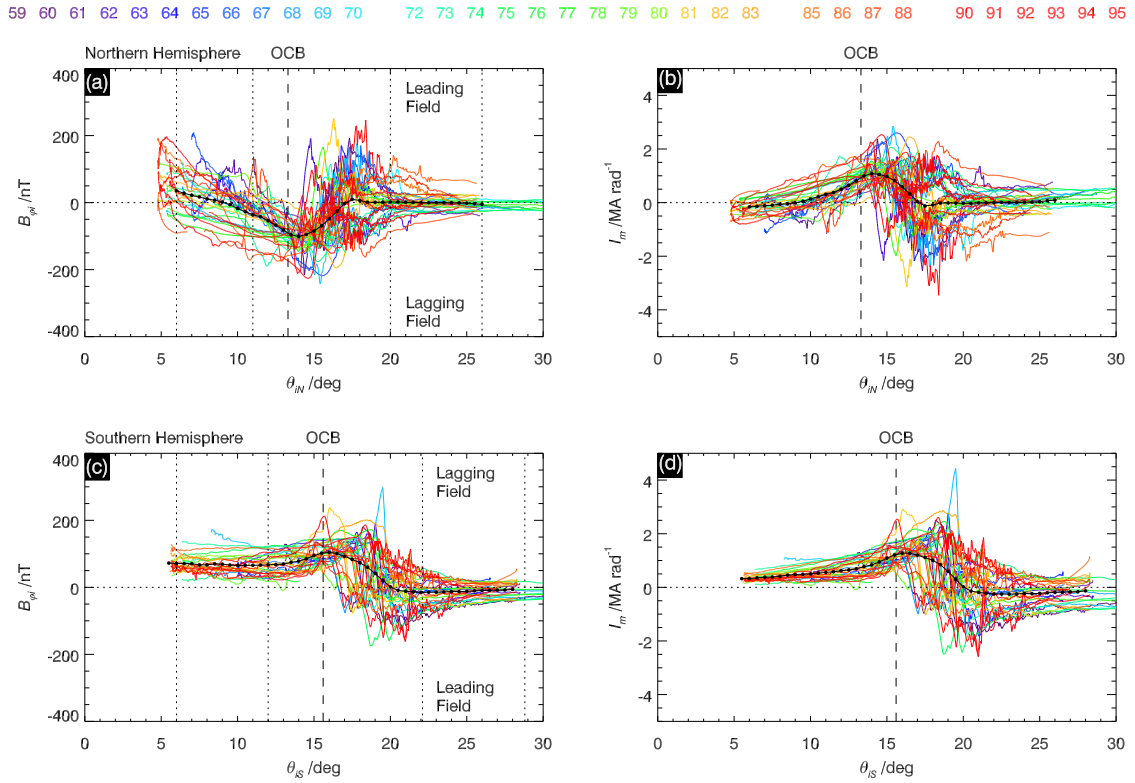


Figure 6.2: Panel (a) shows a composite plot of all the “corrected” northern hemisphere azimuthal field data, $B_{\phi i}$ (nT), mapped to the northern ionosphere using equation (3.1) and plotted versus colatitude from the northern pole, θ_{iS} (deg). The data profiles are colour-coded by Cassini Rev as shown at the top of the figure. The black solid circles joined by black lines show averages obtained in overlapping 1° colatitude bins every 0.5° , derived as described in section 6.2.2. Panel (b) similarly shows the corresponding northern meridional current profiles, I_m (MA per radian of azimuth), obtained using equation (5). Panels (c) and (d) show the corresponding southern hemisphere azimuthal field and meridional current profiles, mapped into the southern ionosphere and plotted versus colatitude from the southern pole, θ_{iS} (deg). The averaged colatitude of the OCB from *Jinks et al.* [2014] is also marked at the top of each plot and by the vertical dashed lines. The vertical dotted lines in Figures 6.2c and 6.2d show the colatitude intervals used in the polar and equatorial ranges in Figure 6.4. In Figures 6.2c and 6.2d we indicate which signs of $B_{\phi i}$ correspond to “lagging” and “leading” fields in each hemisphere.

weight of a single data point is taken to be zero, while an average obtained from ten points has a weight of one, and that from a hundred points a weight of two. All of the related averaged profiles in this paper have been derived using this method.

In considering these profiles we recall from Chapter 2 that lagging fields correspond to negative $B_{\phi i}$ in the northern hemisphere and positive $B_{\phi i}$ in the southern, as indicated in Figure 6.2, with positive equatorward-directed I_m in both hemispheres (equation (3.3)). Oppositely-signed fields with negative poleward-directed currents then

correspond to leading fields. On the assumption that the oscillatory PPO-dependent contributions average to small values over random northern and southern PPO phases, we might expect that the averaged profiles in Figure 6.2 represent a first, smoothed, approximation to those associated with the PPO-independent currents, with dominant lagging fields in both hemispheres if these are associated with plasma subcorotation as expected. Assuming that azimuthal Pedersen currents can be neglected for such near-axisymmetric subcorotation currents, we note that I_m increasing with colatitude implies downward field-aligned current into the ionosphere as given by equation (3.5), while I_m decreasing with colatitude implies upward field-aligned current out of the ionosphere. Variations about the mean values in Figure 6.2 then represent the effect of the PPO-related currents, together with any other natural variations in the system, such as changes in the colatitude of the auroral region associated with changes in the amount of open flux present.

If we first examine the southern profiles in Figures 6.2c and 6.2d, the azimuthal field and related meridional current are consistently positive (lagging) at the smallest southern colatitudes observed, implying subcorotation of the polar plasma. With increasing colatitude the averaged current increases in strength, more rapidly near $\sim 15^\circ$ together with the azimuthal field, and peaks at 1.3 MA rad^{-1} near $\sim 16.5^\circ$, just equatorward of the averaged OCB, thus implying a total distributed downward current over the whole polar region of $\sim 8 \text{ MA}$ assuming axisymmetry. The field and current then fall between $\sim 17^\circ$ and $\sim 20^\circ$ to small negative averaged values, associated with an upward current layer that closes essentially all of the polar current, beyond which the field-aligned currents remain negligible in the region observed. We note that this behaviour is entirely consistent with the averaged PPO-independent current profiles derived through more detailed analysis in Chapters 4 and 5 (see Figures 4.7 and 5.6). The variations about the mean field values at smallest and largest colatitudes then imply the presence of PPO-related oscillations of amplitude $\sim 20\text{-}30 \text{ nT}$ in these regions, also consistent with the results of Chapter 4 (see Figure 4.3). The variations within the main current region, however, are notably larger, $\sim 100 \text{ nT}$ in amplitude.

With regard to the small negative (leading) averaged values of the field and current at largest colatitudes in Figures 6.2c and 6.2d, these might be taken from the above discussion as indicating the presence of weak super-corotation of the plasma in the inner magnetosphere region. However, as noted in Chapter 2, the observed plasma rotation velocities are consistently sub-corotating on corresponding field lines (mapping in the equatorial plane inside of $\sim 9 R_S$), which makes this association highly unlikely. Instead, these weak averaged leading field values were suggested in Chapter 4 to be due to lack of perfect anti-symmetry in the PPO-related fields, with positive values being slightly larger than the negative values during each PPO oscillation cycle as a result of related spatial oscillations in the location of the currents.

Now examining the northern data in Figures 6.2a and 6.2b, it can be seen to a first approximation that these are similar in form to those in the south, but with the averaged $B_{\phi i}$ profile in Figure 6.2a inverted to predominantly negative lagging values, overall consistent with a subcorotation origin. The main meridional currents in Figure 6.2b remain positive, directed equatorward, as in the south. Overall, therefore, the profiles are similarly consistent with a distributed downward current of ~ 7 MA flowing into the polar region, the peak current being ~ 1.1 MA rad^{-1} at $\sim 14^\circ$ colatitude again just equatorward of the averaged OCB, closed by a narrower layer of upward current at larger colatitudes. However, some points of comparison should be made. First, the main layer of upward current is located between $\sim 15^\circ$ and $\sim 17^\circ$ colatitude in the north compared with $\sim 17^\circ$ and $\sim 20^\circ$ in the south, this difference again reflecting the axial quadrupole asymmetry in the background planetary field. As may be expected, these regions of upward current are quite consistent with the positions of the averaged UV auroral ovals determined by *Carbary* [2012] shown in Figures 6.1c and 6.1d. Second, while in the southern hemisphere the PPO-related oscillations in the region poleward of the main upward currents are superposed on a consistently lagging field suggesting plasma subcorotation over the whole polar region, the averaged polar perturbations in the north drop to small values poleward of $\sim 10^\circ$ colatitude, and indeed switch sign to become weakly leading in nature at the smallest colatitudes observed. Since super-

corotating flows at polar colatitudes again seem implausible, this again suggests an origin in a lack of exact anti-symmetry in the PPO-related perturbation fields. It is evident, however, that the lagging field associated with plasma subcorotation is generally much weaker in the north polar region than in the south. We note in this context that the passes employed in this study were obtained ~ 1 year before Saturn equinox in August 2009, when Saturn's northern spin axis was on average inclined $\sim 6^\circ$ away from the Sun (between $\sim 8^\circ$ and $\sim 4^\circ$ over the interval). The region poleward of $\sim 10^\circ$ in the southern hemisphere was thus mostly or wholly illuminated by the Sun during each planetary rotation, while the equivalent region in the north was mostly or wholly unilluminated. The above differences in the polar data may thus relate to much weaker polar ionospheric conductivities in the north compared with the south during this interval [Galand *et al.*, 2011].

6.2.3 Rev-by-rev survey and PPO-related perturbations

While the field and current profiles in Figure 6.2 indicate the range of the PPO-related field and current variations about the mean values, we now make an initial investigation of these variations by examining the field perturbations on individual passes in relation to the concurrent PPO phases. In Figure 6.3 we show data plotted versus northern mapped ionospheric colatitude from six of the thirty-four passes employed in the study, chosen to illustrate a range of conditions of the two PPO phases. Specifically, we have chosen cases in which the main PPO-related currents of the northern and southern systems should both have the same sense according to Figure 2.13, either upward ($\Psi_{N,S} \approx 90^\circ$) or downward ($\Psi_{N,S} \approx 270^\circ$) (Figures 6.3a and 6.3b), or have opposite senses to each other (Figures 6.3c and 6.3d), or where both PPO systems should be close to zero potentially exhibiting the PPO-independent profile $\Psi_{N,S} \approx 180^\circ$ or $0^\circ/360^\circ$ (Figure 6.3e). We also show one of four passes that exhibits unusual behaviour having no clear counterpart in the southern data studied in Chapters 4 and 5 (Figure 6.3f). In each panel of the figure we show from top to bottom (i) a CAPS/ELS electron count rate spectrogram covering the energy range ~ 0.6 eV–28 keV, colour-coded as

shown at the upper right of the figure, (ii) the ionospheric meridional Pedersen current I_m (MA rad^{-1}) derived as in Figure 6.2 using equation (3.3), and (iii) the northern (blue line) and southern (red line) PPO phases $\Psi_{N,S}$ (degrees), obtained from equations (3.7) and (3.6) using the phases determined by *Andrews et al.* [2012]. Vertical dashed lines in the figure indicate the principal field-aligned current layers identified from sequential extrema in the I_m profiles, all of which satisfy the significance criterion discussed in Appendix C. These lines are shown generally in green, but with those bracketing the principal layer of upward current being shown purple. We note that in the lower panels the PPO phases increase significantly with time and hence colatitude from left to right on these northern inbound trajectories (see Figure 6.1), with changes in value exceeding $\sim 180^\circ$ in each case. Unlike the more rapid passes at lower altitudes across the southern auroral region (Figure 6.1), therefore, the northern passes cannot be regarded as occurring at almost fixed values of PPO phase (compare, e.g., with Figure 4.2 of Chapter 4).

If we first examine the current profiles at smallest colatitudes, between $\sim 5^\circ$ and $\sim 10^\circ$, overall these correspond to expectations based on the concurrent northern PPO phase, i.e. I_m values follow the expected $\sin \Psi_S$ dependence (see Figure 2.13 in the polar region and section 3.2.2, noting that $B_{\phi i}$ and I_m always have opposite signs in the northern hemisphere). For example we see negative values of I_m in this regime for $\Psi_N \sim 90^\circ$ in Figure 6.3e, positive values for $\Psi_N \sim 270^\circ$ in Figure 6.3f, and changes from negative towards positive as Ψ_N increases from $\sim 270^\circ$ through $360^\circ/0^\circ$ towards $\sim 90^\circ$ in Figure 6.3b. Senses opposite to those observed would have been found, e.g., in Figures 6.3c and 6.3e, if the field perturbations in this regime had been responding to the southern PPO phase. Similar results were found in Chapters 4 and 5 in the southern polar region with respect to the southern PPO phase, but superposed in that case on a larger PPO-independent positive meridional current (lagging field) that to a first approximation is absent at similar colatitudes in the north, as seen in Figure 6.2.

Beyond $\sim 10^\circ$ colatitude, however, an upward trend in positive I_m (lagging field) values becomes evident in all cases irrespective of the PPO phases (an exception being

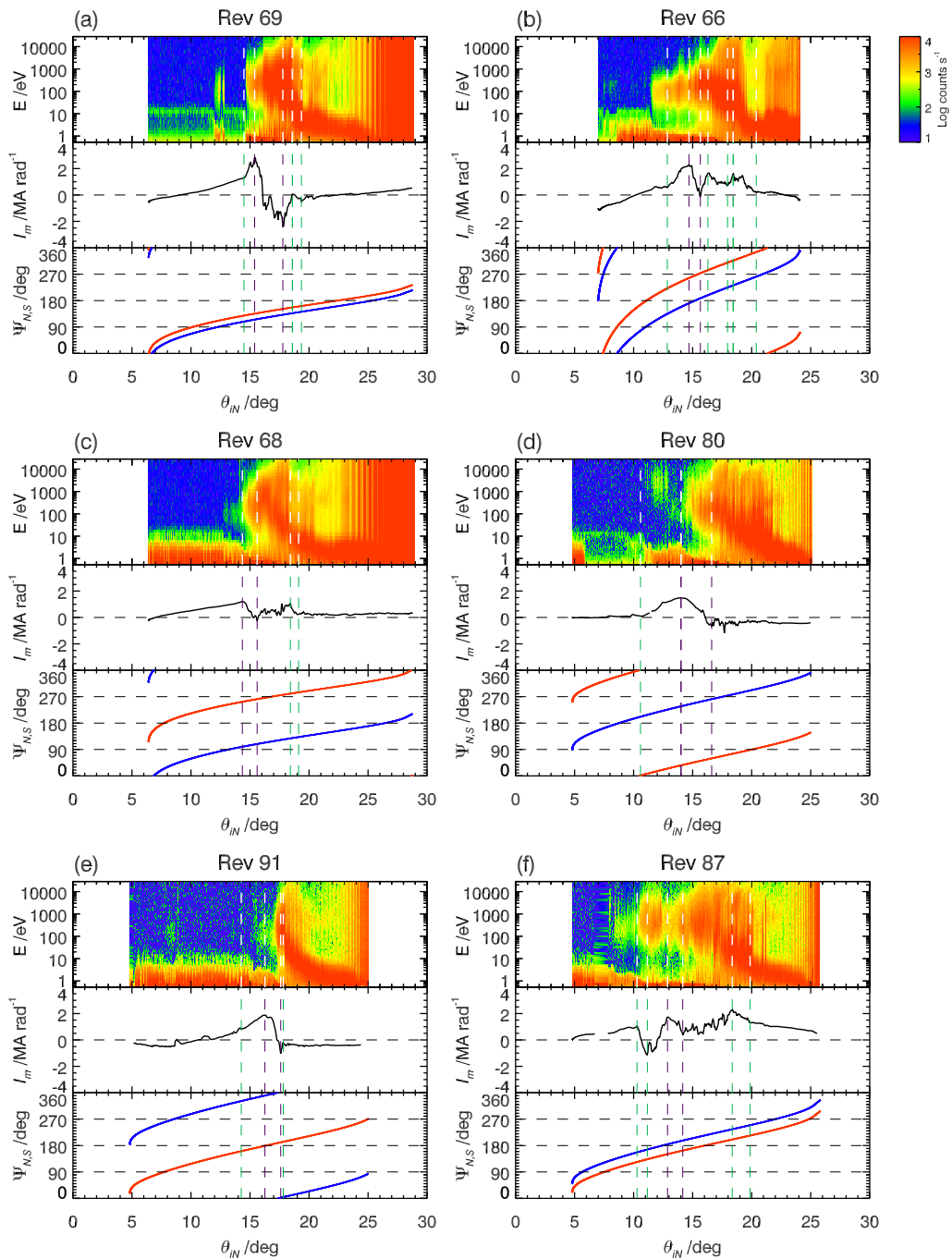


Figure 6.3: See overleaf.

Figure 6.3f discussed separately below), as also seen in the averaged profile in Figure 6.2b, which appears generally to begin on open field lines as judged from the absence of hot electron fluxes, and the averaged OCB at $\sim 13.3^\circ$. In some cases a further specific increase in I_m occurs in association with the OCB, indicative of strongly enhanced downward currents flowing on outermost closed field lines, examples of which are seen in Figures 6.3a and 6.3d, but not in all, such as Figure 6.3c and 6.3e. Such enhanced

downward currents are an almost invariable feature of the southern current profiles, but are evident only intermittently in the north. The equatorward current then typically reaches peak positive values $\sim 1\text{-}2 \text{ MA rad}^{-1}$ at $\sim 14^\circ\text{-}16^\circ$ colatitude, in agreement with the peak averaged profile in Figure 6.2b. The electron spectrograms show that this peak maps near the poleward boundary of the main hot ($\sim 100 \text{ eV}$ to several keV) electron population, which according to our simple field model maps between ~ 14 and $\sim 19 R_S$ in the equatorial outer magnetosphere.

Beyond the peak in I_m , a sharp reduction in value is then almost invariably observed over a $\sim 1^\circ\text{-}3^\circ$ colatitude interval centred near $\sim 15^\circ\text{-}17^\circ$, indicative of a reversal to strong upward-directed field-aligned current, in overall agreement with Figure 6.2b. Examination of individual cases, however, shows that the form of the following field perturbations at larger colatitudes depends significantly on the values of both the northern and southern PPO phases. When both phases lie in the 180° range centred on 90° , both PPO systems are expected to be associated with positive azimuthal (leading) fields on sub-auroral field lines, corresponding to negative (poleward) I_m values, with

Figure 6.3: Data are shown from the northern inbound passes of six Cassini Revs, as marked at the top of each figure, chosen to exemplify differing conditions of the PPO-related phases. From top to bottom, each panel of the figure shows (i) a CAPS/ELS electron count rate spectrogram covering the energy range $\sim 0.6 \text{ eV}\text{-}28 \text{ keV}$, colour-coded as shown at upper right, (ii) the ionospheric meridional current, I_m (MA rad^{-1}), derived from magnetic field data using equation (5), and (iii) the two PPO-related phases, Ψ_N (deg) shown by the blue line and Ψ_S (deg) shown by the red. Spacecraft position has been mapped along model field lines to the northern ionosphere as described in section 2.2, with parameters being plotted versus colatitude measured from the northern pole. Vertical dashed lines indicate the principal field-aligned current sheets drawn between extrema in the I_m data with overall gradients meeting or exceeding the limit discussed in section 2.2. These are shown generally in green, but with the principal upward current region being bracketed by the purple lines. I_m values increasing or decreasing with colatitude indicate downward or upward currents, respectively. In the polar region the intense electron fluxes at energies below $\sim 10 \text{ eV}$ are spacecraft photoelectrons, observed where the spacecraft potential is positive relative to the external medium. These disappear around $\sim 18^\circ$ colatitude as the spacecraft encounters the cool dense plasma of the inner magnetosphere nearer the equator, and charges to a negative potential. The high energy-independent counts recorded equatorward of $\sim 23^\circ$ colatitude are due to penetrating radiation belt particles, striped due to instrument scanning.

upward field-aligned currents in the northern auroral region (Figure 2.13). A typical example is shown in Figure 6.3a (Rev 69), in which the I_m profile correspondingly falls to large negative values across the current layer, associated with a large upward current $\sim 5 \text{ MA rad}^{-1}$ in this case. I_m then returns to near-zero values across a secondary downward current layer of $\sim 2 \text{ MA rad}^{-1}$ centred near $\sim 18^\circ$ colatitude, before relaxing to smaller negative values across a weak adjacent upward current sheet $\sim 0.5 \text{ MA rad}^{-1}$ centred near $\sim 19^\circ$. The latter current is co-located with the equatorward edge of the main hot electron region in the ELS spectrogram, mapping to $\sim 8 R_S$ in the equatorial plane in our simple field model, though hot plasma injection signatures are present at larger colatitudes. The auroral region field-aligned currents between $\sim 15^\circ$ and $\sim 19^\circ$ in this case thus exhibit a four-sheet current profile as marked by the vertical dashed lines in the figure, that strongly resembles those observed in the southern hemisphere when upward-directed PPO currents are present (for southern PPO phases $\sim 270^\circ$, see Figure 2.13e and Figure 4.2 of Chapter 4). At larger colatitudes away from these current sheets the I_m values in Figure 6.3a then slowly increase to small positive values (negative azimuthal fields) as first the southern and then the northern PPO phases increase towards and across 180° .

Similarly, when both phases lie in the 180° range centred on 270° , both PPO systems are expected to be associated with negative azimuthal (lagging) fields on sub-auroral field lines, corresponding to positive (equatorward) I_m values, with downward field-aligned currents in the northern auroral region (Figures 1c-1h). An example is shown in Figure 6.3b (Rev 66), in which the I_m profile initially falls to near-zero values across an upward current layer of $\sim 2 \text{ MA rad}^{-1}$, before returning to smaller positive (lagging field) values across a downward current layer $\sim 1.5 \text{ MA rad}^{-1}$ centred at $\sim 16^\circ$ colatitude. The profile then exhibits variable large positive values before returning to smaller positive values across a secondary upward current sheet centred near $\sim 20^\circ$, again co-located with the inner boundary of the hot electron regime. This profile again strongly resembles the four-sheet profiles observed in the southern hemisphere for downward-directed PPO current (southern PPO phases $\sim 90^\circ$, see Figure 2.13e and Figure 4.2 of

Chapter 4), as marked by the vertical dashed lines in the figure. We note in this case, however, that the poleward boundary of the enhanced downward current region at smallest colatitudes is clearly not co-located with the OCB as judged from the electron spectrogram, as is usually the case in the south. The boundary in the electron data in this case is at $\sim 11.5^\circ$ co-latitude, while the downward current enhancement starts near $\sim 13^\circ$. We also note that the positive I_m region between $\sim 16^\circ$ and $\sim 20^\circ$ colatitude has a double-peaked structure, also not seen in southern profiles, indicative of the presence of weaker central up-down field-aligned currents between the secondary downward and upward currents marked by the vertical dashed lines. At the largest colatitudes observed on this pass we see that the small positive I_m values decline towards zero and then become negative. The latter signature indicates the influence of the southern PPO phase on these values, which we note is approaching $\sim 90^\circ$ at this time expected to be associated with increasing negative values, while the northern phase is approaching $\sim 360^\circ$ expected to be associated with weakening but still positive values.

Figures 6.3c and 6.3d show two cases in which the northern and southern PPO currents have opposite expected senses within the northern auroral region, with the northern phase lying in the 180° range centred on 90° and the southern phase lying in the 180° range centred on 270° in Figure 6.3c, and vice versa in Figure 6.3d. In the case shown in Figure 6.3c (Rev 68), the auroral-region profile appears as an attenuated version of that in Figure 6.3b, with no clear enhancement in the poleward downward current at the OCB, followed by a sharp upward current of $\sim 1 \text{ MA rad}^{-1}$ which reduces the I_m values to near zero, and then a resumption of weaker variable positive values at larger colatitudes indicative of an overall downward current followed by a secondary upward current. This sense of behaviour thus follows expectations based on the southern PPO phase near $\sim 270^\circ$, rather than the northern PPO phase near $\sim 90^\circ$, thus indicating the presence of southern-phase currents in the northern auroral region. In the case shown in Figure 6.3d (Rev 80), a region of enhanced downward current is present on outer closed field lines, but after peaking and then falling near $\sim 15^\circ$ to weak negative values in the usual main upward current region, $\sim 2 \text{ MA rad}^{-1}$ in this case, I_m

then remains at small negative values to large colatitudes. This behaviour suggests the near-cancellation of the usual currents in the larger colatitude regime from $\sim 16^\circ$ to $\sim 20^\circ$ spanning the main hot electron region, as seen in Figures 6.3a and 6.3b, with a southern PPO phase near 90° and northern PPO phase near 270° . However, the generally negative values suggest that the southern perturbations are again the larger of the two at these colatitudes.

In Figure 6.3e (Rev 91) we show a different case where we expect to observe small effects of the PPO-related currents, where the PPO phases are either $\sim 0^\circ/360^\circ$ or 180° in the auroral region (see Figure 2.13), the former for the northern phase, and the latter for the southern phase in the case shown. The current profile indicates a slight steepening towards higher downward currents on outer closed field lines, before falling rapidly between $\sim 16^\circ$ and $\sim 17.5^\circ$ colatitude from peak positive to weaker negative values via an upward current of $\sim 3 \text{ MA rad}^{-1}$. I_m then returns to small negative values via a sharp downward current layer $\sim 1 \text{ MA rad}^{-1}$ at $\sim 18^\circ$, and remains at such values through the remainder of the hot electron regime and at larger colatitudes. The latter negative values are suggestive of dominance of the northern PPO system approaching $\sim 90^\circ$ phase in this case, rather than the southern system approaching $\sim 270^\circ$. As may be expected, the nature of the auroral region current profile is similar in form to the mean current profile in Figure 6.2b, though of somewhat greater magnitude, taken to be an approximation to the form of the PPO-independent current. As in the southern hemisphere, in addition to the principal downward then upward currents, there is also indication of the presence of weaker secondary currents flowing at the equatorward edge of the upward current, a narrow sheet of downward current being evident in this case.

In addition to the more “regular” I_m profiles exemplified in Figures 6.3a-6.3e, four more unusual examples are also found within the northern data set, that have no clear counterpart within the southern data examined in Chapters 4 and 5. One of these, observed on Rev 87, is shown in Figure 6.3f, the other three occurring under similar dual PPO phase conditions on Revs 72, 75, and 95. In these cases a patch of hot electrons is observed at high colatitudes, apparently “disconnected” from the usual hot electron

regime at larger colatitudes, accompanied by a dip in the I_m profile to near zero and, in the present case, negative values. The perturbations at larger colatitudes are then akin to those observed in Figure 6.3b under similar dual PPO phase conditions, and to those observed in attenuated form in Figure 6.3c.

Apart from these somewhat unusual profiles, this overview indicates more generally that, while the current profiles in the northern hemisphere follow similar overall behaviour to those observed in the south discussed previously in Chapters 4 and 5. They also show much less regularity in form compared with the PPO-dependent four-sheet structures usually found in the south. The clear latitudinal motion of the current layers with PPO phase that is present in the south is also absent in the north. No results similar to those in Chapter 5 will therefore be presented in this chapter. This less regular behaviour is undoubtedly linked to the additional finding that, while the field perturbations in the northern polar region appear related to the northern PPO phase, those within the auroral region and at lower latitudes show dual influence of both northern and southern phases. These data thus provide the first observational evidence for the existence of inter-hemispheric PPO-related currents proposed by *Southwood and Kivelson [2007]* (see also Figures 2.13b and 2.13e and related discussion in Chapter 2). We note, however, that no clear evidence for the influence of the northern phase in ordering the southern data was found in Chapters 4 and 5. In the following section we examine the issue of the presence of dual periodicities more quantitatively, not only for the northern, but also for the southern data.

6.3 Results

6.3.1 PPO-related azimuthal fields at small and large colatitudes

We begin by examining the field oscillations at small and large colatitudes away from the main current region, representing the overall effect of the PPO current system on open field lines and in the quasi-dipolar field region, respectively, in both the northern and southern hemispheres (see Figures 2.13). In view of the results of section 6.2.3,

we plot the $B_{\phi i}$ data in these two colatitude regimes versus both the northern and southern phases, $\Psi_{N,S}$, in the upper row of Figure 6.4 for the northern hemisphere data mapped to the northern ionosphere, and in the lower row for the southern hemisphere data mapped to the southern ionosphere. Specifically, from the results in Figure 6.2 we choose the northern colatitude range $\theta_{iN} = 6^\circ - 11^\circ$ for the polar region, and $20^\circ - 26^\circ$ for the equatorward region (mapping to $3.8 - 6.6R_S$ in the equatorial plane according to our field model), compared with $\sim 14^\circ - 17.5^\circ$ for the main current region. These polar and equatorial ranges are shown by the vertical dotted lines in Figure 6.2a. In the southern hemisphere we similarly use the ranges $\theta_{iS} = 6^\circ - 12^\circ$ for the polar region, and $22.1^\circ - 28.8^\circ$ for the equatorward region, shown by the vertical dotted lines in Figure 6.2c, the equatorward range being magnetically conjugate to the equatorward range in the northern hemisphere according to our field model. Both polar regions are expected to lie wholly on open field lines according to the average OCB locations determined by *Jinks et al.* [2014] (see Figure 6.2). The data from individual Revs are colour-coded as in Figure 6.2.

From the discussions in Chapters 2 and 3 we expect that in the equatorward region $B_{\phi i}$ should vary as $\sim \sin \Psi_{N,S}$, while in the polar region it should vary as $\sim -\sin \Psi_{N,S}$, which visual inspection of Figure 6.4 shows is approximately the case for the phases in corresponding hemispheres. More quantitatively, we have fitted sinusoids to these data of the form

$$B_{\phi i} = \langle B_{\phi i} \rangle + B_{\phi i0} \sin(\Psi_{N,S} - \Delta), \quad (6.1)$$

obtained using a Levenberg-Marquardt least squares minimization algorithm [*Marquardt*, 2009], shown in Figure 6.4 by the black solid lines, with the mean value $\langle B_{\phi i} \rangle$ being shown by the black dashed lines. The fit parameters together with the RMS deviation are shown in the upper left hand corner of each panel. The uncertainties in these parameters have been estimated using the ‘jackknife’ statistical resampling method, in which one data set at a time is removed from the analysis and the fit parameters re-computed [e.g. *Quenouille*, 1949; *Miller*, 1974; *Rohde et al.*, 2013]. In this case a data set has been defined as the data from a single Rev, thus resulting in 34 estimates of the

59 60 61 62 63 64 65 66 67 68 69 70 72 73 74 75 76 77 78 79 80 81 82 83 85 86 87 88 90 91 92 93 94 95

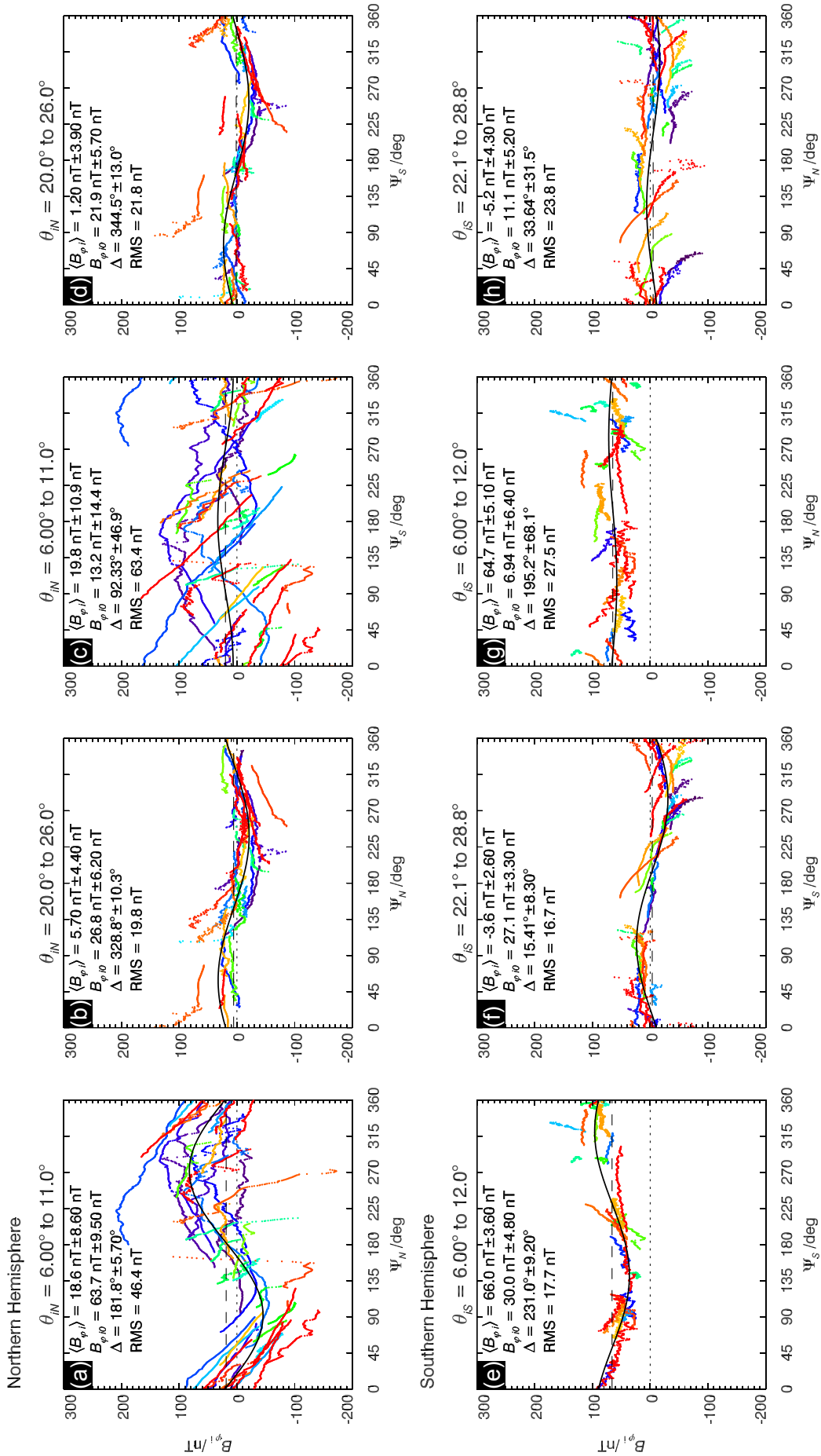


Figure 6.4: See overleaf.

fit parameters considering the 34 Revs included in the northern study. The estimated error in each parameter is given by a modified standard deviation $\sqrt{N-1}\sigma$, where N is the number of estimates (data sets or Revs) and σ the standard deviation of the fit parameter estimates. For the phase angles Δ we employ the ‘‘circular standard deviation’’ of *Mardia and Jupp* [2000](see *Andrews et al.* [2011] equations A1a and A3b). These uncertainties have been checked using a different statistical resampling method called the ‘bootstrap’ method, in which the data sets (Revs) are randomly picked to form a new set of 34, with each Rev being allowed to be picked multiple times. The new set is then used in the fitting analysis, repeated N times to give N estimates of the fit parameters. The estimated uncertainty is the standard deviation of the fit parameter. It was found that ‘bootstrap’ values for $N \approx 1000$ generally produced uncertainty estimates very similar to those obtained from the ‘jackknife’ method. The latter method was chosen for this study, due to its smaller computation requirements.

Turning now to the results, we see in Figure 6.4a that the amplitude of the northern polar oscillation is $\sim 64 \pm 10$ nT, thus accounting for much for the variation about the mean in the corresponding region in Figure 6.2a, while the phase Δ is $\sim 182^\circ \pm 6^\circ$, very close to the expected value of 180° based on the *Andrews et al.* [2012] model. The uncertainty estimates indicate that both these parameters are well-determined. The mean value is $\sim 19 \pm 9$ nT, consistent with the mean values in Figure 6.2a, while the RMS

Figure 6.4: Plots showing the variation of the mapped northern and southern ionospheric azimuthal field $B_{\varphi i}$ (nT) with northern and southern PPO phases $\Psi_{N,S}$ (deg). The northern hemisphere data have been mapped to the northern ionosphere, and the southern data to the southern. Figures 6.4a and 6.4c show northern polar data poleward of the auroral current sheets (6° - 11° northern colatitude) plotted versus northern and southern phases, respectively, while Figures 6.4b and 6.4d correspondingly show the northern equatorial data equatorward of the current sheets (20° - 26° colatitude). Similarly, Figures 6.4e and 6.4g show southern polar data (6° - 12° southern colatitude) plotted versus northern and southern phases, respectively, while Figures 6.4f and 6.4h correspondingly show the southern equatorial data (22.1° - 28.8° colatitude conjugate to the northern equatorial region). The data from each Rev are colour coded as shown at the top of the plot. The black solid lines show sinusoidal fits to these data as described in section 6.3.1 (equation (6.1)), with the fit parameters given in each panel together with the RMS deviation of the data from the fitted line. The black dashed line shows the mean value.

deviation is ~ 46 nT, to which the variation of ~ 70 nT in the mean profile over the chosen polar region in Figure 6.2a must make a significant contribution. For the equatorial data in Figure 6.4b the amplitude is smaller $\sim 27 \pm 6$ nT, while the phase is $\sim 329^\circ \pm 10^\circ$, again well determined. The latter value is equivalent to $-31^\circ \pm 10^\circ$ (modulo 360°), which is modestly but significantly ‘earlier’ compared with the zero value expected on the basis of the *Andrews et al.* [2012] model. Compared with the results in Figure 6.4a, this value implies that the oscillations in the polar region ‘lag’ the equatorial phase by $\sim 33^\circ \pm 12^\circ$. A similar phenomenon was reported in southern data in Chapters 4 and 5, where, allowing for the expected $\sim 180^\circ$ switch between the two regions as above, we found that the southern hemisphere polar oscillations lagged in phase by $\sim 47^\circ$ relative to the southern equatorial oscillations.

Similar analysis of the southern hemisphere data relative to Ψ_S is shown in Figures 6.4e and 6.4f. Here the equatorial amplitude is $\sim 27 \pm 3$ nT similar to the equatorial northern oscillation amplitude in the northern hemisphere in Figure 6.4b, with a phase of $\sim 15^\circ \pm 8^\circ$ which is slightly but significantly larger than the expected value of zero. For the southern polar data, however, the amplitude is $\sim 30 \pm 5$ nT, approximately half that in the northern polar region, with a phase of $\sim 231^\circ \pm 9^\circ$, significantly “later” compared to the expected phase of $\sim 180^\circ$. Again allowing for the expected 180° phase shift between the two regions, the polar oscillations in the south thus lag the equatorial oscillations by $\sim 36^\circ \pm 12^\circ$. Thus very similar phase lags $\sim 35^\circ$ are found between the equatorial and polar regions both north and south, consistent within uncertainties with the slightly larger southern hemisphere value $\sim 47^\circ$ reported previously in Chapter 4. This analysis also shows that for this interval the *Andrews et al.* [2012] phase model best reflects the polar data in the northern hemisphere but the equatorial data in the southern hemisphere, presumably reflecting the relative influence of the equatorial and polar data employed in their analysis.

Given the results in section 6.2.3, we also examine whether oscillations with the southern PPO period can be detected in the northern regions, and vice versa. Results for the northern hemisphere are shown in Figures 6.4c and 6.4d, where the northern

hemisphere polar and equatorial data, respectively, are plotted versus the southern phase Ψ_S . In the polar region neither the data nor the sinusoidal fit show any evident modulation by the southern phase, with the fitted amplitude $\sim 13 \pm 14$ nT consistent with zero. In the equatorial region, however, clear southern modulation is evident with an amplitude $\sim 22 \pm 6$ nT, only slightly smaller than the northern oscillation in Figure 6.4b, and a phase of $\sim 345^\circ \pm 13^\circ$, essentially consistent with the expected value of zero. The latter phase is modestly $\sim 30^\circ \pm 15^\circ$ away from that determined from the southern hemisphere equatorial data in Figure 6.4f. These results thus confirm the conclusions in section 6.2.3, that while southern oscillations are not discernible in the northern polar region, a clear effect is present in the northern equatorial region. The amplitude is comparable with but somewhat lower than that determined from the southern equatorial data, and is also comparable with but somewhat lower than the northern oscillations in the northern equatorial region. The variation of oscillation amplitude with latitude along the equatorial field lines will be examined in greater detail in section 6.3.4.

In Figures 6.4g and 6.4h we similarly show the polar and equatorial southern hemisphere data plotted versus northern phase Ψ_N . In this case there is again no discernible effect in the polar region, with an amplitude of $\sim 7 \pm 6$ nT again consistent with zero. In the equatorial region the amplitude is found to be $\sim 11 \pm 5$ nT, less than half that in the northern hemisphere in Figure 6.4b, and less than that of the southern oscillations in this region by a factor of ~ 2.5 , with a phase $\sim 34^\circ \pm 31^\circ$ with a large uncertainty which is $\sim 66^\circ \pm 33^\circ$ away from the northern phase in Figure 6.4b. This rather marginal result will again be further examined in section 6.3.4.

6.3.2 PPO dependence of northern current colatitude profiles

We now examine the PPO phase dependence of the northern colatitude profiles of the meridional ionospheric current per radian of azimuth I_m , by dividing the northern hemisphere data from all the Revs in the study into fixed ranges of $\Psi_{N,S}$. We recall from Chapter 3 that I_m is derived from the modified azimuthal field values using equa-

tion (3.3), is thus opposite in sign to B_φ and positive directed towards the equator, and that it can be used under appropriate conditions to directly discuss the field-aligned currents that are flowing. In Chapter 4 and section 4.4.2 we performed an equivalent analysis for the southern data by dividing it into eight non-overlapping 45° sectors of Ψ_S , centred on 0° , 45° , 90° , and so on. Here, however, in view of the results in sections 6.2.3 and 6.3.1 which imply that the northern equatorial data depend both on Ψ_N and Ψ_S , we instead divide the data into non-overlapping 90° sectors of both Ψ_N and Ψ_S , each centred on 0° , 90° , 180° , and 270° .

The results are shown in Figure 6.5 in a Ψ_N by Ψ_S grid, where Ψ_N increases from top to bottom and Ψ_S from left to right. Thus row 1 (Figures 6.5a-6.5d) contains all the data for $\Psi_N = 0^\circ \pm 45^\circ$, subdivided into four 90° sectors of Ψ_S , while column 1 (Figures 6.5a, 6.5e, 6.5i, and 6.5m) contains all the data for $\Psi_S = 0^\circ \pm 45^\circ$, subdivided into four 90° sectors of Ψ_N , and so on for the other rows and columns. The data from individual Revs are colour-coded as in previous figures, while the black solid circles joined by straight lines show values averaged as in Figure 6.2 described in section 6.2.2. While the data coverage is generally reasonably good within each of these $\Psi_{N,S}$ sectors, thus justifying the choice of sector size, there are some notable gaps, for example the main current region in Figure 6.5p.

Given the approximate dependency of the ionospheric current on $\Psi_{N,S}$ as $+\sin \Psi_{N,S}$ in the polar region and $\Psi_{N,S}$ in the equatorial (opposite to $B_{\varphi i}$), and neglecting the $\sim 30^\circ$ phase offsets found in section 6.3.1 as modest compared with the 90° sector size used here, we note that the sectors centred on $\Psi_{N,S} = 0^\circ$ or 180° should show minimal effects due to the corresponding PPO current system, while sectors centred on $\Psi_{N,S} = 90^\circ$ and 270° should show maximal effects of opposite sign. Thus the data in columns 1 and 3 should show how the northern current profile varies with northern phase in the approximate absence of southern PPO effects, while rows 1 and 3 should show the equivalent variation of the northern current profile with southern phase in the approximate absence of northern PPO effects. The four remaining sectors not included in either of these columns and rows (Figures 6.5f, 6.5h, 6.5n, and 6.5p) then

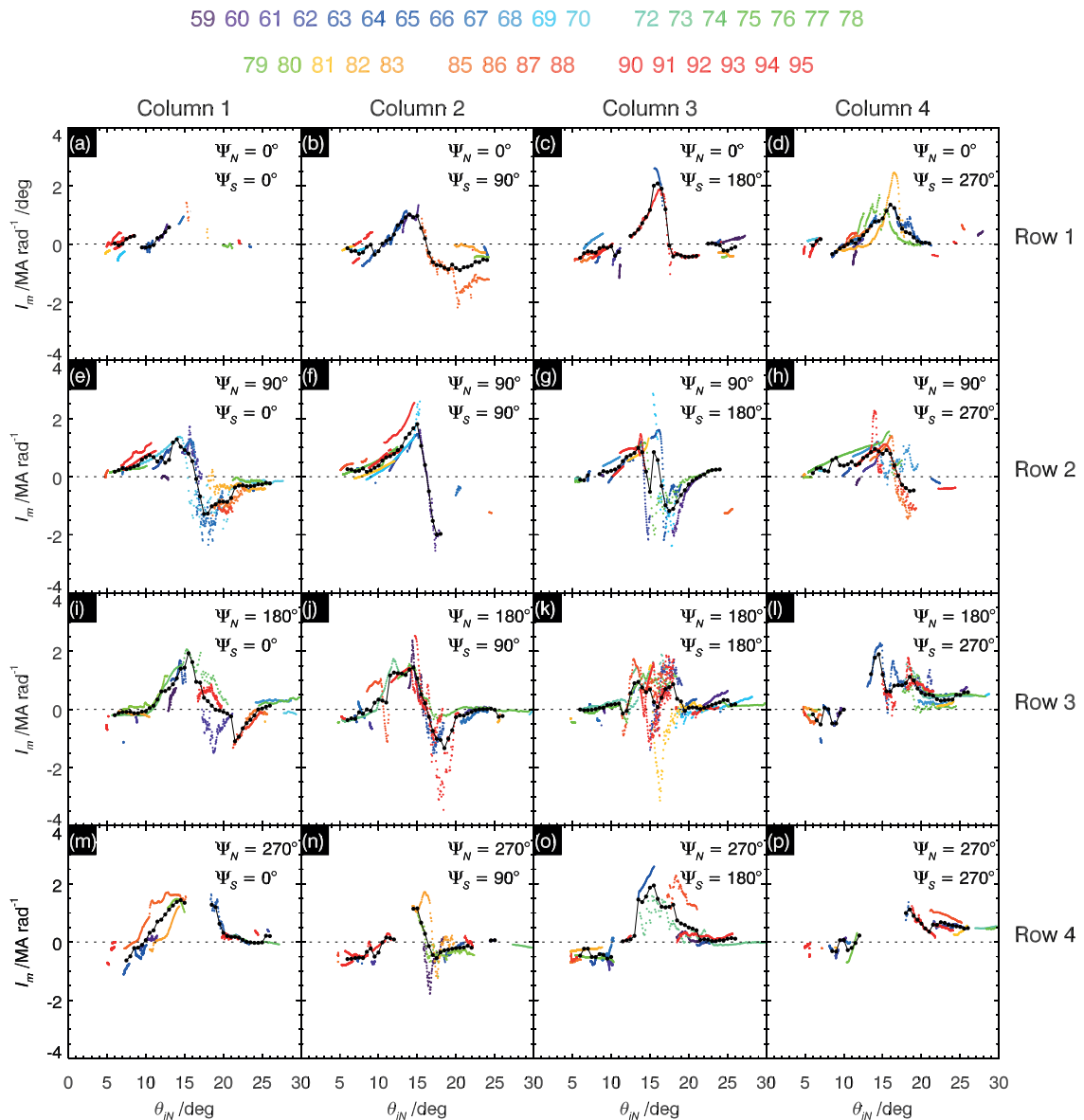


Figure 6.5: Plots showing northern ionospheric colatitude (θ_{iN} (deg)) profiles of the meridional ionospheric current per radian of azimuth I_m (MA rad^{-1}) sub-divided into sixteen non-overlapping 90° sectors of northern and southern PPO phases Ψ_N and Ψ_S (deg). The centre phase values are shown in the top right corner of each panel, with Ψ_N increasing from top to bottom, and Ψ_S increasing from left to right. The data for each Rev are colour coded as shown at the top of the figure, while black circles joined by black lines show weighted averages in overlapping 1° bins of colatitude, evaluated every 0.5° , as for Figure 6.2, where the data coverage is near continuous.

show cases where the two PPO systems either add in phase ($\Psi_{N,S}$ both 90° or both 270°), or partially cancel in antiphase (one 90° and the other 270°).

We first examine the data that lie both in columns 1 and 3 and rows 1 and 3 (Figures 6.5a, 6.5c, 6.5i, and 6.5k), for which both northern and southern PPO effects should be minimal, $\Psi_{N,S}$ both centered on 0° or 180° , such that the profiles should approximate

the PPO-independent current profile in the northern hemisphere. Similar profiles are seen in each case, with small currents in the most poleward region which increase quickly with colatitude beyond $\sim 11^\circ$, indicative of a downward current layer which is initiated generally on open field lines. The ionospheric current then peaks at $\sim 1\text{-}2 \text{ MA rad}^{-1}$ at $\sim 16^\circ$ colatitude (mapping to $\sim 14 R_S$ in the equatorial plane similar to results in Chapters 4 and 5), and then falls rapidly to small values by $\sim 18^\circ\text{-}19^\circ$ (mapping to $\sim 9\text{-}7.5 R_S$ in the equatorial plane), indicative of an upward current layer, then remaining small to large colatitudes. We note, however, the strongly scattered data with a double-peaked averaged profile in Figure 6.5k. The overall profiles resemble less smoothed versions of the mean I_m profile in Figure 6.2b, with small or lagging fields (positive I_m) essentially throughout, and an overall current in the system that is close to zero, with no net change in I_m over the colatitude range observed.

By comparison, the two sectors centred on $\Psi_N = 90^\circ$ in columns 1 and 3 (Figures 6.5e and 6.5g) both show enhanced positive values in the polar region and enhanced negative (leading field) values in the equatorial region, before increasing sharply towards zero by $\sim 21^\circ$ colatitude (mapping to $\sim 5.8 R_S$). These profiles thus indicate the additional presence of an upward current that is comparable in magnitude to the upward current of the PPO-independent system and is approximately collocated with the latter. At the equatorward edge of this current, the return of I_m to near zero values is also indicative of a smaller downward current which reduces the magnitude of the field perturbations in the inner region. Similarly, the two sectors centered on $\Psi_N = 270^\circ$ in columns 1 and 3 (Figures 6.5m and 6.5o) show enhanced negative values in the polar region compared with the profiles for $\Psi_{N,S} = 0^\circ$ and 180° , and enhanced positive values in the equatorward region which again fall to near-zero values at $\sim 20^\circ\text{-}21^\circ$. This indicates the presence of a downward current superposed on the PPO-independent current region together with a smaller upward current at larger colatitudes. These systems will be separated and examined in more detail in section 6.3.3.

Similar examination of rows 1 and 3 gives two independent determinations of the effects on the current profiles associated with the southern PPO phase, with the effects

of the northern PPO signal minimised (Figures 6.5b, 6.5d, 6.5j, and 6.5l). While there is no obvious effect of the southern phase in the polar region, it can be seen that a negative perturbation is present at larger colatitudes for Ψ_S centred on 90° (Figures 6.5b and 6.5j), indicative of an upward current superposed on the equatorward part of the PPO-independent current, while a positive perturbation is seen in the same region for Ψ_S centred on 270° (Figures 6.5d and 6.5l), indicative of a downward current superposed on the PPO-independent current. These currents will also be examined in more detail in section 6.3.3.

The remaining four phase sectors in Figure 6.5 are the cases where both northern and southern PPO effects should have near maximal values, both 90° or both 270° , thus in phase with each other, or where one phase is 90° and the other 270° , thus in antiphase. The case where both phases are centred on 90° is shown in Figure 6.5f, which has the largest negative (leading field) current at large colatitudes within this data set, due to the superposition of two upward PPO-related currents. The other in-phase case, with both phases centred at 270° , is shown in Figure 6.5p, which unfortunately has a large gap with no data in the main current region. However, it does show negative values at small colatitudes and positive values at large colatitudes, as then expected from a superposed net downward current. For the two cases of antiphase, Figures 6.5h and 6.5n, the sign of the polar field perturbations agree with expectations based on Ψ_N , positive at 90° and negative at 270° , while the main current region shows significant data scatter, with the current in the equatorial region near zero at colatitudes greater than $\sim 18^\circ$.

6.3.3 Subcorotation and PPO-dependent current profiles

We now combine the data in Figure 6.5 in various ways to make estimates of the PPO-independent (subcorotation) and the PPO-dependent current profiles, and thus also estimates of the associated field-aligned currents. We also compare these profiles with those derived from the southern hemisphere data investigated in Chapter 4. We begin by considering the PPO-independent current profile, which can be determined

by combining the data centred on $\Psi_{N,S} = 0^\circ$ and 180° (Figures 6.5a, 6.5c, 6.5i, and 6.5k), for which the effects of both northern and southern PPO currents should be minimised. The averaged profile is shown in Figure 6.6a (the average being determined as in Figure 6.2), showing small negative values at smallest colatitudes $\sim 5^\circ$ - 10° similar to Figure 6.2b, then increasing steadily between $\sim 11^\circ$ and $\sim 13.5^\circ$ colatitude (near the averaged northern OCB of *Jinks et al.* [2014]), indicating a downward current of $\sim 1 \text{ MA rad}^{-1}$ in this region with an ionospheric current density of $\sim 25 \text{ nA m}^{-2}$. Only moderate variations in the average value then occur between $\sim 14^\circ$ and $\sim 17^\circ$, followed by a decrease to near-zero values over $\sim 17^\circ$ to $\sim 19^\circ$, showing an essentially equal and opposite upward current flowing in this region of $\sim 1 \text{ MA rad}^{-1}$ again with an ionospheric current density of $\sim 25 \text{ nA m}^{-2}$. However, there is strong variability of the data in the upward current region from Rev to Rev, such that this profile represents an averaged view.

Now we consider the PPO-related current profile due to the northern system. We select the sectors with $\Psi_N = 90^\circ$ and 270° for which $\Psi_S = 0^\circ$ and 180° (Figures 6.5e, 6.5g, 6.5m, and 6.5o). We then combine the $\Psi_S = 0^\circ$ and 180° data to give the best estimate of the profiles for given Ψ_N in the approximate absence of southern PPO effects, and thus determine the mean profiles for $\Psi_N = 90^\circ$ and 270° . Exploiting the expected $m = 1$ symmetry of the PPO system with respect to PPO phase as in Chapters 4 and 5, we then subtract the $\Psi_N = 90^\circ$ profile from the 270° profile (or vice versa) and divide by two to extract the northern PPO-related current that is superposed on the PPO-independent current, the latter being eliminated by the subtraction. The results are shown in Figure 6.6b where the equal and opposite blue and red profiles correspond to $\Psi_N = 90^\circ$ and 270° , respectively. Vertical dotted lines extended from Figure 6.6a indicate the main region of equatorward-directed current and lagging field associated with the PPO-independent system, located between $\sim 11^\circ$ and $\sim 19^\circ$. Essentially within this region the $\Psi_N = 90^\circ$ profile undergoes a strong decrease indicative of an upward current of $\sim 1.5 \text{ MA rad}^{-1}$, while the equal and opposite $\Psi_N = 270^\circ$ profile undergoes a strong increase indicative of a downward current of the same magnitude. The im-

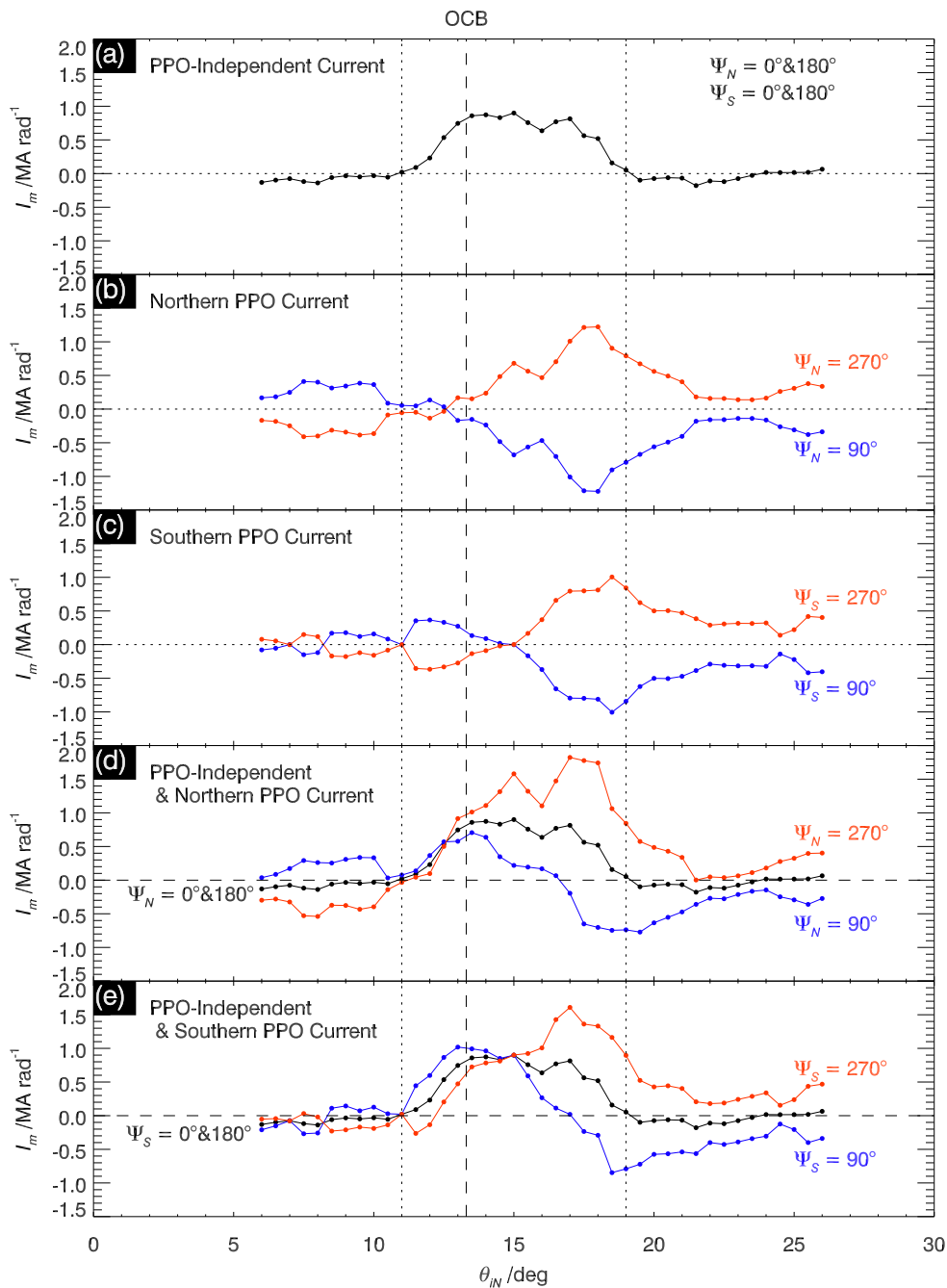


Figure 6.6: See overleaf.

plied overall ionospheric field-aligned current density is $\sim 20 \text{ nA m}^{-2}$. We note that the overall current gradient in this region is comparable to the $\sim 0.3 \text{ MA rad}^{-1}$ limit described in Appendix C. These are the PPO-related field-aligned currents that separate the oppositely-directed current and azimuthal field perturbations in the polar ($\sim 5^\circ - 10^\circ$) and equatorial (beyond $\sim 18^\circ$) regions, as examined in section 6.3.1 and Figure 6.4. We note that the switch in sign between perturbations of opposite senses occurs at $\sim 12.5^\circ$ colatitude, poleward of but close to the northern averaged OCB ($\sim 13.3^\circ$). At

larger colatitudes beyond $\sim 18^\circ$, however, the current drops rapidly to small values of the same sign beyond $\sim 21.5^\circ$. Again the current gradient is significant in the above terms, indicating the presence of field-aligned currents of opposite sense, downward for $\Psi_N = 90^\circ$ and upward for 270° , of magnitude $\sim 1 \text{ MA rad}^{-1}$, which reduce the field perturbations to lower magnitudes in the large colatitude regime. This current layer maps between ~ 9 and $\sim 6 R_S$ in the equatorial plane, and has an associated ionospheric field-aligned current density of $\sim 15 \text{ nA m}^{-2}$. We note that a similar feature of $\sim 0.4 \text{ MA rad}^{-1}$ magnitude was found previously in the southern PPO current profile in Chapters 4 and 5 (see Figures 4.7 and 5.6), but in this case the gradient of the current did not meet the above criterion for the unambiguous presence of field-aligned current, such that it was not described in those terms.

The current profile associated with the southern PPO system in the northern hemisphere is determined in a similar way by combining the data sectors in Figure 6.5 that maximise the southern PPO effects while minimizing the northern PPO effects. Thus we employ the data centred on $\Psi_S = 90^\circ$ and 270° with $\Psi_N = 0^\circ$ and 180° (Figures 6.5b, 6.5d, 6.5j, and 6.5l), combine and average the latter data for given Ψ_S , and then subtract these profiles and divide by two. The results are shown in Figure 6.6c, where the blue

Figure 6.6: Northern colatitude profiles of the meridional ionospheric current I_m (MA rad^{-1}) associated with (a) the PPO-independent (subcorotation) system, (b) the northern-period PPO system where the blue data corresponds to $\Psi_N = 90^\circ$ and the red to $\Psi_N = 270^\circ$, and (c) the southern PPO system where the blue data corresponds to $\Psi_S = 90^\circ$ and the red to $\Psi_S = 270^\circ$. These were derived using data from appropriate sectors in Figure 6.5, as described in section 6.3.3. The vertical dotted lines indicate the main region of equatorward current and lagging azimuthal field in the PPO-independent system between $\sim 11^\circ$ and $\sim 19^\circ$. The vertical dashed line shows the position of the averaged northern OCB of *Jinks et al.* [2014] at 13.3° . Figure 6.6d shows synthesised profiles that add the northern PPO profiles from Figure 6.6b to the PPO-independent profile in Figure 6.6a, to show the combined profiles for $\Psi_N = 90^\circ$ (blue), $\Psi_N = 0^\circ$ and 180° (black) (just Figure 6.6a), and $\Psi_N = 270^\circ$ (red). No contribution is included from the southern system, corresponding to $\Psi_S = 0^\circ$ and 180° throughout. Similarly Figure 6.6e shows synthesised profiles that add the southern PPO profiles from Figure 6.6c to the PPO-independent profile in Figure 6.6a, to show the combined profiles for $\Psi_S = 90^\circ$ (blue), $\Psi_S = 0^\circ$ and 180° (black) (again just Figure 6.6a), and $\Psi_S = 270^\circ$ (red). No contribution is included from the northern system, corresponding to $\Psi_N = 0^\circ$ and 180° throughout.

profile corresponds to $\Psi_S = 90^\circ$ and the red to $\Psi_S = 270^\circ$. As for the northern system in Figure 6.6b, the main currents flow in the region between the dashed vertical lines, implying an upward current of $\sim 1.25 \text{ MA rad}^{-1}$ for $\Psi_S = 90^\circ$ and a downward current of the same magnitude for $\Psi_S = 270^\circ$, modestly smaller than the corresponding current for the northern PPO system indicated above. Again the gradient is significant, indicative of an ionospheric current density of $\sim 13.5 \text{ nA m}^{-2}$. Unlike the northern system, however, poleward of this region the current falls to small values of variable sign, consistent with the null result in Figure 6.4c discussed in section 6.3.1, indicative of the presence of an oppositely-directed field-aligned current of $\sim 0.35 \text{ MA rad}^{-1}$ near $\sim 11.5^\circ$ colatitude. Equatorward of the main layer the current again falls sharply to smaller values of the same sign across $\sim 18.5^\circ$ to $\sim 22.0^\circ$ ($\sim 9.5 R_S$ in the equatorial plane), indicative of a layer of oppositely directed current of $\sim 0.75 \text{ MA rad}^{-1}$ with an ionospheric current density of $\sim 11 \text{ nA m}^{-2}$. Beyond this current layer the I_m values remain near-constant at least to $\sim 26^\circ$ at values comparable with those for the northern PPO system in Figure 6.6b.

Using these results we can synthesise northern current profiles that are not observed directly, such as those corresponding to a fixed northern or southern PPO phase in the absence of the other PPO system. In Figure 6.6d, for example, we show the modulation of the northern current profile by the northern PPO system in the absence of southern effects. Specifically, we combine the PPO-independent profile in Figure 6.6a with the northern PPO profiles for $\Psi_N = 90^\circ$ (blue) and 270° (red) in Figure 6.6b, but do not include a contribution from the southern PPO system, thus corresponding to $\Psi_S = 0^\circ$ or 180° . We also show the PPO-independent profile itself (black), corresponding to both $\Psi_N = 0^\circ$ or 180° and $\Psi_S = 0^\circ$ or 180° . The correspondence of these profiles for the northern system in the northern hemisphere with the results in Chapters 4 and 5 for the southern system in the southern hemisphere is clear (see, e.g., Figures 4.5 and 5.2). For $\Psi_N = 90^\circ$, the counterpart of $\Psi_S = 270^\circ$ in the southern hemisphere (see Figure 2.13), we see from the pole to the equator (a) a downward current layer of $\sim 0.5 \text{ MA rad}^{-1}$ between $\sim 10.5^\circ$ and $\sim 13.5^\circ$, just spanning the averaged OCB at $\sim 13.3^\circ$, (b) an

upward current layer $\sim 1.5 \text{ MA rad}^{-1}$ between $\sim 13.5^\circ$ and $\sim 18^\circ$ spanning the UV auroral oval in Figure 6.1c with “leading” fields (poleward-directed current) in the equatorward portion, and (c) a further downward current $\sim 0.75 \text{ MA rad}^{-1}$ between $\sim 19.5^\circ$ and $\sim 24^\circ$. This three-layer structure is therefore very similar to that observed for $\Psi_S = 270^\circ$ in the south, though a small secondary upward current layer is also present at largest southern colatitudes which is either not present or not resolved here. Similarly, for $\Psi_N = 270^\circ$, the counterpart of $\Psi_S = 90^\circ$ in the southern hemisphere, we see from the pole to the equator (a) a larger downward current layer of $\sim 2 \text{ MA rad}^{-1}$ between $\sim 10^\circ$ and $\sim 15^\circ$, (b) a much smaller upward current layer $\sim 0.5 \text{ MA rad}^{-1}$ between $\sim 15^\circ$ and $\sim 16^\circ$, (c) a small further downward current $\sim 0.75 \text{ MA rad}^{-1}$ between $\sim 16^\circ$ and $\sim 17^\circ$, and (d) a large downward current $\sim 1.75 \text{ MA rad}^{-1}$ between $\sim 17^\circ$ and $\sim 21.5^\circ$. This four-layer structure is very similar in form to that observed for $\Psi_S = 90^\circ$ in the south, overall representing a broad region of equatorward current associated with lagging fields with a “V-shaped” dip in the current magnitude near its the centre.

In Figure 6.6e we similarly show profiles corresponding to fixed values of the southern PPO phase, $\Psi_S = 0^\circ$ or 180° (black), $\Psi_S = 90^\circ$ (blue), and 270° (red) from Figures 6.6a and 6.6c, with no contribution from the northern PPO system, corresponding to $\Psi_N = 0^\circ$ or 180° . A similar modulation of the currents in the equatorward region is evident in this case, though with no clear PPO-related modulation at poleward-most latitudes. The profile for $\Psi_S = 90^\circ$ is again of similar three-layer down-up-down form as that for $\Psi_N = 90^\circ$ in Figure 6.6d, while in the profile for $\Psi_S = 270^\circ$ the expected dip in the centre of the equatorward current region is either absent or unresolved, leading to a two-sheet down-up structure with a near-plateau region between $\sim 14^\circ$ and $\sim 16^\circ$.

We can also use the results in Figures 6.6a-6.6c to synthesise profiles corresponding to other cases, such as where the PPO systems are in phase or in antiphase. In this context it may be noted that the three sets of results shown in Figures 6.6a-6.6c were each derived using a different set of four of the sixteen independent $90^\circ \times 90^\circ$ PPO phase data sets in Figure 6.5, thus corresponding to 12 of the 16 sets. The four remaining data sets not employed so far correspond to cases in which significant effects of both PPO

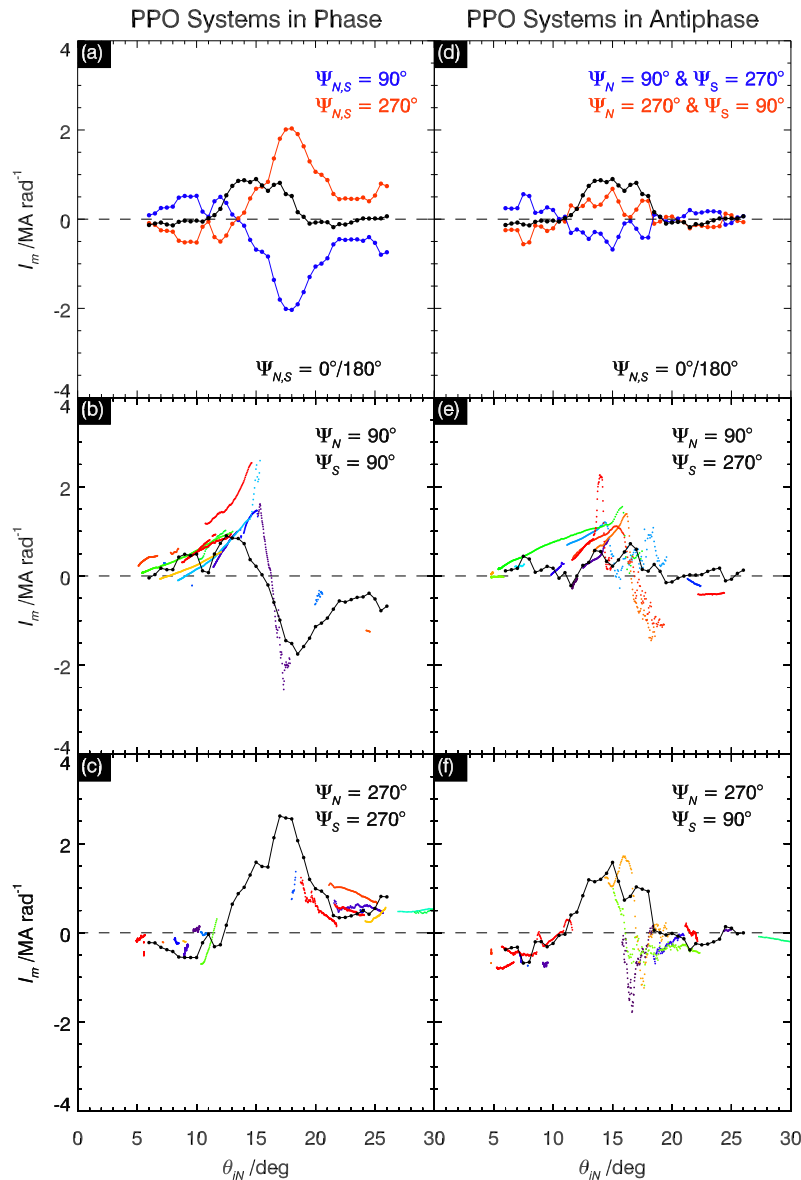


Figure 6.7: See overleaf.

systems should be present, either in phase with each other with $\Psi_N = \Psi_S = 90^\circ$ (Figure 6.5f) or $\Psi_N = \Psi_S = 270^\circ$ (Figure 6.5p), or in antiphase with each other, with either $\Psi_N = 90^\circ$ and $\Psi_S = 270^\circ$ (Figure 6.5h) or vice versa (Figure 6.5n). It is then of interest to see how appropriate combinations of the independently-determined profiles in Figure 6.6 compare with these data, with results shown in Figure 6.7. Figure 6.7a shows the summed northern and southern PPO current profiles from Figures 6.6b and 6.6c for $\Psi_N = \Psi_S = 90^\circ$ (blue) and $\Psi_N = \Psi_S = 270^\circ$ (red), while the black profile shows the PPO-independent current profile from Figure 6.6a. The main poleward PPO currents sum to $\sim 2.5 \text{ MA rad}^{-1}$ under these conditions, with oppositely-directed currents of ~ 1.5

MA rad^{-1} flowing in the equatorward region. Adding the combined current profile for $\Psi_N = \Psi_S = 90^\circ$ to the PPO-independent profile yields the black profile shown in Figure 6.7b, which is superposed on the corresponding independent data from Figure 6.5f. The overall agreement is quite good, though the central upward current layer is somewhat reduced in magnitude and smoothed compared to the data. Overall, a downward current of ~ 1 MA rad^{-1} flows in the poleward region to $\sim 14^\circ$, followed by an upward current of ~ 3 -4 MA rad^{-1} flowing between $\sim 14^\circ$ and $\sim 18^\circ$, and then a second downward current of ~ 1.5 MA rad^{-1} flowing between $\sim 18^\circ$ and $\sim 22^\circ$. Similarly, combining the profile for $\Psi_N = \Psi_S = 270^\circ$ in Figure 6.7a with the PPO-independent current profile yields the black profile in Figure 6.7c, which we compare with the corresponding data from Figure 6.5p. As mentioned in section 6.3.2, this data set unfortunately has a large gap in coverage in the main current region, but there is good agreement with the limited data at small and large colatitudes. Our synthesised profile thus provides an estimate of the currents in this case, corresponding to a region of downward current of ~ 3 MA rad^{-1} flowing between $\sim 12^\circ$ and $\sim 18^\circ$, with a small dip near its centre at $\sim 15.5^\circ$, followed by a smaller upward current of ~ 2 MA rad^{-1} flowing between $\sim 18^\circ$ and $\sim 21^\circ$.

Figure 6.7d shows the opposite case where the two PPO systems in Figures 6.6b and 6.6c are in antiphase, where the blue profile shows the case for $\Psi_N = 90^\circ$ and

Figure 6.7: Plots showing northern colatitude profiles of the meridional ionospheric current I_m (MA rad^{-1}) for cases in which the northern and southern PPO systems are either in phase or in antiphase, synthesised from the profiles in Figure 6.6. Figure 6.7a shows the PPO-independent current profile from Figure 6.6a (black) together with the summed northern and southern PPO system profiles for $\Psi_N = \Psi_S = 90^\circ$ (blue) and $\Psi_N = \Psi_S = 270^\circ$ (red) from Figures 6.6b and 6.6c, corresponding to times when the two PPO systems are in phase. In Figure 6.7b the black and blue profiles are added and compared with the corresponding independent data in Figure 6.5f, while in Figure 6.7c the black and red profiles are added and compared with the corresponding independent data in Figure 6.5p. Figure 6.7d again shows the PPO-independent current profile (black), together with the summed northern and southern PPO system profiles for $\Psi_N = 90^\circ$ and $\Psi_S = 270^\circ$ (blue), and $\Psi_N = 270^\circ$ and $\Psi_S = 90^\circ$ (red), corresponding to times when the two PPO systems are in antiphase. In Figure 6.7e the black and blue profiles are added and compared with the corresponding independent data in Figure 6.5h, while in Figure 6.7f the black and red profiles are added and compared with the corresponding independent data in Figure 6.5n.

$\Psi_S = 270^\circ$, and the red for $\Psi_N = 270^\circ$ and $\Psi_S = 90^\circ$. Again the black profile is the PPO-independent profile. Since the two PPO current profiles in Figures 6.6b and 6.6c are comparable in magnitude and essentially co-located, when combined in this way they cancel to a first approximation, but since the northern system is slightly stronger than the southern, the net current follows the northern system polarity, with opposite currents of $\sim 0.75 \text{ MA rad}^{-1}$ flowing in the poleward part of the region at $\sim 10^\circ$ - 15° , and $\sim 0.5 \text{ MA rad}^{-1}$ at larger colatitudes at $\sim 15^\circ$ - 18.5° . The PPO-independent current profile is then modestly larger compared with the PPO-related currents, opposite to the case when the two PPO systems are in phase. Combining the $\Psi_N = 90^\circ$ and $\Psi_S = 270^\circ$ (blue) profile with the PPO-independent current profile yields the black profile in Figure 6.7e which we show with the corresponding data from Figure 6.5h. The synthesised profile remains small, generally positive, and variable over the colatitude range $\sim 6^\circ$ to 19° , in rough agreement with the generally positive and scattered data. For the opposite case with $\Psi_N = 270^\circ$ and $\Psi_S = 90^\circ$, the combined current yields the black profile in Figure 6.7f, similar in form but slightly enhanced compared with the PPO-independent profile alone, which is shown together with the corresponding data from Figure 6.5n. The synthesised profile has a downward current of $\sim 2 \text{ MA rad}^{-1}$ flowing at $\sim 10^\circ$ - 15° colatitude, followed by a modestly weaker upward current of $\sim 1.5 \text{ MA rad}^{-1}$ between $\sim 15^\circ$ - 19° . The agreement with the data is again reasonable, though the model does not reproduce the sharp negative current features observed in the data at $\sim 16^\circ$ - 17° .

We now compare these results derived from northern hemisphere data with those from the southern hemisphere on the same Revs as determined in Chapter 4. We first consider the PPO-independent currents, and in Figure 6.8a compare the mean northern current profile in Figure 6.6a (black circles and solid lines) with that determined from a similar analysis of the southern data (black crosses and dotted lines), specifically using data for $\Psi_S = 0^\circ$ and 180° ($\pm 45^\circ$). Since the results discussed above show that the northern PPO effect is much smaller than the southern PPO effect in the southern hemisphere, we do not limit the Ψ_N values used in this case. This method is somewhat different to that employed in Chapter 4 (see sections 4.4.2 and 4.4.3), but pro-

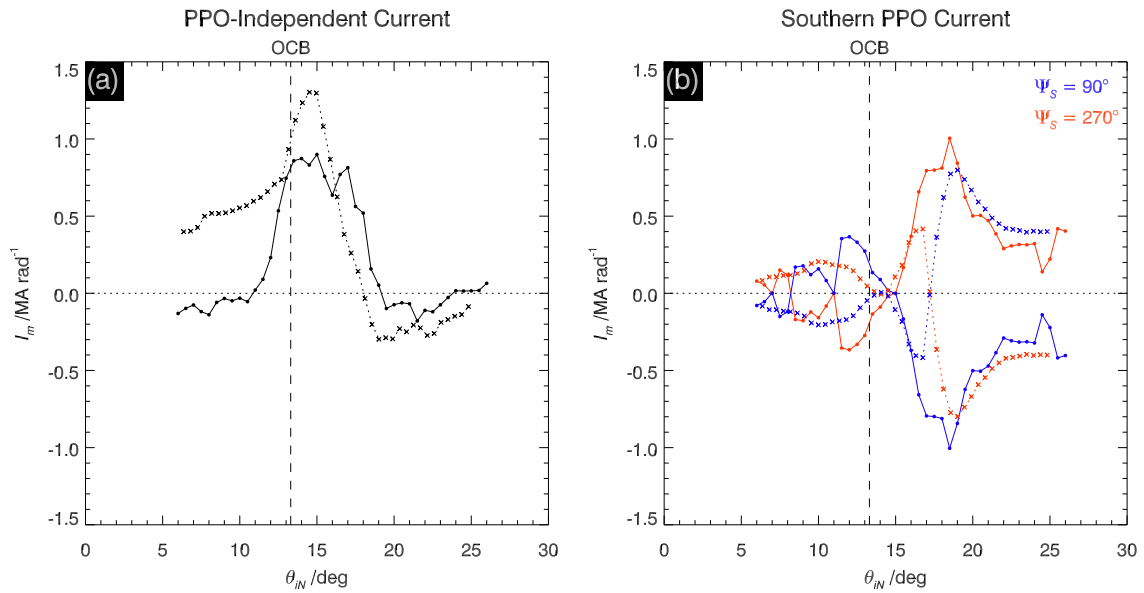


Figure 6.8: Comparison between northern ionospheric meridional current profiles and those mapped along model field lines from the southern hemisphere. Figure 6.8a shows the northern and southern PPO-independent current profiles, where the black circles and solid lines show the northern hemisphere profile from Figure 6.6a, while the black crosses and dotted lines show the mapped southern hemisphere profile, determined from southern hemisphere data for $\Psi_S = 0^\circ$ and 180° ($\pm 45^\circ$) irrespective of Ψ_N . Figure 6.8b compares the southern PPO-related current profile in the northern hemisphere, blue dots and solid lines for $\Psi_S = 90^\circ$ and red dots and solid lines for $\Psi_S = 270^\circ$, from Figure 6.6c, with the southern hemisphere southern PPO-related current profile mapped along field lines into the northern hemisphere, blue crosses and dotted lines for $\Psi_S = 90^\circ$ and red crosses and dotted lines for $\Psi_S = 270^\circ$. The vertical dashed lines in each panel show the position of the averaged northern OCB of *Jinks et al.* [2014].

duces a profile similar to Figure 4.7a in that chapter, and to the overall average shown here in Figure 6.2d. The southern profile is then mapped along model field lines into the northern hemisphere for purposes of direct comparison with the northern PPO-independent profile. For the same plasma subcorotation angular velocity on a given flux shell, and the same effective Pedersen conductivity, I_m is expected to be closely similar in the northern and southern hemispheres, such that a direct comparison is appropriate. It can be seen that in the region of closed lines ($\theta_{iN} > 13.3^\circ$), the profiles are very similar as expected, but with the current in the southern hemisphere peaking at somewhat larger values than in the north, indicative of a modestly higher Pedersen conductivity in the southern hemisphere than in the northern. At smaller colatitudes, however, generally on open field lines, the profiles are clearly different, with the mapped southern profile falling slowly to lower positive values, while the northern

profile falls sharply to near-zero and small negative values for colatitudes smaller than $\sim 11^\circ$. This difference likely reflects the seasonal difference in the polar ionospheric Pedersen conductivity between the north and south under pre-vernal equinox conditions, with the northern spin and magnetic axis tilted away from the Sun by between 8° and 4° over the data interval, combined, possibly, with consequent differences in the open field plasma angular velocity.

In Figure 6.8b we similarly compare the southern PPO-related current in the northern hemisphere for $\Psi_S = 90^\circ$ (blue circles and solid lines) and $\Psi_S = 270^\circ$ (red circles and solid lines) from Figure 6.6c, with the corresponding profiles mapped from the southern hemisphere for $\Psi_S = 90^\circ$ (blue crosses and dotted lines) and for $\Psi_S = 270^\circ$ (red crosses and dotted lines). The southern hemisphere southern PPO profile has been calculated here by similarly averaging the profiles for $\Psi_S = 90^\circ$ and $\Psi_S = 270^\circ$ (irrespective of Ψ_N), subtracting and dividing by two. It can be seen that the main PPO currents are comparable in magnitude in the two hemispheres, $\sim 1.25 \text{ MA rad}^{-1}$, but extend over a significantly larger colatitude range in the northern hemisphere, $\sim 12^\circ$ to $\sim 18.5^\circ$, than in the southern, $\sim 17^\circ$ to $\sim 19^\circ$ as mapped ($\sim 18.5^\circ$ to $\sim 21^\circ$ in the southern hemisphere itself). Equatorward of the main current region, however, the mapped southern profile shows a smaller and less steep decline with increasing colatitude, as mentioned above, such that the values in the southern hemisphere remain modestly larger than those in the northern hemisphere to the limit of the joint data available, consistent with the results in Figures 6.4f and 6.4d. These results thus indicate the presence of a somewhat more complex PPO-related current system in the outer part of the magnetosphere than those shown in Figure 2.13. In the poleward region, $\sim 5^\circ$ - 11° colatitude, the southern data show currents of consistently opposite sign to those at large colatitude, corresponding to the southern PPO polar oscillations in the south, while the northern data show only small variable values, again consistent with the absence of southern PPO oscillations in the northern polar region.

6.3.4 Latitude variation of the equatorial oscillations

The theoretical model of the PPO current system proposed by *Southwood and Kivelson* [2007] envisaged strict hemisphere-to-hemisphere field-aligned currents that would produce a perturbation field essentially symmetric about the magnetic equator. The current systems in Figure 2.13, following *Andrews et al.* [2010a,b] and *Southwood and Cowley* [2014], generalise that picture by admitting the closure of current across the field in the body of the magnetosphere, thereby transmitting a force to the plasma, which would result in the PPO field perturbations reducing in amplitude along field lines from the generating hemisphere. Our results in Figures 6.4b and 6.4f show northern system oscillations in the north and southern system oscillations in the south that are of comparable amplitude, while Figure 6.4h and 6.4d show northern oscillations in the south that are weaker by a factor of ~ 2.5 , and southern oscillations in the north that are weaker by a factor of ~ 1.2 . In this section we examine in detail the variation of the oscillation amplitudes with latitude along the equatorial field lines.

We focus on a flux shell located just equatorward of the region of PPO-related field-aligned currents for which we have good latitude coverage, specifically those mapping to the northern ionosphere between 20° and 26° colatitude (dotted lines in Figure 6.2a), and correspondingly to the southern ionosphere between 22.1° and 28.8° (dotted lines in Figure 6.2c), as employed previously in Figure 6.4. This flux shell is shown shaded gray in the meridian plane view in Figure 6.9, and extends between 3.8 and $6.6 R_S$ in the equatorial plane. The coloured lines show periapsis segments of the Cassini trajectory mapped into the meridian in cylindrical (ρ, z) coordinates, colour-coded as in previous figures, while the radial lines indicate lines of constant latitude $\pm 45^\circ$ about the equator. As indicated above, it can be seen that there is good coverage of the flux shell over this latitude range. We then divide the field data within the shell into overlapping latitude intervals that are 15° wide and step by 7.5° as shown, with centres located between $\pm 37.5^\circ$. We map the data in the flux shell from each latitude interval along the field lines into the northern ionosphere using equation (3.1), this to take account of the variation associated with the convergence of the field-aligned currents towards the planetary

59 60 61 62 63 64 65 66 67 68 69 70 72 73 74 75 76 77 78 79 80 81 82 83 85 86 87 88 90 91 92 93 94 95

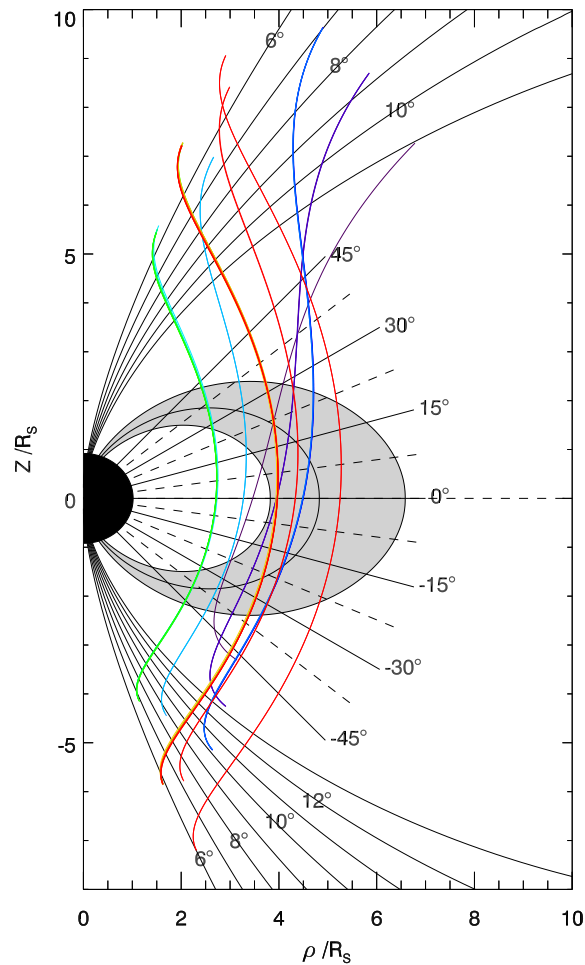


Figure 6.9: Plot of model magnetic field lines and the periapsis sections of the Cassini trajectories for Revs 59-95 mapped into a meridian plane in cylindrical (p, z) coordinates. The colour-coding of the trajectories is shown at the top of the plot and is the same as in previous figures. The gray shaded flux shell is that used to investigate the latitudinal variation of the field oscillations equatorward of the main field-aligned current region in section 6.3.4 with results shown in Figure 6.10, and maps from 20° to 26° colatitude in the northern ionosphere to 22.1° to 28.8° in the southern. The radial lines show the overlapping 15° intervals of latitude λ (deg) used in this study, centred between $\pm 37.5^\circ$. In the polar regions model field lines are shown plotted at 1° intervals of ionospheric colatitude between 6° and 11° in the northern hemisphere, and 6° and 13° in the southern. Data in overlapping 2° colatitude intervals are used in section 6.3.4 to investigate the polar oscillations, with results shown in Figure 6.11.

poles. With regard to the related results shown in Figure 6.4, fitted to one oscillation at a time, we note that mapping a field value into the northern ionosphere rather than the southern, as for the southern data in Figure 6.4e-6.4h, increases its value by $\sim 10\%$, due to the stronger planetary field in the north than in the south. Here we fit these mapped

data to the two-oscillation function

$$B'_{\varphi i} = \langle B_{\varphi i} \rangle + B_{\varphi i0N} \sin(\Phi_N(t) - \varphi - \Delta\Phi_N) + B_{\varphi i0S} \sin(\Phi_S(t) - \varphi - \Delta\Phi_S), \quad (6.2)$$

where $\langle B_{\varphi i} \rangle$ is a constant term, $B_{\varphi i0N,S}$ are the northern and southern system oscillation amplitudes, $\Phi_{N,S}(t)$ are the corresponding phases, specifically those of *Andrews et al.* [2012], φ is the azimuth of the spacecraft measured from noon in the sense of planetary rotation, and $\Delta\Phi_{N,S}$ are possible phase offsets from the *Andrews et al.* [2012] model, as in Figure 6.4 and previously in Chapter 4. The results in Figures 6.4b and 6.4f suggest, for example, that appropriate offsets may be $\Delta\Phi_N \approx -30^\circ$ and $\Delta\Phi_S \approx +15^\circ$.

The basis of the fitting method is as follows. For a given latitude data set we first fix the pair of phase offsets $\Delta\Phi_{N,S}$ at likely values, and then search for the values of the three parameters within a data cube, $\langle B_{\varphi i} \rangle$ in steps of 2.5 nT, and $B_{\varphi i0N,S}$ in steps of 1 nT, that give the minimum RMS deviation between the data and the model in equation (6.2). We then vary the values of $\Delta\Phi_{N,S}$ in steps of 5° to find the values that give the smallest overall RMS deviation over the whole data set. These values were found to be $\Delta\Phi_N = -30^\circ$ and $\Delta\Phi_S = +10^\circ$, which were used throughout in the determination of the other three parameters, yielding the results shown in Figure 6.10. Figure 6.10a shows the latitude profile of the RMS deviation between the data and the model, Figure 6.10b the mean value $\langle B_{\varphi i} \rangle$ in equation (6.2), Figure 6.10c the amplitude of the northern system oscillation $B_{\varphi i0N}$ (blue) and southern system oscillation $B_{\varphi i0S}$ (red), and Figure 6.10d the amplitude ratio $k = B_{\varphi i0N}/B_{\varphi i0S}$, where the vertical scale is linear in k from 0 to 1 in the lower half of the figure and linear in $1/k = k'$ between 1 and 0 in the upper half, thereby covering all possible values of k from zero to infinity. As in Figure 6.4, the uncertainty in each parameter was determined by implementation of the jackknife statistical resampling method, described in section 6.3.1, in which one contributing Rev is removed at a time, with the uncertainty being determined from the modified standard deviation of the set of fitted parameters. These uncertainties have also been verified for several latitude intervals by the more intensive bootstrap resampling method. We note that the RMS deviation values in Figure 6.10a are generally smaller than those in Figure 6.4 when fitting to a single oscillation function, thus indicating that the combination

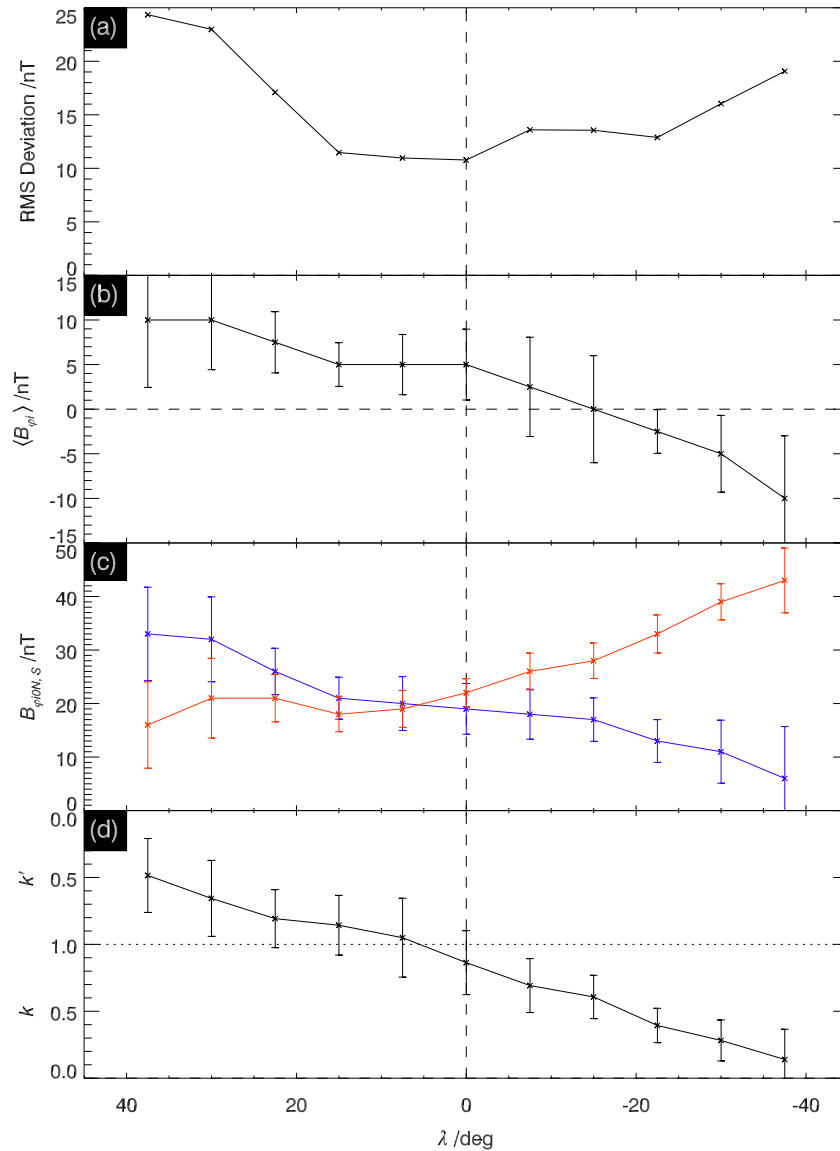


Figure 6.10: Plots showing the latitude variation of oscillation parameters in the flux shell shown gray in Figure 6.9. These were determined from fits of equation (6.2) to the northern-mapped azimuthal field data in overlapping 15° intervals of latitude centred between $\pm 37.5^\circ$ (see Figure 6.9), using $\Delta\Phi_N = -30^\circ$ and $\Delta\Phi_S = +10^\circ$. Figure 6.10a shows the minimum RMS deviation (nT) corresponding to the best fit parameters shown, Figure 6.10b the mean value $\langle B_{\phi i} \rangle$ (nT), Figure 6.10c the amplitudes of the northern (blue) and southern (red) PPO oscillations $B_{\phi i 0 N, S}$, and Figure 6.10d the north/south amplitude ratio $k = B_{\phi i 0 N} / B_{\phi i 0 S}$, the vertical scale being linear in k from 0 to 1 in the lower half and linear in $1/k = k'$ between 1 and 0 in the upper half. The uncertainties in the fitted parameters have been determined using the jackknife statistical resampling method described in section 6.3.1. The vertical dashed line indicates the equator.

of two oscillations in equation (6.2) provides a better overall fit to the data.

Figure 6.10c shows that the mapped northern system amplitude peaks at ~ 33 nT at the highest northern latitude examined, centred at $+37.5^\circ$, and then decreases mono-

tonically with decreasing latitude to ~ 6 nT at -37.5° , consistent with zero within uncertainties. This behaviour is consistent with the values determined from the single-oscillation analyses in Figures 6.4b and 6.4h. Likewise, the southern system amplitude peaks at the larger value of ~ 43 nT at the highest southern latitude examined, centred at -37.5° , decreases monotonically with increasing latitude to ~ 22 nT near the equator, and then remains nearly constant within the uncertainties at ~ 20 nT in the northern hemisphere. This behaviour is also consistent with the values determined from the single-oscillation analyses in Figures 6.4f and 6.4d. Overall, the southern oscillations are seen to dominate the northern at high southern latitudes, fall to comparable values to the northern just north of the equator, and then remain modestly smaller than the northern oscillations throughout the northern hemisphere. This is shown explicitly in Figure 6.10d, where the amplitude ratio k falls near-linearly (using the scales shown) from $k' = 0.5$ at the northernmost latitudes examined (i.e., $k = 2$), to near zero in the southernmost. These results show that the PPO-related field-aligned currents close cross-field in the magnetospheric plasma, nearly wholly for the northern system in the interval studied here, and at least partially for the southern system, mainly in the southern hemisphere in that case.

Figure 6.10b also shows that the mean azimuthal field $\langle B_{\phi i} \rangle$ has small and positive values in the northern hemisphere, consistent with the results in Figures 6.4b and 6.4d, falling to small negative values south of the equator, consistent with results in Figures 6.4f and 6.4h (and with Chapter 4). These perturbations form an otherwise unexpected weak “leading” field configuration, located well equatorward of the main ‘lagging’ field region that terminates near $\sim 19^\circ$ northern colatitude (Figure 6.6a), mapping to $\sim 7.6 R_S$ in the equatorial plane. Previously, in Chapter 4 it was suggested that this field could be due to a phase asymmetry in the PPO field perturbations, that makes the negative half cycle of the southern system B_ϕ oscillation slightly larger in amplitude than the positive half cycle, associated with a latitudinal motion of the southern system currents to higher latitudes and outward displacement in the equatorial plane in the downward current sector at $\Psi_S = 90^\circ$ (positive equatorial B_ϕ), and to lower latitudes and inward

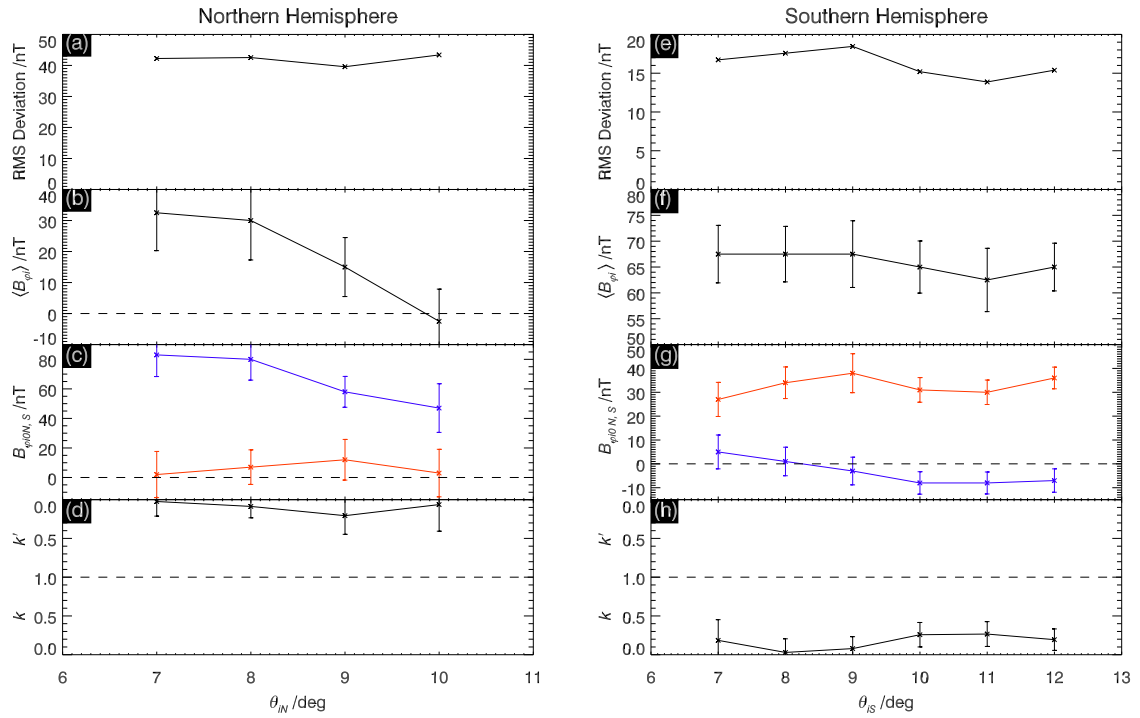


Figure 6.11: Plots in the same format as Figure 6.10 showing the best two-oscillation fits to equation (6.2) for mapped polar azimuthal field data in overlapping 2° intervals of northern (left) and southern (right) ionospheric colatitudes, the field data being mapped to the corresponding ionosphere. The phase offsets employed were $\Delta\Phi_N = 0^\circ$ and $\Delta\Phi_S = 0^\circ$ in the northern hemisphere, and $\Delta\Phi_N = 0^\circ$ and $\Delta\Phi_S = 55^\circ$ in the southern, though we also allow the amplitude of the oscillation from the ‘opposite’ hemisphere to take negative values thus allowing for a possible 180° phase change in the polar region. As in Figure 6.10, the uncertainties have been estimated by an implementation of the jackknife method.

displacement in the equatorial plane in the upward current sector at $\Psi_S = 270^\circ$ (negative equatorial B_ϕ). The same effect would produce the opposite asymmetry for the northern system, associated with a latitudinal motion of the northern system currents to lower latitudes and inward displacement in the equatorial plane in the upward current sector at $\Psi_N = 90^\circ$ (positive equatorial B_ϕ), and to higher latitudes and outward displacement in the equatorial plane in the downward current sector at $\Psi_N = 270^\circ$ (negative equatorial B_ϕ). A dominant northern system in the northern hemisphere and southern system in the southern hemisphere would then produce a reversal in sense of the mean azimuthal field across the equator as found, though we note that the reversal in the amplitude ratio occurs north of the equator while the reversal in the mean azimuthal field occurs to its south.

We now undertake a similar two-oscillation analysis of the mapped polar azimuthal field data, noting that no oscillations from “opposite” hemispheres were detected in the analyses shown in Figure 6.4, nor in previous related studies within a $\sim 10\%$ observational limit by amplitude [e.g., *Andrews et al.* [2012]]. In this case we employ data observed within overlapping 2° bins of ionospheric colatitude, centred between 7° and 10° in the northern hemisphere and 7° and 12° in the southern (see also Figure 6.2), whose corresponding polar flux shells and traversing Cassini Revs are also shown in Figure 6.9. Results are shown in Figures 6.11a-6.11d and 6.11e-6.11h for the northern and southern polar regions, respectively, in a similar format to Figure 6.10, showing from top to bottom the RMS deviation of the fits to equation (6.2), the mean values $\langle B_{\phi i} \rangle$, the northern (blue) and southern (red) amplitudes $B_{\phi i 0 N, S}$, and the modulus of the amplitude ratios (north/south). For the northern data we determined a best-fit northern phase offset of $\Delta\Phi_N = 0^\circ$ consistent with Figure 6.4b, while for the southern data the best-fit offset was found to be $\Delta\Phi_S = 55^\circ$, consistent with Figure 6.4e ($\sim 51^\circ$) and Chapter 4 ($\sim 47^\circ$). In both cases, however, we have no a priori knowledge of the corresponding phase offset for oscillations from the opposite hemisphere, so we have simply set these phase offsets to zero, but allow the fitted amplitude to have either a positive or negative sign (the latter equivalent to taking a phase offset of 180°), on the basis that we do not know whether such oscillations might be essentially in phase or in antiphase with those at lower latitudes. The key results are shown in Figures 6.11c and 6.11g, where we see that the amplitudes from the “opposite” hemisphere are essentially consistent with zero throughout, even switching sign from positive to negative with increasing colatitude in the southern hemisphere. The modulus amplitude ratios are $k' = (1/k) \approx 0-0.2$ in the northern hemisphere in Figure 6.11d, and $k \approx 0-0.3$ in the southern hemisphere in Figure 6.11h, generally consistent with zero. The other parameters in Figure 6.11 are in line with expectation based on Figures 6.2 and 6.4, where in particular we note that the RMS deviations in the northern data in Figure 6.11a are essentially the same as in the single-oscillation analysis in Figure 6.4a, while that in the northern data in Figure 6.11e is essentially the same as that in Figure 6.4e. Inclusion

of a second period thus makes little difference to the degree of model fit to the data in these cases, unlike the equatorial case shown in Figure 6.10.

6.3.5 PPO-independent current system and plasma subcorotation

We now consider the northern PPO-independent current profile and its relation to the subcorotation of magnetospheric plasma, discussed in Chapter 2. Following the analysis for the southern hemisphere presented in Chapter 5 and section 5.2.1, here we apply the same equations to the northern hemisphere and mapped southern current. The ionospheric meridional Pedersen current associated with near-axisymmetric subcorotation of the magnetospheric plasma is given by (see *Cowley et al.* [2008] and references within) equation (5.2).

Figure 6.12a shows the northern PPO-independent current profile in Figure 6.6a and 6.8a (black dots and solid lines) together with the profile expected for a fixed value of Σ_p^* (red) combined with the empirical plasma angular velocity profile in Figure 6.12b. We also show (black crosses and dotted lines) the corresponding profile mapped from the southern hemisphere from Figure 6.8a. The value of Σ_p^* has been somewhat arbitrarily set at 0.6 mho, such that the theoretical profile agrees with observed values in the poleward part of the main current region. The normalised empirical angular velocity profile in Figure 6.12b (red) is the same as that in Chapter 5, but now mapped along field lines into the northern hemisphere. It is based on magnetospheric ion velocities determined by *Wilson et al.* [2009] and *Thomsen et al.* [2014] (black dashed lines and stars, respectively), ion and electron plasma injection dispersion signatures analyzed by *Müller et al.* [2010] (green dashed line), the rotation of plasma ‘blobs’ determined by *Carbary and Mitchell* [2014], further ion measurements in the outer nightside magnetosphere discussed by *Thomsen et al.* [2014], and the theoretical model of *Cowley et al.* [2004a] at polar latitudes where we take the constant value $\omega/\Omega_S = 0.3$ (see Chapter 5 and section 5.2.1 for further discussion). The dotted line at $\omega/\Omega_S = 1$ represents rigid plasma corotation, where Ω_S is taken to correspond to the IAU System III rotation period of 10.65622 h based on a slightly modified version of the principal period

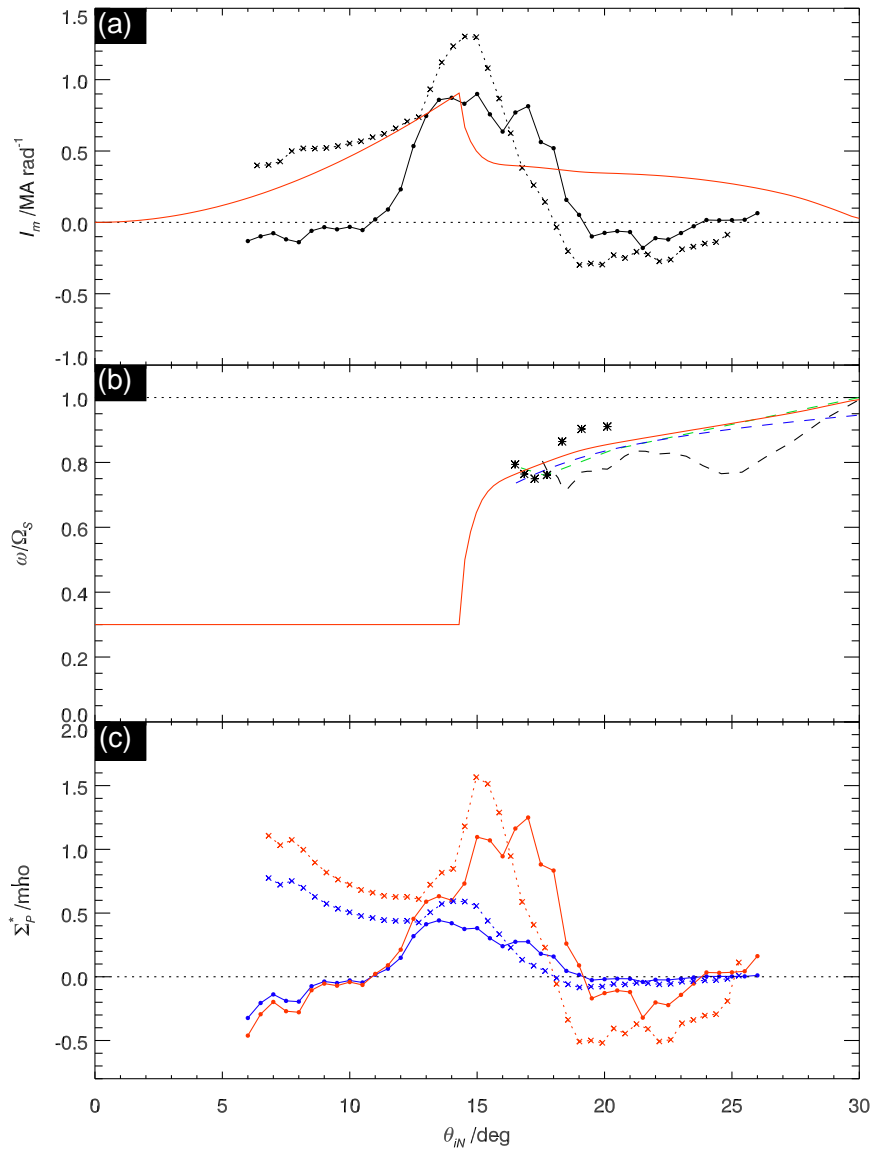


Figure 6.12: See overleaf.

determined from Voyager SKR data by *Desch and Kaiser* [1981].

Given this angular velocity profile, the consequent red current profile in Figure 6.12a derived from equation (5.2) with fixed conductivity indicates distributed downward currents over the polar region, a layer of strong upward current at the OCB where the angular velocity of the plasma suddenly increases, followed by a more distributed region of weaker upward current at larger colatitudes, similar to the theoretical models of *Cowley and Bunce* [2003] and *Cowley et al.* [2004a,b] derived on an essentially equivalent basis. Comparison with the observed northern current profile in Figure 6.12a suggests, however, that variations of the effective Pedersen conductivity in the north-

ern ionosphere must also play an important role, with conductivities much smaller than 0.6 mho at polar latitudes ($\sim 5^\circ$ - 11°), and equatorward of the main current region (beyond $\sim 19^\circ$), where no counterpart of the theoretical weaker secondary region of upward current is present in the data. Larger conductivities are implied, however, in the equatorward part of the main current region ($\sim 15^\circ$ - 18°). Comparison with the southern profile indicates similar features in the equatorward region, but much better agreement with the form of the theoretical profile at polar latitudes.

We use equation (5.5), as shown in Chapter 5, to estimate Σ_p^* from the observed current profiles and the empirical angular velocity model. Results derived from the northern current data using the empirical angular velocity profile are shown in Figure 6.12c by the red dots and solid line, while the blue dots and solid line shows the minimum possible Σ_p^* value obtained by putting $\omega/\Omega_S = 0$ in equation (5.5) (assuming negative values do not occur). The equivalent profiles obtained from the southern data are shown by the red and blue crosses joined by dotted lines, mapped along field lines into the northern hemisphere for comparison. It can be seen that the inferred conductivities in the main current region at $\sim 14^\circ$ to $\sim 18^\circ$ colatitude peak at similar values ~ 1.2

Figure 6.12: Plots showing northern colatitude profiles of the PPO-independent ionospheric meridional current, plasma angular velocity, and effective Pedersen conductivity. In Figure 6.12a the black circles joined by solid lines and the crosses joined by dotted lines show the northern and mapped southern PPO-independent meridional current profiles (MA rad^{-1}), respectively, as in Figure 6.8a. The red line shows a theoretical meridional current profile derived using equation 5.2 and the empirical plasma angular velocity profile shown in Figure 6.12b (red line), assuming a fixed effective Pedersen conductivity of 0.6 mho. For details of the sources employed to construct the empirical angular velocity profile see the text in section 6.3.5. The plasma angular velocity is shown normalised to Saturn's angular velocity Ω_S , taken to correspond to the IAU System III rotation period, such that the horizontal dotted line at unity represents rigid corotation of the plasma. In Figure 6.12c the red circles joined by solid lines show a colatitude profile of the effective Pedersen conductivity of the northern ionosphere (mho), calculated from the northern meridional current profile in Figure 6.12a using equation 5.5 together with the angular velocity profile in Figure 6.12b, while the blue circles and solid lines show minimum conductivity values obtained by putting $\omega/\Omega_S = 0$ into this equation. The red and blue crosses and dotted lines show the corresponding southern conductivity profiles similarly calculated using the mapped southern meridional current profile in Figure 6.12a.

mho in the north and ~ 1.6 mho in the south, which, as in Chapter 5, we presume is due to precipitation of auroral electrons in the region generally containing upward field-aligned currents. We note that this region generally corresponds to the outer region of hot magnetospheric electrons in ELS data (Figure 6.3). In the equatorward region, however, where the inferred ionospheric current falls to small (and negative) values despite the well-documented occurrence of significant plasma subcorotation, the implication is that the effective conductivity of the ionosphere becomes at least an order of magnitude smaller, though of course the negative values derived from the current profile here are not physically meaningful.

Similarly on open field lines poleward of $\sim 13^\circ$ - 14° colatitude, the currents and hence the inferred conductivity also fall to small (and negative) values poleward of $\sim 11^\circ$, again suggestive of conductivities at least an order of magnitude smaller than in the main current region, unlike those inferred in the southern hemisphere. Since the ELS electron data (see Figure 6.3) indicate the lack of hot electrons in these regions in the majority of the data set, this is likely connected with the pre-vernal equinox conditions prevailing in the interval, during which Saturn's northern spin axis was tilted by between $\sim 8^\circ$ and $\sim 4^\circ$ away from the Sun. The northern ionosphere at smaller colatitudes was thus in permanent darkness, but subject to increasing episodes of daily insolation at larger colatitudes. As in Chapter 5 section 5.2.1, these results show that the latitudinal variations in the effective Pedersen conductivity of the ionosphere are equally or even more important in defining the structure of the PPO-independent field-aligned current system as the changes in angular velocity of the equatorial magnetospheric plasma.

6.4 Summary and conclusions

In this chapter we have provided a first detailed analysis of the PPO-dependence of field-aligned currents in Saturn's northern hemisphere. In doing this it was found the northern hemisphere field-aligned currents are not only modulated by the northern PPO system, but also near equally by the southern PPO system. We separate the current

into components that do and do not depend on the PPO phase by using the symmetries involved. This provides the first direct observational evidence for the PPO-related inter-hemispheric currents proposed theoretically by *Southwood and Kivelson* [2007] and later refined by *Southwood and Cowley* [2014]. As a consequence, while the current structures in the north are clearly similar to those in the south, they have much less regularity in form than the usually well-ordered four-sheet structures observed in the south. As a result the analysis performed in Chapter 5 was not possible here. Our principal results are summarised below.

1. The meridional current profile of the northern PPO-independent system (positive equatorward) is found to have small (and negative) values at highest polar latitudes, but increases sharply between $\sim 11^\circ$ and $\sim 13.5^\circ$ northern colatitude on open field lines (the mean OCB in the north lies at $\sim 13.3^\circ$ according to *Jinks et al.* [2014]). Implying a downward current flow of $\sim 1 \text{ MA rad}^{-1}$ in this region, with a corresponding current density of $\sim 25 \text{ nA m}^{-2}$. Assuming axisymmetry, the peak total equatorward current flow in this system is thus $\sim 6 \text{ MA}$. The meridional current then falls towards small (and negative) values between $\sim 17^\circ$ and $\sim 19^\circ$, implying an essentially equal and opposite upward current flow of $\sim 1 \text{ MA rad}^{-1}$ in this region, with a corresponding ionospheric current density also of $\sim 25 \text{ nA m}^{-2}$. The latter current maps between ~ 7.5 and $\sim 11 R_S$ in the equatorial magnetosphere, spanning the inner part of the main hot plasma region. This is similar to the PPO-independent current system in the south, though the peak meridional current values are somewhat larger in the south, and fall off much more slowly with decreasing colatitude in the polar region, extending over the whole polar region observed in that case. This difference likely results from the pre-equinox conditions prevailing at the time of these measurements, with the northern polar axis tilted between $\sim 4^\circ$ and $\sim 8^\circ$ away from the Sun.
2. Combining the PPO-independent meridional current profile with an empirical plasma angular velocity profile suggests that the effective height-integrated ionospheric Pedersen conductivity of the ionosphere is $\sim 0.1 \text{ mho}$ or less in the

poleward-most region of low current flow. While increasing to ~ 0.6 mho in the outer open field region where significant currents are first observed ($\sim 11^\circ$ - 13.5° colatitude). The conductivity then increases further on closed field lines, peaking at ~ 1.2 mho at $\sim 17^\circ$ colatitude, before falling sharply back to small values ~ 0.1 mho or less at $\sim 19^\circ$ equatorward of the main current region. These results again indicate that, as in the south, the variations of the PPO-independent meridional current, and hence of the field-aligned currents, are as strongly influenced by variations in the ionospheric conductivity as by the variations in plasma angular velocity.

3. The northern PPO-related field-aligned current consists of a main layer of either upward (for PPO phase $\Psi_N \approx 90^\circ$) or downward (for $\Psi_N \approx 270^\circ$) current, of peak magnitude ~ 1.5 MA rad^{-1} , flowing between $\sim 12^\circ$ and $\sim 18^\circ$ northern colatitude, essentially co-located with the region of PPO-independent current. The total current flowing in the system, equal and opposite in the two 'halves' of the cycle, is thus ~ 3.5 MA, directly comparable to the current flowing in the PPO-independent system in the same region. The associated ionospheric current density is ~ 20 nA m^{-2} . A second current layer of opposite polarity is located immediately equatorward of the main layer, between $\sim 18^\circ$ and $\sim 21.5^\circ$, which carries ~ 1 MA rad^{-1} (with a total half-cycle current of ~ 2 MA), which strongly reduces the magnitude of the PPO-related currents and fields at larger colatitudes. This current has an ionospheric density of ~ 15 nA m^{-2} , and maps between ~ 6 and $\sim 9 R_S$ in the equatorial plane.
4. The main southern PPO-related field-aligned current is essentially co-located with the northern PPO-related current between $\sim 11.5^\circ$ and $\sim 18.5^\circ$ northern colatitude, and hence with the PPO-independent current, directed upward (for PPO phase $\Psi_S \approx 90^\circ$) or downward (for $\Psi_S \approx 270^\circ$), with peak magnitude ~ 1.25 MA rad^{-1} . The total current flowing in a half-cycle is thus ~ 3 MA, with a corresponding current density of ~ 15 nA m^{-2} . A current of opposite polarity and magnitude ~ 0.35 MA rad^{-1} flows at the poleward border of this system at $\sim 11.5^\circ$, with a

half-cycle current of ~ 0.75 MA, that switches off the southern system perturbations in the north polar region. A larger current of opposite polarity and peak magnitude ~ 0.75 MA rad^{-1} also flows in the region immediately equatorward between $\sim 18.5^\circ$ and $\sim 22^\circ$, again reducing the magnitude of the perturbations at lower latitudes. The half-cycle total current is thus ~ 1.5 MA, with an associated ionospheric current density of ~ 10 nA m^{-2} . Comparison of the southern system field-aligned currents flowing in the northern and southern ionosphere shows that the main PPO currents are of comparable magnitude, ~ 1.25 MA rad^{-1} as above, though spread further poleward in the north than the south, but that the equatorward secondary currents are smaller in the south than the north by a factor of almost two, such that the southern oscillations in the interior region at lower latitudes are stronger in the south than in the north. This finding indicates that the PPO currents involve somewhat more complexity than present theoretical pictures would suggest.

5. Investigation of the latitude dependence of the oscillations observed interior to the main field-aligned current layers, on flux tubes mapping into the northern ionosphere between 20° and 26° , and correspondingly into the southern hemisphere between 22.1° and 28.8° (3.8 to $6.6 R_S$ in the equatorial plane), shows that the northern oscillations fall in amplitude gradually but continuously from the highest northern latitudes observed ($\sim 40^\circ$) to near-zero at corresponding latitudes in the south. The southern oscillations are thus dominant at such high southern latitudes, but also fall with increasing latitude to become comparable with the northern oscillations in the equatorial region, and modestly lower than the northern oscillations at higher northern latitudes (consistent with point 5 above). These variations show that the associated field-aligned currents gradually reduce in magnitude with distance along field lines from the corresponding hemisphere, feeding cross-field currents that flow in the magnetosphere.
6. A related investigation of the polar oscillations confirms the absence of field perturbations associated with the opposite hemisphere found in previous studies

[e.g., *Andrews et al.*, 2012], to within a $\sim 10\%$ observational limit by amplitude. It was also found that the northern polar oscillations lag in phase by $\sim 30^\circ$ compared with the northern oscillations equatorward of the field-aligned current layers, similar to the $\sim 50^\circ$ polar lag for the southern oscillations found previously in Chapter 4. The PPO phases generated by *Andrews et al.* [2012] correspond most closely to those of the equatorial oscillations for the southern system, but to the polar oscillations of the northern system.

In the following chapter there is a summary of the key results presented within this thesis and the future direction and work regarding Saturn's field-aligned currents and periodicities.

Chapter 7

Summary and conclusions

In this chapter we summarise the new results presented within this thesis, as well as the overall conclusions. Following this we discuss some key remaining questions and the future direction of field-aligned current studies within Saturn's magnetosphere.

In Chapter 4 it was shown for the first time that the southern hemisphere night-side field-aligned currents are strongly modulated in form, magnitude, and position by the southern PPO phase. This gives rise to the differing field-aligned current signature types discussed in Chapter 2. Through a statistical study, and by exploiting the expected opposite symmetry of the two main field-aligned current systems, they were approximately separated into the PPO-independent and PPO-related components. The PPO-independent current consists of a distributed downward current over the polar region, followed by an enhanced downward current at the boundary between open and closed field lines. Following this the adjacent upward current then closes these currents. This form is similar to expectations based on the model presented by *Cowley et al.* [2004a,b, 2008]. The PPO-related current system is formed of a main downward current around $\Psi_S \approx 90^\circ$ and an upward current around $\Psi_S \approx 270^\circ$. These were shown to be similar in strength and approximately co-located with the upward current of the PPO-independent system. Thus the total observed current doubles when the PPO-related current is directed upward, while when the PPO-related current is directed downward the PPO-independent current is effectively cancelled out.

The statistical analysis presented in Chapter 4 leads to a smoothing of the individ-

ual current sheets. Chapter 5 therefore focused on the individual current sheets by examining their boundaries. As expected from the results of Chapter 4, the boundary positions and current strengths were shown to be dependant on the southern PPO phase. Employing fits to these boundary properties against Ψ_S , four current sheet profiles were determined and shown to agree with the statistical results of Chapter 4. Overall, the whole current region is modulated in southern colatitude during the PPO cycle with amplitude $\sim 1^\circ$, with the maximum displacement from the pole at $\Psi_S \approx 270^\circ$. By considering the related plasma and atmospheric flows it was shown that this oscillation arises from the PPOs being driven outwards from the atmosphere, and not downwards from the magnetosphere. The colatitudinal profiles of the PPO-independent current showed that latitudinal variations in the effective Pedersen conductivity of the ionosphere were at least as important as the variations in the plasma angular velocity within the magnetosphere in determining the overall large-scale structure of the current system. We also found that there is a phase drift across the current region of $\sim 13^\circ$ per degree of colatitude, which is indicative of poleward phase propagation. In the equatorial plane this maps to a radial phase gradient of $\sim 5^\circ$ per Saturn radius.

Finally, in Chapter 6 the first detailed analysis of the PPO-dependence of field-aligned current in Saturn's nightside northern hemisphere was performed. During the 2008 epoch the field-aligned currents in the northern hemisphere were modulated in form and magnitude by both the northern PPO system and in the closed field region by the southern PPO system as well. This provides the first direct observational evidence for the PPO-related interhemispheric currents first proposed by *Southwood and Kivelson* [2007]. Consequently, the current structures, while similar to the those observed in the southern hemisphere, were much more variable than in the south, such that the four sheet analysis was ineffective. However, as in Chapters 4 the PPO-independent and PPO-related currents were statistically separated. The northern PPO-independent current is similar to the southern case, though in the south the peak meridional current was higher and the fall-off to smaller current values was much slower with decreasing colatitude towards the pole. These differences are likely to be due to the

pre-equinox interval, which results in more of the northern polar region remaining in darkness compared with the southern polar region. As in Chapter 5, the meridional northern PPO-independent current was combined with an angular velocity profile to estimate the effective height-integrated ionospheric Pedersen conductivity, and again it was found that this is as important as the angular velocity profile in defining the structure of the PPO-independent current. In addition the Pedersen conductivities highlighted the seasonal difference between northern and southern polar regions, with lower values in the northern polar region. For the PPO-related currents the main sheets of current were observed at around the expected phases for the systems in the northern hemisphere, upward current around $\Psi_{N,S} \approx 90^\circ$ and downward current around $\Psi_{N,S} \approx 270^\circ$. However, there was an additional oppositely directed current on the equatorward edge of these main current sheets which reduces the magnitude of the field perturbations in the interior region. This finding indicates that the PPO currents involve somewhat more complexity than the present theoretical pictures shown in Chapter 2. Lastly, the amplitudes of the northern and southern oscillations were investigated along a flux tube interior to the field-aligned currents. This revealed that the southern oscillations were present at a modest strength relative to the northern oscillation up to the field-aligned current region in the northern hemisphere, while the northern oscillations were not present in the same region in the southern hemisphere. As in previous studies the oscillations in the polar region (open field lines) were hemispherically pure to within $\sim 10\%$ by amplitude.

These results show that for the pre-equinox interval investigated here, while the field-aligned currents in the southern hemisphere are dominantly modulated by the southern PPO system, both northern and southern systems modulate the northern currents, with the effect of the southern currents being only modestly smaller than those of the northern. Presumably this is a seasonal effect and will reverse in the northern summer. Future investigations are needed to extend the work presented in this thesis to other local times and Saturn seasons as provided by the 2006/07 and 2013 datasets. While the work present in this thesis provides a considerable advancement in

our present understanding of Saturn's field-aligned currents, there are still many unanswered questions involving them and Saturn's periodicities. What seasonal and local time variations do the field-aligned current undergo? How do these variations relate to long-time scale changes in the periodicities observed in Saturn's magnetosphere? Are there flows in the upper atmosphere which can drive the PPO-related currents? What form and position are the inner PPO field-aligned currents? Hopefully, some of these questions can be answered in the coming few years.

Presently, the Cassini spacecraft is generally in good working order. It is returning once more to high latitudes in preparation for the end of the mission in September 2017, which will see two sets of orbits known as the 'F-ring' and 'Proximal' orbits. Firstly, the F-ring orbits will quickly pass through the field-aligned current regions, providing additional local times and hemispheric season coverage. Following these Cassini will, for the first time, pass through the ring plane inside the D ring multiple times, before entering Saturn's atmosphere and ending the mission. These latter orbits will give the unique chance to determine Saturn's internal field to a higher order in the search for Saturn's rotational period. The results contained in this thesis will prove an important reference point for the assessment of these unique observations that will be made during Cassini's Grand Finale mission in 2016-17.

Appendix A

Magnetospheric contribution to observed azimuthal fields

As indicated in section 3.2, the total azimuthal magnetic field observed by Cassini on the orbits illustrated in Figure 4.1 consists of a spatially structured contribution from field-aligned currents associated with magnetosphere-ionosphere coupling, together with weaker more slowly-varying fields produced by more distant magnetospheric currents, specifically by the magnetopause-tail current system that bends field lines out of meridian planes from the dayside towards the tail. Here we have used the paraboloid model of Saturn's magnetosphere to estimate and subtract the latter contribution.

An example is shown in Figure A.1 for Rev 60, the orbit of which is shown by the blue line in Figure 4.1. Here the azimuthal field as measured is shown by the black line, plotted versus time over the periapsis interval from the point at which the mapped footprint of the spacecraft in the ionosphere attains its smallest co-latitude in the northern hemisphere inbound ($\sim 9^\circ$) to when it attains its smallest co-latitude in the southern hemisphere (with respect to the southern pole) outbound ($\sim 13^\circ$). The first vertical dashed line from the left marks the equatorial crossing as indicated, the second the time at which the spacecraft achieved the largest mapped co-latitude in the northern and southern ionosphere when the trajectory is tangent to the model field lines ($\sim 26^\circ$ in the north and $\sim 29^\circ$ in the south), while the third dashed line shows periapsis (~ 3.7

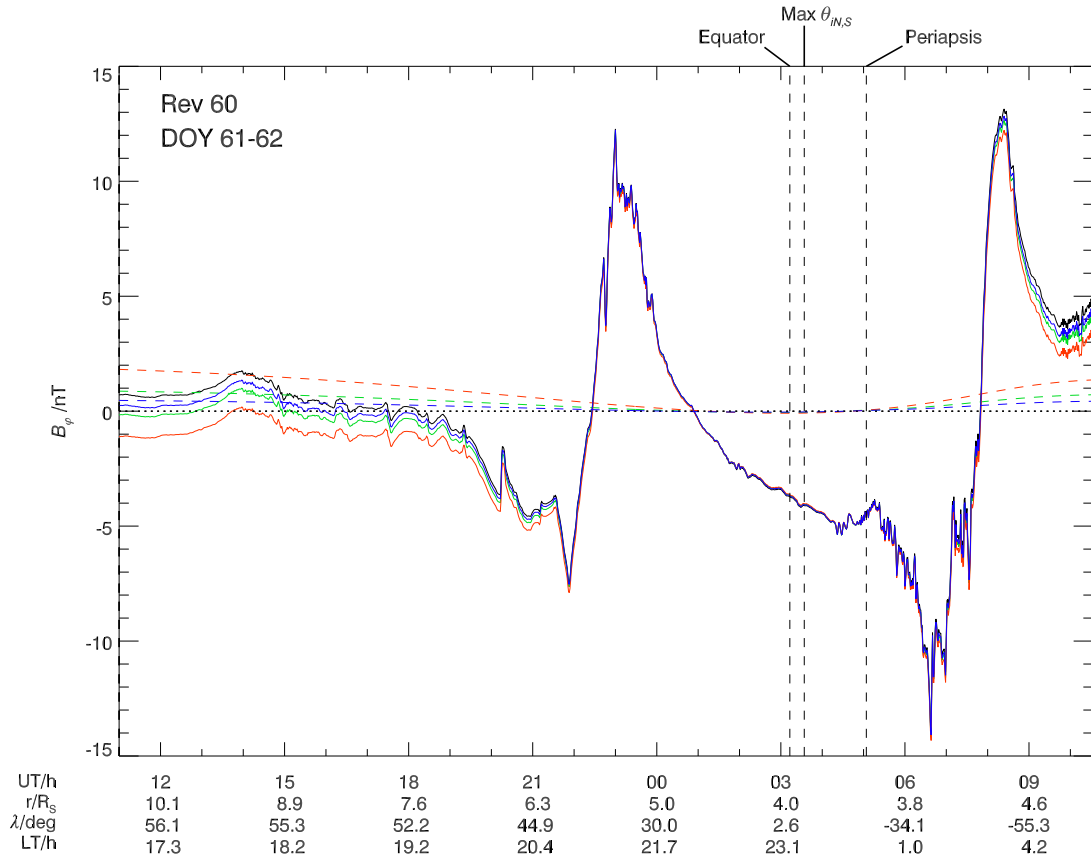


Figure A.1: Plot showing the azimuthal component of the magnetic field measured by Cassini during the periapsis pass of Rev 60 (blue trajectory in Figure 4.1), shown from the point where the mapped position of the spacecraft in Saturn’s ionosphere attains its smallest co-latitude with respect to the northern pole ($\sim 9^\circ$), to where it attains its smallest co-latitude with respect to the southern pole ($\sim 13^\circ$). The data at the bottom of the figure show the UT time (hours) on DoY 61-62 of 2008, and the radial distance (R_S), latitude (deg), and LT (hour) of the spacecraft. From left to right, the vertical dashed lines mark the crossing of the planet’s equator, the time when it achieves the maximum co-latitude with respect to the northern and southern poles ($\sim 26^\circ$ and $\sim 29^\circ$, respectively), and periapsis at $\sim 3.7 R_S$. Colored dashed lines show model fields from external magnetospheric sources, specifically the magnetopause-tail current system, computed using the Saturn paraboloid model corresponding to magnetospheric compressed (red), intermediate (green), and expanded (blue) cases (see Appendix A for details). The black solid line shows the azimuthal field as measured, while the blue, green, and red lines show the values with the model field subtracted. The values used in this study are those of the green line, corresponding to the intermediate model case.

R_S). The strong structured azimuthal fields observed on either side of the equator as the spacecraft passed through the northern and southern auroral regions are evident, peaking at positive and negative values of order ~ 10 nT.

The colored dashed lines show the azimuthal magnetic field due to outer magnetospheric sources, estimated using three variants of the Saturn paraboloid model. These

refer to differing states of compression of the magnetosphere by the solar wind, with the red line corresponding to compressed conditions with a subsolar magnetopause radius of $17.5 R_S$ [Belenkaya et al., 2006], the blue line to expanded cases with a subsolar magnetopause radius of $28 R_S$ [Alexeev et al., 2006], and the green line to intermediate cases with a subsolar magnetopause radius of $22 R_S$ [Belenkaya et al., 2008]. The ‘compressed’ and ‘expanded’ models, specifically, have been validated against Pioneer 11 flyby and Cassini Saturn orbit insertion data, respectively, with the ‘intermediate’ model then using intermediate model parameters. With reference to the Rev 60 trajectory projected into the $Y - Z$ plane shown in Figure 4.1c, the values are positive on the inbound trajectory corresponding to tailward field-line bend-back in the northern dusk sector, pass through zero to become weakly negative near the equatorial crossing, reverse again to positive near periapsis as the spacecraft passes across the midnight meridian, and then remain positive outbound corresponding to related field bend-back in the southern dawn sector.

The main point here, however, is that the peak of such fields in the region of interest are ~ 1 nT in magnitude, thus an order of magnitude less than the measured field. The point is reinforced by the solid colored lines, which show each model subtracted from the measured field, which differ only marginally from the measured field. Nevertheless, the values employed in this study are those in which the intermediate model field has been subtracted, shown by the green line in Figure A.1. This seems a reasonable choice in view of the evident lack of knowledge of upstream solar wind conditions that pertain during any given periapsis pass. We finally note that the model azimuthal field illustrated here for Rev 60 is among the larger of such fields in our data set, due to the larger displacement of the inbound and outbound orbit in this case away from the noon-midnight meridian, where this field passes through zero (Figure 4.1c). These fields thus have only a small effect on the study in the present case.

Appendix B

Mapping azimuthal fields

In this appendix we consider the validity of the procedure by which we map the azimuthal magnetic field component along magnetic field lines into the ionosphere, equation (3.1) in section 3.2, from which the horizontal meridional current per radian of azimuth is given by equation (3.2). As discussed in Chapter 2, the principal field-aligned currents anticipated are those resulting from sub-corotation of the magnetospheric plasma, and those associated with the PPOs. We consider each in turn.

B.1 Subcorotation current system

At ionospheric heights, and in the magnetospheric region extending a few RS above it appropriate to the present investigation, we may expect the effects associated with plasma sub-corotation will be axisymmetric to a first approximation, leading to a near-axisymmetric system of field-aligned currents whose general form is illustrated in Figure 2.7. The azimuthal field associated with the lagging configuration (Figure 2.7c) will thus also be axisymmetric to a first approximation. We may then apply Ampère's law to a circular path of radius ρ centered on the spin/magnetic axis, as shown by the red line in Figure B.1a, giving

$$2\pi\rho B_\varphi = \mu_0 \int_s j_\parallel dS = \mu_0 I_\parallel, \quad (\text{B.1})$$

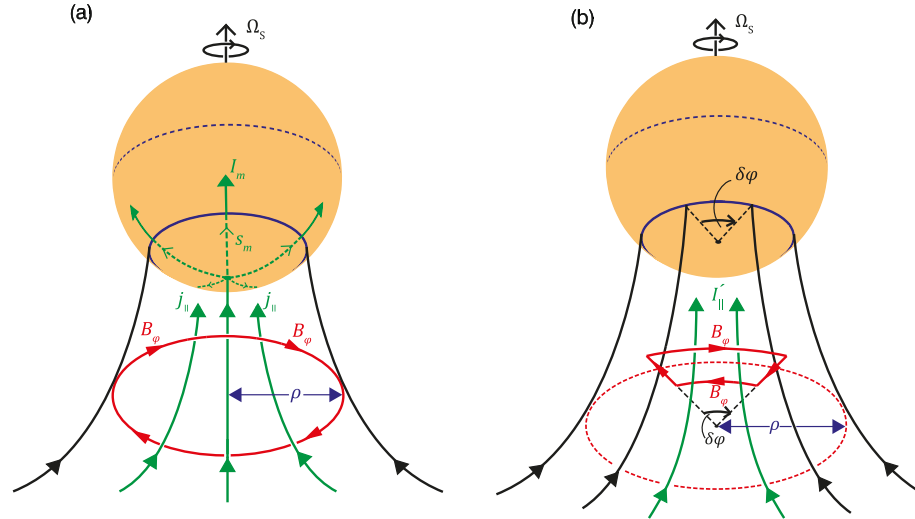


Figure B.1: Sketches illustrating the dependence of the azimuthal field component B_{ϕ} along polar magnetic field lines carrying field-aligned current between transverse closure currents in the magnetosphere at one end and the planet's ionosphere at the other. Black lines indicate background magnetic field lines and green lines the current, while arrowed red lines show the paths on which Ampère's circuital law is applied. Panel (a) illustrates the case of an axisymmetric current system of arbitrary latitudinal form, showing the meridional Pedersen currents (green lines). By current continuity, the total meridional Pedersen current flowing on the blue latitudinal ring at the feet of the field lines, $2\pi I_m$, is equal to the integral of the field-aligned current flowing through the red contour in the magnetosphere. Application of Ampère's law to the red ring then yields equation (3.3) in section 3.2. Panel (b) illustrates the case of a thin latitudinally extended sheet of field-aligned current, I'_{\parallel} , mapping to the blue line ring in the ionosphere, with current continuity maintained by transpolar Pedersen currents feeding adjacent currents with opposite polarity, such as shown in Figure 2.13 for the PPO current system. Ampère's law applied to the red contour path shown, subtending azimuthal angle $\delta\phi$ at the planetary axis, then yields equation (B.2).

where I_{\parallel} is the total field-aligned current enclosed by the path, equal to the integral of the field-aligned current density j_{\parallel} over the area. We note that this expression is valid for any latitudinal variation of the field-aligned current within the axisymmetric approximation. Noting further from current continuity that I_{\parallel} is constant as we move along field lines defining a flux shell in the region between the field-transverse closure currents in the ionosphere and those in the outer magnetosphere, as shown in Figure B.1a, equation (B.1) thus implies that ρB_{ϕ} is exactly constant along the field lines in such regions. Equation (3.1) connecting the azimuthal field observed at cylindrical radius ρ in the magnetosphere and at its magnetic footprint at cylindrical radius ρ_i in the ionosphere thus follows directly. Further, it is also evident from current continuity

that the horizontal meridional Pedersen current per radian of azimuth flowing in the ionosphere at the feet of the field lines, I_m , as shown in Figure B.1a, is directly related to the total parallel current enclosed, I_{\parallel} , by $I_{\parallel} = 2\pi I_m$. Substitution into equation (B.1) then yields equation (3.3) in section 3.2.

B.2 PPO current system

We now consider the current system discussed in section 1.2 in relation to the PPOs, in which a sheet of field-aligned current flows downward into the ionosphere on one side of the pole, and closes in a similar sheet of upward field aligned current on the other side of the pole, via ionospheric Pedersen currents that flow between, as illustrated in Figure 2.13. If we apply Ampère's law to a path consisting of short circular segments lying on either side of the current sheet, as illustrated by the red contour in Figure B.1b, then the azimuthal magnetic field produced by the sheet just outside the sheet, assumed equal and opposite on either side, is given by

$$2\rho B_{\varphi}(\varphi) = \mu_0 I'_{\parallel}(\varphi), \quad (\text{B.2})$$

where I'_{\parallel} is the field-aligned current per radian of azimuth flowing in the current sheet at some arbitrary azimuth φ . Since the latter current is again constant on field lines between the ionospheric and magnetospheric transverse closure currents, so too will ρB_{φ} be constant on field lines just outside the current sheet. Azimuthal fields observed in the regions immediately on either side of such current sheets should therefore also obey equation (3.1), though near-uniform fields from more distant currents may also be present.

B.3 Effect of the mapping

In Figure B.2 we illustrate the degree to which this procedure helps to organize the pass-by-pass data. In Figure B.2a we show the (slightly corrected) azimuthal field measured on a number of color-coded southern hemisphere spacecraft Revs, plotted ver-

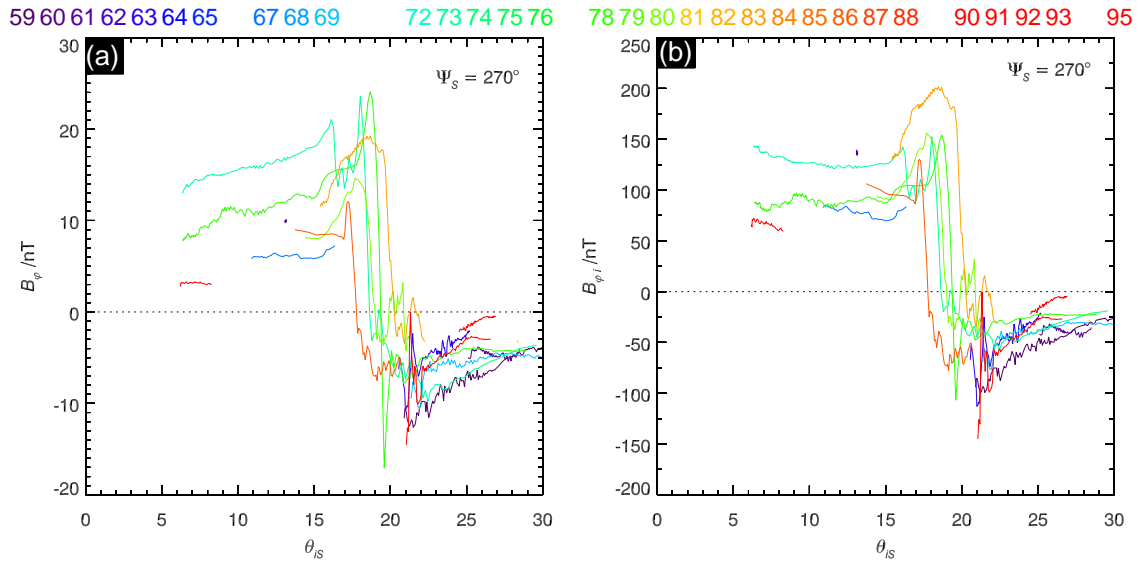


Figure B.2: Azimuthal field data color-coded by Cassini Rev as shown at the top of the figure plotted versus mapped co-latitude in the southern ionosphere, specifically for the 45° sector of PPO phase centered on 270° (Figure 4.4g). Panel (a) shows the field values as measured (with small magnetospheric contribution removed as described in Appendix A), while panel (b) shows the estimated values just above the ionosphere, derived from the measured values using equation (3.1).

versus the southern ionospheric co-latitude θ_{iS} of the measurement, such that the data for a given co-latitude shows the range of perturbation field values determined on a given (model) field line. The mapping employs the same magnetic model as in Figure 4.1d, while the specific data shown is that for which the southern PPO phase lies within 45° of 270° (see Figure 4.4g). Figure B.2b shows the same data segments plotted versus θ_{iS} , but now transformed to estimates of the ionospheric perturbation field using the assumed constancy of ρB_ϕ along field lines (i.e., equation (3.1)), this involving an enhancement in the overall values by a factor of ~ 10 . It can be seen that there remains some significant pass-by-pass variability in the transformed data, particularly in the latitude at which the field drops sharply with increasing co-latitude indicative of an upward field-aligned current, the position of which is not addressed by the transformation. However, it is evident that the data on either side of this current sheet are more closely grouped for the transformed ionospheric field in Figure B.2b than for the directly measured field in Figure B.2a, thus providing support for the validity of this procedure.

Appendix C

Meridional current gradients and field-aligned currents

The general expression for the field-aligned current density flowing into or out of the ionosphere is given by equation (3.4) in section 3.2, involving the variation of the meridional ionospheric current intensity with colatitude and the azimuthal current intensity with longitude. Approximately north-south spacecraft passes across the auroral regions such as those examined here (Figure 4.1d), evidently allow estimation of the former gradients, but not the latter. However, if we can estimate the likely maximum magnitude of the variation of the azimuthal current with longitude, we can use this to set a limit on the variation of the meridional current with colatitude, above which field-aligned currents are most likely present, which can then be estimated from the meridional current gradient.

In spherical polar coordinates

$$(\nabla \times \mathbf{B})_r = \frac{\hat{\mathbf{r}}}{r^2 \sin \theta} \left[\frac{\partial}{\partial \theta} (r \sin \theta B_\varphi) - r \left(\frac{\partial B_\theta}{\partial \varphi} \right) \right]. \quad (\text{C.1})$$

Suppose we can establish a limiting value of $r \left| \frac{\partial B_\theta}{\partial \varphi} \right|$, then if $\left| \frac{\partial}{\partial \theta} (r \sin \theta B_\varphi) \right|$ significantly exceeds this value, then we can be sure that the variation of B_φ concerned is not curl-free and is thus associated with field-aligned currents. So if we assume a certain value

of $\left| \frac{\partial}{\partial \theta} (r \sin \theta B_\varphi) \right|$ then the implied B_θ gradient is

$$\left| \frac{\partial B_\theta}{\partial \varphi} \right|_{\text{imp}} = \frac{1}{r} \left| \frac{\partial}{\partial \theta} (r \sin \theta B_\varphi) \right|, \quad (\text{C.2})$$

for no field-aligned current. Now suppose the gradient in θ is continued for $\Delta\varphi$ radians then the B_θ implied is

$$|B_\theta|_{\text{imp}} \simeq \frac{\Delta\varphi}{2r} \left| \frac{\partial}{\partial \theta} (r \sin \theta B_\varphi) \right|, \quad (\text{C.3})$$

where the factor of 2 assumes $B_\theta \simeq 0$ in the centre of the gradient. In terms of the horizontal meridional current per radian of azimuth, $I_m = r \sin \theta B_\varphi / \mu_0$ at the field line's feet, so the above becomes

$$\left| \frac{\partial I_m}{\partial \theta} \right| \gg \frac{2r_s |B_\theta|_{\text{lim}}}{\mu_0 \Delta\varphi}. \quad (\text{C.4})$$

In terms of ionospheric colatitude, θ_i this becomes

$$\left| \frac{\partial I_m}{\partial \theta_i} \right| \gg 2 \left(\frac{r_s}{R_S} \right)^{3/2} \frac{\cos \theta_i}{\left(1 - \left(\frac{r_s}{R_S} \right) \sin^2 \theta_i \right)^{1/2}} \frac{R_S |B_\theta|_{\text{lim}}}{\mu_0 \Delta\varphi}, \quad (\text{C.5})$$

assuming a dipole field line and variation observed are primarily due to changes in θ at fixed r (circular orbit approximation), these are likely to be true near periapsis when $r_s \approx 4 - 5R_S$.

Now we have $r_s \approx 4 - 5R_S$, $|B_\theta| \approx 5 \times 10^{-9}$ T and $\Delta\varphi \approx \frac{\pi}{2}$. The main upward field-aligned currents are located at a colatitude of $\sim 19^\circ$ in the southern ionosphere. Substituting these values into equation (C.5) we estimate $\left| \frac{\partial I_m}{\partial \theta_i} \right| \approx 0.06$ MA per radian of azimuth per degree of colatitude.

For meridional current gradients significantly larger than this limit, it is then appropriate to assume that the current gradient is indeed associated with a field-aligned current, with the current density approximated by equation (3.4) with the second term on the right neglected. In this paper we set a limiting meridional current gradient of five times this value, i.e. $\left| \frac{\partial I_m}{\partial \theta_i} \right| \approx 0.3$ MA per radian of azimuth per degree of colatitude, at which value, and above, the latter approximation should be well satisfied. For a purely meridional current, this corresponds to a limiting field-aligned current density of ~ 15 - 20 nA m $^{-2}$. We further find that such a limiting gradient also provides a reason-

able empirical division between the major current gradients observed within the main auroral field-aligned current layer, and the lesser gradients that occur on either side.

We finally note that a fully empirical approach to this issue, based on consideration of observed perturbations in the co-latitudinal field possibly associated with azimuthal currents, yields a limit entirely compatible with the above conclusions. A gradient of $\sim 0.3 \text{ MA rad}^{-1}$ per degree of colatitude thus appears to be a suitable limit from both theoretical and empirical perspectives.

References

- Achilleos, N., C. S. Arridge, C. Bertucci, C. M. Jackman, M. K. Dougherty, K. K. Khurana, and C. T. Russell (2008), Large-scale dynamics of Saturn's magnetopause: Observations by Cassini, *J. Geophys. Res.*, *113*, A11209, doi:10.1029/2008JA013265.
- Alexeev, I. I., V. V. Kalegaev, E. S. Belenkaya, S. Y. Bobrovnikov, E. J. Bunce, S. W. H. Cowley, and J. D. Nichols (2006), A global magnetic model of Saturn's magnetosphere and a comparison with Cassini SOI data, *Geophys. Res. Lett.*, *33*, L08101, doi:10.1029/2006GL025896.
- Anderson, B. J., K. Takahashi, and B. A. Toth (2000), Sensing global birkeland currents with iridium engineering magnetometer data, *Geophysical Research Letters*, *27*(24), 4045–4048, doi:10.1029/2000GL000094.
- Andrews, D. J., E. J. Bunce, S. W. H. Cowley, M. K. Dougherty, G. Provan, and D. J. Southwood (2008), Planetary period oscillations in Saturn's magnetosphere: Phase relation of equatorial magnetic field oscillations and Saturn kilometric radiation modulation, *J. Geophys. Res.*, *113*, A09205, doi:10.1029/2007JA012937.
- Andrews, D. J., S. W. H. Cowley, M. K. Dougherty, and G. Provan (2010a), Magnetic field oscillations near the planetary period in Saturn's equatorial magnetosphere: Variation of amplitude and phase with radial distance and local time, *J. Geophys. Res.*, *115*, A04212, doi:10.1029/2009JA014729.
- Andrews, D. J., A. J. Coates, S. W. H. Cowley, M. K. Dougherty, L. Lamy, G. Provan, and P. Zarka (2010b), Magnetospheric period oscillations at Saturn: Comparison of equa-

- torial and high-latitude magnetic field periods with north and south Saturn kilometric radiation periods, *J. Geophys. Res.*, *115*, A12252, doi:10.1029/2010JA015666.
- Andrews, D. J., B. Cecconi, S. W. H. Cowley, M. K. Dougherty, L. Lamy, G. Provan, and P. Zarka (2011), Planetary period oscillations in Saturn's magnetosphere: Evidence in magnetic field phase data for rotational modulation of Saturn kilometric radiation emissions, *J. Geophys. Res.*, *116*, A09206, doi:10.1029/2011JA016636.
- Andrews, D. J., S. W. H. Cowley, M. K. Dougherty, L. Lamy, G. Provan, and D. J. Southwood (2012), Planetary period oscillations in Saturn's magnetosphere: Evolution of magnetic oscillation properties from southern summer to post-equinox, *J. Geophys. Res.*, *117*, A04224, doi:10.1029/2011JA017444.
- Arridge, C. S., N. Achilleos, M. K. Dougherty, K. K. Khurana, and C. T. Russell (2006), Modeling the size and shape of Saturn's magnetopause with variable dynamic pressure, *J. Geophys. Res.*, *111*, A11227, doi:10.1029/2005JA011574.
- Arridge, C. S., C. T. Russell, K. K. Khurana, N. Achilleos, S. W. H. Cowley, M. K. Dougherty, D. J. Southwood, and E. J. Bunce (2008a), Saturn's magnetodisc current sheet, *J. Geophys. Res.*, *113*(4), 1–9, doi:10.1029/2007JA012540.
- Arridge, C. S., K. K. Khurana, C. T. Russell, D. J. Southwood, N. Achilleos, M. K. Dougherty, a. J. Coates, and H. K. Leinweber (2008b), Warping of Saturn's magnetospheric and magnetotail current sheets, *J. Geophys. Res.*, *113*, 1–13, doi:10.1029/2007JA012963.
- Arridge, C. S., et al. (2011), Periodic motion of Saturn's nightside plasma sheet, *J. Geophys. Res.*, *116*, A11205, doi:10.1029/2011JA016827.
- Badman, S. V., and S. W. H. Cowley (2007), Significance of Dungey-cycle flows in Jupiter's and Saturn's magnetospheres, and their identification on closed equatorial field lines, *Ann. Geophys.*, *25*, 941–951, doi:10.5194/angeo-25-941-2007.
- Badman, S. V., E. J. Bunce, J. T. Clarke, S. W. H. Cowley, J.-C. Gérard, D. Grodent, and S. E. Milan (2005), Open flux estimates in Saturn's magnetosphere during the January

- 2004 Cassini-HST campaign, and implications for reconnection rates, *J. Geophys. Res.*, *110*, A11216, doi:10.1029/2005JA011240.
- Badman, S. V., et al. (2012), Rotational modulation and local time dependence of Saturn's infrared H_3^+ auroral intensity, *J. Geophys. Res.*, *117*, A09228, doi:10.1029/2012JA017990.
- Badman, S. V., A. Masters, H. Hasegawa, M. Fujimoto, A. Radioti, D. Grodent, N. Sergis, M. K. Dougherty, and A. J. Coates (2013), Bursty magnetic reconnection at Saturn's magnetopause, *Geophys. Res. Lett.*, *40*, 1027–1031, doi:10.1002/grl.50199.
- Badman, S. V., et al. (2016), Saturn's auroral morphology and field-aligned currents during a solar wind compression, *Icarus*, *263*, 83–93, doi:10.1016/j.icarus.2014.11.014.
- Bagenal, F., and P. a. Delamere (2011), Flow of mass and energy in the magnetospheres of Jupiter and Saturn, *J. Geophys. Res.*, *116*(A5), 1–17, doi:10.1029/2010JA016294.
- Baumjohann, W., and R. A. Treumann (1997), *Basic Space Plasma Physics*, Imperial College Press.
- Belenkaya, E. S., I. I. Alexeev, V. V. Kalegaev, and M. S. Blokhina (2006), Definition of Saturn's magnetospheric model parameters for the Pioneer 11 flyby, *Ann. Geophys.*, *24*, 1145–1156, doi:10.5194/angeo-24-1145-2006.
- Belenkaya, E. S., S. W. H. Cowley, S. V. Badman, M. S. Blokhina, and V. Kalegaev (2008), Dependence of the open-closed field line boundary in Saturn's ionosphere on both the IMF and solar wind dynamic pressure: comparison with the UV auroral oval observed by the HST, *Ann. Geophys.*, *26*, 159–166, doi:10.5194/angeo-26-159-2008.
- Belenkaya, E. S., S. W. H. Cowley, C. J. Meredith, J. D. Nichols, V. V. Kalegaev, I. I. Alexeev, O. G. Barinov, W. O. Barinova, and M. S. Blokhina (2014), Magnetospheric magnetic field modelling for the 2011 and 2012 HST Saturn aurora campaigns – implications for auroral source regions, *Ann. Geophys.*, *32*, 689–704, doi:10.5194/angeo-32-689-2014.

- Brandt, P. C., et al. (2010), Saturn's periodic magnetic field perturbations caused by a rotating partial ring current, *Geophys. Res. Lett.*, *37*, 1–5, doi:10.1029/2010GL045285.
- Bunce, E. (2012), *Auroral Phenomenology and Magnetospheric Processes: Earth and Other Planets*, *Geophysical Monograph Series*, vol. 197, American Geophysical Union, Washington, D. C., doi:10.1029/GM197.
- Bunce, E. J., S. W. H. Cowley, and J. A. Wild (2003), Azimuthal magnetic fields in saturn's magnetosphere: Effects associated with plasma sub-corotation and the magnetopause-tail current system, *Ann. Geophys.*, *21*, 1709–1722, doi:10.5194/angeo-21-1709-2003.
- Bunce, E. J., S. W. H. Cowley, I. I. Alexeev, C. S. Arridge, M. K. Dougherty, J. D. Nichols, and C. T. Russell (2007), Cassini observations of the variation of Saturn's ring current parameters with system size, *J. Geophys. Res.*, *112*, A10202, doi:10.1029/2007JA012275.
- Bunce, E. J., et al. (2008a), Origin of Saturn's aurora: Simultaneous observations by Cassini and the Hubble Space Telescope, *J. Geophys. Res.*, *113*, A09209, doi:10.1029/2008JA013257.
- Bunce, E. J., C. S. Arridge, S. W. H. Cowley, and M. K. Dougherty (2008b), Magnetic field structure of Saturn's dayside magnetosphere and its mapping to the ionosphere: Results from ring current modeling, *J. Geophys. Res.*, *113*, A02207, doi:10.1029/2007JA012538.
- Bunce, E. J., et al. (2010), Extraordinary field-aligned current signatures in Saturn's high-latitude magnetosphere: Analysis of Cassini data during Revolution 89, *J. Geophys. Res.*, *115*, A10238, doi:10.1029/2010JA015612.
- Bunce, E. J., et al. (2014), Cassini nightside observations of the oscillatory motion of Saturn's northern auroral oval, *J. Geophys. Res.*, pp. 3528–3543, doi:10.1002/2013JA019527.

- Burch, J. L., J. Goldstein, T. W. Hill, D. T. Young, F. J. Crary, A. J. Coates, N. André, W. S. Kurth, and E. C. Sittler (2005), Properties of local plasma injections in Saturn's magnetosphere, *Geophys. Res. Lett.*, *32*(14), 1–4, doi:10.1029/2005GL022611.
- Burch, J. L., J. Goldstein, P. Mokashi, W. S. Lewis, C. Paty, D. T. Young, a. J. Coates, M. K. Dougherty, and N. André (2008), On the cause of Saturn's plasma periodicity, *Geophys. Res. Lett.*, *35*, 2–5, doi:10.1029/2008GL034951.
- Burch, J. L., A. D. DeJong, J. Goldstein, and D. T. Young (2009), Periodicity in Saturn's magnetosphere: Plasma cam, *Geophys. Res. Lett.*, *36*, L14203, doi:10.1029/2009GL039043.
- Burton, M. E., M. K. Dougherty, and C. T. Russell (2010), Saturn's internal planetary magnetic field, *Geophys. Res. Lett.*, *37*, L24105, doi:10.1029/2010GL045148.
- Cao, H., C. T. Russell, U. R. Christensen, M. K. Dougherty, and M. E. Burton (2011), Saturn's very axisymmetric magnetic field: No detectable secular variation or tilt, *Earth Planet. Sci. Lett.*, *304*(1-2), 22–28, doi:10.1016/j.epsl.2011.02.035.
- Carbary, J. F. (2012), The morphology of Saturn's ultraviolet aurora, *J. Geophys. Res.*, *117*, A06210, doi:10.1029/2012JA017670.
- Carbary, J. F. (2013), Longitude dependences of Saturn's ultraviolet aurora, *Geophys. Res. Lett.*, *40*, 1902–1906, doi:10.1002/grl.50430.
- Carbary, J. F., and S. M. Krimigis (1982), Charged particle periodicity in the Saturnian magnetosphere, *Geophys. Res. Lett.*, *9*, 1073–1076.
- Carbary, J. F., and D. G. Mitchell (2014), Keogram analysis of ENA images at Saturn, *J. Geophys. Res.*, *119*, 1771–1780, doi:10.1002/2014JA019784.
- Carbary, J. F., D. G. Mitchell, S. M. Krimigis, and N. Krupp (2007), Electron periodicities in Saturn's outer magnetosphere, *J. Geophys. Res.*, *112*, A03206, doi:10.1029/2006JA012077.

- Carbary, J. E., D. G. Mitchell, P. Brandt, C. Paranicas, and S. M. Krimigis (2008), ENA periodicities at Saturn, *Geophys. Res. Lett.*, *35*, L07102, doi:10.1029/2008GL033230.
- Chapman, S., and V. C. A. Ferraro (1930), A New Theory of Magnetic Storms., *Nature*, *126*(3169), 129–130, doi:10.1038/126129a0.
- Clarke, K. E., et al. (2006), Cassini observations of planetary-period oscillations of Saturn's magnetopause, *Geophys. Res. Lett.*, *33*, L23104, doi:10.1029/2006GL027821.
- Clarke, K. E., D. J. Andrews, C. S. Arridge, A. J. Coates, and S. W. H. Cowley (2010a), Magnetopause oscillations near the planetary period at Saturn: Occurrence, phase, and amplitude, *J. Geophys. Res.*, *115*, A08209, doi:10.1029/2009JA014745.
- Clarke, K. E., D. J. Andrews, A. J. Coates, S. W. H. Cowley, and A. Masters (2010b), Magnetospheric period oscillations of Saturn's bow shock, *J. Geophys. Res.*, *115*, A05202, doi:10.1029/2009JA015164.
- Colwell, J. E., P. D. Nicholson, M. S. Tiscareno, C. D. Murray, R. G. French, and E. A. Marouf (2009), The structure of saturn's rings, in *Saturn from Cassini-Huygens*, edited by M. K. Dougherty, L. W. Esposito, and S. M. Krimigis, chap. 13, pp. 375–412, Springer Netherlands, Dordrecht, doi:10.1007/978-1-4020-9217-6_13.
- Connerney, J. E. P., N. F. Ness, and M. H. Acuña (1982), Zonal harmonic model of Saturn's magnetic field from Voyager 1 and 2 observations, *Nature*, *298*(5869), 44–46, doi:10.1038/298044a0.
- Connerney, J. E. P., M. H. Acuña, and N. F. Ness (1983), Currents in Saturn's magnetosphere, *J. Geophys. Res.*, *88*(A11), 8779–8789, doi:10.1029/JA088iA11p08779.
- Cowley, S., and G. Provan (2016), Planetary period oscillations in Saturn's magnetosphere: Further comments on the relationship between post-equinox properties deduced from magnetic field and Saturn kilometric radiation measurements, *Icarus*, *272*(7), 258–276, doi:10.1016/j.icarus.2016.02.051.

- Cowley, S., E. Bunce, and R. Prangé (2004a), Saturn's polar ionospheric flows and their relation to the main auroral oval, *Ann. Geophys.*, *1981*, 1379–1394.
- Cowley, S. W. H. (2000), Magnetospheric Current Systems, *Geophys. Monogr. Ser.*, *118*, doi:10.1029/GM118.
- Cowley, S. W. H., and E. J. Bunce (2001), Origin of the main auroral oval in Jupiter's coupled magnetosphere–ionosphere system, *Planet. Space Sci.*, *49*, 1067–1088.
- Cowley, S. W. H., and E. J. Bunce (2003), Corotation-driven magnetosphere-ionosphere coupling currents in Saturn's magnetosphere and their relation to the auroras, *Ann. Geophys.*, *21*, 1691–1707, doi:10.5194/angeo-21-1691-2003.
- Cowley, S. W. H., and G. Provan (2013), Saturn's magnetospheric planetary period oscillations, neutral atmosphere circulation, and thunderstorm activity: Implications, or otherwise, for physical links, *J. Geophys. Res.*, *118*, 7246–7261, doi:10.1002/2013JA019200.
- Cowley, S. W. H., and G. Provan (2015), Planetary period oscillations in Saturn's magnetosphere: comments on the relation between post-equinox periods determined from magnetic field and SKR emission data, *Ann. Geophys.*, *33*(7), 901–912, doi:10.5194/angeo-33-901-2015.
- Cowley, S. W. H., E. J. Bunce, and J. M. O'Rourke (2004b), A simple quantitative model of plasma flows and currents in Saturn's polar ionosphere, *J. Geophys. Res.*, *109*, A05212, doi:10.1029/2003JA010375.
- Cowley, S. W. H., S. Badman, E. Bunce, J. Clarke, J.-C. Gérard, D. Grodent, C. Jackman, S. E. Milan, and T. K. Yeoman (2005), Reconnection in a rotation-dominated magnetosphere and its relation to Saturn's auroral dynamics, *J. Geophys. Res.*, *110*(A2), A02,201, doi:10.1029/2004JA010796.
- Cowley, S. W. H., D. M. Wright, E. J. Bunce, A. C. Carter, M. K. Dougherty, G. Giampieri, J. D. Nichols, and T. R. Robinson (2006), Cassini observations of planetary-period

- magnetic field oscillations in Saturn's magnetosphere: Doppler shifts and phase motion, *Geophys. Res. Lett.*, 33, L07104, doi:10.1029/2005GL025522.
- Cowley, S. W. H., et al. (2008), Auroral current systems in Saturn's magnetosphere: comparison of theoretical models with Cassini and HST observations, *Ann. Geophys.*, 26, 2613–2630, doi:10.5194/angeo-26-2613-2008.
- Cowling, T. G. (1933), The Magnetic Field of Sunspots, *Mon. Not. R. Astron. Soc.*, 94(1), 39–48, doi:10.1093/mnras/94.1.39.
- Cuzzi, J., R. Clark, G. Filacchione, R. French, R. Johnson, E. Marouf, and L. Spilker (2009), Ring particle composition and size distribution, in *Saturn from Cassini-Huygens*, edited by M. K. Dougherty, L. W. Esposito, and S. M. Krimigis, chap. 15, pp. 459–509, Springer Netherlands, Dordrecht, doi:10.1007/978-1-4020-9217-6_15.
- Davis, L., and E. J. Smith (1990), A model of Saturn's magnetic field based on all available data, *J. Geophys. Res.*, 95(A9), 15,257–15,261, doi:10.1029/JA095iA09p15257.
- Dejong, A. D., J. L. Burch, J. Goldstein, a. J. Coates, and D. T. Young (2010), Low-energy electrons in Saturn's inner magnetosphere and their role in interchange injections, *J. Geophys. Res.*, 115(10), 1–11, doi:10.1029/2010JA015510.
- Desch, M., and M. Kaiser (1981), Voyager measurement of the rotation period of Saturn's magnetic field, *Geophys. Res. Lett.*, 8, 253–256.
- Dougherty, M. K., et al. (2004), The Cassini Magnetic Field Investigation, *Space Sci. Rev.*, 114(1-4), 331–383, doi:10.1007/s11214-004-1432-2.
- Dougherty, M. K., et al. (2005), Cassini magnetometer observations during Saturn orbit insertion., *Science*, 307, 1266–70, doi:10.1126/science.1106098.
- Dougherty, M. K., K. K. Khurana, F. M. Neubauer, C. T. Russell, J. Saur, J. S. Leisner, and M. E. Burton (2006), Identification of a dynamic atmosphere at Enceladus with the Cassini magnetometer., *Science*, 311(March), 1406–1409, doi:10.1126/science.1120985.

- Dungey, J. W. (1961), Interplanetary magnetic field and the auroral zones, *Phys. Rev. Lett.*, 6(2), 47–48, doi:10.1103/PhysRevLett.6.47.
- Espinosa, S., and M. Dougherty (2000), Periodic perturbations in Saturn's magnetic field, *Geophys. Res. Lett.*, 27, 2785–2788.
- Espinosa, S. A., D. J. Southwood, and M. K. Dougherty (2003a), Reanalysis of Saturn's magnetospheric field data view of spin-periodic perturbations, *J. Geophys. Res.*, 108, 1085, doi:10.1029/2001JA005083.
- Espinosa, S. A., D. J. Southwood, and M. K. Dougherty (2003b), How can Saturn impose its rotation period in a noncorotating magnetosphere?, *J. Geophys. Res.*, 108(A2), n/a–n/a, doi:10.1029/2001JA005084.
- Esposito, L. W., et al. (2004), The Cassini Ultraviolet Imaging Spectrograph Investigation, *Space Sci. Rev.*, 115(1-4), 299–361, doi:10.1007/s11214-004-1455-8.
- Felici, M., et al. (2016), Cassini observations of ionospheric plasma in Saturn's magnetotail lobes, *J. Geophys. Res.*, 121(1), 338–357, doi:10.1002/2015JA021648.
- Fischer, G., S.-Y. Ye, J. B. Groene, A. P. Ingersoll, K. M. Sayanagi, J. D. Menietti, W. S. Kurth, and D. A. Gurnett (2014), A possible influence of the Great White Spot on Saturn kilometric radiation periodicity, *Ann. Geophys.*, 32, 1463–1476, doi:10.5194/angeo-32-1463-2014.
- Fischer, G., D. Gurnett, W. Kurth, S.-Y. Ye, and J. Groene (2015), Saturn kilometric radiation periodicity after equinox, *Icarus*, 254, 72–91, doi:10.1016/j.icarus.2015.03.014.
- Galand, M., L. Moore, I. Mueller-Wodarg, M. Mendillo, and S. Miller (2011), Response of Saturn's auroral ionosphere to electron precipitation: Electron density, electron temperature, and electrical conductivity, *J. Geophys. Res.*, 116, A09306, doi:10.1029/2010JA016412.
- Galopeau, P., and A. Lecacheux (2000), Variations of Saturn's radio rotation period measured at kilometer wavelengths, *J. Geophys. Res.*, 105.

- García-Melendo, E., S. Pérez-Hoyos, A. Sánchez-Lavega, and R. Hueso (2011), Saturn's zonal wind profile in 2004-2009 from Cassini ISS images and its long-term variability, *Icarus*, *215*(1), 62–74, doi:10.1016/j.icarus.2011.07.005.
- Giampieri, G., M. K. Dougherty, E. J. Smith, and C. T. Russell (2006), A regular period for Saturn's magnetic field that may track its internal rotation., *Nature*, *441*, 62–4, doi:10.1038/nature04750.
- Goldreich, P., and A. J. Farmer (2007), Spontaneous axisymmetry breaking of the external magnetic field at Saturn, *J. Geophys. Res.*, *112*, doi:10.1029/2006JA012163.
- Goldstein, J., T. W. Hill, J. H. Waite, and J. L. Burch (2014), Analytical model of rotating two-cell convection at Saturn, *J. Geophys. Res.*, *119*, 1980–1993, doi:10.1002/2013JA019615.
- Gurnett, D., J. Groene, T. F. Averkamp, W. Kurth, S.-Y. Ye, and G. Fischer (2011), An SLS4 longitude system based on a tracking filter analysis of the rotational modulation of Saturn kilometric radiation, *Planet. Radio Emiss. VII*, pp. 51–64.
- Gurnett, D. a., a. M. Persoon, W. S. Kurth, J. B. Groene, T. F. Averkamp, M. K. Dougherty, and D. J. Southwood (2007), The variable rotation period of the inner region of Saturn's plasma disk., *Science*, *316*, 442–445, doi:10.1126/science.1138562.
- Gurnett, D. A., A. Lecacheux, W. S. Kurth, A. M. Persoon, J. B. Groene, L. Lamy, P. Zarka, and J. F. Carbary (2009a), Discovery of a north-south asymmetry in Saturn's radio rotation period, *Geophys. Res. Lett.*, *36*, L16102, doi:10.1029/2009GL039621.
- Gurnett, D. A., A. M. Persoon, J. B. Groene, A. J. Kopf, G. B. Hospodarsky, and W. S. Kurth (2009b), A north-south difference in the rotation rate of auroral hiss at Saturn: Comparison to Saturn's kilometric radio emission, *Geophys. Res. Lett.*, *36*, L21108, doi:10.1029/2009GL040774.
- Gurnett, D. A., J. B. Groene, A. M. Persoon, J. D. Menietti, S.-Y. Ye, W. S. Kurth, R. J. MacDowall, and A. Lecacheux (2010), The reversal of the rotational modulation rates of

- the north and south components of Saturn kilometric radiation near equinox, *Geophys. Res. Lett.*, 37, L24101, doi:10.1029/2010GL045796.
- Hansen, C. J., L. Esposito, A. I. F. Stewart, J. Colwell, A. Hendrix, W. Pryor, D. Shemansky, and R. West (2006), Enceladus' Water Vapor Plume, *Science*, 311(5766), 1422–1425, doi:10.1126/science.1121254.
- Hansen, C. J., et al. (2008), Water vapour jets inside the plume of gas leaving Enceladus., *Nature*, 456(7221), 477–9, doi:10.1038/nature07542.
- Hill, T. (1979), Inertial limit on corotation, *J. Geophys. Res.*, 84, 6554–6558.
- Hill, T. W., et al. (2005), Evidence for rotationally driven plasma transport in Saturn's magnetosphere, *Geophys. Res. Lett.*, 32(14), 1–4, doi:10.1029/2005GL022620.
- Hill, T. W., et al. (2008), Plasmoids in Saturn's magnetotail, *J. Geophys. Res.*, 113(A1), A01,214, doi:10.1029/2007JA012626.
- Hubbard, W. B., M. K. Dougherty, D. Gautier, and R. Jacobson (2009), *Saturn from Cassini-Huygens*, chap. The Interior of Saturn, pp. 75–81, Springer Netherlands, Dordrecht, doi:10.1007/978-1-4020-9217-6_4.
- Hughes, W. (1995), The magnetopause, magnetotail, and magnetic reconnection, in *Introduction to Space Physics*, edited by M. G. Kivelson and C. T. Russell, chap. 10, pp. 227–287, Cambridge University Press.
- Iess, L., et al. (2014), The Gravity Field and Interior Structure of Enceladus, *Science*, 344(6179), 78–80, doi:10.1126/science.1250551.
- Iijima, T., and T. A. Potemra (1976), The amplitude distribution of field-aligned currents at northern high latitudes observed by Triad, *J. Geophys. Res.*, 81(13), 2165–2174, doi:10.1029/JA081i013p02165.
- Isbell, J., A. J. Dessler, and J. H. Waite (1984), Magnetospheric energization by interaction between planetary spin and the solar wind, *J. Geophys. Res.*, 89, 10,716, doi:10.1029/JA089iA12p10716.

- Jackman, C., G. Provan, and S. Cowley (2016), Reconnection events in Saturn's magnetotail: Dependence of plasmoid occurrence on planetary period oscillation phase, *J. Geophys. Res.*, *121*(2), n/a–n/a, doi:10.1002/2015JA021985.
- Jackman, C. M. (2004), Interplanetary magnetic field at ~9 AU during the declining phase of the solar cycle and its implications for Saturn's magnetospheric dynamics, *J. Geophys. Res.*, *109*(A11), A11,203, doi:10.1029/2004JA010614.
- Jackman, C. M., C. T. Russell, D. J. Southwood, C. S. Arridge, N. Achilleos, and M. K. Dougherty (2007), Strong rapid dipolarizations in Saturn's magnetotail: In situ evidence of reconnection, *Geophys. Res. Lett.*, *34*(11), 2–6, doi:10.1029/2007GL029764.
- Jackman, C. M., R. J. Forsyth, and M. K. Dougherty (2008), The overall configuration of the interplanetary magnetic field upstream of Saturn as revealed by Cassini observations, *J. Geophys. Res.*, *113*(8), 1–10, doi:10.1029/2008JA013083.
- Jackman, C. M., J. a. Slavin, and S. W. H. Cowley (2011), Cassini observations of plasmoid structure and dynamics: Implications for the role of magnetic reconnection in magnetospheric circulation at Saturn, *J. Geophys. Res.*, *116*(A10), A10,212, doi:10.1029/2011JA016682.
- Jackman, C. M., et al. (2015), Field dipolarization in Saturn's magnetotail with planetward ion flows and energetic particle flow bursts: Evidence of quasi-steady reconnection, *J. Geophys. Res.*, *120*(5), 3603–3617, doi:10.1002/2015JA020995.
- Jasinski, J. M., J. A. Slavin, C. S. Arridge, G. Poh, X. Jia, N. Sergis, A. J. Coates, G. H. Jones, and J. H. Waite (2016), Flux transfer event observation at saturn's dayside magnetopause by the cassini spacecraft, *Geophysical Research Letters*, *43*(13), 6713–6723, doi:10.1002/2016GL069260, 2016GL069260.
- Jia, X., and M. G. Kivelson (2012), Driving Saturn's magnetospheric periodicities from the upper atmosphere/ionosphere: Magnetotail response to dual sources, *J. Geophys. Res.*, *117*, A11219, doi:10.1029/2012JA018183.

- Jia, X., M. G. Kivelson, and T. I. Gombosi (2012), Driving Saturn's magnetospheric periodicities from the upper atmosphere/ionosphere, *J. Geophys. Res.*, *117*, A04215, doi:10.1029/2011JA017367.
- Jinks, S. L., et al. (2014), Cassini multi-instrument assessment of Saturn's polar cap boundary, *J. Geophys. Res.*, *119*, 8161–8177, doi:10.1002/2014JA020367.
- Kaiser, M. L., M. D. Desch, J. W. Warwick, and J. B. Pearce (1980), Voyager Detection of Nonthermal Radio Emission from Saturn, *Science*, *209*(4462), 1238–1240, doi:10.1126/science.209.4462.1238.
- Kanani, S. J., et al. (2010), A new form of Saturn's magnetopause using a dynamic pressure balance model, based on in situ, multi-instrument Cassini measurements, *J. Geophys. Res.*, *115*, A06207, doi:10.1029/2009JA014262.
- Kane, M., D. G. Mitchell, J. F. Carbary, S. M. Krimigis, and F. J. Crary (2008), Plasma convection in Saturn's outer magnetosphere determined from ions detected by the Cassini INCA experiment, *Geophys. Res. Lett.*, *35*, L04102, doi:10.1029/2007GL032342.
- Kellett, S., C. S. Arridge, E. J. Bunce, A. J. Coates, S. W. H. Cowley, M. K. Dougherty, A. M. Persoon, N. Sergis, and R. J. Wilson (2011), Saturn's ring current: Local time dependence and temporal variability, *J. Geophys. Res.*, *116*, A05220, doi:10.1029/2010JA016216.
- Khurana, K. K., D. G. Mitchell, C. S. Arridge, M. K. Dougherty, C. T. Russell, C. Paranicas, N. Krupp, and A. J. Coates (2009), Sources of rotational signals in Saturn's magnetosphere, *J. Geophys. Res.*, *114*, 1–11, doi:10.1029/2008JA013312.
- Kivelson, M. G., and X. Jia (2014), Control of periodic variations in Saturn's magnetosphere by compressional waves, *J. Geophys. Res.*, *119*(10), 8030–8045, doi:10.1002/2014JA020258.
- Knight, S. (1973), Parallel electric fields, *Planet. Space Sci.*, *21*, 741–750.

- Kopf, A. J., et al. (2010), Electron beams as the source of whistler-mode auroral hiss at Saturn, *Geophys. Res. Lett.*, *37*, L09102, doi:10.1029/2010GL042980.
- Kurth, W., et al. (2016), Saturn kilometric radiation intensities during the Saturn auroral campaign of 2013, *Icarus*, *263*, 2–9, doi:10.1016/j.icarus.2015.01.003.
- Kurth, W. S., et al. (2005), An Earth-like correspondence between Saturn's auroral features and radio emission, *Nature*, *433*(7027), 722–725, doi:10.1038/nature03334.
- Kurth, W. S., A. Lecacheux, T. F. Averkamp, J. B. Groene, and D. A. Gurnett (2007), A Saturnian longitude system based on a variable kilometric radiation period, *Geophys. Res. Lett.*, *34*(2), L02,201, doi:10.1029/2006GL028336.
- Kurth, W. S., T. F. Averkamp, D. A. Gurnett, J. B. Groene, and A. Lecacheux (2008), An update to a Saturnian longitude system based on kilometric radio emissions, *J. Geophys. Res.*, *113*, A05222, doi:10.1029/2007JA012861.
- Lamy, L. (2011), Variability of southern and northern periodicities of Saturn Kilometric Radiation, pp. 15–17.
- Lamy, L., B. Cecconi, R. Prangé, P. Zarka, J. D. Nichols, and J. T. Clarke (2009), An auroral oval at the footprint of Saturn's kilometric radio sources, colocated with the UV aurorae, *J. Geophys. Res.*, *114*, A10212, doi:10.1029/2009JA014401.
- Lamy, L., et al. (2010), Properties of Saturn kilometric radiation measured within its source region, *Geophys. Res. Lett.*, *37*, L12104, doi:10.1029/2010GL043415.
- Lamy, L., et al. (2011), Emission and propagation of Saturn kilometric radiation: Magnetoionic modes, beaming pattern, and polarization state, *J. Geophys. Res.*, *116*, A04212, doi:10.1029/2010JA016195.
- Lamy, L., R. Prangé, W. Pryor, J. Gustin, S. V. Badman, H. Melin, T. Stallard, D. Mitchell, and P. C. Brandt (2013), Multispectral simultaneous diagnosis of Saturn's aurorae throughout a planetary rotation, *J. Geophys. Res.*, *118*, 4817–4843, doi:10.1002/jgra.50404.

- Mardia, K., and P. Jupp (2000), *Directional statistics*, Wiley series in probability and statistics, Wiley.
- Markwardt, C. B. (2009), Non-linear Least-squares Fitting in IDL with MPFIT, *Astron. Data Anal. Softw. Syst. XVIII ASP Conf. Ser.*, 411.
- Masters, A. (2015), The dayside reconnection voltage applied to Saturn's magnetosphere, *Geophys. Res. Lett.*, pp. 2577–2585, doi:10.1002/2015GL063361.
- Masters, A., N. Achilleos, M. K. Dougherty, J. A. Slavin, G. B. Hospodarsky, C. S. Arridge, and A. J. Coates (2008), An empirical model of Saturn's bow shock: Cassini observations of shock location and shape, *J. Geophys. Res.*, 113(10), 1–18, doi:10.1029/2008JA013276.
- Masters, A., N. Achilleos, J. C. Cutler, A. J. Coates, M. K. Dougherty, and G. H. Jones (2012), Surface waves on Saturn's magnetopause, *Planet. Space Sci.*, 65(1), 109–121, doi:10.1016/j.pss.2012.02.007.
- Mauk, B. H., et al. (2009), Fundamental plasma processes in Saturn's magnetosphere, in *Saturn from Cassini-Huygens*, edited by M. K. Dougherty, L. W. Esposito, and S. M. Krimigis, chap. 11, pp. 281–331, Springer Netherlands, Dordrecht, doi:10.1007/978-1-4020-9217-6_11.
- McAndrews, H. J., C. J. Owen, M. F. Thomsen, B. Lavraud, a. J. Coates, M. K. Dougherty, and D. T. Young (2008), Evidence for reconnection at Saturn's magnetopause, *J. Geophys. Res.*, 113(4), 1–12, doi:10.1029/2007JA012581.
- Melin, H., et al. (2011), Simultaneous Cassini VIMS and UVIS observations of Saturn's southern aurora: Comparing emissions from H, H₂ and H₃⁺ at a high spatial resolution, *Geophys. Res. Lett.*, 38, L15203, doi:10.1029/2011GL048457.
- Meredith, C. J., I. I. Alexeev, S. V. Badman, E. S. Belenkaya, S. W. H. Cowley, M. K. Dougherty, V. V. Kalegaev, G. R. Lewis, and J. D. Nichols (2014a), Saturn's dayside ultraviolet auroras: Evidence for morphological dependence on the direction of

- the upstream interplanetary magnetic field, *J. Geophys. Res.*, *119*, 1994–2008, doi:10.1002/2013JA019598.
- Meredith, C. J., S. W. H. Cowley, and J. D. Nichols (2014b), Survey of Saturn auroral storms observed by the Hubble Space Telescope: Implications for the storm time scales, *J. Geophys. Res.*, *119*, 9624–9642, doi:10.1002/2014JA020601.
- Miller, R. G. (1974), The jackknife—a review, *Biometrika*, *61*(1), 1–15.
- Mitchell, C. J., C. C. Porco, and J. W. Weiss (2015), Tracking the Geysers of Enceladus Into Saturn’s E Ring, *Astron. J.*, *149*(5), 156, doi:10.1088/0004-6256/149/5/156.
- Müller, A. L., J. Saur, N. Krupp, E. Roussos, B. H. Mauk, A. M. Rymer, D. G. Mitchell, and S. M. Krimigis (2010), Azimuthal plasma flow in the Kronian magnetosphere, *J. Geophys. Res.*, *115*, A08203, doi:10.1029/2009JA015122.
- Müller-Wodarg, I. C. F., M. Mendillo, R. V. Yelle, and A. D. Aylward (2006), A global circulation model of Saturn’s thermosphere, *Icarus*, *180*(1), 147–160, doi:10.1016/j.icarus.2005.09.002.
- Nagy, A. F., A. J. Kliore, M. Mendillo, S. Miller, L. Moore, J. I. Moses, I. Müller-Wodarg, and D. Shemansky (2009), Upper atmosphere and ionosphere of saturn, in *Saturn from Cassini-Huygens*, edited by E. L. W. K. S. M. Dougherty, M. K., chap. 8, pp. 181–201, Springer, Dordrecht, doi:10.1007/978-1-4020-9217-6_8.
- Narvaez, P. (2004), The Magnetostatic Cleanliness Program for the Cassini Spacecraft, *Space Sci. Rev.*, *114*(1-4), 385–394, doi:10.1007/s11214-004-1433-1.
- Nichols, J. D., J. T. Clarke, S. W. H. Cowley, J. Duval, A. J. Farmer, J.-C. Gérard, D. Grodent, and S. Wannawichian (2008), Oscillation of Saturn’s southern auroral oval, *J. Geophys. Res.*, *113*, A11205, doi:10.1029/2008JA013444.
- Nichols, J. D., B. Cecconi, J. T. Clarke, S. W. H. Cowley, J.-C. Gérard, A. Grocott, D. Grodent, L. Lamy, and P. Zarka (2010a), Variation of Saturn’s UV aurora with SKR phase, *Geophys. Res. Lett.*, *37*, L15102, doi:10.1029/2010GL044057.

- Nichols, J. D., S. W. H. Cowley, and L. Lamy (2010b), Dawn-dusk oscillation of Saturn's conjugate auroral ovals, *Geophys. Res. Lett.*, *37*, L24102, doi:10.1029/2010GL045818.
- Nichols, J. D., et al. (2014), Dynamic auroral storms on Saturn as observed by the Hubble Space Telescope, *Geophys. Res. Lett.*, pp. 3323–3330, doi:10.1002/2014GL060186.
- Nichols, J. D., S. V. Badman, E. J. Bunce, J. T. Clarke, S. W. H. Cowley, G. J. Hunt, and G. Provan (2016), Saturn's northern auroras as observed using the Hubble Space Telescope, *Icarus*, *263*, 17–31, doi:10.1016/j.icarus.2015.09.008.
- Owens, M. J., and R. J. Forsyth (2013), The heliospheric magnetic field, *Living Reviews in Solar Physics*, *10*(5), doi:10.1007/lrsp-2013-5.
- Parker, E. N. (1958), Dynamics of the Interplanetary Gas and Magnetic Fields., *Astrophys. J.*, *128*, 664, doi:10.1086/146579.
- Persoon, A. M., et al. (2009), A diffusive equilibrium model for the plasma density in Saturn's magnetosphere, *J. Geophys. Res.*, *114*, A04211, doi:10.1029/2008JA013912.
- Pilkington, N. M., N. Achilleos, C. S. Arridge, A. Masters, N. Sergis, A. J. Coates, and M. K. Dougherty (2014), Polar confinement of Saturn's magnetosphere revealed by in situ Cassini observations, *J. Geophys. Res.*, *119*(4), 2858–2875, doi:10.1002/2014JA019774.
- Pilkington, N. M., et al. (2015a), Internally driven large-scale changes in the size of Saturn's magnetosphere, *J. Geophys. Res.*, *120*(9), 7289–7306, doi:10.1002/2015JA021290.
- Pilkington, N. M., et al. (2015b), Asymmetries observed in Saturn's magnetopause geometry, *Geophys. Res. Lett.*, *42*(17), 6890–6898, doi:10.1002/2015GL065477.
- Pontius, D. H., and T. W. Hill (2009), Plasma mass loading from the extended neutral gas torus of Enceladus as inferred from the observed plasma corotation lag, *Geophys. Res. Lett.*, *36*, L23103, doi:10.1029/2009GL041030.

- Porco, C., D. DiNino, and F. Nimmo (2014), How the Geysers, Tidal Stresses, and Thermal Emission Across the South Polar Terrain of Enceladus Are Related, *Astron. J.*, *148*(3), 45, doi:10.1088/0004-6256/148/3/45.
- Porco, C. C., et al. (2006), Cassini observes the active south pole of Enceladus., *Science*, *311*, 1393–401, doi:10.1126/science.1123013.
- Prangé, R., L. Pallier, and K. Hansen (2004), An interplanetary shock traced by planetary auroral storms from the Sun to Saturn, *Nature*, *432*, 7–10.
- Provan, G., D. J. Andrews, C. S. Arridge, A. J. Coates, S. W. H. Cowley, S. E. Milan, M. K. Dougherty, and D. M. Wright (2009a), Polarization and phase of planetary-period magnetic field oscillations on high-latitude field lines in Saturn's magnetosphere, *J. Geophys. Res.*, *114*, A02225, doi:10.1029/2008JA013782.
- Provan, G., S. W. H. Cowley, and J. D. Nichols (2009b), Phase relation of oscillations near the planetary period of Saturn's auroral oval and the equatorial magnetospheric magnetic field, *J. Geophys. Res.*, *114*, A04205, doi:10.1029/2008JA013988.
- Provan, G., D. J. Andrews, B. Cecconi, S. W. H. Cowley, M. K. Dougherty, L. Lamy, and P. M. Zarka (2011), Magnetospheric period magnetic field oscillations at Saturn: Equatorial phase “jitter” produced by superposition of southern and northern period oscillations, *J. Geophys. Res.*, *116*, A04225, doi:10.1029/2010JA016213.
- Provan, G., D. J. Andrews, C. S. Arridge, A. J. Coates, S. W. H. Cowley, G. Cox, M. K. Dougherty, and C. M. Jackman (2012), Dual periodicities in planetary-period magnetic field oscillations in Saturn's tail, *J. Geophys. Res.*, *117*, A01209, doi:10.1029/2011JA017104.
- Provan, G., S. W. H. Cowley, J. Sandhu, D. J. Andrews, and M. K. Dougherty (2013), Planetary period magnetic field oscillations in Saturn's magnetosphere: Postequinox abrupt nonmonotonic transitions to northern system dominance, *J. Geophys. Res.*, *118*, 3243–3264, doi:10.1002/jgra.50186.

- Provan, G., L. Lamy, S. W. H. Cowley, and M. K. Dougherty (2014), Planetary period oscillations in Saturn's magnetosphere: Comparison of magnetic oscillations and SKR modulations in the postequinox interval, *J. Geophys. Res.*, *119*(9), 7380–7401, doi:10.1002/2014JA020011.
- Provan, G., C. Tao, S. W. H. Cowley, M. K. Dougherty, and A. J. Coates (2015), Planetary period oscillations in Saturn's magnetosphere: Examining the relationship between abrupt changes in behavior and solar wind-induced magnetospheric compressions and expansions, *J. Geophys. Res.*, *120*(11), 9524–9544, doi:10.1002/2015JA021642.
- Quenouille, M. H. (1949), Approximate tests of correlation in time-series, *Journal of the Royal Statistical Society. Series B (Methodological)*, *11*(1), 68–84.
- Radioti, A., D. Grodent, J. C. Gérard, B. Bonfond, J. Gustin, W. Pryor, J. M. Jasinski, and C. S. Arridge (2013), Auroral signatures of multiple magnetopause reconnection at Saturn, *Geophys. Res. Lett.*, *40*, 4498–4502, doi:10.1002/grl.50889.
- Richardson, J. D. (1986), Thermal ions at Saturn - Plasma parameters and implications, *J. Geophys. Res.*, *91*, 1381–1389, doi:10.1029/JA091iA02p01381.
- Richardson, J. D., and E. C. Sittler (1990), A plasma density model for Saturn based on Voyager observations, *J. Geophys. Res.*, *95*, doi:10.1029/JA095iA08p12019.
- Rohde, R., R. Muller, R. Jacobsen, S. Perlmutter, and S. Mosher (2013), Berkeley Earth Temperature Averaging Process, *Geoinformatics Geostatistics An Overv.*, *01*(02), doi:10.4172/2327-4581.1000103.
- Sandel, B., and D. Shemansky (1982), Extreme ultraviolet observations from the Voyager 2 encounter with Saturn, *Science*, *215*, 548–553.
- Sandel, B. R., and A. L. Broadfoot (1981), Morphology of Saturn's aurora, *Nature*, *292*, 679–682, doi:10.1038/292679a0.
- Schippers, P., et al. (2008), Multi-instrument analysis of electron populations in Saturn's magnetosphere, *J. Geophys. Res.*, *113*, A07208, doi:10.1029/2008JA013098.

- Schippers, P., N. André, D. A. Gurnett, G. R. Lewis, A. M. Persoon, and A. J. Coates (2012), Identification of electron field-aligned current systems in Saturn's magnetosphere, *J. Geophys. Res.*, *117*, A05204, doi:10.1029/2011JA017352.
- Seidelmann, P. K., and N. Divine (1977), Evaluation of Jupiter longitudes in System III (1965), *Geophys. Res. Lett.*, *4*(2), 65–68, doi:10.1029/GL004i002p00065.
- Slavin, J. A., E. J. Smith, J. R. Spreiter, and S. S. Stahara (1985), Solar wind flow about the outer planets: Gas dynamic modeling of the Jupiter and Saturn bow shocks, *J. Geophys. Res.*, *90*(A7), 6275, doi:10.1029/JA090iA07p06275.
- Smith, A. W., C. M. Jackman, and M. F. Thomsen (2016a), Magnetic reconnection in Saturn's magnetotail: A comprehensive magnetic field survey, *J. Geophys. Res.*, *121*(4), 2984–3005, doi:10.1002/2015JA022005.
- Smith, C. G. A. (2006), Periodic modulation of gas giant magnetospheres by the neutral upper atmosphere, *Ann. Geophys.*, *24*(10), 2709–2717, doi:10.5194/angeo-24-2709-2006.
- Smith, C. G. A. (2011), A Saturnian cam current system driven by asymmetric thermospheric heating, *Mon. Not. R. Astron. Soc.*, *410*, 2315–2328, doi:10.1111/j.1365-2966.2010.17602.x.
- Smith, C. G. A. (2014), On the nature and location of the proposed twin vortex systems in Saturn's polar upper atmosphere, *J. Geophys. Res.*, *119*(7), 5964–5977, doi:10.1002/2014JA019934.
- Smith, C. G. A., and N. Achilleos (2012), Axial symmetry breaking of Saturn's thermosphere, *Mon. Not. R. Astron. Soc.*, *422*, 1460–1488, doi:10.1111/j.1365-2966.2012.20719.x.
- Smith, C. G. A., A. D. Aylward, G. H. Millward, S. Miller, and L. E. Moore (2007), An unexpected cooling effect in Saturn's upper atmosphere., *Nature*, *445*(7126), 399–401, doi:10.1038/nature05518.

- Smith, C. G. A., L. C. Ray, and N. Achilleos (2016b), A planetary wave model for Saturn's 10.7-hour periodicities, *Icarus*, 268, 76–88, doi:10.1016/j.icarus.2015.12.041.
- Smith, E. J., L. Davis, D. E. Jones, P. J. Coleman, D. S. Colburn, P. Dyal, and C. P. Sonett (1980), Saturn's Magnetic Field and Magnetosphere., *Science*, 207(4429), 407–410, doi:10.1126/science.207.4429.407.
- Smith, H. T., M. Shappirio, E. C. Sittler, D. Reisenfeld, R. E. Johnson, R. A. Baragiola, F. J. Crary, D. J. McComas, and D. T. Young (2005), Discovery of nitrogen in saturn's inner magnetosphere, *Geophysical Research Letters*, 32(14), n/a–n/a, doi:10.1029/2005GL022654, 114S03.
- Southwood, D. J., and S. W. H. Cowley (2014), The origin of Saturn's magnetic periodicities: Northern and southern current systems, *J. Geophys. Res.*, 119, 1563–1571, doi:10.1002/2013JA019632.
- Southwood, D. J., and M. G. Kivelson (2007), Saturnian magnetospheric dynamics: Elucidation of a camshaft model, *J. Geophys. Res.*, 112, A12222, doi:10.1029/2007JA012254.
- Southwood, D. J., and M. G. Kivelson (2009), The source of Saturn's periodic radio emission, *J. Geophys. Res.*, 114, A09201, doi:10.1029/2008JA013800.
- Spencer, J. R., A. C. Barr, L. W. Esposito, P. Helfenstein, A. P. Ingersoll, R. Jaumann, C. P. McKay, F. Nimmo, and J. H. Waite (2009), Enceladus: An active cryovolcanic satellite, in *Saturn from Cassini-Huygens*, edited by M. K. Dougherty, L. W. Esposito, and S. M. Krimigis, chap. 21, pp. 683–724, Springer Netherlands, Dordrecht, doi:10.1007/978-1-4020-9217-6_21.
- Stallard, T., S. Miller, H. Melin, M. Lystrup, M. Dougherty, and N. Achilleos (2007), Saturn's auroral/polar H_3^+ infrared emission, *Icarus*, 189, 1–13, doi:10.1016/j.icarus.2006.12.027.
- Stallard, T., S. Miller, M. Lystrup, N. Achilleos, C. Arridge, and M. Dougherty (2008), Dusk-brightening event in saturn's H_3^+ Aurora, *Astrophys. J.*, 673, 203–206.

- Stallard, T. S., S. Miller, L. M. Trafton, T. R. Geballe, and R. D. Joseph (2004), Ion winds in Saturn's southern auroral/polar region, *Icarus*, *167*, 204–211, doi:10.1016/j.icarus.2003.09.006.
- Stallard, T. S., A. Masters, S. Miller, H. Melin, E. J. Bunce, C. S. Arridge, N. Achilleos, M. K. Dougherty, and S. W. H. Cowley (2012), Saturn's auroral/polar H₃⁺ infrared emission: The effect of solar wind compression, *J. Geophys. Res.*, *117*, doi:10.1029/2012JA018201.
- Stanley, S. (2010), A dynamo model for axisymmetrizing Saturn's magnetic field, *Geophys. Res. Lett.*, *37*(5), 3–7, doi:10.1029/2009GL041752.
- Stevenson, D. J. (1980), Saturn's Luminosity and Magnetism, *Science*, *208*(4445), 746–748, doi:10.1126/science.208.4445.746.
- Talboys, D. L., C. S. Arridge, E. J. Bunce, A. J. Coates, S. W. H. Cowley, and M. K. Dougherty (2009a), Characterization of auroral current systems in Saturn's magnetosphere: High-latitude Cassini observations, *J. Geophys. Res.*, *114*, A06220, doi:10.1029/2008JA013846.
- Talboys, D. L., C. S. Arridge, E. J. Bunce, A. J. Coates, S. W. H. Cowley, M. K. Dougherty, and K. K. Khurana (2009b), Signatures of field-aligned currents in Saturn's nightside magnetosphere, *Geophys. Res. Lett.*, *36*, L19107, doi:10.1029/2009GL039867.
- Talboys, D. L., E. J. Bunce, S. W. H. Cowley, C. S. Arridge, A. J. Coates, and M. K. Dougherty (2011), Statistical characteristics of field-aligned currents in Saturn's nightside magnetosphere, *J. Geophys. Res.*, *116*, A04213, doi:10.1029/2010JA016102.
- Thomsen, M. F., D. B. Reisenfeld, D. M. Delapp, R. L. Tokar, D. T. Young, F. J. Crary, E. C. Sittler, M. A. McGraw, and J. D. Williams (2010), Survey of ion plasma parameters in Saturn's magnetosphere, *J. Geophys. Res.*, *115*, A10220, doi:10.1029/2010JA015267.
- Thomsen, M. F., C. M. Jackman, R. L. Tokar, and R. J. Wilson (2014), Plasma flows in saturn's nightside magnetosphere, *J. Geophys. Res.*, *119*, 4521–4535, doi:10.1002/2014JA019912.

- Thomsen, M. F., C. M. Jackman, D. G. Mitchell, G. Hospodarsky, W. S. Kurth, and K. C. Hansen (2015), Sustained lobe reconnection in Saturn's magnetotail, *J. Geophys. Res.*, *120*, 10,257–10,274, doi:10.1002/2015JA021768.
- Thomsen, M. F., A. J. Coates, E. Roussos, R. J. Wilson, K. C. Hansen, and G. R. Lewis (2016), Suprathermal electron penetration into the inner magnetosphere of Saturn, *J. Geophys. Res.*, *121*, 5436–5448, doi:10.1002/2016JA022692.
- Vasyliūnas, V. M. (1983), Plasma Distribution and Flow, in *Phys. Jovian Magnetos.*, edited by A. J. Dessler, pp. 395–453, Cambridge University Press, Cambridge UK.
- Warwick, J., J. Pearce, and D. Evans (1981), Planetary radio astronomy observations from Voyager 1 near Saturn, *Science*, pp. 1–5.
- Warwick, J., D. Evans, and J. Romig (1982), Planetary radio astronomy observations from Voyager 2 near Saturn, *Science*, *215*, 582–587.
- Wilson, R. J., R. L. Tokar, M. G. Henderson, T. W. Hill, M. F. Thomsen, and D. H. Pontius (2008), Cassini plasma spectrometer thermal ion measurements in Saturn's inner magnetosphere, *J. Geophys. Res.*, *113*, A12218, doi:10.1029/2008JA013486.
- Wilson, R. J., R. L. Tokar, and M. G. Henderson (2009), Thermal ion flow in Saturn's inner magnetosphere measured by the Cassini plasma spectrometer: A signature of the Enceladus torus?, *Geophys. Res. Lett.*, *36*, L23104, doi:10.1029/2009GL040225.
- Young, D. T., et al. (2004), Cassini Plasma Spectrometer Investigation, *Space Sci. Rev.*, *114*, 1–112, doi:10.1007/s11214-004-1406-4.